

The Pennsylvania State University
The Graduate School

**DUCTED FAN INLET/EXIT AND ROTOR TIP FLOW
IMPROVEMENTS FOR VERTICAL LIFT SYSTEMS**

A Dissertation in
Aerospace Engineering
by
Ali Aktürk

© 2010 Ali Aktürk

Submitted in Partial Fulfillment
of the Requirements
for the Degree of

Doctor of Philosophy

August 2010

The thesis of Ali Aktürk was reviewed and approved* by the following:

Cengiz Camci
Professor of Aerospace Engineering
Dissertation Advisor, Chair of Committee

Savaş Yavuzkurt
Professor of Mechanical Engineering

Dennis K. McLaughlin
Professor of Aerospace Engineering

Edward C. Smith
Professor of Aerospace Engineering

Kenneth S. Brentner
Professor of Aerospace Engineering

Michael H. Krane
Research Associate, Applied Research Laboratory

George A. Lesieutre
Professor of Aerospace Engineering
Head of the Department of Aerospace Engineering

*Signatures are on file in the Graduate School.

Abstract

Ducted fan based vertical lift systems are excellent candidates to be in the group of the next generation vertical lift vehicles, with many potential applications in general aviation and military missions for both manned and unmanned systems. Ducted fans provide a higher static thrust/power ratio, improved safety and lower noise levels for a given diameter when compared to open rotors. Although ducted fans provide high performance in many “*Vertical Take-Off and Landing*” (VTOL) applications, there are still unresolved problems associated with these unique machines. The main problems are distortion of inlet flow due to forward flight and tip leakage related problems. Distorted inlet flow results in lip separation on the inner side of the lip section severely limiting the lift generation and controllability of vertical lift systems. Inlet flow distortions passing through a typical ducted fan rotor become increasingly detrimental with increasing forward flight velocity. Fan rotor tip leakage flow is another source of aerodynamic loss for ducted fan systems. Tip leakage related problems adversely affect the general performance of VTOL “*Uninhabited Aerial Vehicles*” (UAV) systems.

The current research utilized experimental and computational techniques in 5” and 22” diameter ducted fan test systems that have been custom designed and manufactured. Qualitative investigation of flow around the ducted fan was also performed using smoke flow visualizations. Quantitative measurements consisted of 2D and 3D velocity measurements using planar and Stereoscopic Particle Image Velocimetry (PIV and SPIV), high resolution total pressure measurements using Kiel total pressure probes and real time six-component force and torque measurements. The computational techniques used in this thesis included a recently developed radial equilibrium based rotor model(REBRM) and a three dimensional Reynolds-Averaged Navier Stokes (RANS) based CFD model.

A radial equilibrium based rotor model (REBRM) developed by the author was effectively integrated into a three-dimensional RANS based computational system. The PIV measurements and computational flow predictions using (REBRM) near the fan inlet plane were in a good agreement at hover and forward flight conditions. The aerodynamic modifications resulting from the fan inlet flow distortions in forward flight regime were clearly captured in 2D PIV results. High resolution total pressure measurements at the downstream of the fan rotor showed that tip leakage, rotor hub separation, and passage flow related total pressure losses were dominant in hover condition. However, the losses were dramatically increased in forward flight because of inlet lip separation and distortion.

A novel ducted fan inlet flow conditioning concept named “*Double Ducted Fan*” (DDF) was developed. The (DDF) concept has a potential to significantly improve the performance and controllability of VTOL UAVs and many other ducted fan based vertical lift systems. The new concept that will significantly reduce the inlet lip separation related performance penalties used a secondary stationary duct system to control “*inlet lip separation*” occurring especially at elevated forward flight velocities. The (DDF) is self-adjusting in a wide forward flight velocity range. DDFs corrective aerodynamic influence becomes more pronounced with increasing flight velocity due to its inherent design properties.

RANS simulations of the flow around rotor blades and duct geometry in the rotating frame of reference provided a comprehensive description of the tip leakage and passage flow in the flow environment of the two ducted fan research facilities developed throughout this thesis. The aerodynamic measurements and results of the RANS simulation showed good agreement especially near the tip region. A number of novel tip treatments based on custom designed pressure side extensions were introduced. Various tip leakage mitigation schemes were introduced by varying the chordwise location and the width of the extension in the circumferential direction. The current study showed that a proper selection of the pressure side bump location and width were the two critical parameters influencing the success of the tip leakage mitigation approach. Significant gains in axial mean velocity component were observed when a proper pressure side tip extension was used. It is also observed that an effective tip leakage mitigation scheme significantly reduced the tangential velocity component near the tip of the axial fan blade. Reduced tip clearance related flow interactions were essential in improving the energy efficiency and range of ducted fan based vehicle. Full and inclined pressure side tip sealers were designed. Squealer tips were effective in changing the overall trajectory of the tip vortex to a higher path in radial direction. The interaction of rotor blades and tip vortex was effectively reduced and aerodynamic performance of the rotor

blades was improved. The overall aerodynamic gain was a measurable reduction in leakage mass flow rate. This leakage reduction increased thrust significantly. Full and inclined pressure side tip sealers increased thrust obtained in hover condition by 9.1 % and 9.6 % respectively. A reduction or elimination of the momentum deficit in tip vortices is essential to reduce the adverse performance effects originating from the unsteady and highly turbulent tip leakage flows rotating against a stationary casing. The novel tip treatments developed throughout this thesis research are highly effective in reducing the adverse performance effects of ducted fan systems developed for VTOL vehicles.

Table of Contents

List of Figures	xi
List of Tables	xviii
List of Symbols	xix
Acknowledgments	xxiii
Chapter 1	
Introduction	1
1.1 Background: Ducted Fan Vertical Take-off Unmanned Vehicles	1
1.2 Patents Related to Ducted Fan Powered Vertical Lift Systems and Their Operation in Forward Flight	6
1.3 Past Studies of Ducted Fan Aerodynamics	17
1.4 Tip Leakage Flow	24
1.5 Objective of Current Research	28
Chapter 2	
Inlet/Exit Flow Aerodynamic Performance of	
Ducted Fan in Hover and Forward Flight	32
2.1 Experimental Setup	33
2.1.1 Ducted Fan Model	33
2.1.2 Crosswind Blower	35
2.2 Experimental Method	36
2.2.1 Planar Particle Image Velocimetry (PIV) Measurement Technique	36
2.3 Experimental Results in Hover and Forward Flight Conditions . .	38

2.4	Radial Equilibrium Based Analysis of Ducted Fan in Hover and Forward Flight	45
2.4.1	Computational Model Description	45
2.4.2	Boundary Conditions	45
2.4.2.1	Hover	45
2.4.2.2	Forward Flight	46
2.4.3	Actuator Disk Model	47
2.4.4	Computational Results	51
2.4.4.1	Grid Refinement Study	51
2.4.4.2	Model Validation at hover and forward flight . .	52
2.4.5	Summary	54

Chapter 3

A Novel Inlet Flow Conditioning Concept: Double Ducted Fan (DDF)		58
3.1	Introduction	58
3.2	Upstream Lip Region Flow Physics for Ducted Fans in Forward Flight	60
3.3	Lip Separation at High Angle of Attack	61
3.4	Adverse Effects of Upstream Lip Separation in Forward Flight . .	62
3.5	Reference Ducted Fan Characteristics	63
3.6	Double Ducted Fan (DDF)	64
3.6.1	Geometric Definition of DDF	66
3.6.2	Converging-Diverging Channel in the Duct	67
3.7	Various Possible Double Ducted Fan Geometries	67
3.8	DDF Concept Validation	71
3.8.1	Air Breathing Character of DDF in Forward Flight	71
3.9	A Comparative Evaluation of Local Velocity Magnitude, Stream- lines and Total Pressure for All Three Ducts	78
3.9.1	CASE-A Tall (DDF) versus Baseline Duct Results /at 10 m/s and 20 m/s	78
3.9.2	CASE-B Short (DDF) versus Baseline Duct Results at 10 m/s and 20 m/s	83
3.10	Upstream Lip Region Local Flow Improvements in (DDF)	87
3.10.1	Static Pressure Distribution around the Lip Section of the Baseline Duct	88
3.10.2	Static Pressure Distribution around the Lip section of the Double Ducted Fan (DDF)	89

3.10.3	Skin Friction Distribution around the Leading Edge of the Duct	90
3.11	Summary	91
Chapter 4		
Influence of Tip Clearance and Inlet Flow Distortion on Ducted Fan Performance in VTOL UAVs		94
4.1	Experimental Set-up	95
4.1.1	Penn State Mid-sized Wind Tunnel	95
4.1.2	Ducted Fan Model	95
4.1.3	Instrumentation	98
4.1.3.1	Thrust Measurements	98
4.1.3.2	Total Pressure Measurements	99
4.2	Experimental Results	100
4.2.1	Hover Condition Results	101
4.2.2	Forward Flight Results	103
4.2.3	Forward Flight Flow Visualization	105
4.2.4	Forward Flight Total Pressure Results	107
4.2.5	Effect of Tip Clearance in Forward Flight	109
4.2.6	Forward Flight Penalty	111
4.2.7	Effect of Forward Flight Speed	112
4.3	Computational Analysis of Ducted Fan in Hover Condition	114
4.3.1	Computational Model Description	115
4.3.1.1	Discretization of Governing Equations	115
4.3.1.2	Turbulence Model	118
4.3.1.3	Rotational Forces	120
4.3.2	Boundary Conditions for Hover	120
4.3.2.1	Interfaces Between Rotating and Stationary Frames	122
4.3.3	Hover Condition Results and Flow Field around the Fan Rotor	122
4.3.3.1	Validation of Numerical Results	123
4.3.3.2	Grid Refinement Study	124
4.3.3.3	Fan Rotor Exit Total Pressure	125
4.3.3.4	Effect of Rotor Hub Shape	126
4.4	Summary	128
Chapter 5		
Novel Tip Platform Extension Designs for Ducted Fan Tip Leakage Control		131

5.1	Experimental Set-up	132
5.1.1	Test rig	132
5.1.2	Ducted Fan Description and Performance	133
5.1.3	Stereoscopic PIV system	135
5.2	Experimental Methodology	136
5.2.1	Measurement Domain	136
5.2.2	Specific Rotor Positions for Phase-locked Measurements	137
5.2.3	Statistical Stability of SPIV Measurements	138
5.3	The General Impact of Tip Platform Extensions	140
5.3.1	Geometrical Definition of the Five Tip Platform Extensions	141
5.4	Experimental Results and Discussion	142
5.5	Summary	151

Chapter 6

6.1	Development of a Realistic Ducted Fan Research Facility and Novel Tip Leakage Control Devices	153
6.1.1	22" Diameter Ducted Fan Test System	154
6.1.2	Facility Description	154
6.1.2.1	Ducted Fan Model	154
6.1.2.2	Inlet Lip and Diffuser	155
6.1.2.3	Fan Rotor	157
6.1.3	Instrumentation of the 22" Ducted Fan	161
6.1.3.1	Rotor Exit Total Pressure Measurements	161
6.1.3.2	Six Component Force and Moment Measurement	165
6.1.3.3	Fan Rotor Rotational Speed Measurement	166
6.2	Baseline Aerodynamic Measurements	166
6.2.1	Force and Torque Measurements	167
6.2.2	Total Pressure Measurements at Rotor Exit	169
6.3	Design of Novel Tip Treatments for Effective Leakage Control	172
6.3.1	Computational Method	173
6.3.1.1	Computational Domains and Boundary Conditions	173
6.3.1.2	Grid Refinement Study	174
6.3.1.3	Validation of Numerical Results	175
6.3.1.4	Computational Result for Baseline	178
6.3.2	Tip Treatments	186
6.3.2.1	Partial Bump Tip Platform Extension	188
6.3.2.2	Full Bump Tip Platform Extension	188
6.3.2.3	Full Bump and Partial Squealer Tip Platform Extension	190

6.3.2.4	Full Squealer Tip Platform Extension	193
6.3.2.5	Inclined Full Squealer Tip Platform Extension . .	193
6.3.2.6	Overall Benefits of Tip Treatmens	195
6.4	Novel Tip Treatment Concept Development via Ducted Fan Experiments	198
6.4.1	Manufacturing Tip Platform Extensions Using a Stereolithography Based Rapid Prototyping Technique .	198
6.4.2	Force and Torque measurements	199
6.4.3	Total Pressure Measurements	202
6.5	Summary	203
Chapter 7		
Conclusions and Future Work		207
7.1	Summary and Conclusions	208
7.1.1	Forward Flight Related Investigations	208
7.1.1.1	Conclusions	209
7.1.2	Tip Leakage Related Investigations	211
7.1.2.1	Conclusions	213
7.2	Recommendations for Future Work	215
Appendix A		
Implementation Radial Equilibrium Theory Based Rotor Model in ANSYS FLUENT Using User Defined Functions		217
A.1	Introduction	217
A.2	UDF for Fan Boundary Condition " <i>fan.c</i> "	217
Appendix B		
Uncertainty Analysis		223
B.1	Introduction	223
Appendix C		
Six Component Force and Torque Transducer Calibration and Accuracy Reports		225
Bibliography		228

List of Figures

1.1	Hiller's flying platform and AROD unmanned vehicle	2
1.2	Sikorsky Cypher I and Sikorsky Cypher II	3
1.3	iSTAR micro air vehicle	4
1.4	Dragon-Stalker (Traffic Surveillance Drone project UAV) and BAE systems IAV2	4
1.5	GoldenEye-50 VTOL UAV	5
1.6	Honeywell MAV	6
1.7	La Sapienza UAV by University of Rome	7
1.8	Piasecki air jeep	9
1.9	Side view and a partial section of a VTOL design by Wen	10
1.10	Control vanes, spoilers and thrust reverser designs of Moller	10
1.11	Sikorsky Cypher I with two co-axial counter-rotating rotors in a ducted fan arrangement	11
1.12	Sikorsky Cypher II with pusher propellers	14
1.13	A ducted fan based VTOL vehicle including a fuselage having a longitudinal axis and a transverse axis, two counter rotating ducted fan lift producing propellers	16
1.14	Thrust variation with rpm and tip gap surface flow visualization of rotor induced separation in the tip path plane obtained by Martin and Tung	19
1.15	Control devices tested by Fleming <i>et al.</i>	20
1.16	Tested inlet lip shapes Graf <i>et al.</i>	21
1.17	Notched and stepped duct designs by Martin and Boxwell	23
1.18	Schematic of leakage flowfield in an axial flow compressor or fan	25
1.19	Tip end plates designed for reducing tip leakage flow Corsini <i>et al.</i>	27
1.20	Tip treatments used by Wisler	28
1.21	Thesis organization chart	31
2.1	Cross wind blower, the ducted fan and the PIV system orientation	34
2.2	Five inch diameter five-bladed ducted fan	35

2.3	Influence of ensemble averaging “ <i>image sample size</i> ” on the axial velocity component	38
2.4	Streamlines at inlet and exit of ducted fan for HOVER (a) and FORWARD FLIGHT (b) (PIV measurements at 9000 rpm)	39
2.5	Streamlines at inlet and exit of ducted fan for HOVER (a) and FORWARD FLIGHT (b) (PIV measurements at 15000 rpm)	40
2.6	Axial Velocity Distribution at the inlet and exit of ducted fan at 9000 rpm	41
2.7	Axial (a) and Radial (b) velocity components at HOVER condition (PIV measurements at 9000 rpm)	42
2.8	Axial (a) and Radial (b) velocity components at HOVER condition (PIV measurements at 15000 rpm)	42
2.9	Axial (a) and Radial (b) velocity components at FORWARD FLIGHT condition (PIV measurements at 9000 rpm)	43
2.10	Axial (a) and Radial (b) velocity components at FORWARD FLIGHT condition (PIV measurements at 15000 rpm)	44
2.11	Flowchart of the 3D RANS based computational method including the actuator disk.	46
2.12	Boundary conditions for hover	47
2.13	Boundary conditions for forward flight	48
2.14	Velocity triangles at the inlet and exit of the ducted fan rotor	49
2.15	Grid indepence study	51
2.16	Medium mesh used in computations	52
2.17	Comparison of axial velocity at fan inlet 3 mm away from the duct surface at hover condition 9000 rpm.	53
2.18	Comparison of axial velocity at fan exit 3 mm away from the duct surface at hover condition 9000 rpm.	54
2.19	Comparison of CFD and PIV axial velocity contours at hover condition at hover condition 9000 rpm.	55
2.20	Comparison of CFD and PIV axial velocity contours and streamlines at forward flight 9000 rpm and 6 m/s.	56
3.1	Upstream duct lip stall in function of angle of attack for X-22A ducted fan by Mort and Gamse	62
3.2	Reference ducted fan and fan rotor used for DDF development effort	64
3.3	Separated flow near the forward lip section of a standard ducted fan (left) and the flow improvements from the novel concept Double Ducted Fan (DDF) at 9000 rpm,colored by the magnitude of velocity	65

3.4	(a)Reference duct airfoil definition in a standard ducted fan arrangement, (b)Double Ducted Fan (DDF) geometry as a novel concept	66
3.5	(a)Baseline ducted fan (Standard duct), (b)CASE-A tall double ducted dan (DDF)	68
3.6	(a)CASE-B short double ducted fan (b)Eccentric double ducted fan	69
3.7	Rotor disk mass flow rate versus forward flight speed at 9000 rpm	72
3.8	Rotor inlet total pressure deficit at elevated forward flight speed for the baseline ducted fan $P_{t,inlet@10m/s} = 61.25$ pa , $P_{t,inlet@20m/s} = 245$ pa	75
3.9	Reduction in rotor inlet flow distortion between the leading side and trailing side of (DDF) CASE-B short double ducted fan $P_{t,inlet@20m/s} = 245$ pa	77
3.10	Velocity magnitude and total pressure distribution,baseline duct versus CASE-A tall double ducted fan (DDF) at 10 m/s forward flight velocity	80
3.11	Total pressure distribution at rotor exit plane (horizontal) baseline duct versus CASE-A tall double ducted fan (DDF) at 10 m/s forward flight velocity	81
3.12	Velocity magnitude and total pressure distribution, baseline duct versus CASE-A tall double ducted fan (DDF) at 20 m/s forward flight velocity	82
3.13	Total pressure distribution at rotor exit plane (horizontal) baseline duct versus CASE-A tall double ducted fan (DDF) at 20 m/s forward flight velocity	83
3.14	Velocity Magnitude and total pressure distribution, baseline duct versus CASE-B short double ducted fan (DDF) at 10 m/s forward flight velocity	84
3.15	Total pressure distribution at rotor exit plane (horizontal) baseline duct versus CASE-B short double ducted fan (DDF) at 10 m/s forward flight velocity	85
3.16	Velocity magnitude and total pressure distribution, baseline duct versus CASE-B short double ducted fan (DDF) at 20 m/s forward flight velocity	86
3.17	Total pressure distribution at rotor exit plane (horizontal) baseline duct versus CASE-B short double ducted fan (DDF) at 20 m/s forward flight velocity	87

3.18	Sampling locations for static pressure and skin friction coefficient computations near the leading side of the inner duct for (DDF) CASE-B	88
3.19	Comparison of the static pressure distribution on the baseline lip section and inner duct lip section of the (DDF) CASE-B airfoil	89
3.20	Comparison of the skin friction coefficient distribution on the baseline lip section and inner duct lip section of the (DDF) airfoil	91
4.1	The Penn State mid-sized wind tunnel	95
4.2	Wind tunnel model simulating VTOL UAV at forward flight	96
4.3	Ducted fan, five-bladed fan rotor and tip clearance definition	97
4.4	5" diameter ducted fan test system	99
4.5	United Sensors Kiel total pressure rake	100
4.6	Rotor exit velocity triangle and orientation of Kiel probe	101
4.7	Disk loading versus rotational speed at hover condition for the current VTOL UAV wind tunnel model	102
4.8	Radial distribution of total pressure coefficient at 12000 rpm hover condition	103
4.9	Wind tunnel experimental setup for forward flight condition	104
4.10	Smoke visualization at 6000 rpm and 5 m/s	106
4.11	Comparison of hover and forward flight at 12000 rpm and 10 m/s forward flight speed	108
4.12	Comparison of tip clearance effect at forward flight at 12000 rpm and 10 m/s forward flight speed	110
4.13	Forward flight penalty calculated at 12000 rpm and 10 m/s forward flight speed 0°	112
4.14	Effect of forward flight speed for 5.8% tip clearance	113
4.15	Effect of forward flight speed for 3.6% tip clearance	114
4.16	Two dimensional mesh element	116
4.17	Tetrahedral element used in computations	117
4.18	Computational domain and boundary conditions for hover condition	121
4.19	Convergence history plot of mass flow rate at the downstream of fan rotor	123
4.20	Comparison of experimental results to computational results at hover condition at 12000 rpm.	124
4.21	Grid independency study	125
4.22	Fan rotor exit total pressure contour	126
4.23	Computationally obtained streamlines near the ducted fan at 12000 rpm, in the relative frame of reference	127

4.24 Streamlines drawn around fan rotor hub for two different configurations (a) rotor hub without a cavity on center and step on corner (b) rotor hub with a cavity on center and step on corner	129
5.1 Test rig and stereoscopic SPIV setup	132
5.2 Axial flow fan as seen from the exit plane and the SPIV system orientation	133
5.3 Geometric and blade section parameters of axial flow fan	134
5.4 Axial flow fan performance	135
5.5 SPIV measurement plane (horizontal) downstream of the rotor exit and the coordinate system	137
5.6 Influence of sample size in SPIV ensemble averaging	139
5.7 Novel tip platform extensions for tip leakage mitigation	140
5.8 Velocity profiles measured at location 3 for two different tip clearances	143
5.9 Velocity profiles measured at location 3 ($340 \text{ m}^3/\text{min}$, 32 Pa)	144
5.10 Velocity profiles measured at location 4 ($340 \text{ m}^3/\text{min}$, 32 Pa)	145
5.11 Velocity profiles measured at location 5 ($340 \text{ m}^3/\text{min}$, 32 Pa)	146
5.12 Velocity profiles measured at location 3 (high ΔP with 19.6% perforated plate, $80\text{m}^3/\text{min}$, 140 Pa)	147
5.13 Total velocity contour and streamlines at location 3 for baseline profile ($340 \text{ m}^3/\text{min}$, 32 Pa)	148
5.14 Total velocity contour and streamlines at location 3 for 2^{nd} profile ($340 \text{ m}^3/\text{min}$, 32 Pa)	149
5.15 Flow coefficient calculated at location 3 ($340 \text{ m}^3/\text{min}$, 32 Pa)	150
6.1 Schematic of the 22" diam. ducted fan test system	156
6.2 Instrumentation of the 22" diam. ducted fan system	156
6.3 Cross section view of inlet lip(a) and diffuser(b)	157
6.4 Rotor power loading vs disk loading chart	159
6.5 Cross section view of inlet lip(a) and diffuser(b)	160
6.6 Circumferential distribution of tip clearance in the ducted fan	162
6.7 Yaw angle in absolute frame calculated from initial computations	163
6.8 Influence of acquisition time in ensemble averaging	164
6.9 Applied force and torque vector on transducer	166
6.10 Thrust coefficient versus fan rotational speed during hover (baseline rotor)	168
6.11 Thrust coefficient vs power coefficient for the baseline rotor	170
6.12 Figure of Merit (FM) vs fan rotational speed for the baseline rotor	170
6.13 Total pressure measured at downstream of the rotor at 2400 rpm	171

6.14	Total pressure ratio for three tip clearances at 2400 rpm	171
6.15	Baseline tip (a) and squealer tip (b) sketch	172
6.16	Computational domains and boundary conditions used in computations	175
6.17	Grid independence study	176
6.18	Medium size computational mesh used in computations	177
6.19	Total pressure coefficient comparison for experimental and computational analysis at 2400 rpm	178
6.20	Absolute velocity magnitude and streamlines drawn on half of vertical cross section	180
6.21	Streamlines around the baseline rotor blade with 1.71 % tip clearance and rotor hub at 2400 rpm	181
6.22	Relative total pressure distribution at the rotor exit plane for the baseline blade with 1.71 % tip clearance	182
6.23	Relative total pressure distribution at the rotor exit plane for the baseline blade with 3.04 % tip clearance	184
6.24	Location of blade tip constant circumferential planes	185
6.25	Blade tip constant circumferential planes drawn for baseline rotor tip with 3.04 % tip clearance	185
6.26	Tip treatments (a) Partial bump tip platform extension (t.p.e.), (b) Full bump t.p.e., (c) Full bump and partial squealer t.p.e., (d) Full squealer t.p.e., (e) Inclined full squealer t.p.e.	187
6.27	Blade tip constant circumferential angle planes drawn for “ <i>partial bump</i> ” tip extension with 3.04 % tip clearance	189
6.28	Blade tip constant circumferential angle planes drawn for “ <i>full bump</i> ” tip extension with 3.04 % tip clearance	191
6.29	Blade tip constant circumferential angle planes drawn for “ <i>full bump and partial squealer</i> ” tip extension with 3.04 % tip clearance	192
6.30	Blade tip constant circumferential angle planes drawn for “ <i>full squealer</i> ” tip extension with 3.04 % tip clearance	194
6.31	Blade tip constant circumferential angle planes drawn for “ <i>inclined squealer</i> ” tip extension with 3.04 % tip clearance	196
6.32	Leakage surface used to compute leakage mass flow rate.	197
6.33	Comparison of stagnation total pressure distribution for all the blade treatments and baseline rotor tip.	198
6.34	Squealer and inclined squealer tip extensions designed for SLA manufacturing	199
6.35	Inclined squealer t.p.e. applied to the rotor blade	200
6.36	Thrust coefficient versus rotational speed for the rotor with squealer and inclined squealer tips at 3.04 % tip clearance	201

6.37	Thrust coefficient versus rotational speed for rotor with squealer and inclined squealer tips at 5.17 % tip clearance	201
6.38	Figure of merit versus rotational speed for rotor with squealer and inclined squealer tips at 3.04 % tip clearance	202
6.39	Figure of merit vs rotational speed for rotor with squealer and inclined squealer tips at 5.17 % tip clearance	202
6.40	Total pressure measured at downstream of the rotor at 2400 rpm for squealer tips wit 3.04 % tip clearence	204
6.41	Total pressure measured at downstream of the rotor at 2400 rpm for squealer tips wit 5.17 % tip clearence	204
C.1	Full scale loads and applied loads during calibration for six component F/T transducer	226
C.2	Full scale errors for six component F/T transducer	227

List of Tables

2.1	Geometric specifications of five inch ducted fan	35
3.1	Computed rotor mass flow rate for all fan configurations during hover and forward flight	71
4.1	Geometric specifications of five inch ducted fan	98
5.1	Uncertainties of ensemble averaged velocities components	138
6.1	Fan rotor geometric and blade section properties	158
6.2	Penn State 22" fan rotor tip clearance measurements.	161
6.3	Tip treatments and their computed performance in hover condition at 2400 rpm	197
B.1	Standard Deviations (σ) calculated for P_{ti}, P_{te} and U_m	224

List of Symbols

C	Chord length (m)
c_1	Rotor inlet absolute velocity ($\frac{m}{s}$)
c_2	Rotor exit absolute velocity ($\frac{m}{s}$)
C_p	Static pressure coefficient
C_{pt}	Total pressure coefficient, $C_{pt} = \frac{P_{te} - P_{ti}}{\frac{1}{2}\rho U_m^2}$
c_θ	Tangential(swirl) component of the velocity ($\frac{m}{s}$)
C_P	Power coefficient, $C_P = \frac{\text{Power}}{\rho\omega^3 D^5}$
C_T	Thrust coefficient, $C_T = \frac{\text{Thrust}}{\rho\omega^2 D^4}$
c_x	Axial component of the velocity ($\frac{m}{s}$)
D	Shroud (casing) inner diameter (m)
D_L	Shroud (duct) lip diameter (m)
D_R	Fan rotor diameter (m)
e_1	Rotor inlet internal energy (Joule)
e_2	Rotor exit internal energy (Joule)
FM	Figure of merit, $FM = \frac{C_T^{3/2}}{\sqrt{2}C_P}$
h	Blade height (m)
\dot{m}	Mass flow rate ($\frac{kg}{s}$)

N	Number of SPIV speckle images
P	Static pressure (Pa)
P_T	Total pressure (Pa)
r	Radial position, ($r=0.0$ at axis of rotation) (m)
\mathfrak{R}	Ideal gas constant,(for air $\mathfrak{R} = 287 \frac{J}{kg \cdot K}$)
R	Radius (m)
t	Effective tip clearance (in)
T	Static temperature (K)
U_a	Averaged inlet axial velocity ($\frac{m}{s}$)
U_m	Rotor speed at mid span ($\frac{m}{s}$)
V_{ref}	Reference Velocity ($\frac{m}{s}$)
w_1	Rotor inlet relative velocity ($\frac{m}{s}$)
w_2	Rotor exit relative velocity ($\frac{m}{s}$)
X	Axial coordinate measured from the inlet plane of the standard duct (m)
x	$x = X/C$, non-dimensional axial distance
y^+	Non-dimensional wall distance

Greek

β_1	Blade section inlet angle (degrees)
β_2	Blade section exit angle (degrees)
ϵ	Experimental uncertainty
μ	Viscosity ($\frac{kg}{s \cdot m}$)

- μ_t Eddy viscosity ($\frac{kg}{s \cdot m}$)
 ϕ Flow coefficient, $\phi = \frac{c_x}{\Omega r}$
 ρ Density ($\frac{kg}{m^3}$)
 k Turbulent kinetic energy
 σ Standard deviation
 Ω Rotational speed ($\frac{rad}{s}$)
 ω Turbulent frequency (radians)
 ν Kinematic viscosity ($\frac{m^2}{s}$)

Subscripts

- 1 Rotor inlet
 2 Rotor exit
 a Ambient(pressure or temperature)
 H Hover
 hub Rotor hub
 FF Forward flight (Edgewise flight)
 m Rotor mid-span
 max Maximum
 tip Rotor tip

Abbreviations

<i>AC</i>	Alternating Current
<i>CCD</i>	Charge-Coupled Device
<i>CFD</i>	Computational Fluid Dynamics
<i>DC</i>	Direct Current
<i>DPIV</i>	Digital Particle Image Velocimetry
<i>DDF</i>	Double Ducted Fan
<i>ESC</i>	Electronic Speed Controller
<i>FFP</i>	Forward flight penalty
<i>HOVTOL</i>	Horizontal or Vertical Take-Off and Landing
<i>LED</i>	Light-Emitting Diode
<i>MAV</i>	Micro Aerial Vehicles
<i>OGV</i>	Outlet Guide Vane
<i>PLIF</i>	Phosphorescence Laser Induced Flourosence
<i>RANS</i>	Reynolds-Averaged Navier Stokes
<i>REBRM</i>	Radial Equilibrium Based Rotor Model
<i>SPIV</i>	Stereoscopic Particle Image Velocimetry
<i>VTOL</i>	Vertical Take-Off and Landing
<i>V/STOL</i>	Vertical/Short Take-Off and Landing
<i>UAV</i>	Uninhabited Aerial Vehicles

Acknowledgments

I would first and foremost like to express my sincere gratitude to my advisor, Professor Cengiz Camcı, whose support and guidance made my thesis work possible. I am very grateful for his patience, motivation, enthusiasm, and immense knowledge. Throughout my doctoral study, he provided encouragement, advice, good company, and lots of good ideas.

I owe also many thanks to the members of my dissertation committee, Dr. Kenneth S. Brentner, Dr. Savaş Yavuzkurt, Dr. Dennis K. McLaughlin, Dr. Edward C. Smith and Dr. Michael H. Krane for reading drafts and providing valuable references, insight, and constructive suggestions.

I also gratefully acknowledge the financial support provided by the PSU Vertical Lift Center of Excellence (VLRCOE) and National Rotorcraft Technology Center (NRTC) (Under U.S. Army Research Office grant # W911W6-06-2-0008).

I warmly thank my friend and colleague Özhan Turgut for his friendship, patience and scientific support. I also wish to thank Dr. Jeremy Veltin for his help in flow visualization experiments.

I am also indebted to Mr. Harry Houtz his outstanding technical support. Additional thanks go to Richard Auhl and Kirk Heller for facility support.

I owe special thanks to my friends who shared the difficulties with me and gave me encouragement and spiritual companionship. Especially I want to thank Dr. Çaglan Kumbur, Hakan and Ezgi Arslan, Sinem Turgut, Ceyda Çoruh, Cihangir and Gonca Çelik, Dr. Ahmet Turhan and Dr. Başar Başbuğ for their valuable friendship, motivation and support.

My parents, Kemal and Ruhiye Aktürk deserve my highest respect and deepest

gratitude for their constant support and encouragement in all the steps that I took over the years. They did all the things that perfect parents do, and more. I feel so lucky to have them.

Last but by no means least, I would like to express my deepest thanks and gratitude to my wife Esra for her endless emotional support throughout the long process of this thesis. I would definitely not have been able to complete my PhD work successfully without her extensive help, patience, sacrifice, support, encouragement and prayers.

Chapter 1

Introduction

1.1 Background: Ducted Fan Vertical Take-off Unmanned Vehicles

Ducted fan type propulsion offers an attractive solution by providing operational safety as well as compact vehicle/payload packaging. Ducted fans have several advantages compared to free rotors. They provide higher thrust to power ratio compared to free rotors, that is the result of diffusion of the propeller jet stream. They also provide an impact protection for the blades and improve personnel safety. Using ducted fans as propulsion systems for vertical-take-off-and-landing (VTOL) aircrafts is not new. The Hiller flying platform which is shown in Figure 1.1a was one of the first ones [1]. This vehicle was 8 feet in diameter, 7 feet high, weighted 180lbs empty.

After Hiller 's flying platform, Sandia National Laboratories developed Airborne Remotely Operated Device (AROD) [2] which is shown in Figure 1.1b. AROD was a 16" diameter ducted fan VTOL unmanned aerial vehicle (UAV) that could easily translate through the air and provide short range aerial surveillance. The most recent generation AROD vehicle was using 26-horsepower, two-stroke gasoline engine, driving a single lifting propeller. AROD also used exit flow control vanes to control forward and sideward pitch, and rotation.

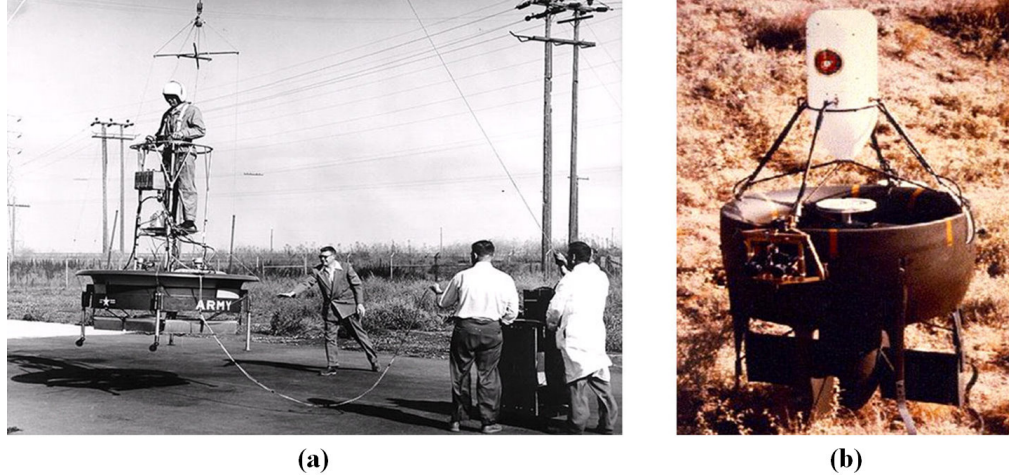


Figure 1.1. (a) Hiller’s flying platform [1] and (b) AROD unmanned vehicle [2]

In early 1990’s, Sikorsky developed Cypher ducted-rotor VTOL craft to meet the US close-range UAV requirement [3]. The Cypher which is shown in Figure 1.2a makes use of Sikorsky’s co-axial advancing-blade concept rotor system and fantail ducted tail-rotor technology in a doughnut-shaped shrouded-rotor UAV. The first prototype of Cypher was 6.2 feet in diameter, 2 feet tall and weighed 240 pounds. This design was powered by a Wankel rotating piston engine, 37kW (50 hp). After finishing tests with Cypher, Sikorsky produced two prototypes for the US Marine Corps. They called the Cypher II “*Dragon Warrior*”. The Cypher II shown in Figure 1.2b is similar in size to its predecessor, but has an additional pusher shrouded propeller along with its rotor and can be fitted with wings for long-range missions.

In its winged configuration, the Cypher II has a range of over 115 miles and a top speed of 145 mph (230 km/h). This vehicle used elevons in the fixed wing section to counteract pitch-up moments produced in high forward flight speeds. One of the recent ducted fan based VTOL UAV was produced at Georgia Tech. The Mass HeliSpy [4] has capabilities of both a helicopter and an airplane. The HeliSpy could take off and land vertically and maneuvers laterally like a helicopter. The HeliSpy was 11 inches in diameter and 27 inches tall and weighed 6 pounds. A control system was designed and tested for HeliSpy at Georgia Tech.

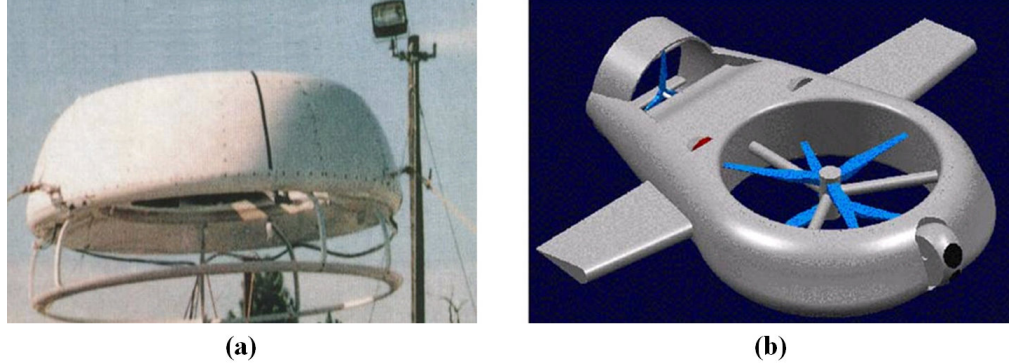


Figure 1.2. (a) Sikorsky Cypher I and (b) Sikorsky Cypher II [3]

The Allied Aerospace company developed the iSTAR micro air vehicle (MAV) in the year 2000 [5]. The iSTAR which is illustrated in Figure 1.3 was a 9-inch diameter ducted air vehicle weighing approximately 4 pounds. It was also 12 inch tall. The iSTAR used an OS-32 SX single cylinder engine which develops 1.2hp. It also used directly driven fixed pitch propeller. The structure is comprised of an outer duct enclosing the fan system, center body (for avionics and subsystems), fixed stators and movable vanes operated by actuators (for thrust vectoring). The engine is housed in the center body, and fuel tanks are located in the forward section of the duct. A variety of payloads may be carried in either the nose, tail or duct of the vehicle.

The Dragon-Stalker which is shown in Figure 1.4a was developed by Georgia Tech Research Institute's Advanced Vehicle Development and Integration Laboratory for the Traffic Surveillance Drone project [6]. The vehicle was designed around an aluminum chassis with a carbon composite body structure. It used a 17 hp air cooled two cycle engine and a 4 bladed rotor and weighed 200 pounds.

Recently, BAE Systems developed IAV2 [7]. Like the other VTOL UAVs, IAV2 which is illustrated in Figure 1.4b was designed to operate in hover and forward wing-borne flight modes, the latter providing increased operational range and fuel efficiency. It used a 22-inch-diameter fan with a nominal outside diameter of 37 inches. The vehicle was about 5 feet tall and was flown with simulated payloads of up to 25 pounds.

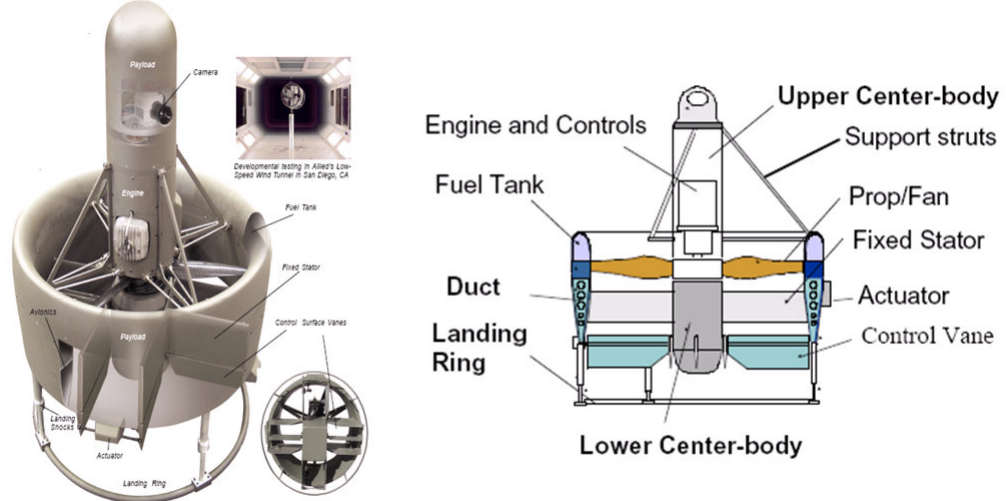


Figure 1.3. iSTAR micro air vehicle [5]

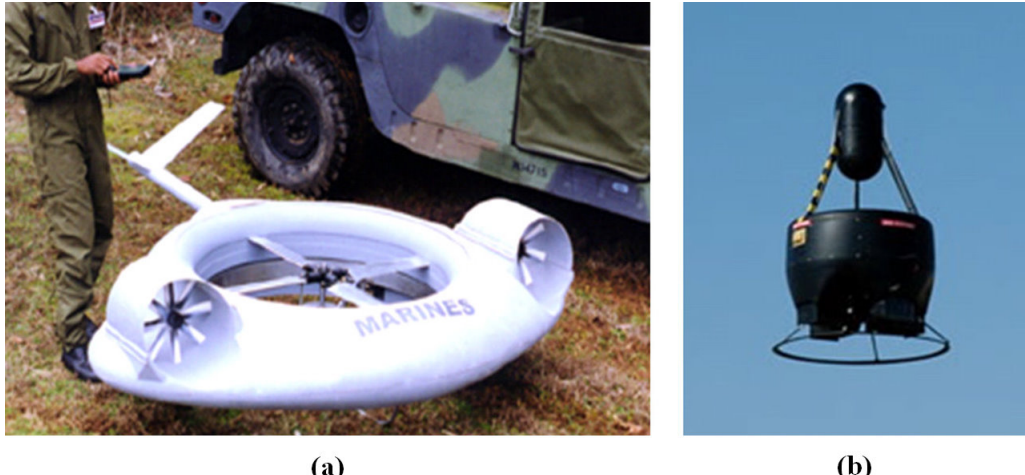


Figure 1.4. (a)Dragon-Stalker (Traffic Surveillance Drone project UAV) [6] and (b)BAE systems IAV2 [7]

GoldenEye-50 shown in Figure 1.5 was designed to carry surveillance and chemical agent detection sensors to restricted, hard-to-reach, or dangerous locations [8]. GoldenEye-50 was 70 cm tall with a wingspan of 1.4 m. It had a gross takeoff weight of 10 kg, and a payload of 1 kg. The aircraft was able to cruise up to 1 hour at 100 km/h with a maximum speed of 280 km/h.



Figure 1.5. GoldenEye-50 VTOL UAV [8]

Honeywell designed a MAV which was used for the first time in combat missions by US army [9]. This MAV as illustrated in Figure 1.6 was small enough to carry in a backpack and was equipped with video cameras that relay information back to foot soldiers using a portable hand held terminal. The 13 inch diameter vehicle had a circular cross section and just weighted 16 pounds. This MAV can be launched in 15-knot winds and operated in 20-knot winds. Honeywell's MAV used a 56cc Bower Twin piston engine and will deliver a power of 4.2bhp at 8200 rev/min using JP8 fuel.

Apart from these, a challenging VTOL UAV was designed at Polytechnic of Turin and University of Rome “La Sapienza” [10]. This UAV as shown in Figure 1.7 was designed for research and test purposes. The specific vehicle was in many aspects an innovative system and its size and performance allowed applications such as coastal observation, geological surveying, reconnaissance and autonomous package delivery and collection in remote areas. This vehicle is a shrouded-fan-type UAV that has a diameter of 1.9 meter. It uses counter rotating rotors for propulsion and control purposes. Maximum take-off weight of the craft was 900N and It had a



Figure 1.6. Honeywell MAV [9]

capability to carry a 100N payload and 201 N of fuel. This UAV has one engine out flight capacity. The fuselage and shroud of the UAV is manufactured from carbon fiber. Each rotor had six blades that are 0.5m long. The clearance between rotor blade tip and fuselage is 0.002m (0.4 % of blade radius). The power plant of the UAV includes three Vittorazi two-stroke, air-cooled one-cylinder engines. Each engine produced 14 horsepower at 11,000 rev/min. Detailed information about their design can be found in the study [10] carried at Polytechnic of Turin and University of Rome 'La Sapienza' .

1.2 Patents Related to Ducted Fan Powered Vertical Lift Systems and Their Operation in Forward Flight

Ducted fans are very popular among the vertical lift systems. They have been used in many conceptually designed VTOL vehicles. Patents related to ducted fan powered vertical take-off vehicles are described in this section.

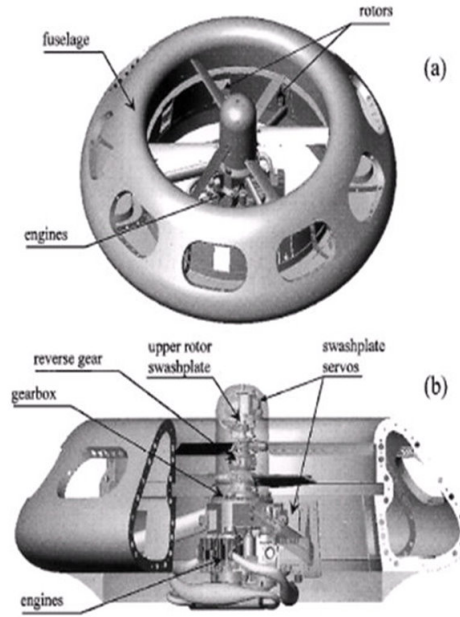


Figure 1.7. La Sapienza UAV by University of Rome [10]

Dorman, 2,951,661 (1960): Four ducted fan/propeller units located on each quadrant of a square vehicle footprint are used as lift generating components to be used in a heavier than air VTOL vehicle, Dorman [11]. The axis of rotation of each ducted fan unit is normal to the horizontal plane. This is one of the earliest presentations of using ducted fans in VTOL vehicle applications. This patent does not include any discussion on lip separation problem in forward flight regime.

Bright, 2,968,453 (1961): Bright [12] presented an early form of the two well known and more recent vehicle concepts from Yoeli [13] (Xhawk) and Piasecki [14] (Piasecki Air Jeep). Two ducted fans are embedded into a relatively flat fuselage with two fixed wings extending from the sides of the fuselage. An extensive adjustable shutter based exit flow control system was used to control the side force, yaw, pitch and roll motions of the vehicle. Inlet flow to the ducted fan units were not treated using louvers, vanes or shutters of any kind. Leading side lip separation problem is not mentioned.

Fletcher, 2,988,301 (1961): A V/STOL aircraft concept using a counter rotating ducted fan embedded in a flat airfoil shaped fuselage was presented by Fletcher [15] in an effort to transition a V/STOL aircraft to propel itself in high speed flight. Forward flight related propulsive force was obtained from a conventional propeller mounted on the aft section of the vehicle. This vehicle has a provision to close the inlet surface of the fan rotor system completely in forward flight only relying on the lift force generated by the airfoil shaped fuselage and the propulsive force of the aft propeller. Inlet lip separation problem inherent to most ducted fan based systems of this type was never mentioned in this reference.

Piasecki, 3,184,183 (1965): This patent[14] explains Frank Piasecki's well publicized "Air Jeep" concept shown in Figure 1.8 that uses two counter rotating lifting rotors in a tandem ducted fan arrangement. This approach was unique because of a novel control linkage for its ducted vertical lift rotors for adjusting cyclic pitch and collective pitch of the rotating blades. The propulsive force in Piasecki's approach [14] was obtained by cyclic and collective control of the rotor blades operating in a ducted fan arrangement. The rotor performance variation affected the local flow features near the leading side lip section of the duct. A significant component in this patent was the use of a movable spoiler in the inner part of the leading side lip of the duct. A movable spoiler that had a serrated edge is used to control local flow characteristics over the lip radius in an effort to reduce the drag (aerodynamic loss) generated over this area, especially in horizontal flight. This is one of the first known attempts to correct the inlet lip separation problem using a movable spoiler located over an arc length of the inlet lip. However, the specific corrective action taken for the lip separation problem is based on adjustable inlet boundary layer tripping.

Boyd, 3,159,224 (1970): This invention from Boyd [16] focused on a circular aircraft using an outer circumferential fan type ducted rotor mounted on air bearings. The ducted rotor was driven by outboard gas generators. This system used adjustable radial stator blades above the rotor. The stator blades were differentially adjustable in the forward and rearward quadrants to control the attitude

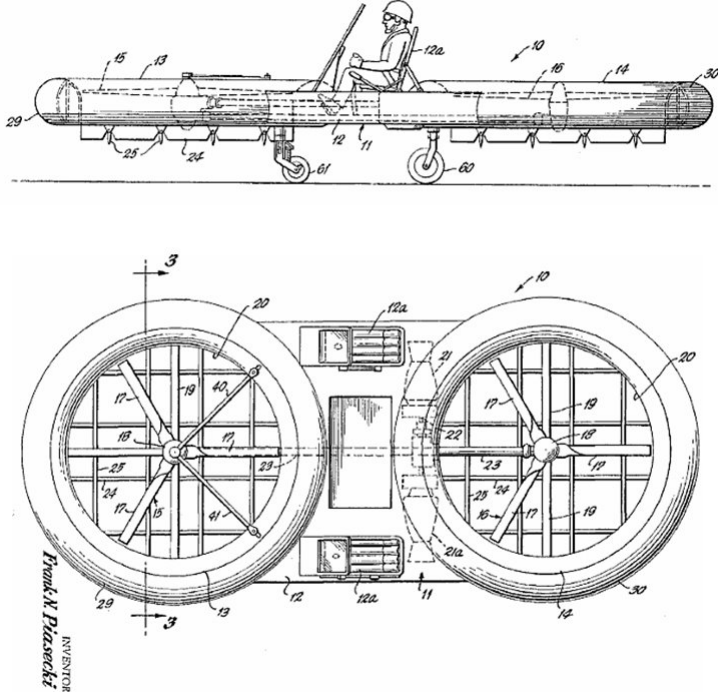


Figure 1.8. Piasecki air jeep [14]

of the aircraft with respect to its pitch axis. The stator blades in the left and right side quadrants could control the attitude of the aircraft with respect to its roll axis. The heading of the aircraft was controlled by means of a set of radial stator blades at the exit of the rotor. This approach only deals with the attitude control of a circular V/STOL vehicle and there is no treatment in this document in regard to possible inlet lip separation problem.

Wen 4,049,218 (1977): Wen *et al.* [17] described a VTOL aircraft using a centrifugal impeller generating a fan exit jet that can attain high exit jet velocities for effective vertical take off. His concept is shown in Figure 1.9. The centrifugal impeller output is passed through a diffuser section and deflected down to lift the aircraft. The impeller may be retracted down along its axis of rotation during transition to horizontal flight. The impeller exit is directed towards an exit nozzle at the aft section of the aircraft for the horizontal thrust needed for transition and forward flight. Although this is an interesting concept utilizing a centrifugal fan, its inlet flow characteristics and the influence of inlet flow distortion on the fan

performance are not discussed in this patent document [17].

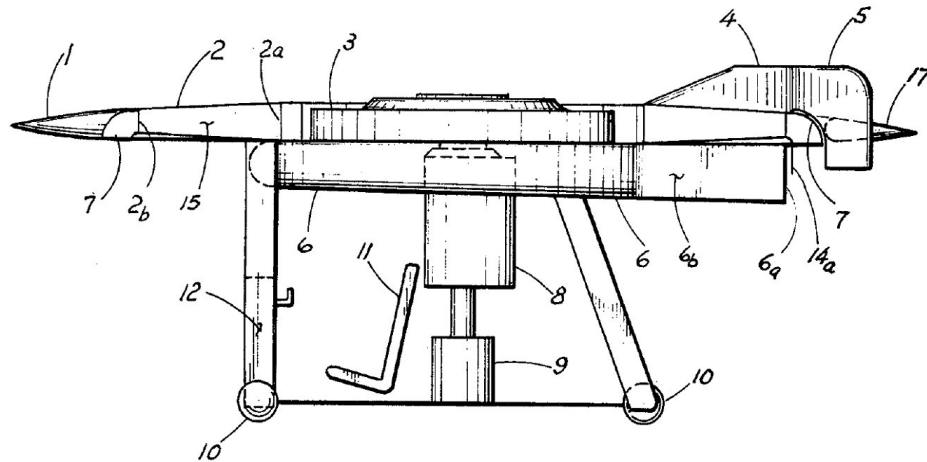


Figure 1.9. Side view and a partial section of a VTOL design by Wen *et al.* [17]

Moller, 4,795,111 (1989): One of the earliest patents is a flying robotic platform using a conventional ducted fan and a set of two mutually perpendicular vane systems from Moller [18]. The patent focuses on flexible variable camber flaps and exit flow control features which are illustrated in Figure 1.10 with no mention of inlet lip separation problem for this type of vehicle. Radio control of flexible control surfaces and unique arrangements of spoilers and flaps are described.

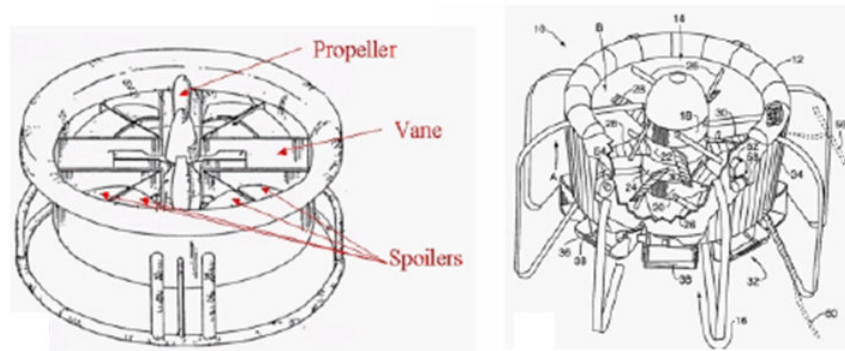


Figure 1.10. Control vanes, spoilers and thrust reverser designs of Moller [18]

Cycon et al. 5,152,478 (1992): Sikorsky Cypher [19] shown in Figure 1.11 was an uninhabited aerial vehicle that included a toroidal fuselage and two co-axial counter-rotating rotors in a ducted fan arrangement. The two rotors provided both the vertical and horizontal thrust needed in hover and forward flight. A vertical take off required a completely horizontal operation for obtaining a vertical down wash of the rotors to obtain the necessary lift for the aircraft. Transition to forward flight was achieved by tilting the fuselage in a “*Nose-down*” mode to generate a horizontal thrust component. In the forward flight mode, the rotor inlet flow was usually altered such that the leading side lip had significant flow separation and the trailing side of the duct had incoming flow impinging on the inner side of the shroud creating a drag penalty. The inlet nose separation, impingement on the aft part of the shroud and the interaction of this inlet flow distortion with the rotors resulted in significant pitch-up moment generation on this vehicle. Cypher is one of the few VTOL vehicles that used cyclic pitch of the rotors in encountering the nose-up pitch pitching moment generation. Although this control feature unique to Cypher reduced the excessive pitching moment, it required considerable amount of power and did not eliminate the drag generation on the trailing side of the shroud.

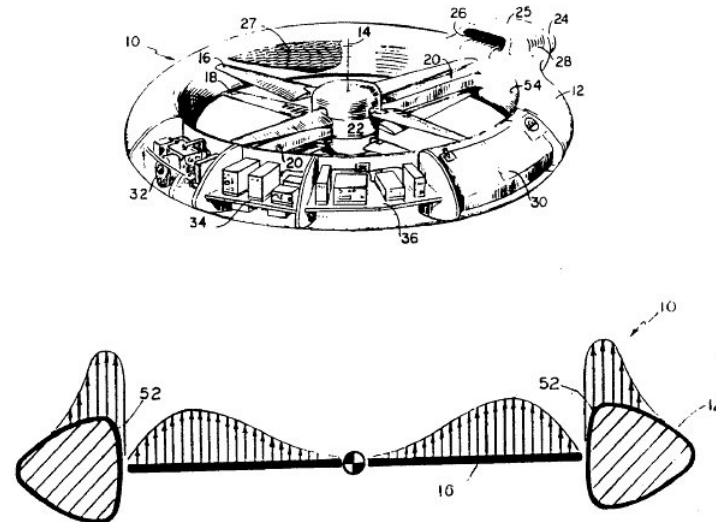


Figure 1.11. Sikorsky Cypher I with two co-axial counter-rotating rotors in a ducted fan arrangement [19]

Moffit *et al.* 5,150,857 (1992): Another solution in reducing the pitching moment was the use of an optimized toroidal fuselage airfoil profile, Moffit *et al.* [20] The cross sectional geometry of the toroidal airfoil was optimized such that the increasing pitching up moment with increased forward flight velocity was measurably reduced. The pitching up moment reduction was very effective from 20 knots vehicle speed up to 70 knots, which was the maximum flight velocity tested in a wind tunnel. The lift of the shroud was also effectively increased via this toroidal fuselage airfoil optimization. While incorporation of an optimized toroidal airfoil was a viable option, to counteract nose-up pitching moments, there was a manufacturing penalty associated with the new profile and an adverse effect on higher speed flight characteristics.

Flemming *et al.* 5,419,513 (1995): Adding a highly cambered fixed wing to a toroidal fuselage was a significant method of dealing with excessive pitch-up moment generation encountered in forward flight of Cypher. Flemming *et al.* [21] used a high-lift high-camber airfoil with a center of lift located significantly aft of the quarter chord line of the airfoil. The symmetrically mounted fixed wings had centers of lift located aftwardly of the fuselage axis of the toroidal fuselage in forward flight mode such that the fixed wings generate a nose-down pitching moment to counteract the nose-up pitching moment originating from the separated air flow over the leading side lip of the duct. The fixed wings were mounted in a fixed arrangement at a predetermined angle of incidence although a variable incidence system for the fixed wing is possible.

Swinson *et al.* 5,890,441 (1999): An autonomously controlled, gyroscopically stabilized, horizontal and vertical take off and landing (HOVTOL) vehicle using vertical lift devices was presented by Swinson *et al.* [22]. Although this vehicle had similarities to most of the systems reviewed in this section, the specific patent focused on the autonomous controllability of the vehicle rather than the aerodynamic features and inlet lip separation problem.

Cycon *et al.* 6,170,778 (January 2001): A new method of reducing nose-up pitching moment during forward flight on a ducted uninhabited aerial vehicle

was presented by Cycon *et al.* [23] The vehicle shown in Figure 1.12 consisted of a doughnut shaped fuselage that had a counter rotating ducted fan with fixed wings attached to it for improved forward flight characteristics. The system also had a shrouded pusher propeller for horizontal thrust in forward flight. Cycon *et al.* [23] used the method of adding high lift cambered airfoils to the sides of the toroidal fuselage of Cypher to counteract the nose-up moments generated in forward flight. The specific fixed wings also had flaperons for the precise adjustments of lift forces needed at different horizontal flight regimes. This system also had directional turning vanes at the aft section of the pusher propeller to deflect propeller thrust downward, creating additional lift to counteract nose up moments in high speed forward flight. They also noted that locating the pusher prop assembly aft of the duct reduced drag on the aircraft. The pusher prop has been found to draw turbulent air over the duct that would otherwise flow into the duct. Cycon [23] also suggested an excellent way of concealing the rotor system in high speed flight. Conventional systems used relatively heavy and complex covers to block the air entrance to the ducted fan in high speed forward flight. Operating the counter rotating rotors at zero pitch resulted in a virtual cover system impeding the airflow into the duct. By blocking the flow and forcing it to flow over and under the aircraft, drag was effectively reduced without the weight and complexity of rigid covers.

Cycon *et al.* 6,270,038 (August 2001): In addition to the flaperons in the fixed wings and the directional turning vanes in the propeller shroud exit, this invention [24] reported one or more deflectors mounted to the bottom of the fuselage for further drag reduction. The deflectors effectively controlled airflow into the duct from the bottom of the fuselage during forward flight. These deflectors were passive and required no actuation. They opened and closed automatically based on the airflow through and over the duct. The combination of zero pitch counter rotating rotors and passive flow deflectors on the bottom of the duct reduced the drag component on the aircraft between the open rotor and completely covered duct by about 80 %.

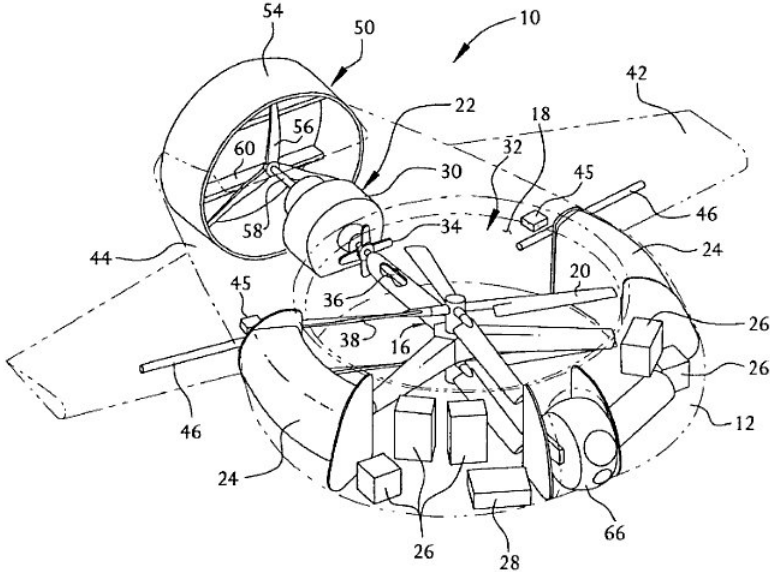


Figure 1.12. Sikorsky Cypher II with pusher propellers [24]

Moller, 6,450,445 (2002): A remotely controlled flying platform or a robotic platform was previously presented by Moller [18]. This concept more recently presented by Moller [25] used a counter rotating set of axial rotors in a ducted fan arrangement. Although an extensive set of fan exit flow control surfaces were used in this system, the inlet lip separation problem was not mentioned. The specific exit flow control surfaces are named “*multiple adjustable air deflector assemblies*” controlled by two servo motors. The invention focuses on the actuation of the individual air deflectors via servo mechanisms.

Yoeli, 6,464,166 (2002): This approach introduced by Yoeli [13] uses a plurality of parallel spaced vanes located in front of and behind the ducted fan rotor of a VTOL vehicle illustrated in Figure 1.13. The vanes are selectively pivotal to produce a desired horizontal force component to the lift force applied to the vehicle. Many vane arrangements are presented for producing side force, roll, pitch and yaw movements of the vehicle. Symmetrical airfoil sections spaced at one chord length from each other are used. Each vane is split into two halves, each half of all the vanes are being separately pivotal from the other half. This method does not

deal with any aspects of upstream lip separation that will occur especially during horizontal flight of this VTOL vehicle.

Wagner, 6,886,776 (2005): A VTOL personal aircraft (PAC) comprising of a fixed wing a fuselage and multiple of independently powered thrusters was explained by Wagner [26]. The thrusters preferably integrated into the wing generated a flight system with a lift to drag ratio equal or greater than two. At least one thruster on each side of the fuselage preferably comprised a “*levitator*” to create additional lift from the airfoil like air inlet. Although multiple of ducted fan units were utilized on both sides of the fuselage, the inlet lip separation problem was not mentioned in the manuscript.

Yoeli, 6,883,748 (2005): This invention [27] deals with the use of two ducted fans, four ducted fans and multiple free propellers on VTOL vehicle types already discussed by Yoeli in his previous patents. In addition to many military configurations possible with this vehicle, a hovercraft version using a flexible skirt extending below the fuselage is discussed.

Yoeli, 0,034,739 (2007): A ducted fan based VTOL vehicle including a fuselage having a longitudinal axis and a transverse axis, two counter rotating ducted fan lift producing propellers are described by Yoeli [28] . Many variations are described enabling the vehicle to be used not only as a VTOL vehicle, but also as a multi function utility vehicle. An unmanned version of the same vehicle is also described. Although an extensive use of inlet louvers and exit control surfaces are in place, there is no mention of an inlet lip separation control system near the leading side of the fans. The specific approach uses means for enabling the external flow penetrating the walls of the forward ducted fan for minimizing the momentum drag of the vehicle.

Yoeli, 7,275,712 (2007): This patent [29] described an enhancement of his 2002 concept [13] of parallel spaced vanes located in front of and behind the ducted fan rotor of a VTOL vehicle. Additional vane arrangements were presented for producing side force, roll, pitch and yaw movements of the vehicle. The left and

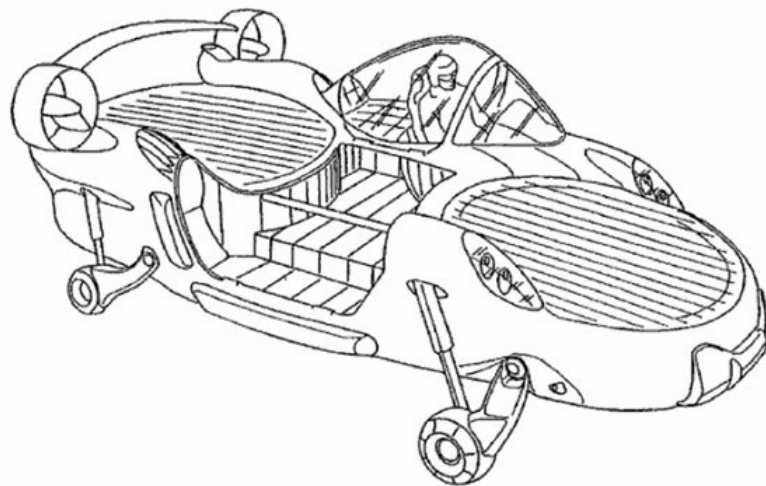
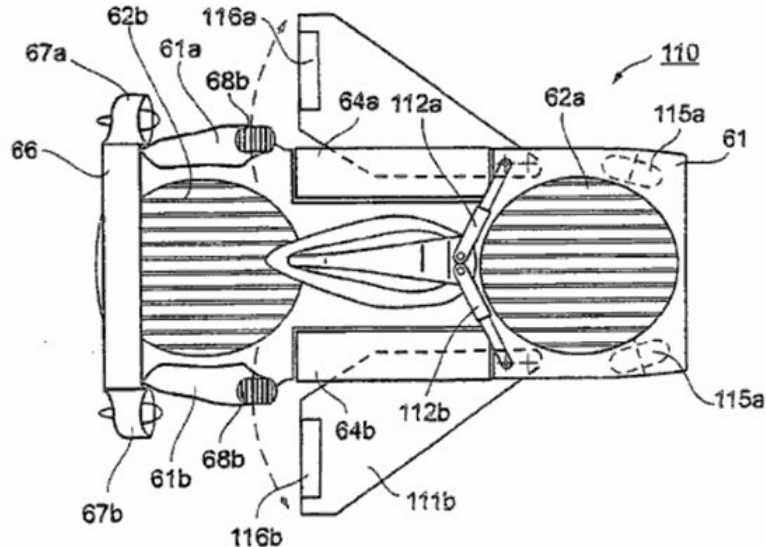


Figure 1.13. A ducted fan based VTOL vehicle including a fuselage having a longitudinal axis and a transverse axis, two counter rotating ducted fan lift producing propellers [13, 27–29]

right sides of the circular area at the rotor inlet and exit had parallel spaced vanes that were not in the direction of horizontal flight. The angle between the vanes and the flight direction was about 45 degrees for this specific patent. This patent did not have any description of inlet lip separation problem.

1.3 Past Studies of Ducted Fan Aerodynamics

The viscous flow characteristics of the ducted fan are complex. These vehicles need to be capable of flight in a broad range of atmospheric conditions, including the complex turbulent flow fields around buildings and trees. When a V/STOL ducted fan is in horizontal flight, because of the relative inlet flow dominantly parallel to its inlet plane, problems related to flow separation at the leading edge duct lip are encountered. When the V/STOL vehicle is in perfect horizontal flight the angle between the relative inlet flow direction and the axis of rotation of the rotor is about 90° . This angle is usually termed as “*angle of attack*”. At high angle of attack, the inlet flow separation leads to problems within the duct and may result in a high nose-up pitching moment as the forward speed is increased. Therefore, measuring and predicting the mean flow characteristics of ducted fans is crucial to understand the problems related to reliable and controllable horizontal flights. Numerous studies have been undertaken in order to quantify the flow field characteristics around ducted fans. The operation of an axial flow fan with strong inlet flow distortion severely affects the performance of the rotor especially near the tip region of the blades.

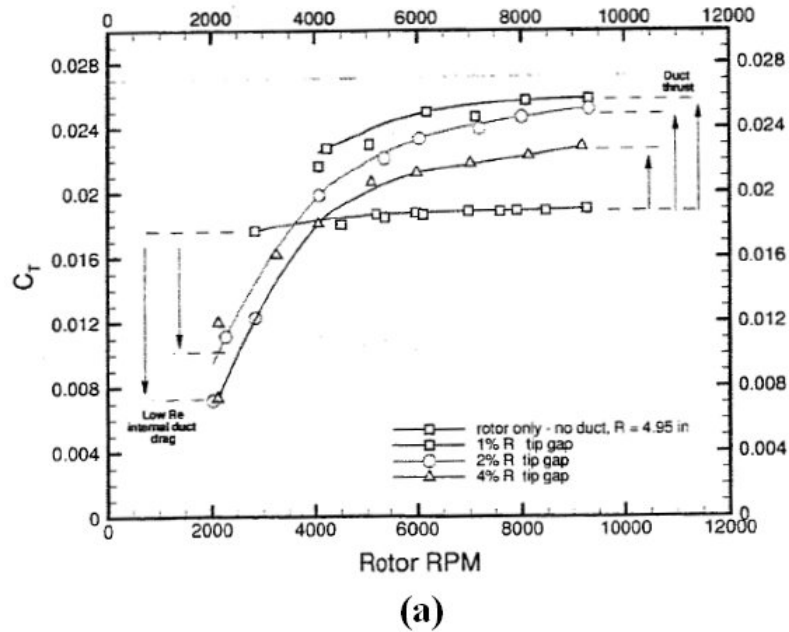
Experimental investigation has been the major approach to study the mean flow characteristics of the conventional ducted fan. Abrego and Bulaga [30] performed wind tunnel tests to determine the performance characteristics of ducted fans for axial and forward flight conditions. Their study resulted in showing important effect of exit vane flap deflection and flap chord length on providing side force.

Martin and Tung [31] tested a ducted fan V/STOL UAV with a 10-inch diameter rotor. They measured aerodynamic loads on the vehicle for different angles of attack(from 0° to 110°) in hover and different crosswind velocities (41 knots, 70 ft/s). Both models were tested with fixed-pitch propellers of varying diameters, to test tip clearances from 1% to 4% (based on rotor tip radius). They also included hot-wire velocity surveys at inner and outer surface of the duct and across the downstream wake emphasizing the effect of tip gap on the thrust force produced. In addition, their study showed the effect of leading edge radius of the duct on the

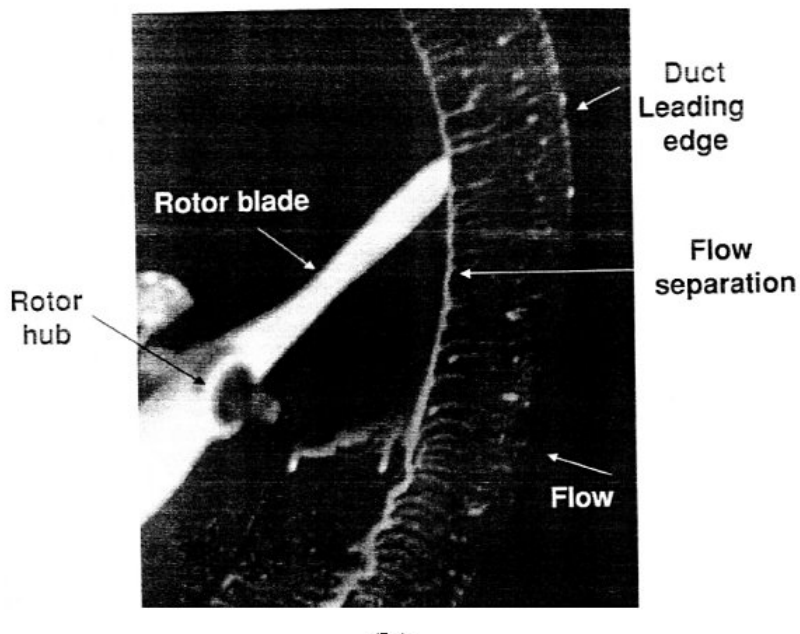
stall performance and stability of the vehicle. Figure 1.14 illustrates thrust of the system is decreasing with increasing tip gap height. Their results also showed that for lower rotational speeds open rotor thrust was higher than ducted fan thrust. They explained this by pointing out the increase in viscous losses inside the duct for low rotational speed operations. Figure 1.14b shows their oil flow visualization study. They have shown interaction of duct boundary layer and tip leakage vortex in their study.

Fleming *et al.* [32] published the results of a study on the performance performance of ducted fan inlet lips and exit vanes, in crosswind. Beside the experimental study they performed in wind tunnel, they also run computational analysis on Vertical Take-Off and Landing Unmanned Aerial Vehicles (VTOL UAV) ducted fans. Beside conventional control vanes, they tested seven different auxiliary control devices in crosswind. These control devices are an internal duct vane and thrust reverser that are adapted from Moller's control device [18], a “*duct deflector*” on the windward side of the internal duct wall; a trailing edge flap on the leeward side of the duct, which increases the effective camber of the duct profile; an inlet lip spoiler at the windward side; “*leading edge slat*” on the leeward side of the inlet; and lip flow control using normal and tangential flow blowing at the lip. Figure 1.16 shows control devices tested by Fleming *et al.* [32]. They have tested their 10 inch diameter ducted fan model in hover and crosswind up to 50 ft/s. They have selected “*lip flow control by blowing*”, “*internal duct vane*” and “*internal duct deflector with bleed*” as efficiently performing devices. At low crosswind speeds, control vanes performed better than other methods. However, as the crosswind speed increased, the authors observed that the control vanes are stalled.

Graf *et al.* [33, 34] improved ducted fan forward flight performance with a recently designed leading edge geometry, which became a significant factor in offsetting the effects of adverse aerodynamic characteristics for elevated horizontal flight speeds. They have tested the effects of five different lip geometries. They have concluded that the duct lip shape is the most influential feature in offsetting the effects of the adverse aerodynamic characteristics. While a particular lip shape may perform well in hover conditions, its performance in crosswind conditions can



(a)



(b)

Figure 1.14. (a) Thrust variation with rpm and tip gap(b) surface flow visualization of rotor induced separation in the tip path plane [31]

be inferior to other designs.

Lazareff [35] investigated the aerodynamic performance of ducted fans by using

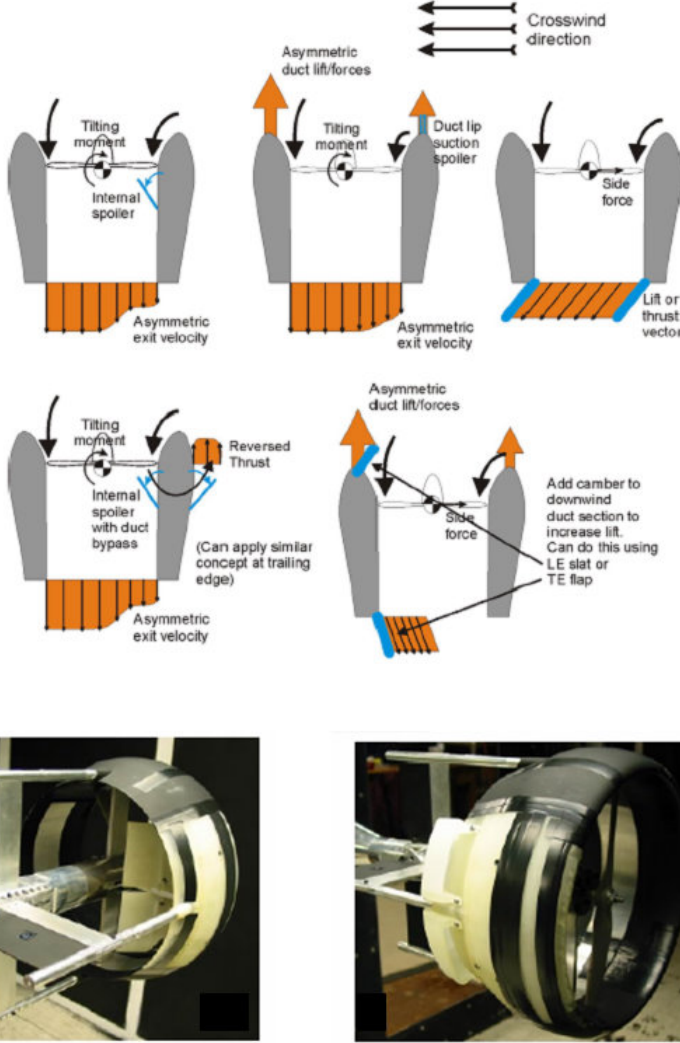


Figure 1.15. Control devices tested by Fleming *et al.* [32]

both theoretical and experimental methods. The flight performance calculations are also shown in that study. The difference between ducted fans and free propellers is extensively discussed.

Weelden and Smith tried investigated ducted fan aerothermodynamic performance by utilizing systematic component build-up approach [36]. They emphasized the importance of the inlet and diffuser in performance of ducted fans.

Kriebel and Mendenball also carried out a theoretical and experimental study

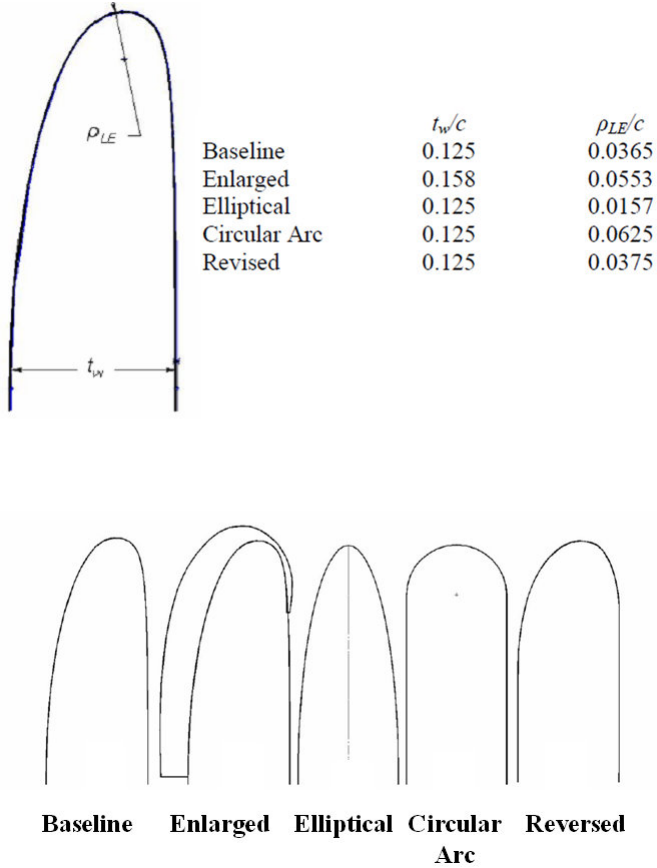


Figure 1.16. Tested inlet lip shapes Graf *et al.* [33, 34]

to predict ducted fan performance [37]. They developed methods for predicting the forces and moments on the duct, duct surface pressure distributions and boundary-layer separation. They have compared their predictions with measurements made on the Bell X-22A and Doak VZ-4 aircraft models. Their model qualitatively predicted the force and moment, the pressure distribution , and the separation of the boundary layer over the entire operating range of propeller thrust and free-stream angle of attack.

Mort and Gamse [38] investigated aerodynamic characteristics of a seven foot diameter ducted propeller which was used on the Bell Aerosystems Company X-22A airplane. They reported aerodynamic characteristics for variations of power, free-stream velocity, blade angle, and duct angle of attack. Stall of both the upstream and downstream duct lips of this seven foot diameter ducted fan was ex-

amined as a function of angle of attack. It was found that the onset of separation on the upstream lip will be encountered; however, complete separation on this lip will be encountered only during conditions of low power and high duct angle of attack.

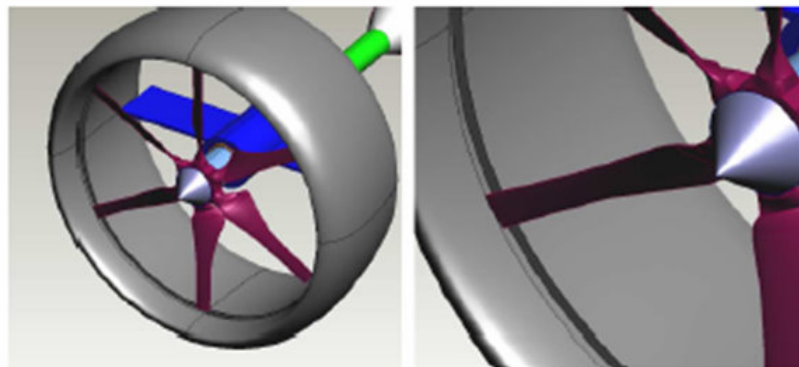
Mort and Yaggy [39, 40] performed hover and forward flight tests on a four foot diameter wing-tip mounted ducted fan that is used on Doak VZ-4-DA. Performance characteristics for the ducted fan were reported. They emphasized that pitching moment was rapidly changed and required power was increased due to separation, which occurred at windward side duct lip. They also reported that ducted fan supported by a fixed wing required less power in comparison to free flying ducted fan.

Weir has a study on experimental and theoretical performance of ducted fans with different inlet lip configurations [41]. In this study the moments and forces affecting the ducted fan were measured for different configurations. The design of exit vanes and fan rotor is also mentioned in the paper. The effect of the inlet lip radius on the lift and pitching moment combined with a diffuser is carefully investigated. As the inlet lip radius is increased the lift force of the ducted fan is also increased slightly. Adding a diffuser to the system has also positive effects on the lift. However, they both produce increased pitching moments.

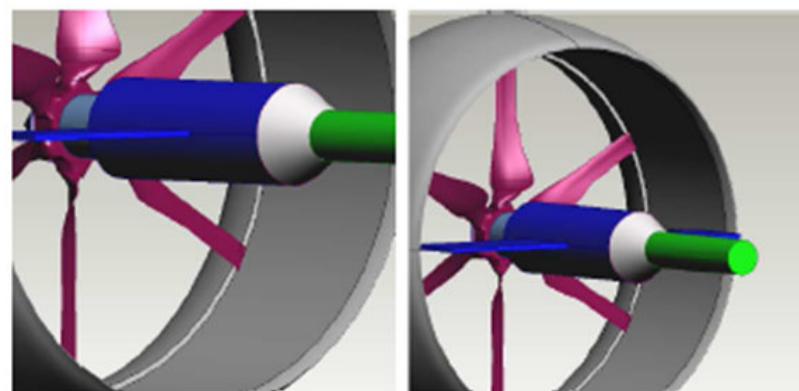
Pereira performed an experimental study on the effects of various shroud profile shapes on the performance of MAV-scale shrouded rotors [42]. Seventeen ducted fan models with a nominal rotor diameter of 16 cm (6.3 in) and various values of diffuser expansion angle, diffuser length, inlet lip radius and blade tip clearance were tested at various rotor collective angles. Tests performed for open rotor and a single shrouded-rotor model at a single collective in translational flight, at angles of attack from 0° (axial flow) to 90° (edgewise flow), and at various advance ratios are reported.

Martin and Boxwell [43] tested two ducted fan models that were designed to effectively eliminate the tip leakage. Both models were derived from the baseline

(10-inch inner-diameter shroud) which is explained in their previous study [31]. In their first design, they have created a notch and fit the propeller inside the notch. In their second design, a rearward-facing step was cut into the inner shroud. Their designs are shown in Figure 1.17. The computational analysis resulted in an increase in inlet lip suction and an increase in performance. However, the experimental thrust and power measurements, showed no difference in performance of these designs when compared to their baseline duct.



Notched duct



Rearward-facing stepped duct

Figure 1.17. Notched and stepped duct designs [43]

In addition to experimental studies, the ducted fan design and performance analyses were widely performed by using computational flow modeling. Lind *et*

al. [44] carried out a computational study using a panel method. They compared their results to the experimental results from Martin and Tung [31]. He and Xin [45] developed the ducted fan models based on a non-uniform and unsteady ring vortex formulation. A numerical study in axial and horizontal flight conditions was conducted and validated with measured data. Chang *et al.* [46] developed an accurate grid generation methodology known as “*the curve adaptive option*” to model several industrial ducted fans. An axisymmetric, incompressible Navier-Stokes solver was implemented to calculate the flow field of a duct fan. The computational results agreed well with available wind tunnel data. Ahn *et al.* [47] applied a computational method to their ducted fan system to identify the design parameters which affect its performance. Their ducted fan system was designed by using the stream-surface based axisymmetric analysis which considered overall physical characteristics and design parameters of the system. Ko *et al.* [48] developed a computer code aimed at the preliminary design of a ducted fan system. This code was validated using data from many wind tunnel and flight tests. It was also extensively used in the design of commercial ducted fans. Recently, Zhao and Bil [49] proposed a CFD simulation to design and analyze an aerodynamic model of a ducted fan UAV in preliminary design phase with different speeds and angles of attacks.

1.4 Tip Leakage Flow

The flow field resulting from the region between the stationary duct and rotor tip of an ducted fan is complex because of the interaction of the tip leakage flow, annulus wall boundary layer and rotor wake. The inherent pressure difference between the pressure side and suction side of blade tip generates a tip leakage flow that is responsible for a substantial portion of aerodynamic losses in ducted fans. The leakage flow also rolls into a highly three dimensional tip leakage vortex with significantly turbulent and unsteady flow features in each passage. The tip leakage vortex is a complicated flow phenomenon that is one of the dominant mechanisms of noise generation by unsteady interactions in a turbomachinery system. It is a major energy loss mechanism in axial flow fan systems.

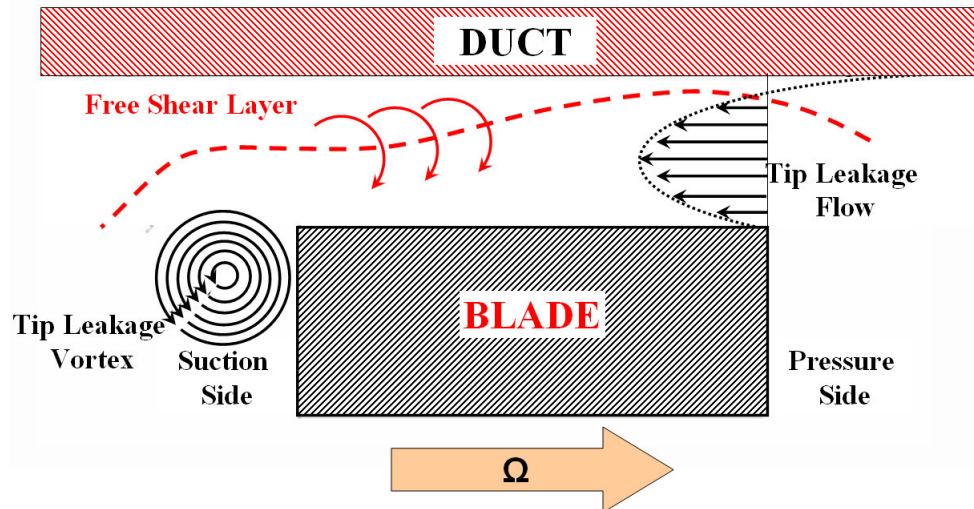


Figure 1.18. Schematic of leakage flowfield in an axial flow compressor or fan

Contributing factors to the tip leakage flow mechanism include:

- Because of the pressure difference between suction and pressure side of a rotating axial flow fan, compressor or turbine blade, a pressure driven flow occurs from pressure side to the suction side through the tip gap [50–54].
- The shear flow near the casing results in three-dimensional separation and increases aerodynamic losses [50–54].
- Relative movement of rotor blade and the stationary casing boundary layer encourage the leakage flow through the tip gap for the case of a fan blade [50–54].
- When the size of the tip gap is increased, resistance to flow mechanisms related to pressure driven flow and relative movement of blade and casing boundary layer is decreased [50–54].

There has been a limited number of studies about three dimensional flow structure of leakage vortex in axial flow fans, in open literature [55–58]. Inoue and Kuroumaru et al. [59] made detailed flow measurements before and behind an

axial flow rotor with different tip clearances. In their study, they investigated the clearance effect on the behavior of tip leakage flow. Furukawa and Inoue et al. [60] also investigated breakdown of tip leakage vortex in a low speed axial flow compressor. Reducing tip leakage mass flow rate improves the aerodynamic performance of axial flow fans and compressors. Implementation of treatments in the non-rotating part over the blade tip is also an efficient way of tip leakage flow reduction. References [61] and [62] investigate different casing treatments for axial flow compressors.

The wake developed from an axial flow fan has a strong influence on the system performance. It is a significant source of aerodynamic loss and affects the efficiency and vibration characteristics. References [63–65] deal with extensive investigations of the wake flow features such as mean velocities, turbulence and decay characteristics on turbomachinery performance. The wake flow system is likely to interact with the complex flow system originating in the tip gap region.

Stereoscopic Particle Image Velocimetry (SPIV) is an effective way of measuring all three velocity components of an instantaneous flow field over a selected area [66–70]. A comprehensive discussion of the specific stereoscopic PIV technique used in this thesis is given by Kahveci and Camci in [67–69]. Yoon and Lee et al. [70] investigated the flow structure around an axial flow fan using a SPIV technique. The time averaged results clearly show the evolution and dissipation of tip vortices. Yen and Lin et al. [71] analyzed exit flow performance and properties of an axial flow fan with winglet-blades at various impeller angles using SPIV. The velocity profiles show the most stable and the best fan performance, resulting from winglet-blades which increase the lift and reduce the drag. Wernet et al. [72] made phase-locked three-dimensional Digital Particle Image Velocimetry (DPIV) measurements near the tip region of a low speed compressor rotor to characterize behavior of rotor tip clearance flow. Comparison of the DPIV measurements to Navier-Stokes flow simulations was also presented.

Corsini et al. [73–77] presented the results of a computational study of an axial flow fan using “*improved tip concepts*”. The first two endplates were with constant

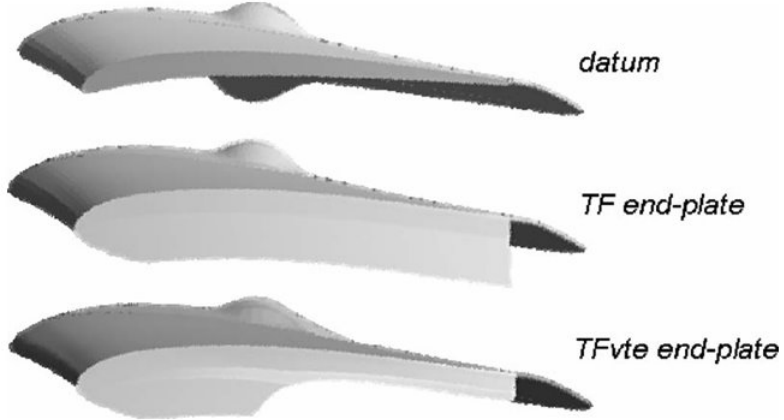


Figure 1.19. Tip end plates designed for reducing tip leakage flow Corsini *et al.* [73]

and variable thickness distributions while the last two were designed by combining the end-plates with a stepped gap on the tip. The investigation was based on a finite element Navier-Stokes solver for the physical interpretation of the detailed 3D leakage flow field. The specific fan performance experiments showed that the improved tip concepts introduced a small performance penalty, but the efficiency curves give evidence of an improvement with better peak performance and a wider high efficiency curve towards the rotor stall margin. An aeroacoustic investigation showed a reduction of the rotor aeroacoustic signature.

Wisler [78] presented a study on tip clearance and leakage effects in compressors and fans. He discussed the effect of clearance, duct design, tip treatments, active clearance control, and improving stall margin of rotor blade in his study. He came up with several tip treatment geometries that are shown in figure 1.20. He has tested squealer tip, groove, pressure and suction side winglet, knife type tip configurations. The most common one of these treatments is the squealer tip obtained by thinning rotor the tip. The main reason for a squealer tip is the reduction of the contact surface during a “*rubbing*” incidence. A squealer tip has measurable aerodynamic benefits too. Relative to flat tip the deep groove treatment and the pressure surface winglet implementation reduced the leakage by 15 % as shown in Figure 1.20.

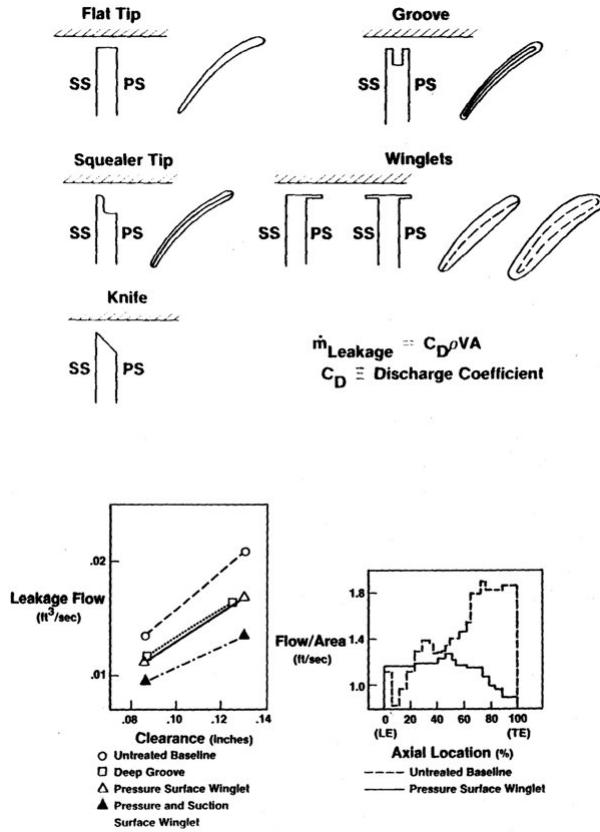


Figure 1.20. Tip treatments used by Wisler [78]

1.5 Objective of Current Research

Ducted fan type propulsion systems have many advantages compared to free propellers. It provides augmented thrust while providing enhanced safety when compared to free propellers. Because of these advantages, ducted fans are very popular in Vertical Take-off Landing (VTOL) vehicles. Despite the high performance, they can provide for VTOL vehicles, they also introduce significant technical problems.

The primary objective of this experimental and computational study is to inves-

tigate performance losses that ducted fan powered vertical lift systems experience in forward flight and hover conditions. In forward flight, flow separations can occur on the windward side of their inlet lip. A comprehensive investigation of this separation problem is one of the main goals of this study. An inlet conditioning concept called the Double Ducted Fan (DDF) is also developed. The effect of the duct on the fan rotor performance is another issue that affects the performance of the system. Understanding the mechanisms that results in tip aerodynamic losses is another goal of this study. The most important source of the tip losses is the tip vortex that originates from the fan rotor. Tip vortices can be weakened by using proper casing and blade tip treatments. The current study presents a number of novel tip treatments in order to deal with tip region aerodynamic losses. This study consisted of both quantitative and qualitative measurements. Velocity distributions at the inlet and exit of the fan rotor are obtained using high resolution particle image velocimetry (PIV) technique. Total pressure measurements are also performed at the exit of fan rotor. Flow visualizations at the inlet of ducted fan are used to understand flow separation problem experienced in forward flight. Obtaining a reliable set of experimental data for validation of analytical and computational tools is another goal of this study. Besides experimental techniques, numerical solutions of Reynolds-Averaged Naiver-Stokes (RANS) equations are obtained by using commercial codes ANSYS FLUENT and ANSYS CFX. Numerical simulations are used during design studies of tip treatments and inlet conditioning concept. Some of the results presented and discussed in this thesis may also be found in Akturk and Camci [79–82]

The organization of this thesis is as follows. An introduction is presented in Chapter 1. Chapter 2 describes aerodynamic performance investigation of five inch diameter ducted. Detailed velocity distributions obtained via planar particle image velocimetry (PIV) method are shown. A radial equilibrium based computational method is also developed and validated using the velocity measurements. This method replaces the complex rotor flow field with a relatively simple inviscid rotor model. Implementation of this radial equilibrium based rotor model (REBRM) into 3D RANS based flow solver simplifies the ducted fan analysis remarkably. The computational development of a novel inlet flow conditioning concept, the Double

Ducted Fan (DDF), is described in Chapter 3. This chapter utilizes the REBRM developed in Chapter 2. DDF significantly reduces inlet lip separation related performance penalties in forward flight. The effect of tip gap height on aerodynamic performance of ducted fans is outlined in Chapter 4. A comprehensive experimental study is performed in hover and forward flight conditions at the downstream of the fan rotor for quantification of performance loss due to tip clearance. A flow visualization technique is used for investigating flow separation problem in forward flight. A development and validation of numerical technique for simulating fan rotor are also presented in this chapter. Chapter 5 discusses the design of tip platform extensions for “*a low disk loading*” axial flow fan. Stereoscopic PIV technique is used in measuring three-components of the velocity vector downstream of the fan rotor. Design of tip treatments including tip platform extensions and squealer tips for a highly loaded ducted fan used for vertical systems are discussed in chapter 6. Their conceptual design is performed using numerical simulations that is outlined in Chapter 4. Exit total pressure surveys and high resolution force and moment measurements are performed for testing treatments in hover condition. A summary of results, conclusions and future work recommendations are presented in Chapter 7. A Summary of the thesis organization can be viewed in Figure 1.21.

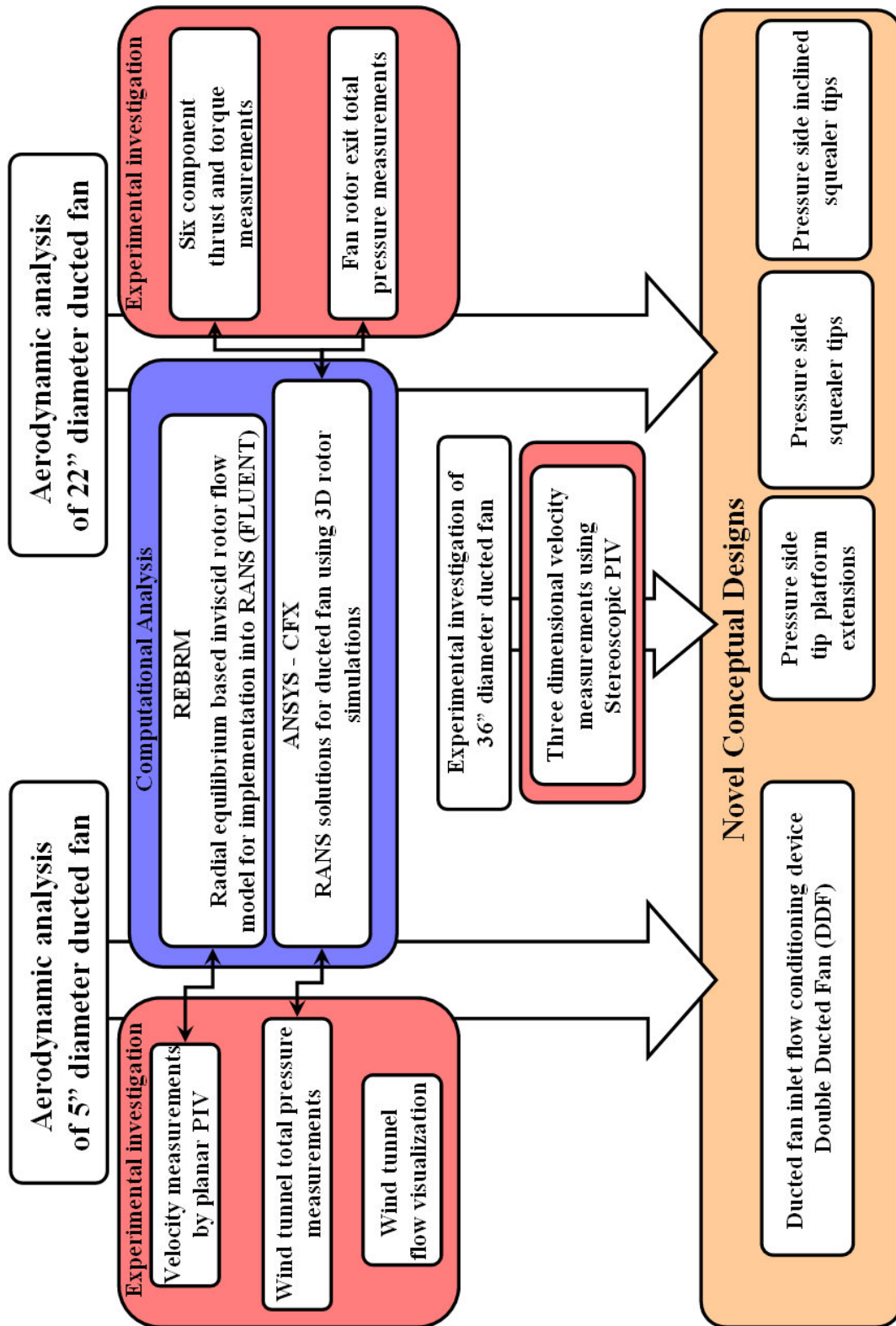


Figure 1.21. Thesis organization chart

Chapter **2**

Inlet/Exit Flow Aerodynamic Performance of Ducted Fan in Hover and Forward Flight

This chapter describes experimental and 3D computational analysis around a 5" diameter ducted fan. These analyses investigate the complicated flow field around the ducted fan in hover and horizontal flight conditions. Flow features such as inlet lip separation, distortion of inlet flow features, influence of rotor tip speed, influence of horizontal flight velocity and the influence of the cross wind with fan exit flow are investigated through experiments and computations. For high-resolution mean flow experiments, particle image velocimetry (PIV) is used. Axial and radial velocity components at the inlet/exit region of the ducted fan are measured in hover and forward flight. By measuring axial and radial velocity components, the effect of leading edge duct lip separation on the flow field into the fan rotor is analyzed.

For the computational investigations, 3D incompressible Reynolds Averaged Navier-Stokes (RANS) equations are solved using a commercial solver, FLUENT. In order to accelerate the viscous flow computations, a rotor disk model based on

radial equilibrium equation, energy equation and the conservation of angular momentum principle is integrated into the viscous flow solver. The specific actuator disk based fan model developed in this thesis uses a prescribed static pressure rise across the rotor disk for a time efficient simulation of the fan rotor. This chapter describes a method to compute the static pressure rise at each radial position of the rotor blade as a function of the rotor inlet absolute velocity. The current actuator disk model implementation is a highly time efficient method of replacing the complex rotor flow field in a 3D RANS computation.

The study presented in this chapter is motivated by the need to investigate aerodynamic performance of ducted fans in hover and forward flight and to discern the critical problems related to the forward flight. How ducted fan inlet and exit flows are affected from forward flight is addressed. The following sections provide the detailed explanations of the integrated experimental and computational approach and important conclusions of this specific study.

2.1 Experimental Setup

A test rig is designed and manufactured to investigate the local flow features in and around a 5" diameter ducted fan using a planar PIV system. The set-up has also provisions for seeding the fan flow field with a smoke generator based on a fluidized based system using fog fluid which is a mixture of triethylene glycol, propylene glycol, 1,3 butylene glycol and de-ionized water. Figure 2.1 shows a sketch of the experimental setup.

2.1.1 Ducted Fan Model

The five bladed ducted fan rotor is driven by a brushless DC electric motor. This motor is speed controlled by an electronic speed control (ESC) system. The high efficiency electric motor driving the fan can deliver 1.5 kW power (2.14 HP) and spin 1050 rpm per volt supplied to the motor. The phase-locked PIV measure-

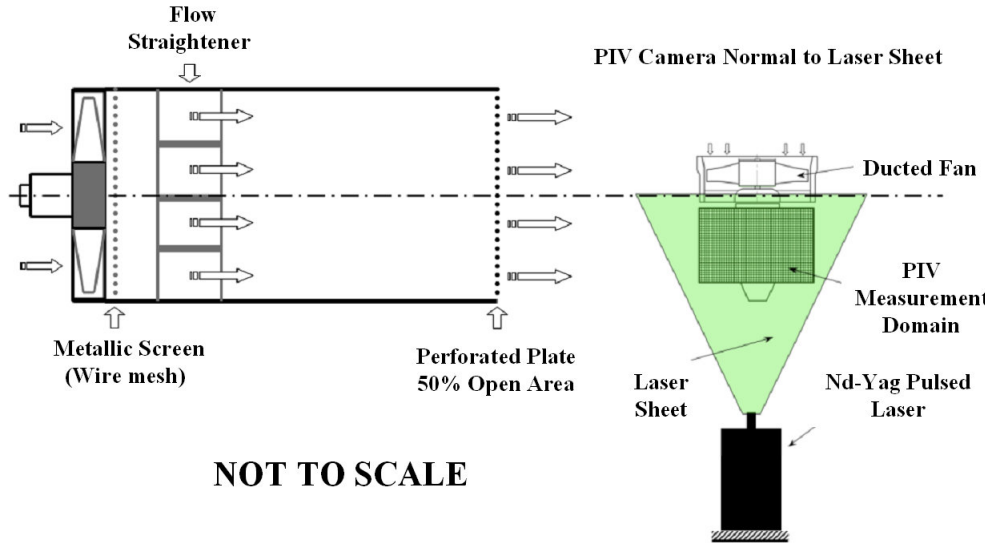


Figure 2.1. Cross wind blower, the ducted fan and the PIV system orientation

ments are triggered by using an optical once-per-revolution device located near the hub of the rotor exit. An infrared beam is reflected from a highly reflective surface (1 mm wide shiny metallic film) attached to the rotor hub. This once-per-rev pulse provides a phase-locked triggering of the PIV data collection system. The position of the rotor can be adjusted accurately in relation to the position of the laser light sheet that contains the rectangular PIV measurement domain. The PIV domain can be located at the upstream and downstream of the rotor as shown in Figure 2.1. Figure 2.2 shows the five bladed ducted fan that is used in the present PIV experiments. The geometric specifications are presented in Table 2.1.

This ducted fan unit is designed for small scale uninhabited aircraft. This unit is manufactured from carbon composite material and has six vanes at the exit of the fan in order to remove some of the swirl and torque existing at the exit of the rotor. A tail cone is used to cover the motor surface and hide the electrical wiring.

Rotor hub diameter	52 mm
Rotor tip diameter	120 mm
Blade height h	34 mm
Tip clearance t/h	5.8 %
Max blade thickness at rotor tip	1.5 mm
Tailcone diameter	52 mm
Tailcone length	105 mm
Rotor blade section properties	
	Hub Mid Span Tip
Blade inlet angle β_1	60° 40° 30°
Blade exit angle β_2	30° 45° 60°
Blade chord	32 mm 30 mm 28 mm

Table 2.1. Geometric specifications of five inch ducted fan

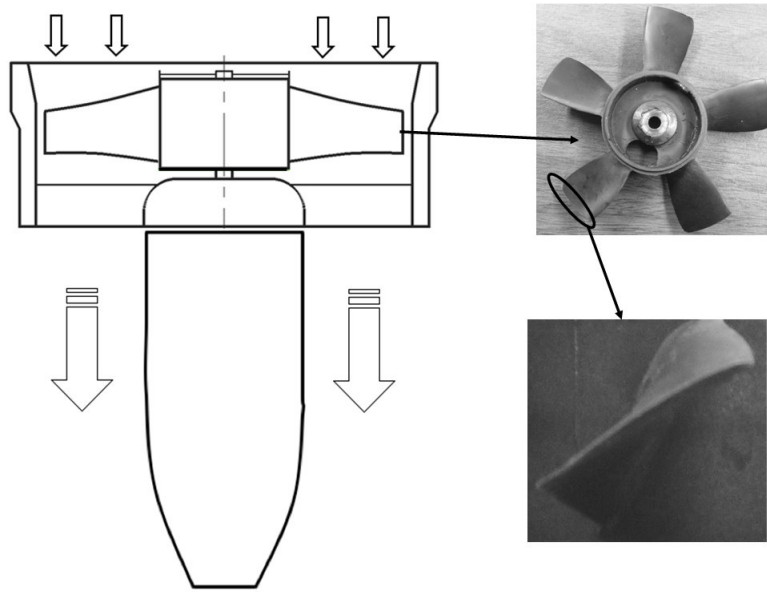


Figure 2.2. Five inch diameter five-bladed ducted fan

2.1.2 Crosswind Blower

Figure 2.1 shows a sketch of the crosswind blower that can generate about 6 m/s uniform mean flow just upstream of the ducted fan unit. The axial flow fan driving the cross wind blower is capable of generating $5.58 \text{ m}^3/\text{s}$ (10,594 cfm). There is a wire mesh screen at just downstream of the axial flow fan. The flow passes through a 10 inch wide flow straightener section. Finally, there is a perforated plate (50% open area) at the exit of the crosswind blower. The grill, flow

straightener and the perforated plate at the exit provide a uniform mean flow at the exit of the system. The uniformity of the blower exit mean flow (6 m/s) is determined by a hot wire anemometer. The measured turbulence intensity of the uniform flow is less than 1 % based on the rms fluctuation velocity fluctuations normalized by the mean flow magnitude. An AC inverter connected to the three phase AC motor of the axial fan unit can adjust the rotor rpm and mean flow velocity magnitude.

2.2 Experimental Method

2.2.1 Planar Particle Image Velocimetry (PIV) Measurement Technique

The PIV technique [66–69, 83] measures instantaneous velocity components of a flow field over a determined area. Small particles existing in a fog generated by a fluidized bed system are introduced into the fluid flow, and the region of interest is illuminated by a light sheet provided by short Nd-Yag laser pulses lasting as short as a few nanoseconds. The subsequent step is the recording of the displacement of particles via one or two CCD cameras depending on the specific PIV technique used. As a summary, four basic steps should be mentioned in an experimental procedure:

- Flow is seeded.
- The flow region of interest is illuminated.
- Scattering light from the particles forming the speckle images is recorded by cameras.
- Recordings are analyzed by means of a correlation based software system.

The scattered light from the seeding particles is recorded by a camera. The initial position of a particle is recorded on the first frame of the camera when the first laser pulse fires. In general, a typical duration of a laser pulse is about

30 nano seconds in a flow field similar to the current study. Its final position is recorded in the same way on the second frame of the same camera when the second laser pulse fires. The time interval between the two frames is usually determined by the mean flow speed in the area of investigation. The order of magnitude of this time separation between the two frames is in the order of “*micro seconds*” for the current effort. Since the displacement of the particle and the time interval between the two subsequent laser pulses are known, the velocity of the particle can be calculated by the simple equation: speed=distance/time. A comprehensive explanation of this technique is given by R.J. Adrian [66, 69].

In this current study, the inlet and exit mean flow performance of a 5 inch diameter ducted fan was quantified by using the PIV technique. Axial and radial components of velocity profiles were measured near the inlet and exit planes of the ducted fan. Two separate measurement domains of [156 mm x 96 mm] are used in inlet and exit flow. Figure 2.1 illustrates the PIV setup in which the fan exit field is measured by keeping the PIV light sheet unchanged. For the measurement of inlet flow velocities, the ducted fan is flipped vertically. The PIV measurement domains are illuminated by a double cavity frequency doubled pulsating Nd-Yag laser which has an emitted radiation wavelength of 532 nm (green) and 120 mJ pulse energy level. Pairs of images from measurement domains are captured by an 80C60 HiSense PIV/PLIF camera. CCD camera is positioned normal to the laser sheet.

In planar PIV measurements, two components of the velocity vector are measured in the plane illuminated by a laser sheet. The current study focuses on measuring the axial and radial components of the local velocity vectors. These measurements are based on the image maps obtained by the CCD camera. The size of seeding particle is $0.25\text{-}60 \mu\text{m}$. The image pairs of PIV domains are recorded. The image maps are divided into 32×32 pixel interrogation areas and 25% overlapping is used. “*Flowmap*” software provided by DANTEC [83] used for capturing PIV images and correlation analysis. All 700 image pairs are adaptive correlated, moving average validated and then ensemble averaged to obtain true mean flow.

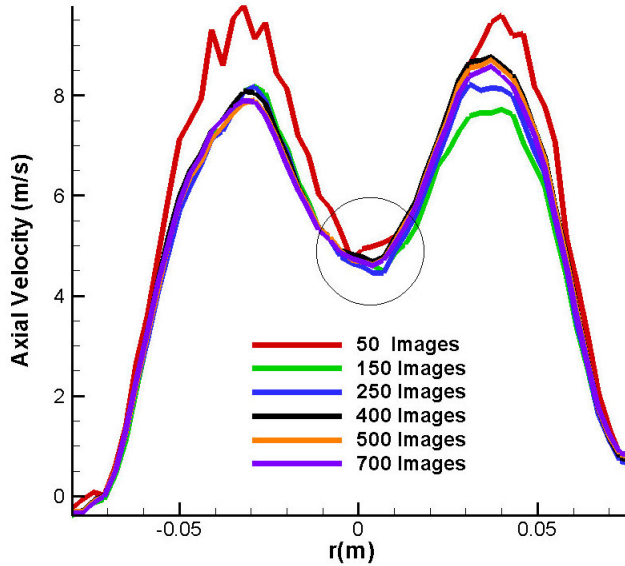


Figure 2.3. Influence of ensemble averaging “image sample size” on the axial velocity component

The ensemble size is of critical importance in achieving statistically stable mean velocity distributions in any PIV data reduction process. Figure 2.3 presents the influence of ensemble averaging sample size on the spanwise distribution of the most significant velocity component that is axial component. Figure 2.3 indicates that an ensemble size of 400 is sufficient in achieving a statistically stable average in the current set of experiments.

2.3 Experimental Results in Hover and Forward Flight Conditions

Experiments were performed at two different rotational speeds at 9000 and 15000 rpm. The performance of the ducted fan was analyzed in hover and forward flight conditions. The forward flight condition is simulated with a crosswind of 6 m/s velocity produced by the crosswind blower shown in Figure 2.1.

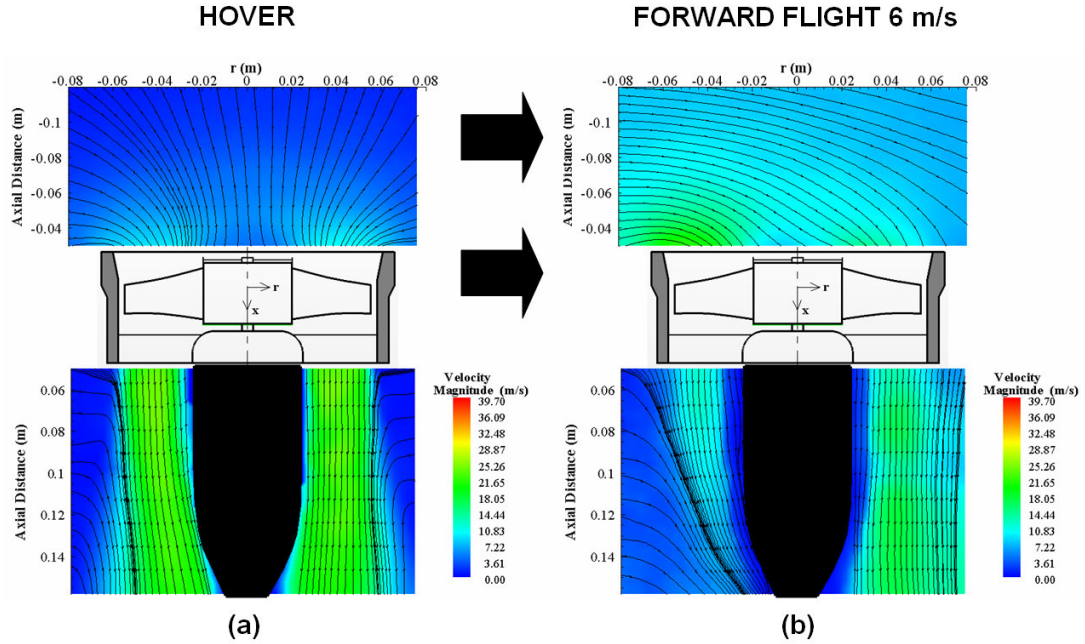


Figure 2.4. Streamlines at inlet and exit of ducted fan for HOVER (a) and FORWARD FLIGHT (b) (PIV measurements at 9000 rpm)

Figures 2.4a and 2.5a show streamlines obtained from PIV measurements at different rotational speeds (9000 and 15,000 rpm) in hovering. The figures are contour plotted and colored with the magnitude of measured velocity. As expected, the magnitude of velocity is increasing at both inlet and exit regions by increasing rotational speed of the fan rotor. The streamline structure and the local magnitude of the velocity vector show a reasonable axisymmetry in hover mode as shown in Figures 2.4a and 2.5a. The exit jet from the fan unit show a visible flow entrainment from the still air region into the exit jet at both rotational speeds. In addition to the flow entrainment, the exit jet region at 15,000 rpm exhibit slight momentum deficit near $x=0.1\text{m}$. This momentum deficit could be explained with the existence of the wakes of the six bladed exit guide vanes in the fan unit. The final form of this distribution is also controlled by the unique rotor position defined by the current phase-locking approach.

Figure 2.4b illustrates the change of inlet/exit flow field caused by the forward flight effect at 9000 rpm. With the influence of the crosswind at 6 m/s, the

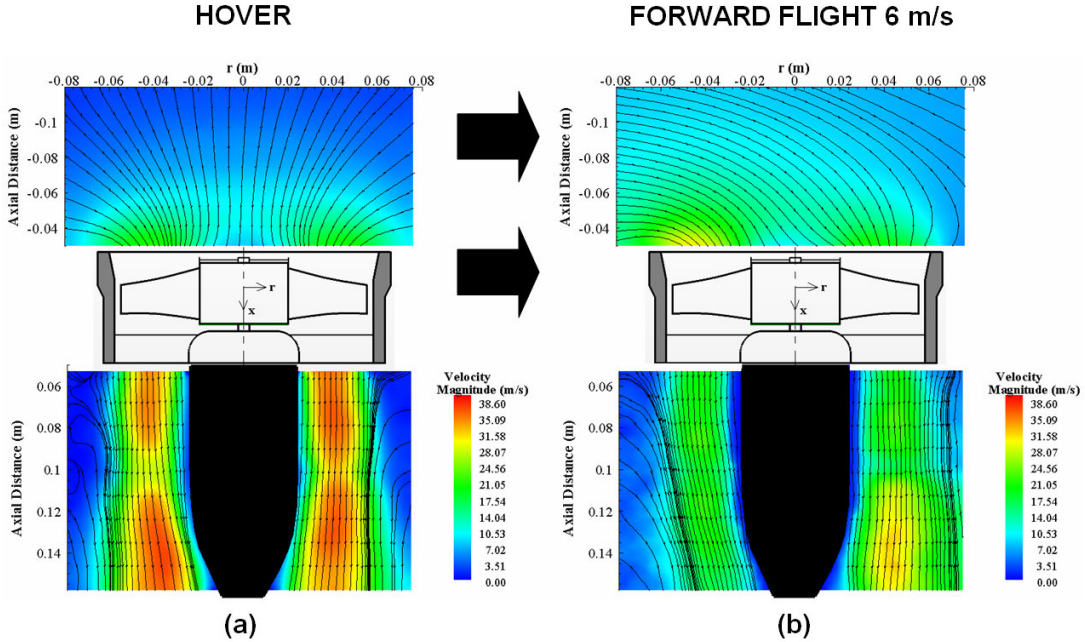


Figure 2.5. Streamlines at inlet and exit of ducted fan for HOVER (a) and FORWARD FLIGHT (b) (PIV measurements at 15000 rpm)

distribution of the velocity magnitude at the inlet is distorted due to the separation from the leading side duct lip. Due to the separation region, the breathing area of the fan rotor is reduced. At the leading side of the duct, maximum velocity magnitude is shifted towards to hub because of the effect of lip separation.

Figure 2.6 clearly supports the observation that the “*leading side*” peak in axial velocity at the inlet plane is shifted towards the rotor hub due to inlet lip separation. However, the trailing side peak in inlet plane is shifted towards the blade tip. When the peak is shifted towards the rotor tip section, the work addition to fan exit flow is more significant as shown in Figure 2.6. Due to more distorted inflow at the leading side, exit flow average velocity magnitude is slightly decreased at the leading side. The streamlines near the trailing side at the inlet plane are more normal to the fan inlet plane indicating slightly higher mass flow rate on this side than the leading side. The trailing side of the duct is affected less from the crosswind. Streamlines at the exit flow clearly show the influence of forward flight velocity on the high momentum jet exit fluid. With the effect of the crosswind, the

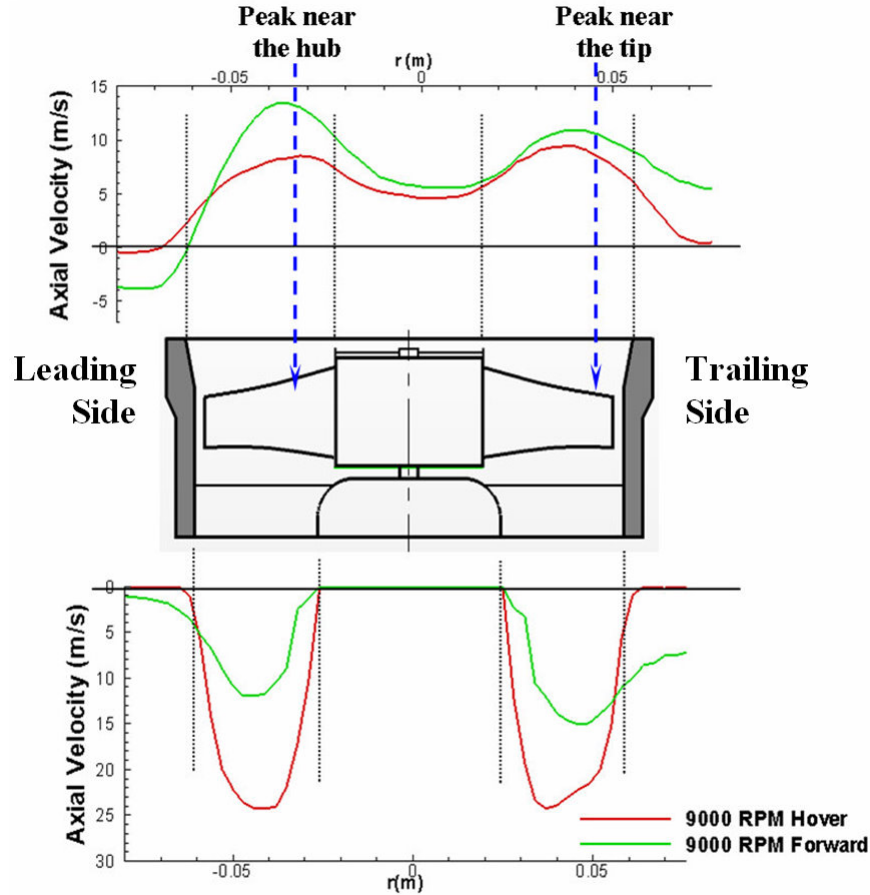


Figure 2.6. Axial Velocity Distribution at the inlet and exit of ducted fan at 9000 rpm

exit jet is deflected and pushed towards to the tip of the tail cone surface at the leading side. The trailing side is affected less than the leading side as expected.

Axial velocity plot shown in Figure 2.6 is drawn along a horizontal line 3 mm away from the exit and inlet surfaces to demonstrate the effect of crosswind velocity on the axial velocity component. Introduction of crosswind simulates the forward flight results in a reduced axial velocity near the leading edge duct lip. That can be explained by the occurrence of a separation bubble on the leading side lip inside the duct. Figure 2.6 also indicates that the axial velocity near the trailing side lip is relatively enhanced when compared to the hover condition.

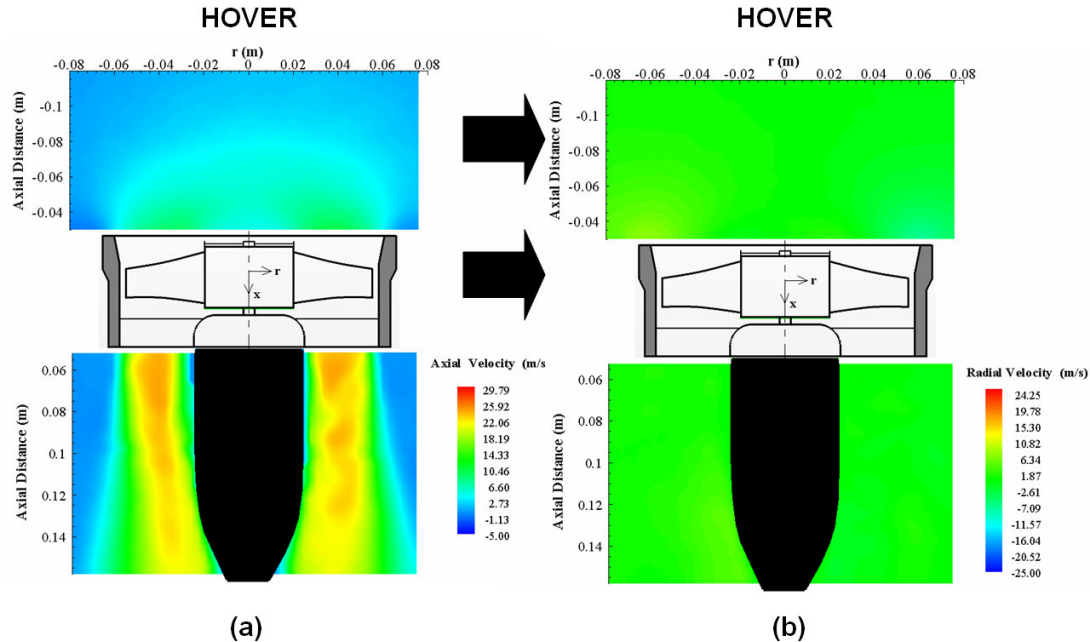


Figure 2.7. Axial (a) and Radial (b) velocity components at HOVER condition (PIV measurements at 9000 rpm)

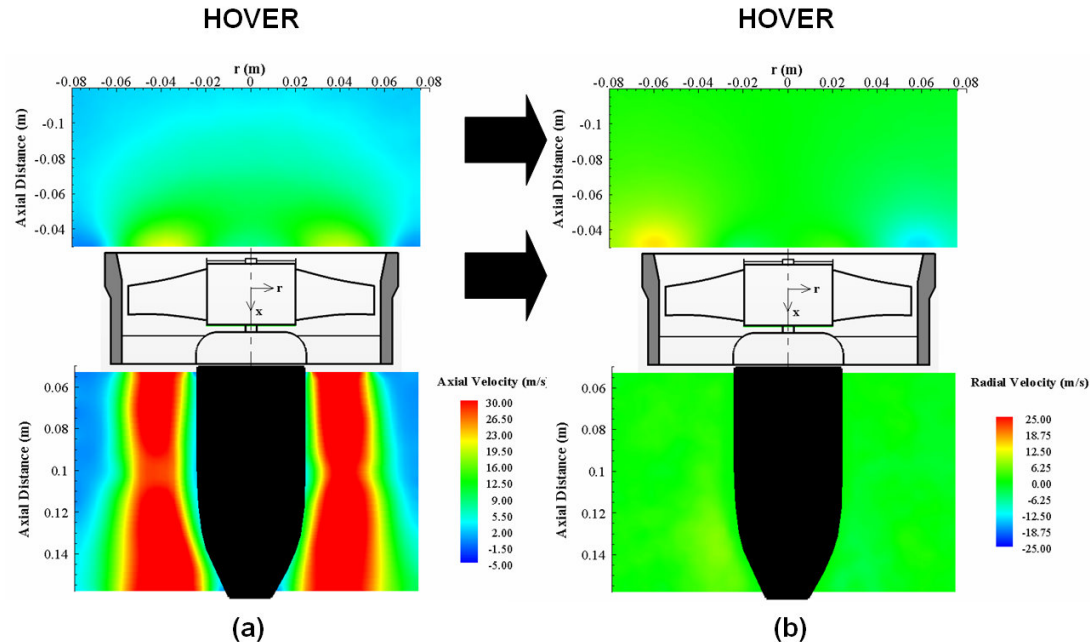


Figure 2.8. Axial (a) and Radial (b) velocity components at HOVER condition (PIV measurements at 15000 rpm)

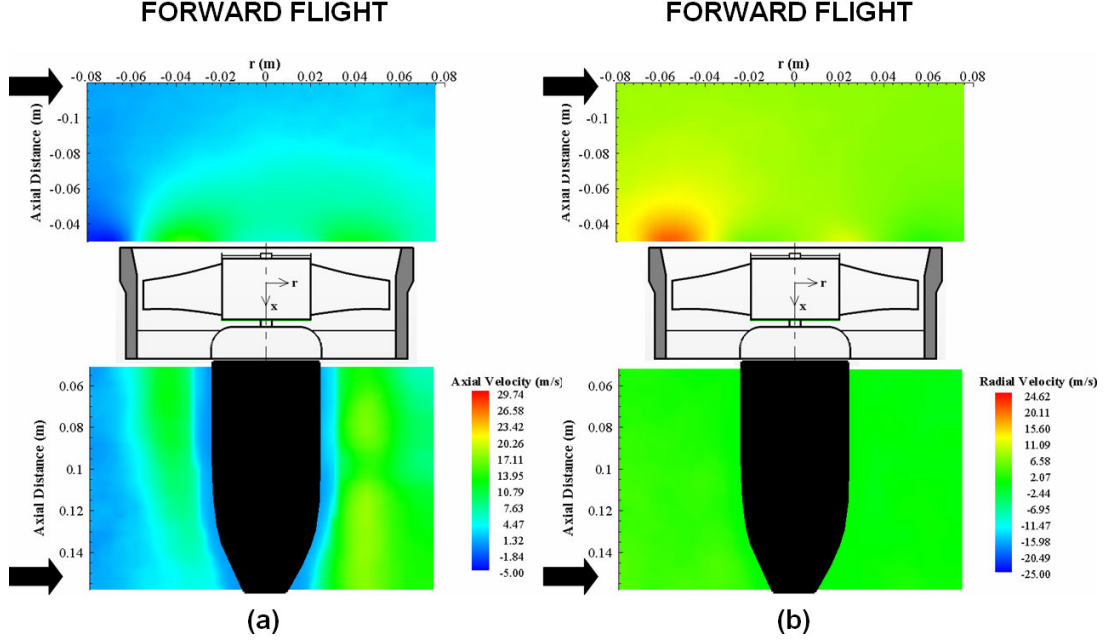


Figure 2.9. Axial (a) and Radial (b) velocity components at FORWARD FLIGHT condition (PIV measurements at 9000 rpm)

Figure 2.5b shows the effects of forward velocity at 15000 rpm. An increase in the rotational speed at forward flight, effectively energizes the air flow at the inlet. The effect of separation at the leading edge is reduced by increasing rotational speed of the fan. The streamlines near the inlet are more normal to the inlet surface at 15000 rpm. The streamlines in the exit jet area are much less influenced by the mainstream flow. Figure 2.5a shows that the mass flow rate passing from the ducted fan at 15000 rpm is much higher than the case for 9000 rpm. The axial velocity peak in exit plane is almost doubled when the rotational speed is increased to 15000 rpm.

Figures 2.7 and 2.8 illustrates the axial and radial velocity components at 9000 and 15000 rpm for hover condition. Increase in axial velocity by a rotational speed increase, results in a significant enhancement of axial momentum of the system. The radial velocities that are usually in much smaller magnitudes than the axial components show a symmetrical distribution with respect to the axis of rotation. The axial and radial velocity components in hover condition results in a reasonably uniform distribution of side forces around the duct.

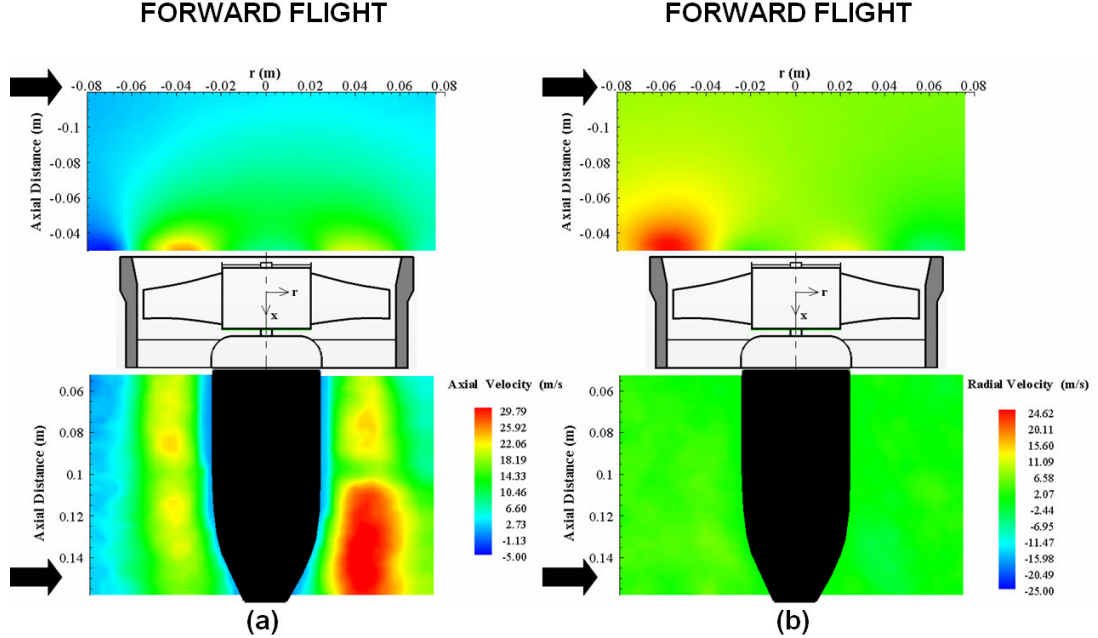


Figure 2.10. Axial (a) and Radial (b) velocity components at FORWARD FLIGHT condition (PIV measurements at 15000 rpm)

Introducing a crosswind velocity to the field changes the distribution of radial flow velocity around the duct. Figures 2.9b and 2.10b indicates an abrupt increase near the leading side of the duct lip. That increase in radial velocity is the result of the strong re-circulatory flow near the leading side as expected. The flow non-uniformities near the leading side of the lip and the strong variations between the leading and the trailing side of the exit jet result in strong pitch-up moment acting on the ducted fan. It is also observed that by the increase of rotational speed, the radial velocity is also increasing. But the same amount of increase can also be seen on the radial velocity distribution in hovering mode. As increasing rotational velocity, axial momentum of the flow is increased. The mass flow rate passing through the duct is increasing by rotational speed of fan rotor. The increased mass flow rate produces stronger fan exit flow.

2.4 Radial Equilibrium Based Analysis of Ducted Fan in Hover and Forward Flight

2.4.1 Computational Model Description

A simulation of the mean flow field around the ducted fan was performed by using a commercial code Ansys-Fluent [84]. The specific computational system solves the 3D Reynolds-Averaged Navier-Stokes equations using a finite volume method. The transport equations describing the flow field are solved in the domain that is discretized by using an unstructured computational mesh. For the analysis of the flow field around ducted fan rotors, there are many computational modeling options in general purpose fluid dynamics solvers. The most complex and time consuming computational model is the modeling of unsteady/viscous/-turbulent flow in and around the fan rotor by using an exact 3D model of rotor geometry using a sliding mesh technique. This type of solution is usually lengthy and requires significant computer resources especially in the forward flight mode when an axisymmetric flow assumption is not applicable. The current RANS computations use a simplified rotor model termed as “*Actuator disk model*” for the generation of the general inviscid flow features of the fan rotor. A $k - \epsilon$ turbulence model was invoked for the current computations, in areas other than the actuator disk. Figure 2.11 shows a flowchart of the method used.

2.4.2 Boundary Conditions

2.4.2.1 Hover

Figure 2.12 shows the specific boundary conditions and computational domain size implemented in the solver for hover condition. The duct and tailcone surfaces are considered as solid walls with no-slip condition. On the side surfaces, a symmetry condition is assumed. For the hover condition, a pressure inlet boundary is assumed on the top surface. Atmospheric static pressure is prescribed on the top surface. Pressure inlet boundary is treated as loss-free transition from stagnation to inlet conditions. The solver calculates the static pressure and velocity

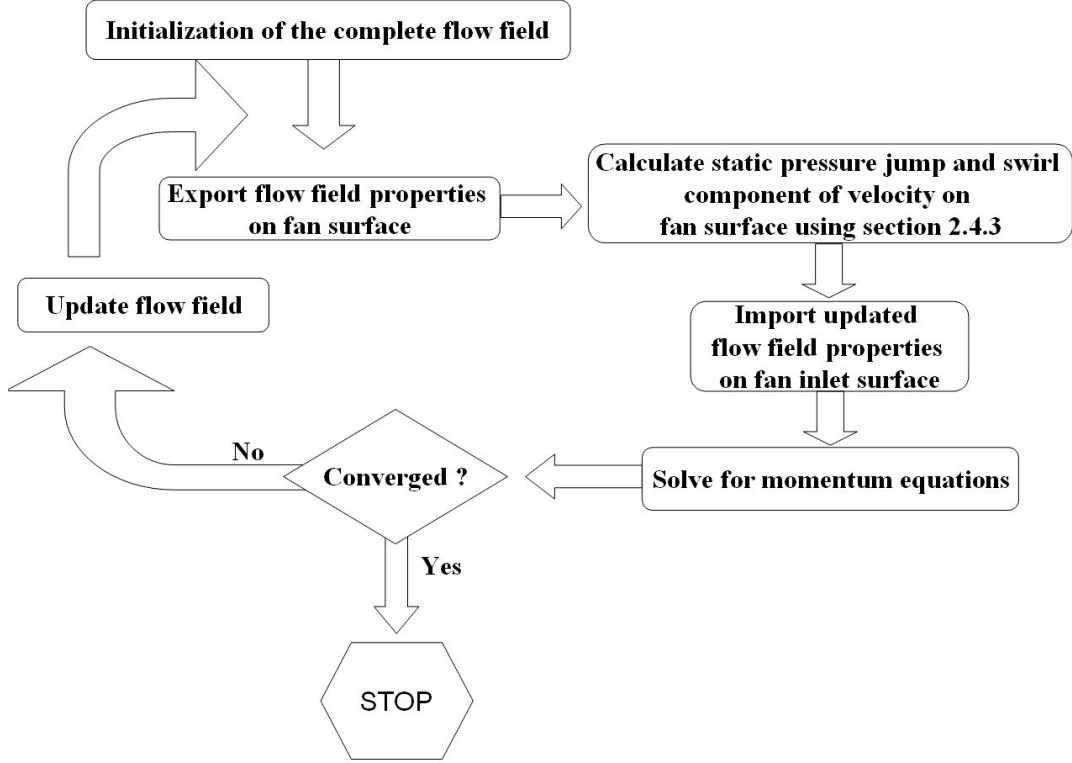


Figure 2.11. Flowchart of the 3D RANS based computational method including the actuator disk.

at the inlet. Mass flux through boundary varies depending on interior solution and specified flow direction. Pressure outlet boundary condition is assumed on the bottom surface for hovering condition. Pressure outlet boundary interpreted as atmospheric static pressure of environment into which the flow exhausts. An additional “Fan” type condition was used for the implementation of the specific actuator disk model described in section 2.4.3.

2.4.2.2 Forward Flight

Figure 2.13 shows the specific boundary conditions implemented in the solver for forward flight. Like hover condition, the duct and tailcone surfaces are considered as solid walls with no-slip condition. Velocity inlet boundary condition is assigned on the windward side of the computational domain. Using this boundary condition velocity and turbulent intensity at the windward side is prescribed. For

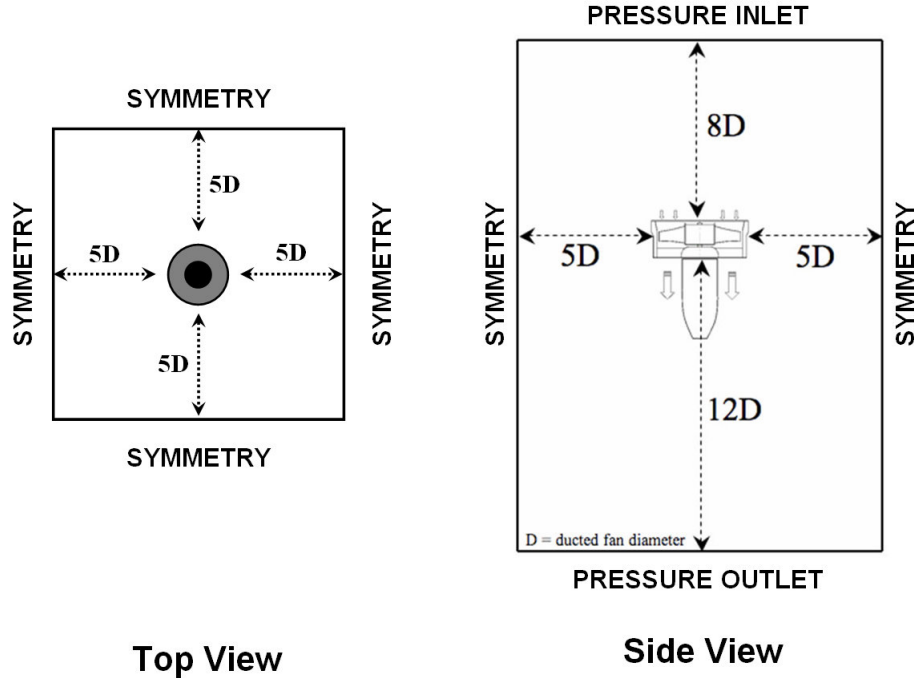


Figure 2.12. Boundary conditions for hover

the leeward side of the domain an outflow condition is assigned. For the top, bottom and remaining side surfaces symmetry boundary condition is assigned. Like the hover condition, “*Fan*” type condition was set using an “*actuator disc model*” replacing the ducted fan rotor. Details of the actuator disk model is explained in section 2.4.3.

2.4.3 Actuator Disk Model

The complex 3D rotor flow field in the rotating frame of reference is replaced by a simplified “*actuator disc model*” originating from the simultaneous use of the radial equilibrium equation, energy equation and the conservation of angular momentum principle across the fan rotor. The radial equilibrium equation is the force balance in the radial direction at a given axial position, balancing the pressure forces in radial direction with the centrifugal force. The viscous effects are ignored in this simplified and easy to implement “*actuator disc model*”.

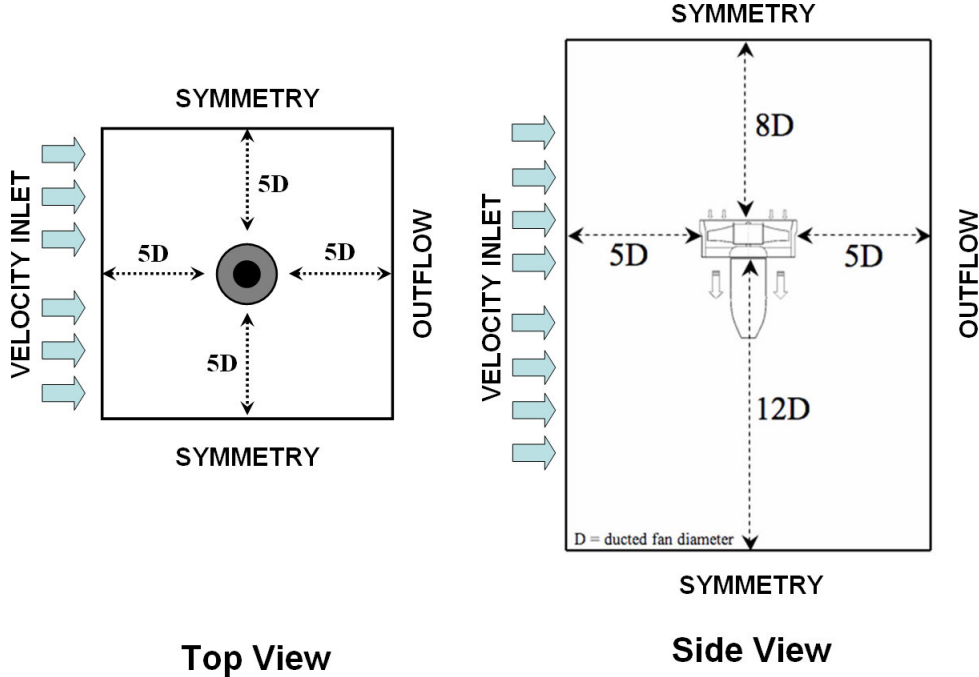


Figure 2.13. Boundary conditions for forward flight

In this approach, a pressure change term is computed at each radial position of the rotor from hub to tip. The magnitude of the static pressure jump term across the rotor is closely related to the amount of stagnation enthalpy change from the rotor inlet to exit. The stagnation enthalpy increase from the rotor inlet to exit is the same as the rate of energy provided to the fluid by the rotor per unit mass flow rate of the duct flow. The conservation of angular momentum principle and energy equation suggests that the magnitude of this jump is mainly controlled by the tangential (swirl) component $c_{\theta 2}$ of the flow velocity in the absolute frame of reference at the exit of the rotor and rotor angular velocity.

Figure 2.14 presents the velocity triangles of the ducted fan rotor at inlet (1) and exit (2). β_1 and β_2 are the blade inlet and exit angles measured from the axial direction. Since the tip Mach number (0.28) of the rotor is not in the compressible flow range, it is reasonable to assume that the internal energy at the rotor inlet e_1 and exit e_2 is the same, $e_1=e_2$. In a ducted fan rotor, it is realistic to assume that the “*axial component*” of the absolute velocity vector is also conserved from inlet

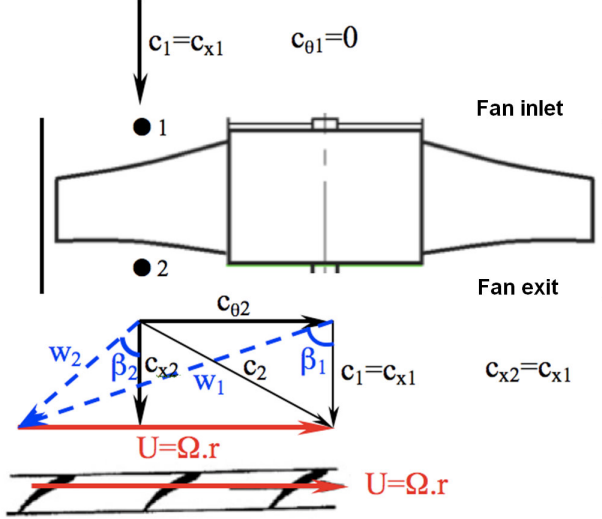


Figure 2.14. Velocity triangles at the inlet and exit of the ducted fan rotor

to exit $c_{x2}=c_{x1}$. The flow is assumed to be axial at rotor inlet where $c_1=c_{x1}$ and $c_{\theta 1}=0$ under design conditions. The relative velocity vector at the exit of the rotor w_2 is smaller than the relative velocity w_1 at the rotor inlet. While the relative flow w_2 is diffusing in the relative frame of reference, the absolute flow velocity vector c_2 is accelerated at the rotor exit, because of added energy to the flow by the rotor.

Equation 2.1 represents the change of stagnation enthalpy in the ducted fan rotor system. The right hand side of this equation is the rate of work per unit mass flow rate of air passing from the rotor. The right hand side is also the same as the product of the rotor torque and angular speed of the fan rotor.

$$h_{O2} - h_{O1} = U(c_{\theta 2} - c_{\theta 1}) \text{ where } U = \Omega r \text{ and } c_{\theta 1} = 0 \quad (2.1)$$

$$(h_2 + c_2^2/2) - (h_1 + c_1^2/2) = U c_{\theta 2} \quad (2.2)$$

$$\left(e_2 + \frac{p_2}{\rho_2} + c_2^2/2 \right) - \left(e_1 + \frac{p_1}{\rho_1} + c_1^2/2 \right) = U c_{\theta 2} \quad (2.3)$$

Equation 2.1 is a simplified form of the energy equation from rotor inlet to

exit of a ducted fan unit. When $e_1=e_2$ is substituted into equation 2.3 because of incompressibility condition, the “*Euler equation*” or “*pump equation*” results in as equation 2.4. Using equations 2.4 and 2.5, an equation for the calculation of static pressure jump between the rotor inlet and exit can be obtained.

The determination of $c_{\theta 2}$ is performed by using the velocity triangles in Figure 2.14. Since the blade inlet/exit angle distribution for 1 and 2 in radial direction is known from the existing rotor geometrical properties, shown in Table 2.1. w_2 can be calculated from the assumption that $c_{x2}=c_{x1}=c_1$. The absolute rotor exit velocity c_2 is determined by adding $U = \Omega r$ to w_2 in a vectorial sense.

$$\frac{1}{\rho} (P_{O2} - P_{O1}) = U c_{\theta 2} \quad (2.4)$$

$$\left(p_2 + \rho \frac{c_2^2}{2} \right) - \left(p_1 + \rho \frac{c_1^2}{2} \right) = \rho U c_{\theta 2} \quad (2.5)$$

$$\Delta p = p_2 - p_1 = \rho \left[U c_{\theta 2} - \frac{1}{2} (c_2^2 - c_1^2) \right] \quad (2.6)$$

Equation 2.6 allows enforcing a prescribed pressure jump Δp in function of density, radial position, rotor angular speed Ω , rotor exit swirl velocity $c_{\theta 2}$, c_1 and c_2 . The rate of energy (per unit mass flow rate) added to the flow by the rotor is specified by the product $U c_{\theta 2}$ as shown in equations 2.4 and 2.5. Equation 2.6 could be evaluated at each radial position between the rotor hub and tip resulting in the radial distribution of the static pressure jump required by the general purpose viscous flow solver for a “*Fan*” type boundary condition. Δp can be effectively specified in a user defined function “*UDF*” in the solver (See Appendix A for details on UDF). The “*Fan*” type boundary condition is an effective and time efficient method of implementing a rotor flow field via an “*actuator disk model*” in a 3D viscous flow computation.

2.4.4 Computational Results

2.4.4.1 Grid Refinement Study

A grid independence study was performed to show that the computational results are not dependent on the computational mesh and that the resolution of the mesh is adequate to capture the significant flow characteristics. The grid independence is evaluated by comparing the computational solutions from 3 different mesh sizes, comprising a coarse mesh with 350,000 nodes, a medium mesh with 750,000 nodes and a fine mesh with 1,200,000 nodes. The axial velocity distributions at the exit of ducted fan are plotted as shown in figure 2.15 for three different grid densities. The profile suggests that the computational results are reasonably grid independent when the 750,000 grid node number is exceeded. Therefore, the medium mesh is used for all predictions in this chapter. Figure 2.16 shows a view from the mesh used in computations.

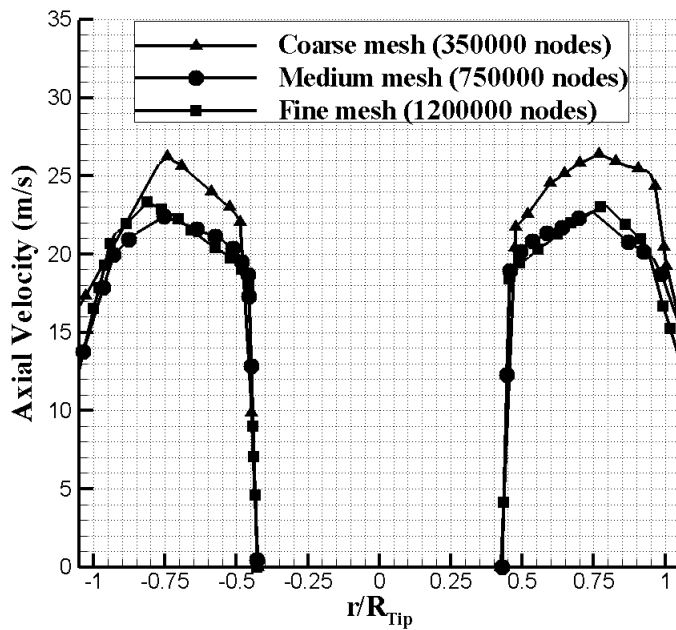


Figure 2.15. Grid independence study

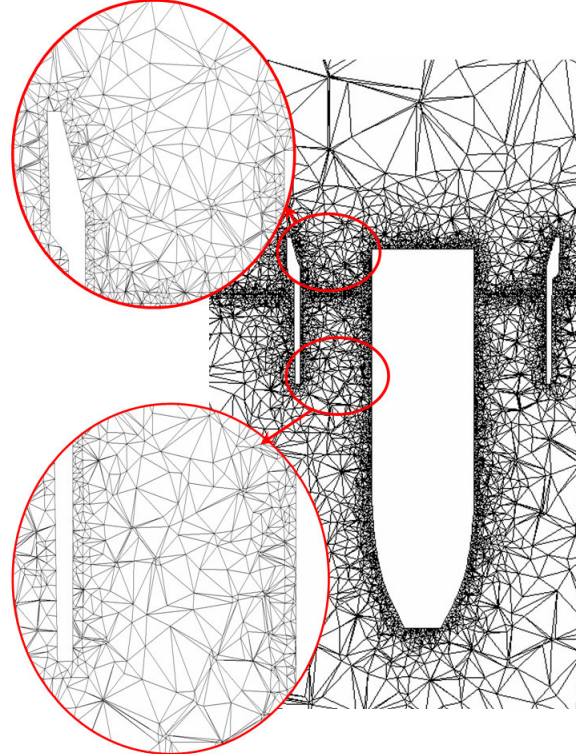


Figure 2.16. Medium mesh used in computations

2.4.4.2 Model Validation at hover and forward flight

Hover Condition Results

In this section, the results of 3D computations are compared to the PIV experiments performed on the 5" diameter ducted fan. The computed axial velocity component at 3 mm away from the duct inlet surface is compared to the results of PIV measurements as shown in Figure 2.17. The computational and experimental results are in good agreement near the leading side of the fan at the inlet plane. The computational predictions near the leading side and the trailing side show an almost symmetrical axial velocity distribution.

The simulation underpredicts the flow as measured by PIV near the trailing side of the duct as shown in Figure 2.17. In a phase-locked PIV approach, measurements are always performed at the same circumferential position of the rotor blade. Since we used a five bladed fan rotor, the right side of the domain in Figure 2.17 contains a rotor blade in the laser sheet. However the left side of the domain

where $r \leq 0$ does not contain a rotor blade in the laser sheet. The slight under-prediction is related to the specific phase-locked position of the rotor during the PIV measurements. Because of the blockage effect introduced by the rotor blade in the laser sheet plane, the PIV measured axial flow velocity magnitude is slightly altered when compared to the computational result.

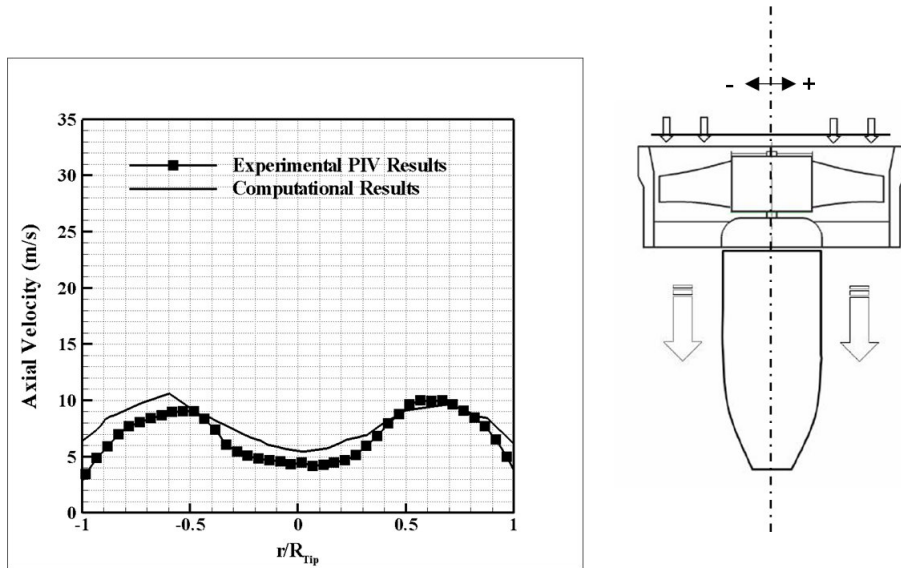


Figure 2.17. Comparison of axial velocity at fan inlet 3 mm away from the duct surface at hover condition 9000 rpm.

The comparison of PIV measurements and computed axial velocity components at 3 mm away from the duct exit surface are shown in figure 2.18. Since the computational method doesn't have any tip loss related term, there is an over prediction of axial velocity near the casing of the ducted fan. It can also be observed that the rotating rotor hub related losses are not predicted well by computations.

Figure 2.19 shows comparison of contour plots obtained from computational predictions and PIV measurements. Computational results are slightly over predicting the measured axial velocity at the inlet of the ducted fan. In addition, predictions near the hub is lower than the measurements, because the rotating hub is not simulated in computations. The hub separation usually exists in small

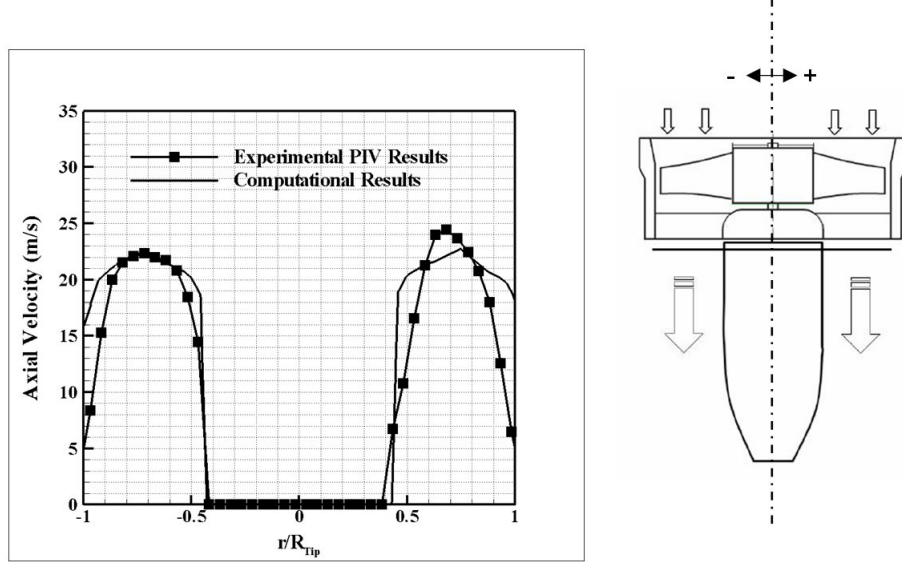


Figure 2.18. Comparison of axial velocity at fan exit 3 mm away from the duct surface at hover condition 9000 rpm.

diameter low Reynolds number ducted fan rotors. The current actuator disk approach neglects the hub separation features acting in the 5" diameter ducted fan.

Forward Flight Condition Results

The comparison of PIV measurements and computed axial velocity components are shown in figure 2.20 for 6 m/s forward flight. Axial velocity computed at the inlet of the ducted fan shows good agreement with PIV measurements. Flow near the hub is underpredicted because the rotating hub effect is not included in computations. It is also noted that the exit axial velocities are overpredicted. At the windward side of the ducted fan, axial velocities are disturbed at the exit windward side of the ducted fan. Losses are shown to be higher in PIV results near the tailcone at the leeward side of the ducted fan.

2.4.5 Summary

The velocity field around the ducted fan was measured using a planar PIV system. Axial and radial velocity components at the inlet/exit region of the ducted fan were measured in hover and horizontal flight at 6m/s.

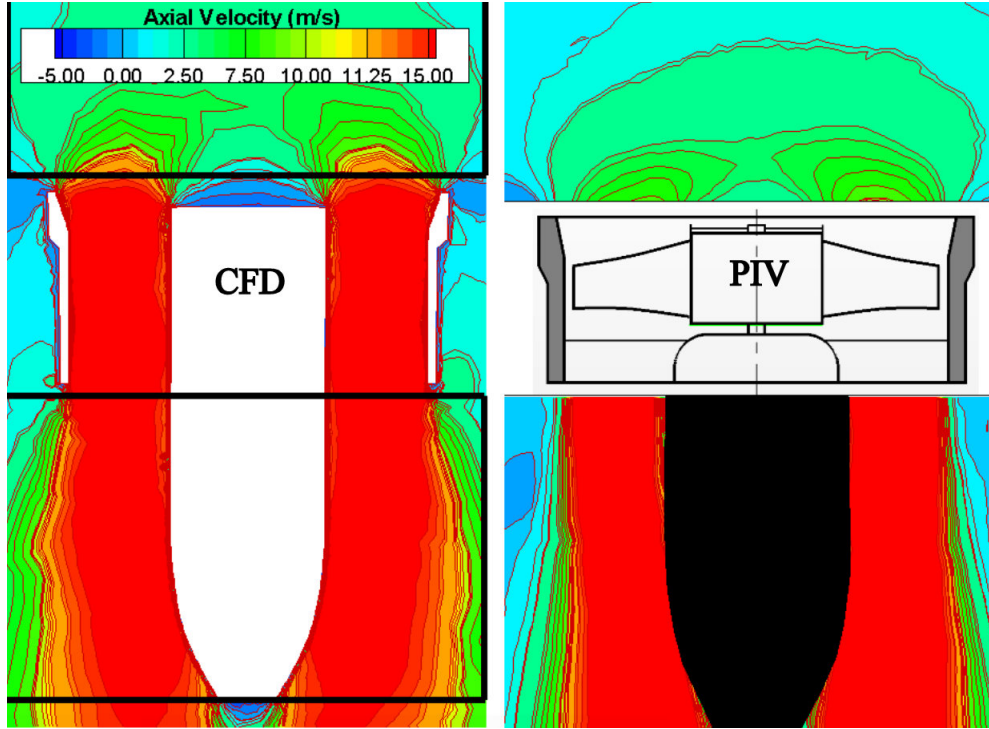


Figure 2.19. Comparison of CFD and PIV axial velocity contours at hover condition at hover condition 9000 rpm.

Beside the experimental study, a computational study based on solving incompressible Navier-Stokes equations was carried out. The specific actuator disk based fan-model developed in this study uses a prescribed static pressure rise across the rotor disk for a time efficient simulation of the fan rotor.

The results of the PIV measurements have proven that the performance of the ducted fan was highly affected from the crosswind velocity. In crosswind, by the effect of the forward flight velocity, a separation region restricting the effective breathing area of the fan rotor, was always observed at the leading side of the ducted fan. That separation bubble significantly affects the exit flow of the fan rotor.

By the introduction of inlet distortion at the leading side, the flow characteristics of the fan were highly altered compared to the fan design conditions. The

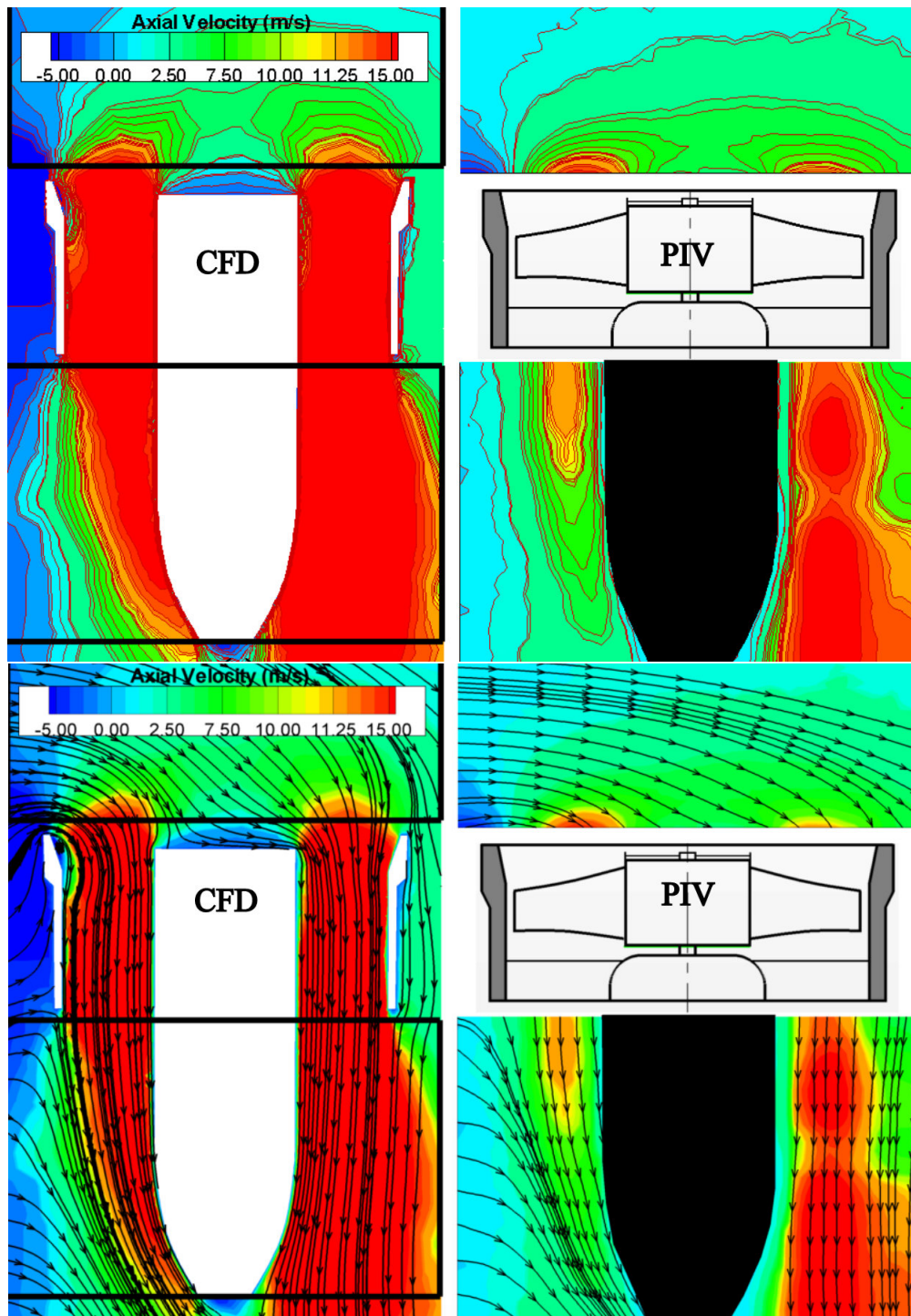


Figure 2.20. Comparison of CFD and PIV axial velocity contours and streamlines at forward flight 9000 rpm and 6 m/s.

inlet flow distortion due to the leading side lip separation results in a measurable drop in thrust force generated by the system.

The measured differentials existing between the leading side and trailing side of inlet flow are likely to generate excessive moment imbalance during the forward flight of the ducted fan based V/STOL UAV. The measured local flow differentials at the inlet plane directly translate into non-uniformities in the exit jet of the ducted fan.

The experimental results showed that an increase in the rotational speed of the fan enhances the axial velocity component at the inlet and exit sections in hover condition, as expected. That increase in the rotational speed of the fan rotor has proven to improve the performance of the ducted fan in forward flight due to improved axial momentum change in the ducted fan.

An increase in the rotational speed of the fan from 9000 rpm to 15000 reduced the effect of the leading side separation bubble.

The radial equilibrium based computational analysis was able to predict the inlet flow axial flow velocity distribution well at the 9000 rpm hover condition.

Chapter **3**

A Novel Inlet Flow Conditioning Concept: Double Ducted Fan (DDF)

3.1 Introduction

This chapter is motivated by the need to improve ducted fan forward flight performance by developing inlet flow control and conditioning approach based on the results presented in chapter 2. A novel ducted fan inlet flow conditioning concept that will significantly improve the performance and controllability of V/STOL “*vertical/short take-off and landing*” UAVs “*uninhabited aerial vehicles*” and many other ducted fan based systems is described. The new concept that will measurably reduce the inlet lip separation related performance penalties in the forward flight zone is named “*DOUBLE DUCTED FAN (DDF)*”. The current concept uses a secondary stationary duct system to control “*inlet lip separation*” related momentum deficit at the inlet of the fan rotor, occurring at elevated forward flight velocities. The DDF is self-adjusting in a wide forward flight velocity range, in terms of its lip separation control ability. The following sections provide the detailed conceptual design approach of DDF and computational analysis.

The current conceptual design study clearly shows that the DDF approach is

applicable to any axial flow fan unit in which there is an inlet flow distortion mainly because the inlet flow direction is not well aligned with the axis of rotation of the axial fan system.

A few other examples that will easily benefit from the DDF concept described in this document are;

- Cooling and utility fans that are flush mounted to external surfaces in marine vehicles.
- The cooling fans that are horizontally mounted at the roof of electric/diesel train locomotive propulsion cabins.
- Air conditioning fans frequently installed at the roofs of passenger buses.

Current approach for proving concept validity: A conventional baseline duct without any lip separation control feature is compared to two different double ducted fans named DDF-A and DDF-B via 3D, viscous and turbulent computational flow analysis. Both hover and forward flight conditions are considered. Significant relative improvements from DDF-A and DDF-B are in the areas of vertical force (thrust) enhancement, nose-up pitching moment control and recovery of mass flow rate in a wide horizontal flight range. The results show a major reduction of highly 3D and re-circulatory inlet lip separation zone when the DDF concept is implemented. The improved uniformity of fan exit flow and reduced differentials between the leading side and trailing side are obvious performance enhancing features of the novel concept. The local details of the flow near the entrance area of the leading side of the ducted fan are explained via detailed static pressure distributions and skin friction coefficients obtained from 3D viscous and turbulent flow analysis including a simulated rotor in the duct. The current rotor flow energy addition simulation is via a radial equilibrium analysis which is a highly time efficient approach implemented into a RANS based flow model.

3.2 Upstream Lip Region Flow Physics for Ducted Fans in Forward Flight

Ducted fan systems horizontally moving at 90° angle of attack all inherently have an inlet flow direction that significantly deviates from the axis of the rotation. The inlet flow distortion near the leading side of all of these fan inlets becomes more problematic with increasing vehicle speed. The inlet flow distortion passing through a typical axial flow fan rotor becomes increasingly detrimental with elevated forward flight velocity. The lip separation occurring on the inner side of the lip section severely limits the lift generation and controllability of V/STOL UAVs. In general, the leading side of the fan near the lip separation zone breathes poorly when compared to the trailing side of the ducted fan. The trailing side total pressure is usually much higher than the total pressure observed near the leading side at the exit of the rotor. The flow near the leading side is adversely influenced by a separated flow zone that is characterized as highly re-circulatory, low momentum, unsteady and turbulent.

Conventional ducted fan systems also have a tip clearance loss that is proportional with the effective tip gap size inherent to each design. The specific shape of the tip platform and the surface properties and arrangement designed onto the casing surface also influences the magnitude of tip clearance loss. This aerodynamic deficiency is measured as a significant total pressure loss near the tip at the exit of the rotor all around the circumference when the vehicle is only hovering with no horizontal flight. When the vehicle transits into a horizontal flight, the total pressure loss/deficit at the exit of the rotor near the leading side is much more significant than “*hover only*” loss of the ducted fan. In addition to the conventional tip clearance energy loss, the rotor generates additional losses near the leading side, because of the re-circulatory low momentum fluid entering into the rotor near the tip section. This is clearly an off-design condition for an axial flow fan that is designed for a reasonably uniform inlet axial velocity profile in the spanwise direction. The immediate results of any inlet flow distortion entering into an axial fan rotor in horizontal flight are the loss of rotor’s energy addition capability to the fluid near the leading side, an imbalance of the local mass flow

rate between the leading side and trailing side, an imbalance of the total pressure resulting at the rotor exit between the leading side and trailing side, a significant loss of lifting ability due to highly non-axisymmetric and unnecessarily 3D fan exit jet flow, unwanted nose-up pitching moment generation because the local static distributions imposed on the duct inner surfaces.

3.3 Lip Separation at High Angle of Attack

The new concept named “*Double-Ducted Fan (DDF)*” is based on a very effective fluid mechanics scheme of reducing and controlling the upstream lip separation in a ducted fan operating at high angle of attack. Early research results clearly demonstrating the limits of onset of upstream lip separation as a function of angle of attack are summarized in Figure 3.1. A full scale duplicate of the V/STOL ducted propeller used on the Bell Aerosystems Co. X-22A airplane was tested in Ames Research center by Mort and Gamse [39, 40]. Stall of both the upstream and downstream duct lips of this seven foot diameter ducted fan was examined in function of angle of attack. The angle of attack of the ducted fan is the angle between the approaching flow direction and the axis of rotation of the rotor. It was found that the onset of separation on the upstream lip will be encountered; however, complete separation on this lip will be encountered only during conditions of low power and high duct angle of attack corresponding to high rates of descent.

Tests of a wing-tip-mounted 4-foot-diameter ducted fan were performed for a limited range of operating conditions by Mort and Yaggy [38]. At large duct angles of attack, the inside of the upstream duct lip stalled causing a rapid change in the duct pitching moments and accompanying increase in the power required. At low horizontal velocities this lip stall would probably limit the rate of descent of a vehicle with a wing tip mounted ducted fan. The wind tunnel test results shown in Figure 3.1 are highly relevant in demonstrating the beneficial aerodynamic characteristics of the double ducted fan DDF concept presented in this section.

Although, the reference ducted fan rotor had a tip clearance of $t/h=5.8\%$, the

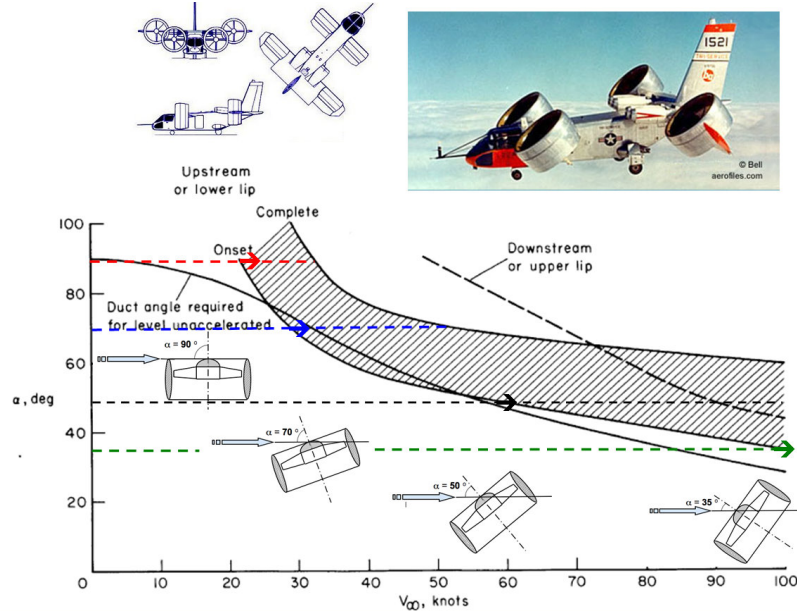


Figure 3.1. Upstream duct lip stall in function of angle of attack for X-22A ducted fan [39, 40]

tip clearance influence on the rotor downstream flow was knowingly excluded from the current 3D computational flow effort. The present simplified rotor flow model does not include tip clearance effects since the current effort is focused on the accurate simulation of the lip separation flow during forward flight of the vehicle. A radial equilibrium theory based rotor disk without a tip gap was chosen as a simplified and time efficient rotor model in this section.

3.4 Adverse Effects of Upstream Lip Separation in Forward Flight

At high angle of attack, the onset separation at the upstream duct lip is accompanied by the formation of a separation bubble. Existence of a significant separation bubble severely distorts inlet flow of the fan rotor especially near the leading side and in the tip clearance region. Distorted inlet flow causes an asymmetric loading of the ducted fan which increases the power required for level unaccelerated flight and noise level. The immediate results of operating a ducted fan

in horizontal flight regime especially at high angle of attack are as follows:

- Increased aerodynamic losses and temporal instability of the fan rotor flow when “*inlet flow distortion*” from “*the lip separation area*” finds its way into the tip clearance gap leading to the loss of “*energy addition capability*” of the rotor.
- Reduced thrust generation from the upstream side of the duct due to the rotor breathing low-momentum and re-circulatory, turbulent flow.
- A severe imbalance of the duct inner static pressure field resulting from low momentum fluid entering into the rotor on the leading side and high momentum fluid unnecessarily energized near the trailing side of the rotor.
- A measurable increase in power demand and fuel consumption when the lip separation occurs to keep up with a given operational task.
- Lip separation and its interaction with the tip gap flow requires a much more complex vehicle control system because of the severe non-uniformity of the exit jet in circumferential direction and excessive nose-up pitching moment generation.
- At low horizontal speeds a severe limitation in the rate of descent and vehicle controllability may occur because of more pronounced lip separation. Low power requirement of a typical descent results in a lower disk loading and more pronounced lip separation.
- Excessive noise and vibration from the rotor working with a significant inlet flow distortion.
- Very complex unsteady interactions of duct exit flow with control surfaces.

3.5 Reference Ducted Fan Characteristics

Figure 3.2 shows the five bladed reference ducted fan that is used in the present DDF development effort. The relatively poor forward flight characteristics of the

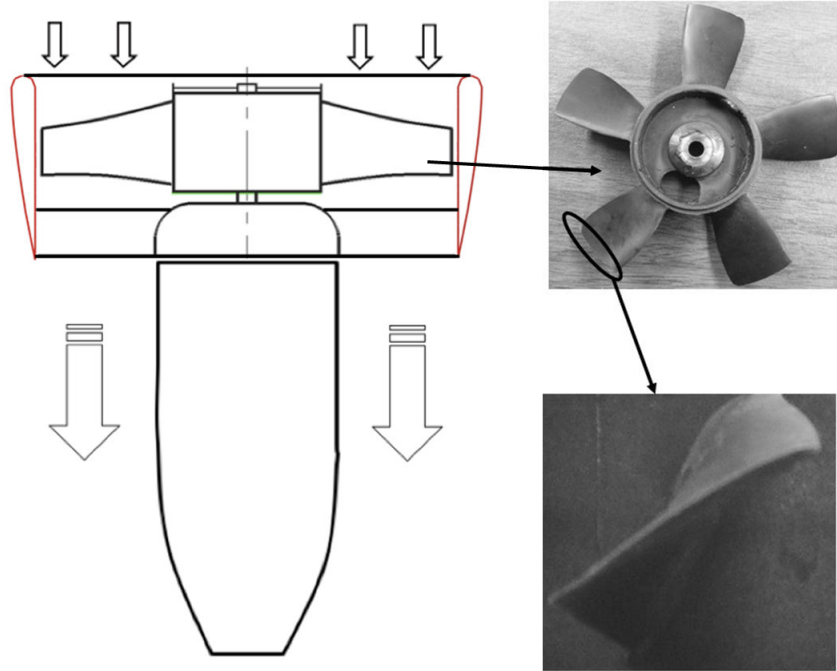


Figure 3.2. Reference ducted fan and fan rotor used for DDF development effort

reference ducted fan shown in Figure 3.2 are significantly improved via the new double ducted fan (DDF) concept that is explained in the next few paragraphs. The geometric specifications of the reference ducted fan unit that is designed for small scale uninhabited aircraft are presented in table 2.1. This unit is manufactured from carbon composite material and has six vanes at the exit of the fan in order to remove some of the swirl existing at the exit of the rotor. A tail cone is used to cover the motor surface and hide the electrical wiring. All computational 3D flow simulations of the reference duct including the rotor flow field are performed at 9000 rpm using the geometry defined in Figure 3.2.

3.6 Double Ducted Fan (DDF)

A novel ducted fan concept as a significant improvement over a standard ducted fan is explained in Figure 3.3. The poor forward flight characteristics of the reference duct as shown in Figure 3.3a are effectively improved with the “*Dou-*

ble Ducted Fan" concept as presented in Figure 3.3b. A typical deficiency of a standard ducted fan is mainly related to the forward lip separation increasingly occurring when the forward flight velocity is gradually increased as shown in the streamline patterns of Figure 3.3a.

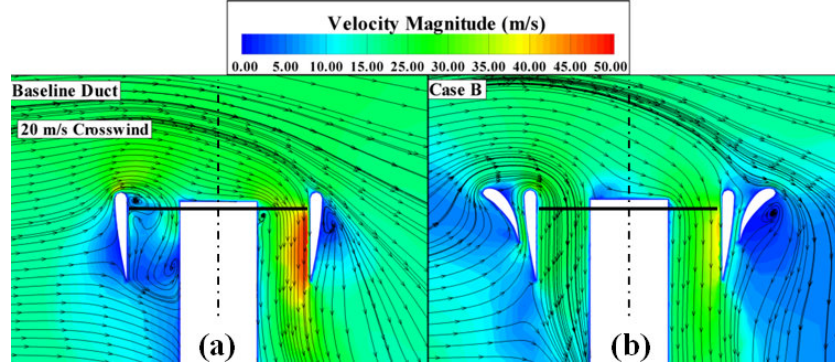


Figure 3.3. Separated flow near the forward lip section of a standard ducted fan (left) and the flow improvements from the novel concept Double Ducted Fan (DDF) at 9000 rpm, colored by the magnitude of velocity

The inlet flow near the leading side of the standard duct is highly separated, low-momentum and turbulent. The apparent flow imbalance between the leading side and trailing side of the standard ducted fan as shown in Figure 3.3a is also called an "*inlet-flow-distortion*". Flow simulations in Figure 3.3a show that the rotor barely breathes at the inlet section of the leading side although the trailing side passes a significant amount of flow. This flow imbalance amplified during the rotor "*energy adding process*" is one of the reasons of significant nose-up pitching moment generation. Figure 3.3b also presents the Double Ducted Fan (DDF) flow simulations indicating the effective inlet flow distortion reduction due to the unique aerodynamic properties of the (DDF) system. The upstream lip separation near the leading side is almost eliminated resulting in a more balanced rotor exit flow field between the leading side and the trailing side. More detailed descriptions of the local flow field improvements resulting from the novel Double Ducted Fan (DDF) concept are discussed in the final part of this document. Although there may be many other potentially beneficial variations of the Double Ducted Fan concept, only the specific (DDF) form defined in Figure 3.3b will be explained in detail in the preceding sections.

3.6.1 Geometric Definition of DDF

The DDF concept uses a second duct using a lip airfoil shape that has a much shorter axial chord length than that of the standard duct. The key parameter in obtaining an effective DDF arrangement is the size of the lip diameter D_L of the standard ducted fan. The second duct airfoil that is relatively cambered has a leading edge diameter set to 0.66 D_L as explained in Figure 3.4b. The angular orientation and axial position of the second duct airfoil is extremely important in achieving a good level of flow improvement near the leading side of the rotor. The leading edge circle of the second duct airfoil is slightly shifted up in the vertical direction for proper inlet lip separation control. The vertical distance between the duct inlet plane touching the standard duct and the plane touching the second duct is about 0.33 D_L as shown in Figure 3.4b. The horizontal distance between the centers of the leading edge circles of the standard duct and outer duct is about 4 D_L . The axial chord of the second duct airfoil is about 5 D_L . The separation distance between the standard duct and second duct is controlled by the recommended throat width of 0.8 D_L as shown in Figure 3.4b.

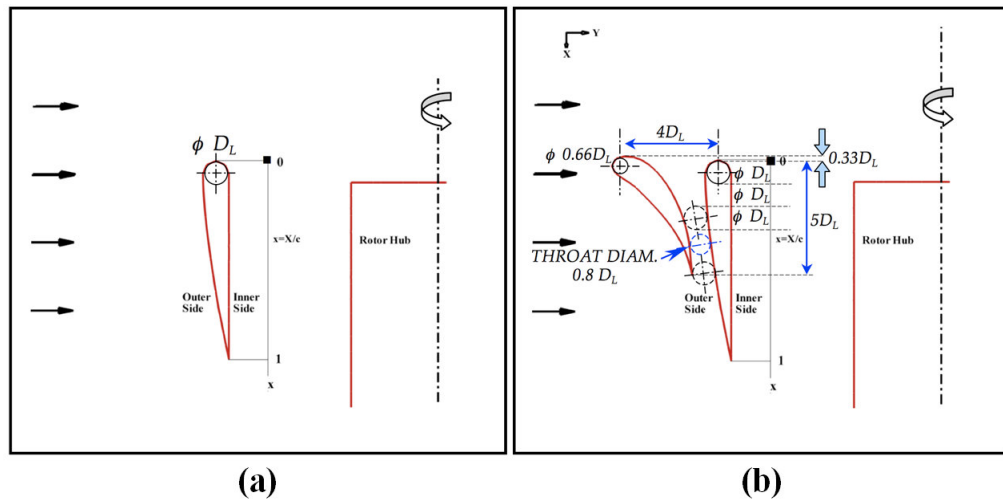


Figure 3.4. (a)Reference duct airfoil definition in a standard ducted fan arrangement, (b)Double Ducted Fan (DDF) geometry as a novel concept

3.6.2 Converging-Diverging Channel in the Duct

The second duct and the standard duct forms a converging-diverging channel starting from the trailing edge of the second (outer) duct that is located at about $X=5D_L$. The axial position of the throat section is about $0.45c$ where c is the axial chord of the inner duct as shown in Figure 3.4b. The duct width at the entrance of the converging-diverging duct is D_L . The entrance to the converging-diverging channel is at the trailing edge point of the second duct. There is a (vertically up) net flow in the converging-diverging duct of the DDF. This flow is due to increasing dynamic pressure at the entrance of the converging-diverging duct at $X=5D_L$ when the forward flight velocity is increased. The diverging part of the channel flow between the standard and outer duct is extremely important in this novel concept, since this decelerating flow is instrumental in adjusting the wall static pressure gradient just before the lip section of the leading edge of the standard duct. The self-adjusting dynamic pressure of the inlet flow into the converging-diverging duct is directly proportional with the square of the forward flight velocity of the vehicle. The converging-diverging duct flow is in vertically up direction near the leading edge of the vehicle. The flow in the intermediate channel is vertically down when one moves away from the frontal section of the vehicle. This flow direction is caused by the relatively low stagnation pressure at the inlet of the intermediate channel at circumferential positions away from the leading edge. This vertically down flow induced by the static pressure field of the inner duct exit flow is likely to generate measurable additional thrust force for the DDF based vehicle.

3.7 Various Possible Double Ducted Fan Geometries

The standard duct and three possible variations of the Double Ducted Fan (DDF) concept described in this study are presented in Figures 3.5 and 3.6. Three dimensional solid models of the four duct configurations, a horizontal cross section and a vertical cross section are included in these figures.

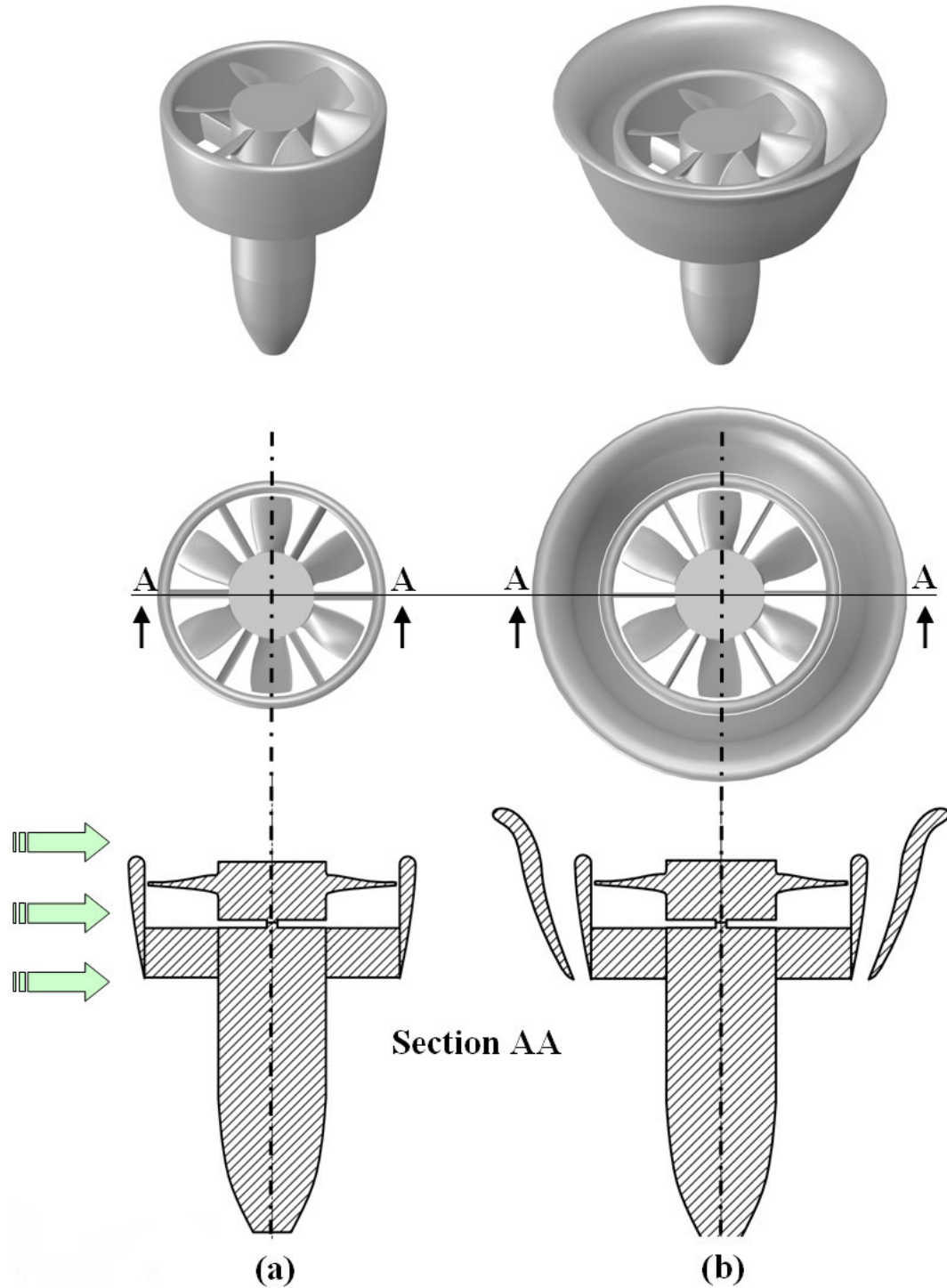


Figure 3.5. (a)Baseline ducted fan (Standard duct), (b)CASE-A tall double ducted fan (DDF)

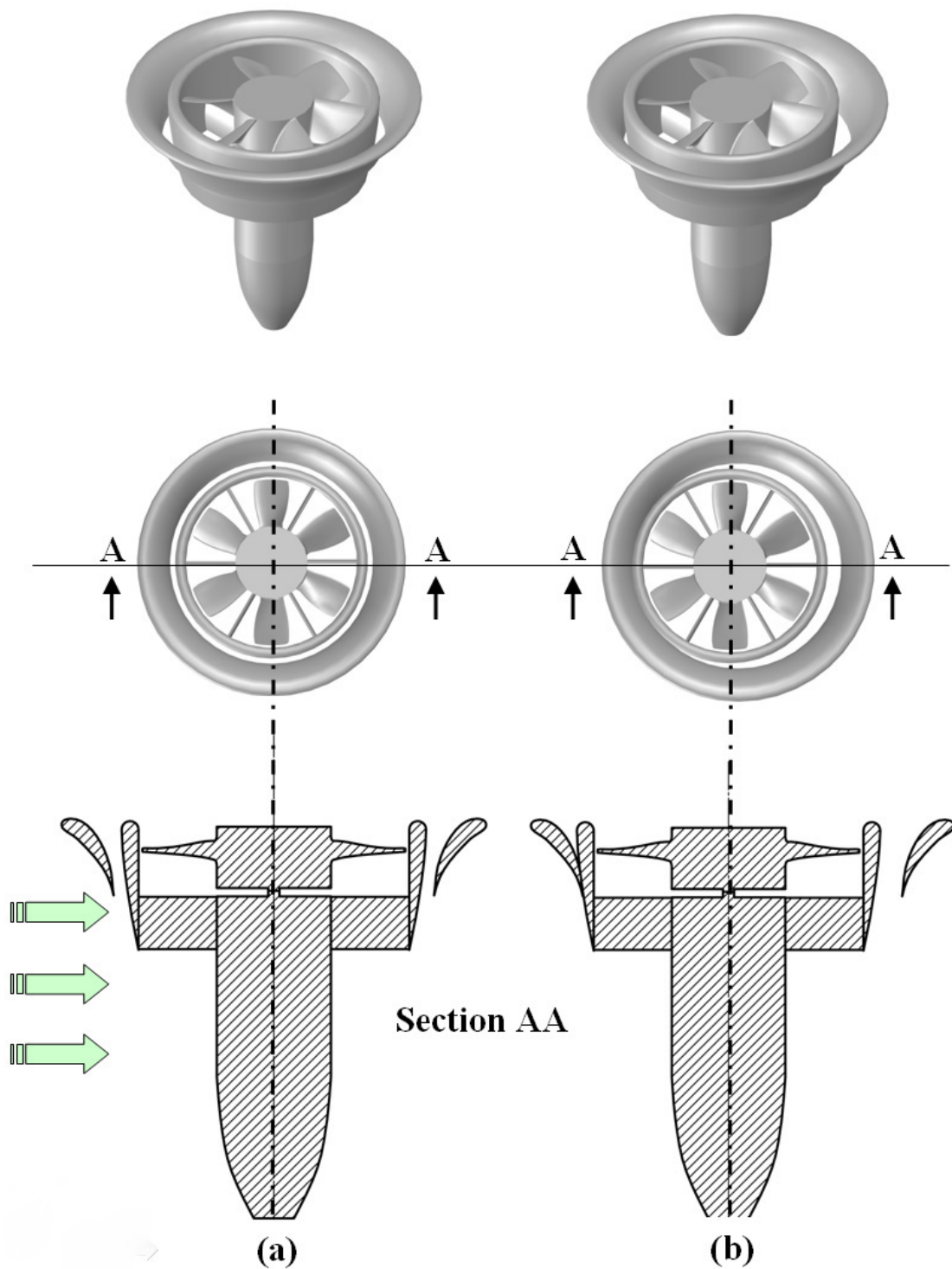


Figure 3.6. (a)CASE-B short double ducted fan (b)Eccentric double ducted fan

CASE-A as shown in Figure 3.5b is termed as the tall DDF. The tall DDF is able to generate a significantly higher thrust in hover position than that of the standard duct containing an identical rotor. However, in forward flight, due to the extended axial chord of the outer duct, the nose-up pitching moment generation is also significant in this design. This design has a throat section located at the trailing edge of the duct airfoils. Since the axial chord of the outer duct is longer than that of the inner duct this design may have a drag penalty when compared to the standard ducted fan.

Figure 3.6a shows the most effective Double Ducted Fan (DDF) configuration CASE-B since it has the ability to generate a significant amount of thrust when compared to that of the standard ducted fan configuration. Another important characteristic of CASE-B is its ability to operate without enhancing the nose-up pitching moment of the vehicle in forward flight. This configuration was analyzed in great detail mainly because of its combined ability to enhance thrust and reduce nose-up pitching moment in forward flight without a significant drag increase.

An ECCENTRIC DOUBLE DUCTED FAN (DDF) concept is also shown in Figure 3.6b. This concept requires a movable outer duct in order to control the throat area in the intermediate duct of the vehicle for a highly optimized forward flight performance. Variable throat mechanism introduced in this concept provides a greater range of operation in a DDF type vehicle offering a more accurate lip flow control over a much wider forward flight velocity range. Figure 3.6b shows a highly blocked second duct that is proper for very low forward flight velocity. It is required that the throat area is enlarged by moving the outer duct as the forward flight velocity is increased. Although an almost optimal lip separation control can be achieved with an eccentric (DDF), its mechanical complexity and weight penalty is obvious. The outer duct airfoil definition of this concept is the same as CASE-B that is described in detail in Figure 3.4b.

3.8 DDF Concept Validation

A three dimensional simulation of the mean flow field around the ducted fan was performed using a custom developed actuator disk model based on radial equilibrium theory implemented into the commercial code Ansys-Fluent. The specific computational system solves the Reynolds Averaged Navier-Stokes (RANS) equations using a finite volume method. Details of the computational method can be found in section 2.4.

3.8.1 Air Breathing Character of DDF in Forward Flight

Table 3.1 presents the computed fan rotor mass flow rate for all ducted fan types studied in this paper for both hover and forward flight conditions. In addition to hover conditions, the results are also presented for 10 m/s and 20 m/s forward flight velocities at 9000 rpm rotor speed that is constant for all computations.

	Fan Mass Flow Rate (kg/s)	Thrust (N)	Pitching Moment (N.m)	Flight Condition
Baseline Duct	0.30	3.04	0.00	No Crosswind (Hover)
Baseline Duct	0.29	3.47	0.17	10 m/s Crosswind
Baseline Duct	0.20	3.11	0.27	20 m/s Crosswind
MODIFIED DUCTS (DDF)				
Case A	—	—	0.00	No Crosswind (Hover)
Case A	0.31	4.93	0.37	10 m/s Crosswind
Case A	0.26	5.07	0.83	20 m/s Crosswind
Case B	—	—	0.00	No Crosswind (Hover)
Case B	0.30	3.72	0.16	10 m/s Crosswind
Case B	0.28	4.86	0.29	20 m/s Crosswind

Table 3.1. Computed rotor mass flow rate for all fan configurations during hover and forward flight

Constant rpm flow simulations provide a basis for comparisons of 3D mean flow, fan thrust, nose-up pitching moment, total pressure and static pressure fields. Although the rotor speed is constant for all computations, the amount of mechanical energy transferred to the air during its passage through the rotor varies, because of highly varying inlet flow field into the ducted fan unit during hover, forward flight at 10 m/s and 20 m/s. Table 3.1 also provides the computational estimates of thrust, nose-up pitching moment for hover and forward flight conditions.

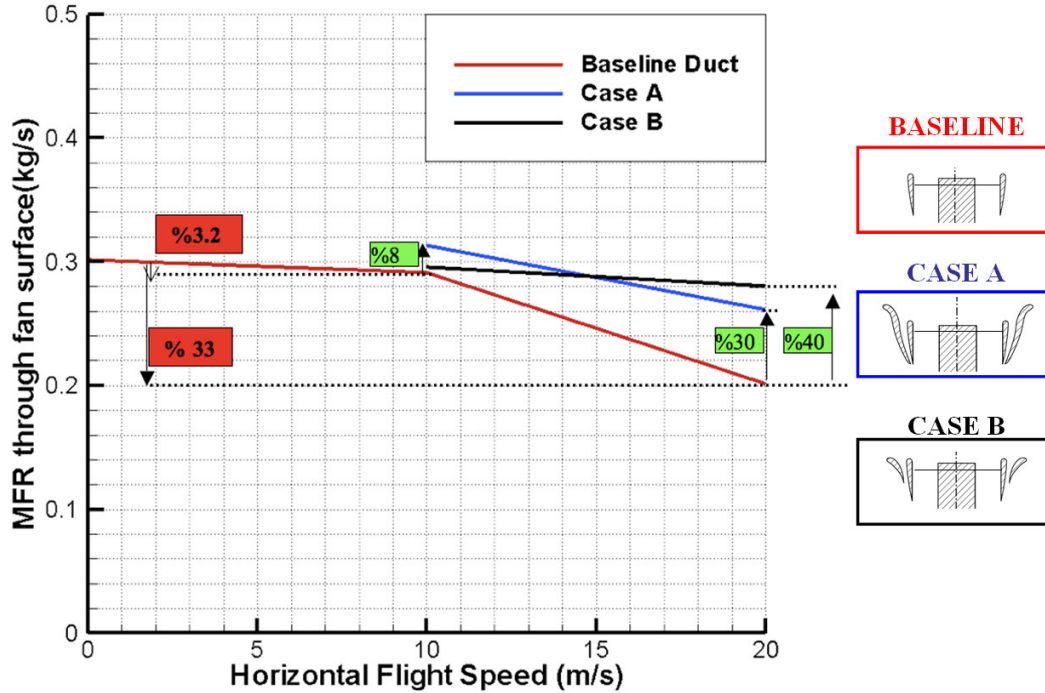


Figure 3.7. Rotor disk mass flow rate versus forward flight speed at 9000 rpm

Figure 3.7 shows that the baseline duct suffers from a high level of “*inlet flow distortion*” at 10 m/s and 20 m/s forward flight velocity. The overall mass flow rate passing from the ducted fan is reduced to 66 % of the hover mass flow rate as shown by the red line in Figure 3.7 (for 20 m/s forward flight). This significant limitation on the rotor mass flow rate is mainly the result of the large separated flow region occurring at just downstream of the lip section of the leading side of the duct as shown in Figure 3.3. While the leading side of the baseline duct passes a severely limited amount of air mass, the trailing side of the duct is able to breathe at a better rate than the leading side. It is apparent that the leading side of the baseline duct is partially blocked at high forward flight velocities. Figure 3.7 also shows a significant drop in rotor mass flow rate when the forward flight velocity is increased from 10 m/s to 20 m/s.

Baseline duct mass flow rate, thrust and nose-up pitching moment:
Table 3.1 contains nose-up pitching moment information for all flight regimes showing a measurable increase in the pitching moment when the baseline vehicle

moves at 10 m/s and 20 m/s in comparison to hover conditions. The nose-up pitching moment is measured with respect to the center of gravity of the ducted fan unit for all cases. At 20 m/s forward flight condition, the predicted pitching moment is 1.6 times that of the pitching moment at 10 m/s flight velocity. The pitching moment generation on a typical ducted fan in forward flight is directly related to the extent of inlet lip separation, the impingement of the rotor inlet flow on the duct inner surface (aft shroud surface) on the trailing side of the duct, imbalance of the rotor exit field between the leading side (low momentum) and trailing side (high momentum), aerodynamic profiling of the duct outer surface especially near the leading side.

Predicted baseline ducted fan thrust values at 10 m/s and 20 m/s increase to 1.5 times and 1.7 times of the thrust of the baseline duct at hover conditions. This relative thrust improvement is due to the specific external shape of the baseline duct and modified rotor inlet conditions at elevated forward speed levels.

Mass flow rate, thrust and nose-up pitching moment characteristics of CASE-A : The air breathing character of the baseline duct can be significantly improved by implementing the tall double ducted fan (DDF) designated as CASE-A as shown in Figure 3.7. The mass flow rate of CASE-A is about 8 % more than that of the baseline duct operating at the forward speed of 10 m/s. The rotor mass flow rate improvement for CASE-A at 20 m/s is much higher than that of the baseline duct operating at 20 m/s. A 30 % improvement over the baseline duct is possible. This relative mass flow rate improvement is a direct result of reduced inlet lip separation near the leading side of the duct designs at forward flight.

The predicted thrust for the tall double ducted fan (DDF) CASE-A is markedly higher than that of the baseline duct. At 10 m/s horizontal flight velocity, the thrust of CASE-A is about 1.7 times that of the baseline duct. When the flight velocity is elevated to 20 m/s, CASE-B produces an augmented thrust value of 1.9 times that of the baseline duct. The reduction of the inlet lip separation results in a direct improvement of the ducted fan exit flow near the leading side of the duct. The thrust improvements are due to both ducted fan exit flow im-

provements near the leading side of the unit, the external aerodynamic shape of the outer duct. The leading side of the DDF CASE-A rotor plane breathes air from the inlet at a much-improved rate than that of the trailing side. The tall (DDF) CASE-A also entrains a measurable amount of air into the outer duct from the inlet area of the unit especially near the trailing side. The flow in the outer duct is in opposite direction to the rotor flow near the leading side. However, the outer duct flow for the circumferential positions away from the leading side of the duct is in the same direction as the main rotor flow direction. Additional thrust augmentation is possible in the outer duct at positions away from the leading edge.

Although the tall (DDF) CASE-A is an excellent thrust producer at high forward flight velocities, it has the capability of augmenting the usually unwanted nose-up pitching moment mainly because of the external shape of the outer lip at elevated forward flight velocities. The pitching moment predicted at 10 m/s is about 2.2 times that of the baseline duct. At 20 m/s, the pitching moment produced by CASE-A is about 3.1 times that of the baseline duct value. The reason the short ducted fan CASE-B was designed and developed was the need to reduce the unwanted pitching up moment generation unique to CASE-A.

An effective DDF design CASE-B with highly reduced nose-up pitching moment: CASE-B as shown in Figure 3.7 is a shorter version of the double ducted fan design concept. CASE-B is designed to produce a significantly reduced nose-up pitching moment when compared to CASE-A. Another goal with CASE-B is to obtain similar thrust gains over the baseline duct. The short double ducted fan (DDF) CASE-B controls the lip separation as effectively as the tall (DDF) CASE-A without producing a high nose-up pitching moment. The airfoil geometry forming the outer duct has an axial chord length that is about half of the axial chord of the inner duct (also termed as standard fan or baseline fan). A detailed description of obtaining a short double ducted fan (DDF) CASE-B is given in Figure 3.4a. starting from a baseline duct. Figure 3.7 indicates that the mass flow rate improvement (black line) of CASE-B is very similar to CASE-A (blue line). The short (DDF) CASE-B's sensitivity to increasing forward flight velocity is much less when compared to tall (DDF) CASE-A. Implementation of a second

duct as shown in Figure 3.4b enhances the lip separation controlled flight zone further into higher forward flight velocities. The thrust values predicted for the short (DDF) are much higher than the standard duct predictions at 10 m/s and 20 m/s. There is a slight reduction in thrust when comparison is made against the tall (DDF) CASE-A. The most significant property of CASE-B is its ability to control nose-up pitching moment effectively. The pitching moment generation for the short (DDF) CASE-B is very much suppressed when compared to tall (DDF) CASE-A. CASE-B nose-up pitching moments are about the same as the values predicted for the baseline duct. The short (DDF) concept described in Figure 6.b is a highly effective scheme of improving the lip separation related inlet flow distortion problem for the rotor of a ducted fan based VTOL/STOL vehicle. CASE-B is able to improve thrust without increasing the nose-up pitching moment generation. Since the leading side of the fan exit jet is well balanced against the trailing side of the exit jet, the effectiveness of the control surfaces at the exit of the ducted fan are expected to function much effectively for the short (DDF) CASE-B.

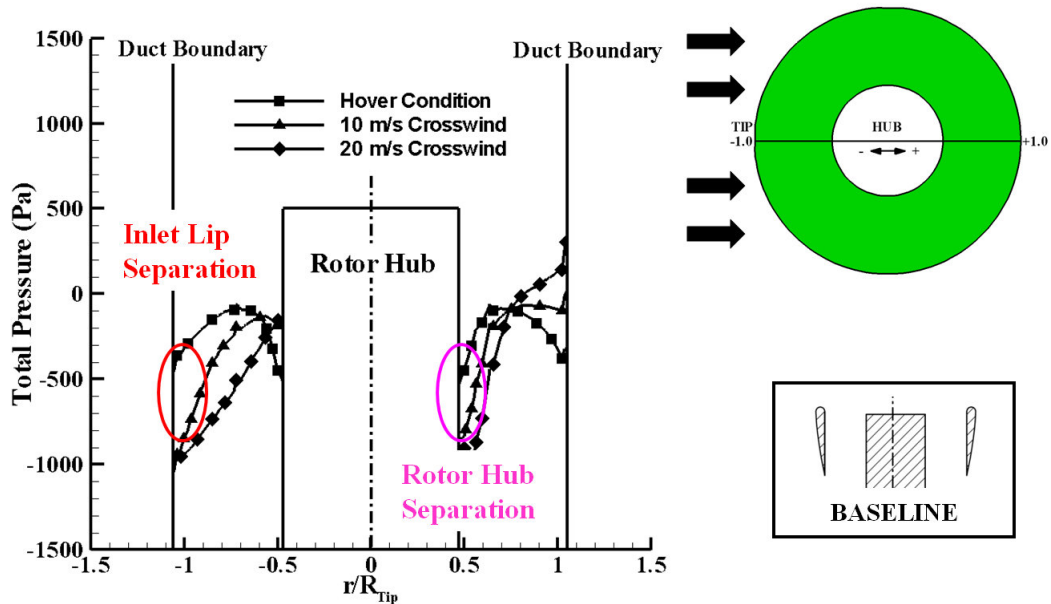


Figure 3.8. Rotor inlet total pressure deficit at elevated forward flight speed for the baseline ducted fan $P_{t,inlet}@10m/s = 61.25 \text{ pa}$, $P_{t,inlet}@20m/s = 245 \text{ pa}$

Figure 3.8 shows the total pressure obtained 1mm upstream of the baseline

ducted fan rotor for hover, and two forward flight velocities. The spanwise total pressure distribution between the duct leading edge and trailing edge for hover condition shows a relatively flat total pressure distribution at the inlet surface. The inlet field is symmetrical between the leading side and trailing side along a radial line passing from the axis of rotation.

When the baseline ducted fan increases its forward flight speed to 10 m/s, a very visible inlet total pressure defect due to leading side lip separation is apparent as shown by the green symbols in Figure 10. At 20 m/s forward flight speed, the total pressure defect near the leading side of the duct is significantly increased (blue symbols). The low momentum fluid entering the leading side of the rotor occupies a much wider portion of the blade span.

The trailing side of the rotor shows a very different inlet total pressure distribution along the flight direction as shown in Figure 3.8. The inlet flow passing over the inlet plane tends to stagnate on the trailing side of the baseline duct aft surface (shroud) due to the specific orientation of inlet streamlines in this region, especially at elevated forward flight velocities. The triangular and diamond symbols representing 10 m/s and 20 m/s forward flight velocities show the elevated levels of total pressure near the trailing side of the duct inner surface. This type of total pressure augmentation only occurring during forward flight is directly related to an unwanted drag force acting in opposite direction to forward flight direction.

Figure 3.8 also reveals another local flow separation zone in the trailing side of the baseline duct inlet surface. The inlet flow progressing to enter into the trailing portion of the duct also separates from the the rotor hub surface, generating a low momentum zone as shown in Figure 3.8.

Figure 3.8 clearly shows the imbalance between the leading side and trailing side of the duct inlet flow field in terms of local total pressure. The duct has tremendous air breathing difficulty near the leading side of the duct. Due to blocked nature of the leading side flow, the trailing side sees an inlet flow with an unnecessarily elevated level of total pressure near the shroud surface. However

there is a significant total pressure deficit near the hub surface for forward flight conditions due to rotor hub corner separation.

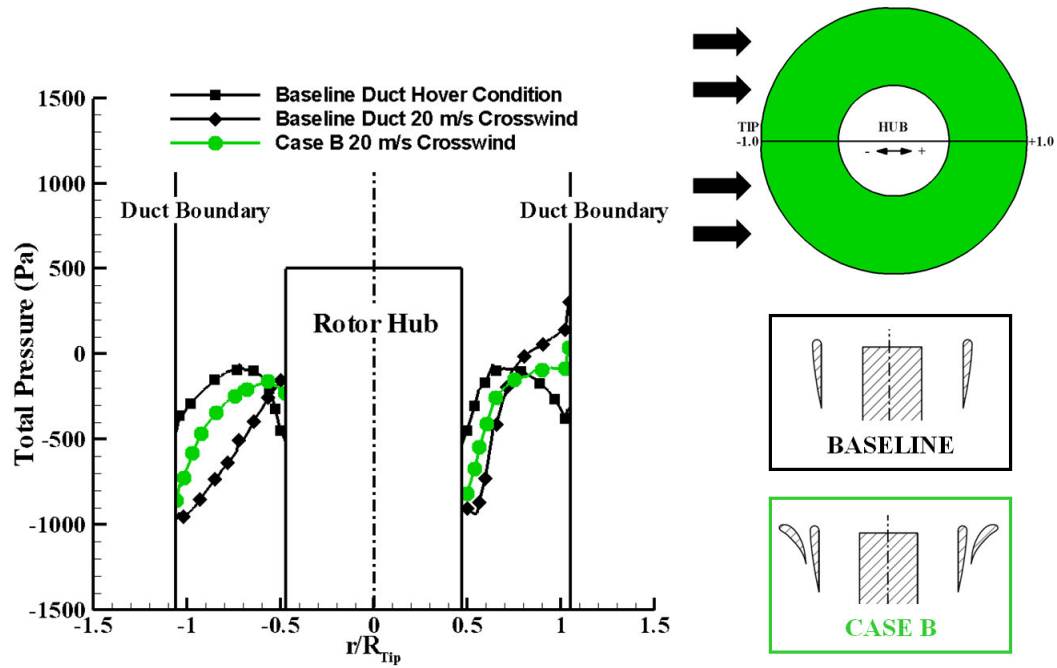


Figure 3.9. Reduction in rotor inlet flow distortion between the leading side and trailing side of (DDF) CASE-B short double ducted fan
 $P_{t,inlet@20m/s} = 245 \text{ pa}$

The short double ducted fan (DDF) CASE-B has an ability to control the inlet lip separation leading to improved thrust and well controlled nose-up pitching moment. Figure 3.9 shows the lip separation improvements of CASE-B in comparison to the baseline duct. The black square symbols define the rotor inlet total pressure distribution in spanwise direction for the baseline fan under hover conditions. The inlet flow under hover conditions does not have any significant inlet flow distortion for the baseline ducted fan.

Inlet flow character of the baseline ducted fan in horizontal flight is represented by the black diamond symbols for the forward flight speed of 20 m/s. The green circular symbol shows the inlet total pressure distribution generated by the short

double ducted fan (DDF) CASE-B. The inlet lip separation related total pressure deficit of the baseline configuration is effectively reduced by the use of the short double-ducted fan (DDF) CASE-B (green circular symbols in Figure 3.9). The local mass flow rate passing from the leading side of the duct is much improved because of the short double-ducted fan (DDF) CASE-B. The unnecessarily elevated total pressure observed near the aft shroud of the baseline ducted fan (trailing side) as shown by black diamond symbols is also controlled when CASE-B is implemented (green circular symbols). This reduction of total pressure on the trailing side of (DDF) CASE-B is beneficial in balancing the leading side and trailing side flow of the fan rotor exit flow field. CASE-B also reduces drag generation occurring near the aft part of the shroud.

3.9 A Comparative Evaluation of Local Velocity Magnitude, Streamlines and Total Pressure for All Three Ducts

As part of the (DDF) concept validation, local flow field details including magnitude of velocity, streamlines and total pressure distributions are presented over a surface passing through the duct leading edge, axis of rotation and the trailing edge of the duct system. Comparisons of the specific (DDF) design against the corresponding baseline duct at 9000 rpm are discussed using the computational predictions explained in the previous paragraphs. The baseline duct; Case-A, the tall DDF; and CASE-B, the short DDF results are compared in detail.

3.9.1 CASE-A Tall (DDF) versus Baseline Duct Results /at 10 m/s and 20 m/s

Figure 3.10 compares the flow fields of tall double ducted fan designated as CASE-A and the baseline duct. A slight forward lip separation is observed at 10 m/s forward flight velocity. The tall double ducted fan CASE-A produces an

enhanced thrust level of 1.73 times that of the baseline ducted fan at 10 m/s. The mass flow rate of CASE-A at 9000 rpm is also enhanced when compared to the baseline ducted fan, as shown in Figure 3.10. The total pressure distributions clearly show the low momentum regions due to inlet lip separation and hub corner separation on the rotor disk inlet surface as shown by dark blue areas in Figure 3.10. The tall ducted fan provides a reduction in the size of the low momentum flow areas downstream of the inlet lip and hub corner when compared to the baseline duct.

Although the “*hub corner separation*” area is relatively smaller than the “*inlet lip separation*” area, the flow blockage created by the hub corner separation affects the flow downstream of the rotor as shown in Figure 3.10. The total pressure imbalance observed at downstream of the rotor for the baseline duct is significant. The existence of the tall double ducted fan CASE-A slightly improves the total pressure on the leading side of the rotor exit flow for 10 m/s forward flight velocity.

Figure 3.11 explains the effect of inlet flow distortion existing in the baseline duct and tall double ducted fan design at 10 m/s forward flight velocity by using rotor exit total pressure predictions. The light green zone near the leading side of the baseline ducted fan shows the highest level of aerodynamic loss resulting from “*inlet lip separation*” at 10 m/s. This area is where the relative flow tends to separate because of the existence of the duct lip near the leading side. The fan inlet surface also has another aerodynamic loss region (green) at just downstream of the “*hub corner*” on the trailing side of the duct. The beneficial influence of the tall double ducted fan design CASE-A is shown in Figure 3.11. The aerodynamic loss areas in the baseline duct distribution are effectively reduced in the tall double ducted fan design. The red total pressure zone near the trailing side of the baseline duct shows the highest levels of total pressure over the rotor exit plane. The trailing side tends to pass most of the inlet mass flow rate including the fluid that is skipping over (deflected by) the lip separation region. This is a common observation in most standard ducted fans in horizontal flight.

The aft part of the fan usually generates additional drag force because of this

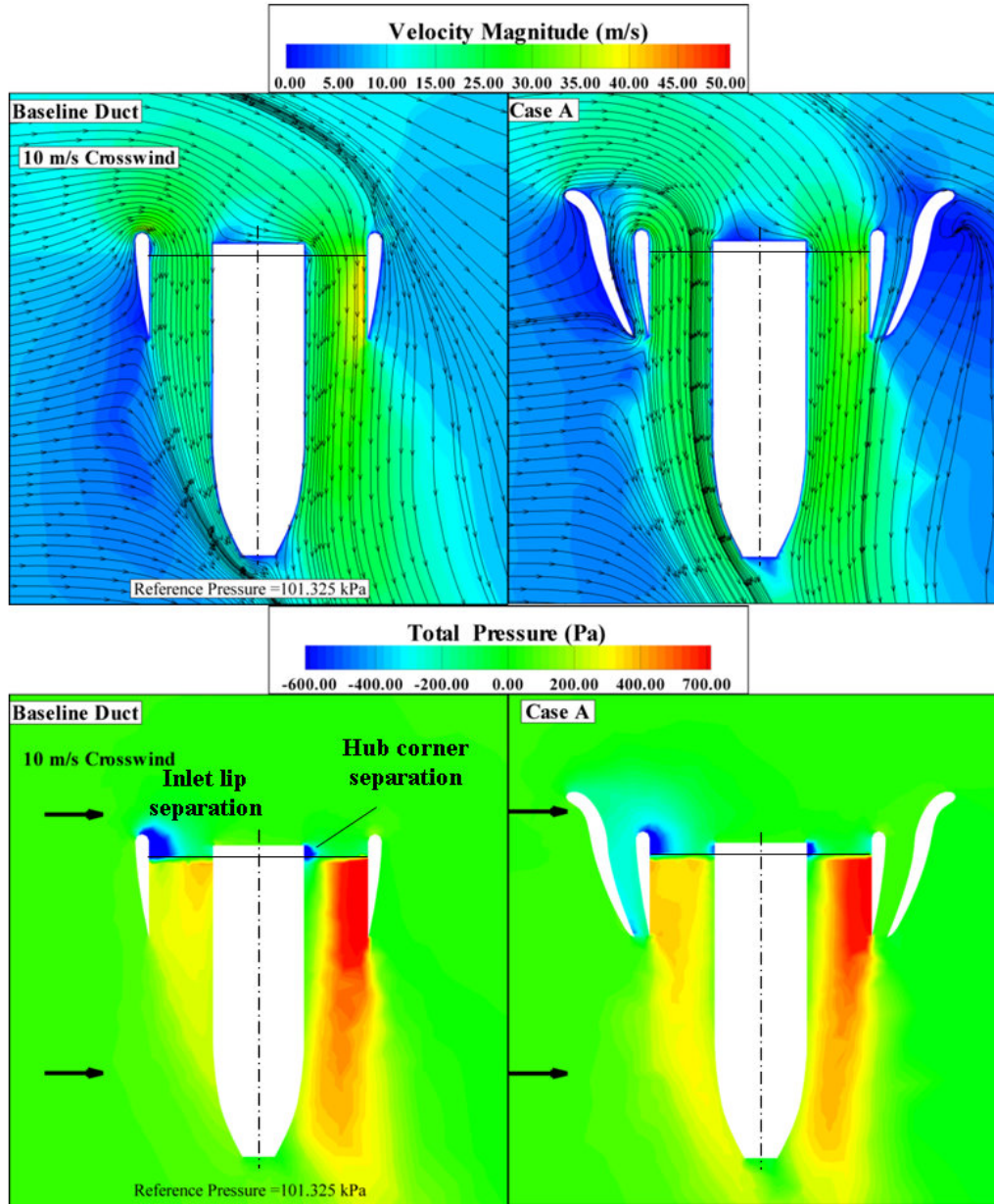


Figure 3.10. Velocity magnitude and total pressure distribution,baseline duct versus CASE-A tall double ducted fan (DDF) at 10 m/s forward flight velocity

red high total pressure zone at the exit plane. The implementation of the tall double ducted fan makes the total pressure distortion between the leading side and trailing side much more balanced. The inlet flow distortion is efficiently dealt with with the implementation of the second duct configuration termed as CASE-A,

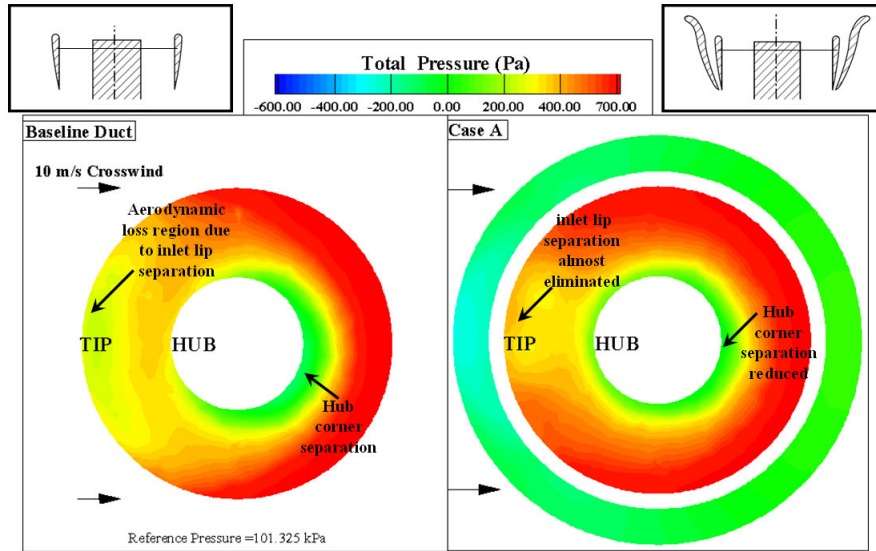


Figure 3.11. Total pressure distribution at rotor exit plane (horizontal) baseline duct versus CASE-A tall double ducted fan (DDF) at 10 m/s forward flight velocity

Figure 3.11.

When forward flight velocity is increased to 20 m/s, Figure 3.12 shows the highly adverse character of the separated flow zone behind the inlet lip section in the baseline duct. The flow also tends to separate behind the hub corner on the trailing side of the duct. Figure 3.12 demonstrates that the flow is nearly blocked by the existence of a large separated flow zone and the flow is effectively induced into the trailing side of the duct. The imbalance in the local mass flow rate between the leading side of the duct and the trailing side of the duct at 20 m/s is much more apparent when compared to 10 m/s results. Figure 3.12 displays the significant flow improvement in the lip separation area for the tall double ducted fan (DDF) CASE-A. The re-circulatory flow is almost eliminated downstream of the lip. The leading side of the duct starts breathing effectively because of CASE-A's ability to eliminate inlet flow distortion near the leading side. The (DDF) CASE-A results show a low momentum region that could be viewed as a three dimensional wake region behind the vehicle at 20 m/s forward flight velocity. The outer duct flow near the leading side is in a direction opposite to rotor flow direction. The outer

duct flow near the leading side is an essential component of the (DDF) concept because of its highly important role in reversing the inner lip region separated flow conditions. The outer duct flow smoothly reverses into the rotor flow direction away from the leading side.

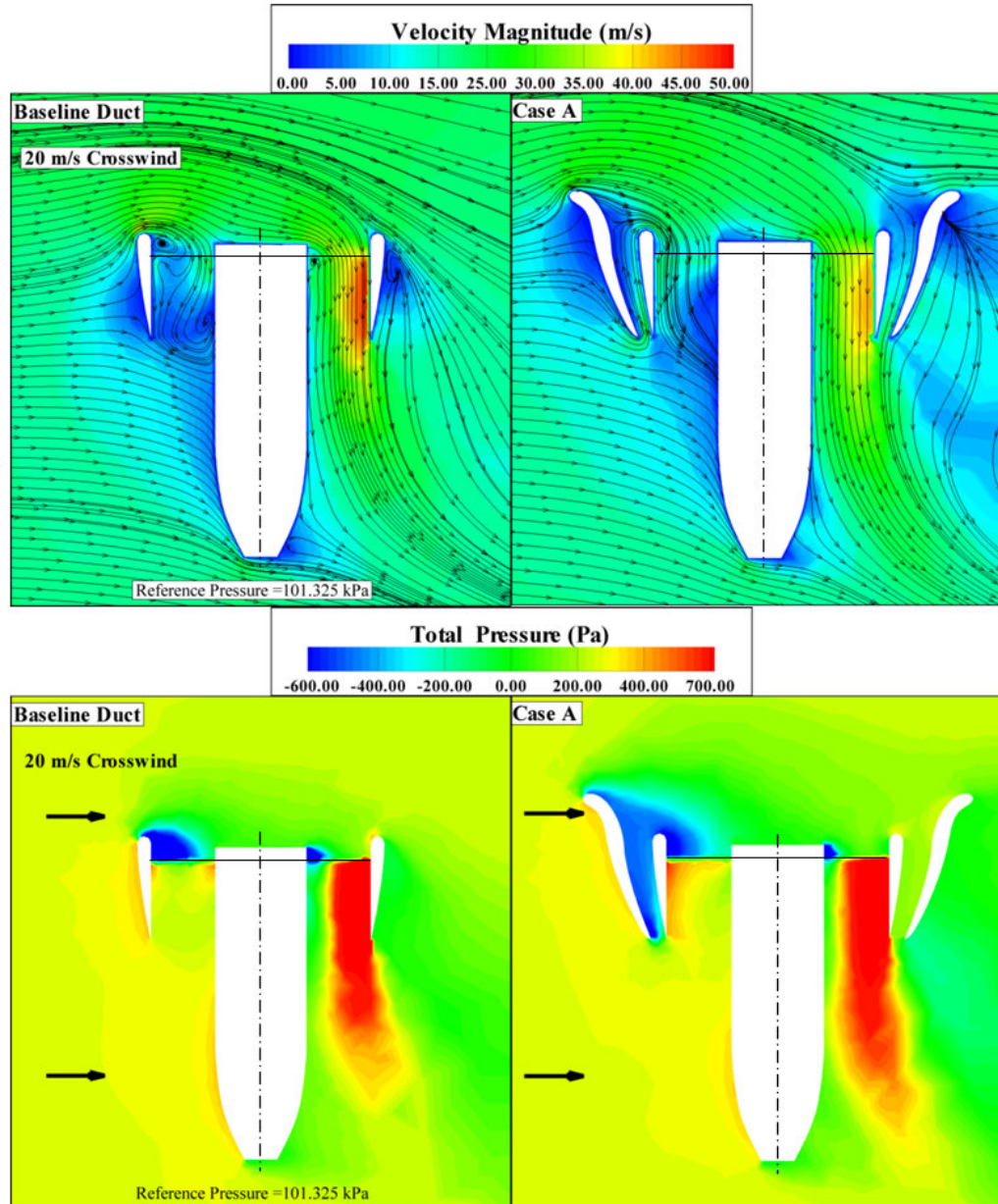


Figure 3.12. Velocity magnitude and total pressure distribution, baseline duct versus CASE-A tall double ducted fan (DDF) at 20 m/s forward flight velocity

The rotor exit plane total pressure distribution shown in Figure 3.13, (DDF) CASE-A reveals a significant lip separation improvement leading to a much uniform inlet flow distribution between the leading side and trailing side of the inner duct. The DDF duct local flow distribution at the rotor exit is much improved in comparison to the baseline duct. Hub corner separation area is also reduced in (DDF) CASE-A. Most circumferential positions of the second duct (other than the leading side of the duct) contributes to the generation of thrust because of the measurable outer duct flow observed in this area.

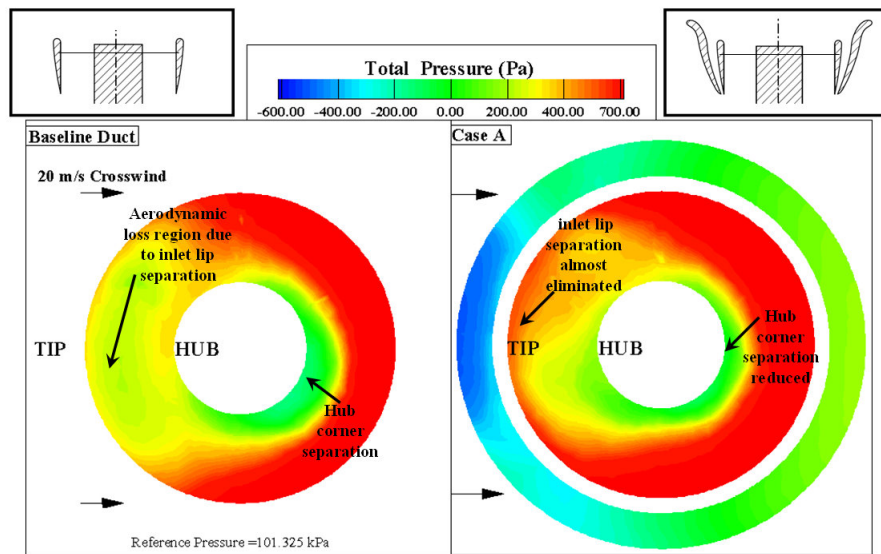


Figure 3.13. Total pressure distribution at rotor exit plane (horizontal) baseline duct versus CASE-A tall double ducted fan (DDF) at 20 m/s forward flight velocity

3.9.2 CASE-B Short (DDF) versus Baseline Duct Results at 10 m/s and 20 m/s

Figures 3.14 and 3.15 show the most effective double ducted fan (DDF) treatment results obtained for a forward flight velocity of 10 m/s. A detailed geometrical definition of the short double ducted fan (DDF) CASE-B was discussed in Figure 3.4b.

The short DDF has the ability to improve thrust in relative to the baseline case

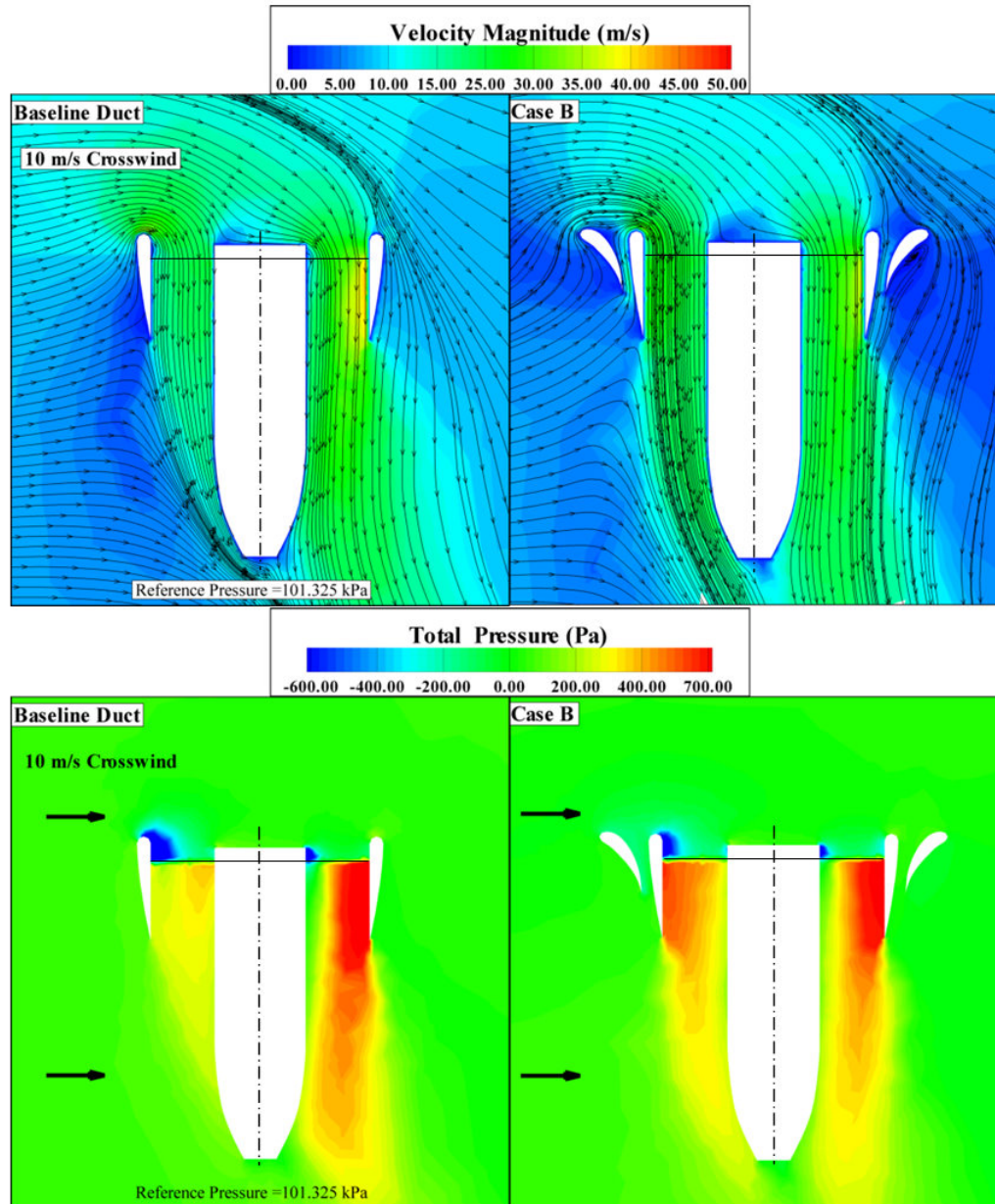


Figure 3.14. Velocity Magnitude and total pressure distribution, baseline duct versus CASE-B short double ducted fan (DDF) at 10 m/s forward flight velocity

“without producing a significant nose-up pitching moment” by effectively reducing inlet lip separation and hub corner separation areas. The short double ducted fan configuration is a self adjusting lip separation control system preserving its separation control features in a wide range of forward flight velocities. The effectiveness of the short DDF treatment is shown in the total pressure distribution presented

in Figure 3.14 for 10 m/s flight velocity. In addition to the area reduction of the separated flow areas (dark blue), the total pressure imbalance between the leading side and trailing side is almost eliminated. The leading side of the inner duct of the short DDF CASE-B breathes at a much improved rate as compared to the baseline case. The red high total pressure areas provide a well-balanced fan exit jet near the leading side and trailing side of the fan.

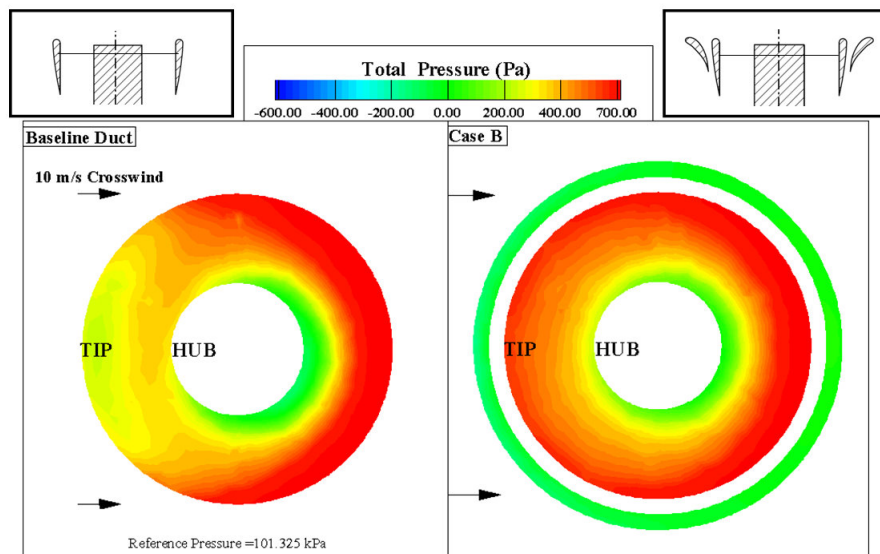


Figure 3.15. Total pressure distribution at rotor exit plane (horizontal) baseline duct versus CASE-B short double ducted fan (DDF) at 10 m/s forward flight velocity

Figure 3.15 indicates a high level of rotor exit total pressure uniformity for CASE-B in contrast to the strong flow distortion generated by the baseline duct. When short double ducted fan is used, the lip separation and hub corner separation control is highly effective at 10 m/s flight velocity. The level of total pressure values between the leading side and trailing side are much better balanced in CASE-B as shown in Figure 3.15.

When the short double ducted fan arrangement (DDF) CASE-B is evaluated at 20 m/s flight velocity, the loss elimination features near the leading side lip, hub corner area are much apparent. Highly separated lip region flow adversely blocking the leading side of the inner duct is successfully dealt with the flow control features

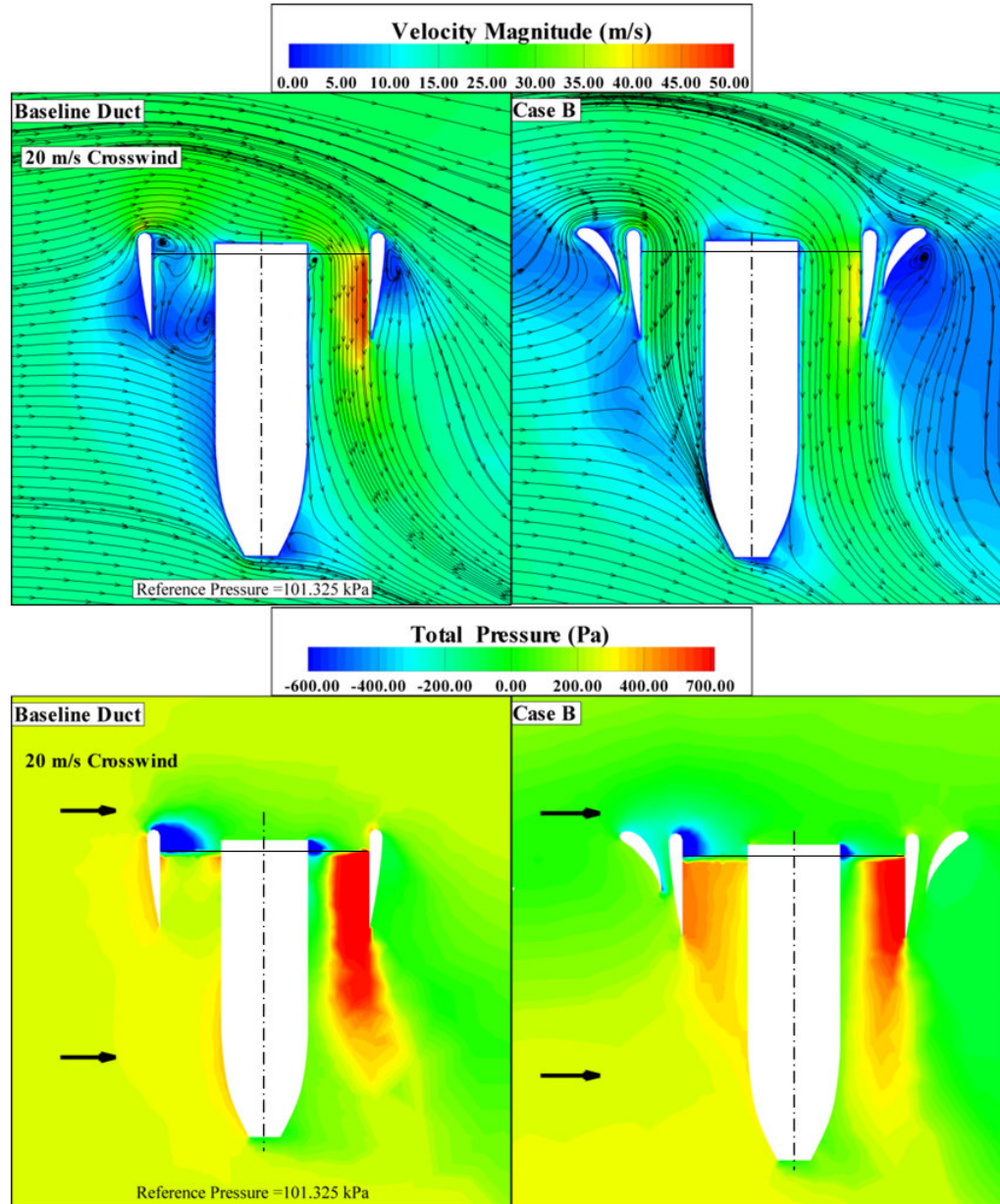


Figure 3.16. Velocity magnitude and total pressure distribution, baseline duct versus CASE-B short double ducted fan (DDF) at 20 m/s forward flight velocity

of the short (DDF) as shown in Figure 3.16. A well-balanced short (DDF) exit flow provides a higher level of thrust when compared to the baseline duct. The flow improvements and thrust enhancement from the short (DDF) comes with no additional nose-up pitching moment generation when compared to baseline as explained in Table 3.1 and Figure 3.16. A highly effective inlet flow distortion

control ability of the short ducted fan can be apparently seen in Figure 3.17. A vehicle using the short (DDF) concept CASE-B generates a higher level of thrust with a well balanced ducted fan exit flow without excessive generation of nose-up pitching moment. This approach results in improvements of the performance of the control surfaces and improved range because the energy efficiency of the ducted fan is improved. The elimination of severe inlet flow distortion is likely to improve the rotor exit flow quality before further interaction with typical control surfaces.

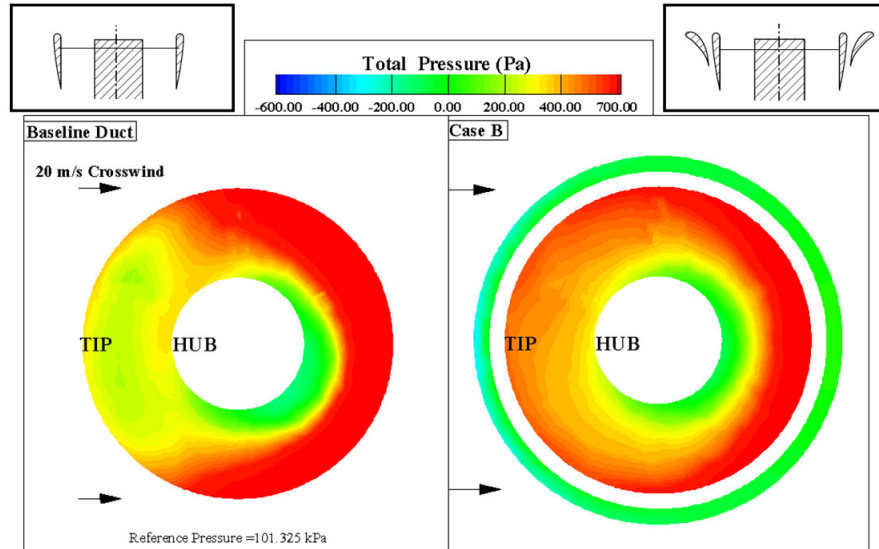


Figure 3.17. Total pressure distribution at rotor exit plane (horizontal) baseline duct versus CASE-B short double ducted fan (DDF) at 20 m/s forward flight velocity

3.10 Upstream Lip Region Local Flow Improvements in (DDF)

Figure 3.18 defines the local sampling locations for static pressure and skin friction coefficient computations on the airfoil of the inner duct at the leading edge location. The lowercase characters represent the “*rotor side*” locations and the uppercase characters show the “*outer side*” sampling locations for static pressure and skin friction coefficient on the inner duct airfoil section. The “*outer side*”

denotes the channel between the baseline duct and secondary duct.

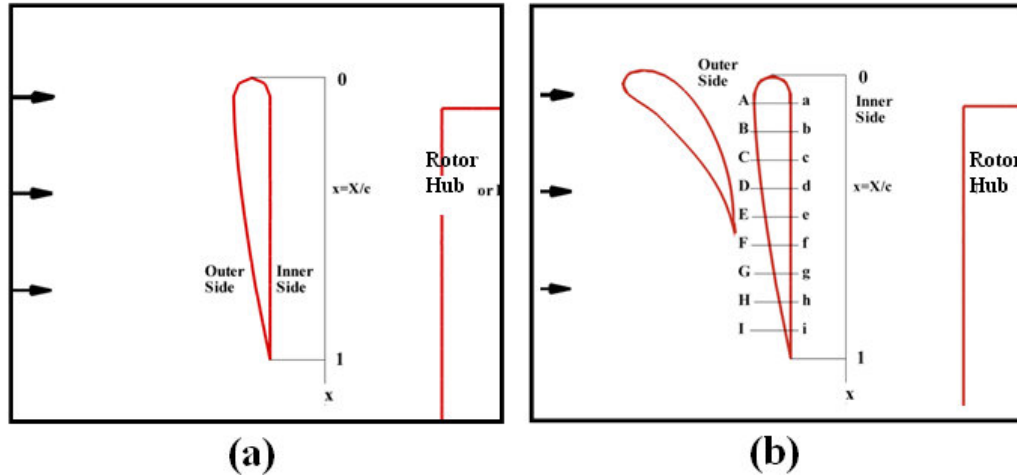


Figure 3.18. Sampling locations for static pressure and skin friction coefficient computations near the leading side of the inner duct for (DDF) CASE-B

3.10.1 Static Pressure Distribution around the Lip Section of the Baseline Duct

Figure 3.19 shows the static pressure distribution for the baseline duct and double ducted fan (DDF) CASE-B for the forward flight velocity of 20 m/s. The distributions presented in Figure 3.19 are plotted around the airfoil of the baseline duct. The pressure gradient occurring around the leading edge radius of the inner duct is the most significant parameter controlling severeness of the leading edge lip separation problem. Point $x=X/c=0$ shows the leading edge and $x=X/c=1$ shows the trailing edge location of the baseline duct airfoil. The external flow stagnates on the the baseline duct airfoil at point D as shown in Figure 3.19 . The approaching flow to the duct is divided into a stream reaching up to the leading edge and a second stream approaching down to the trailing edge of the duct airfoil at point D. The static (or stagnation) pressure from point D to J remains almost constant. The external flow slightly accelerates to the leading edge point from point C to A for the baseline duct. There is a strong acceleration zone between point A and the leading edge point O, as clearly shown by the favorable pressure

gradient between the point A and O. This is the area within the leading edge diameter of the inner lip section. The geometrical leading edge point O is the minimum pressure point for the baseline duct airfoil. The flow on the inner side of the lip sees a very strong adverse pressure gradient around the leading edge circle. The strong flow separation character shown in Figure 3.19 is mainly due to the strong adverse pressure gradient affecting the boundary layer growth between points O, a and finally b. The rotor process described in equations from 2.1 to 2.6 results in the sudden pressure rise on the inner part of the baseline duct between b and c.

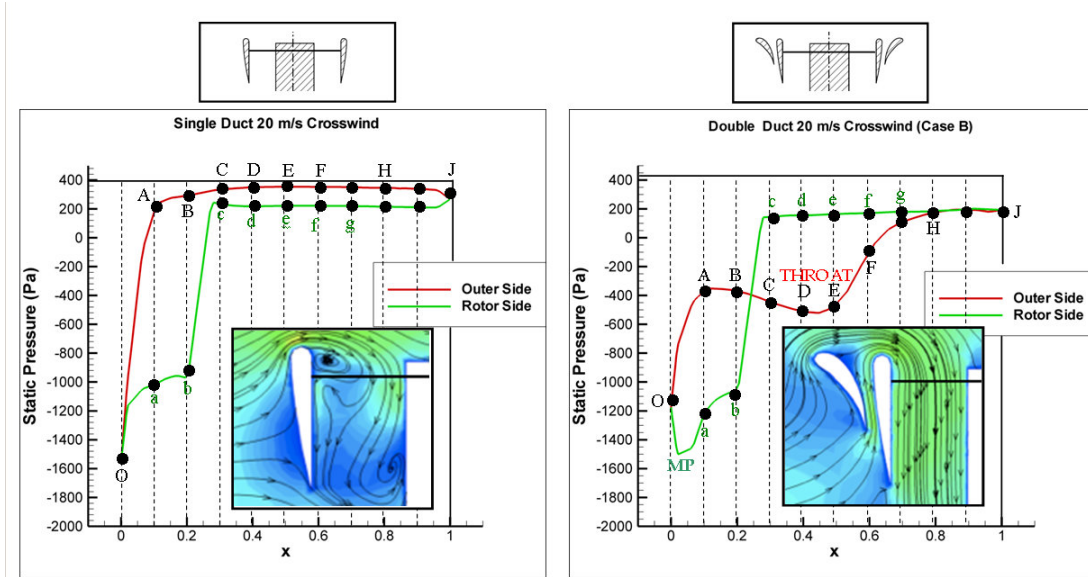


Figure 3.19. Comparison of the static pressure distribution on the baseline lip section and inner duct lip section of the (DDF) CASE-B airfoil

3.10.2 Static Pressure Distribution around the Lip section of the Double Ducted Fan (DDF)

Figure 3.19 also shows the static pressure distribution around the lip section of the short double ducted fan (DDF) CASE-B. The vertically upward channel flow in the outer duct section is established by the dynamic pressure of the external flow in forward flight. The vertically upward flow exists in a narrow leading edge

region as clearly shown in Figure 3.16 and the results showing the axial velocity vectors from the computations. The outer duct flow that is proceeding vertically up generates a unique wall static pressure distribution in a converging-diverging channel. The external flow in horizontal flight stagnates on the shorter outer airfoil and turns upward towards the leading edge of the outer duct airfoil. Most of the flow stagnating at the lower part of the vehicle is directed towards the converging diverging channel of the outer duct. There is a wide stagnation region between points J and H on the outer side of the inner duct. The flow accelerates towards the throat section of the outer duct near D. The flow after the throat section smoothly decelerates up to the point A that is very close to the leading edge circle of the leading edge. The existence of the diverging channel is responsible from a much softer acceleration around the leading edge diameter of the lip section between A and O. The flow is still accelerating when it is passing through the geometrical leading edge point O. The minimum pressure point (MP) in (DDF) configuration is on the inner side of the lip section at $x=X/c=0.03$ in contrary to the baseline duct location O. The flow starts decelerating after this minimum pressure point MP. The adverse pressure gradient region after the minimum pressure point MP in (DDF) is much shorter and the adverse pressure gradient between MP and a is much milder than that of the baseline duct. Figure 3.19 clearly shows the favorable modified nature of the static pressure distribution around the lip section of (DDF) leading to the elimination of the severe inlet lip separation region that is unique to the baseline duct in forward flight. The (DDF) approach is extremely useful in controlling the inner lip flow separation originating the adverse pressure gradient region.

3.10.3 Skin Friction Distribution around the Leading Edge of the Duct

Figure 3.20 presents the skin friction coefficient distributions on the baseline duct lip section and inner duct lip section of the (DDF) configuration. The skin friction coefficient c_f is defined as the local wall shear stress normalized by inlet dynamic head defined as the lowest level of the predicted wall shear stress is on

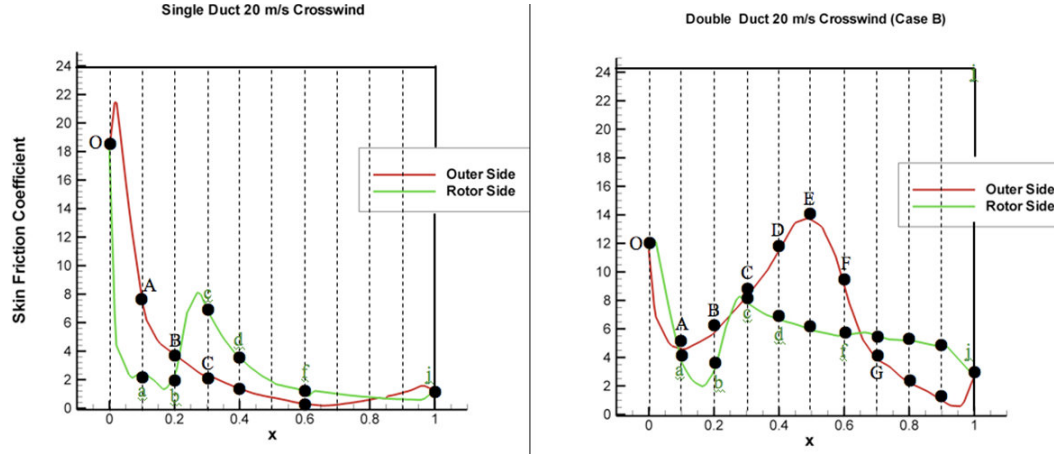


Figure 3.20. Comparison of the skin friction coefficient distribution on the baseline lip section and inner duct lip section of the (DDF) airfoil

the lip surface along the separated flow region for the baseline duct. This low momentum region is between points O and a corresponding to the highest level of adverse pressure gradients before the rotor inlet plane. The overall level of wall shear stress is higher between points a and b for the double duct configuration showing the immediate influence of weakened adverse pressure gradients resulting from the (DDF) geometry. The DDF geometry significantly reduces the aerodynamic shear stress occurring near the inner lip of the DDF system especially near the leading edge.

3.11 Summary

This chapter describes a novel ducted fan inlet flow conditioning concept that will significantly improve the performance and controllability of VTOL “*vertical take-off and landing*” vehicles, UAVs “*uninhabited aerial vehicles*” and many other ducted fan based systems. The new (DDF) concept developed in this study deals with most of the significant technical problems in ducted fans operating at almost 90° angle of attach, in the forward flight mode. The technical problems related to this mode of operation are as follows:

- Increased aerodynamic losses and temporal instability of the fan rotor flow when “*inlet flow distortion*” from “*the lip separation area*” finds its way into the tip clearance gap leading to the loss of energy addition capability of the rotor.
- Reduced thrust generation from the upstream side of the duct due to the rotor breathing low-momentum re-circulatory turbulent flow.
- A severe imbalance of the duct inner static pressure field resulting from low momentum fluid entering into the rotor on the leading side and high momentum fluid unnecessarily energized on the trailing side of the rotor.
- A measurable increase in power demand and fuel consumption when the lip separation occurs to keep up with a given operational task.
- Lip separation and its interaction with the tip gap flow requires a much more complex vehicle control system because of the severe non-uniformity of the exit jet in circumferential direction and excessive pitch-up moment generation.
- At low horizontal speeds a severe limitation in the rate of descent and vehicle controllability may occur because of more pronounced lip separation. Low power requirement of a typical descent results in a lower disk loading and more pronounced lip separation.
- Excessive noise and vibration from the rotor working with a significant inlet flow distortion.
- Very complex unsteady interactions of duct exit flow with control surfaces.

The new concept that will significantly reduce the inlet lip separation related performance penalties in the forward flight zone is named “*DOUBLE DUCTED FAN (DDF)*” . The current concept development uses a time efficient 3D computational viscous flow solution approach developed specifically for ducted fan flows. The present chapter summarizes only the most optimal approach after evaluating nine different double ducted fan geometries for a wide range of forward flight velocities.

The current concept uses a secondary stationary duct system to control “*inlet lip separation*” related momentum deficit at the inlet of the fan rotor occurring at elevated forward flight velocities. The DDF is self-adjusting in a wide forward flight velocity regime.

DDFs corrective aerodynamic influence becomes more pronounced with increasing flight velocity due to its inherent design properties.

The DDF can also be implemented as a “*Variable Double Ducted Fan*” (VDDF) for a much more effective inlet lip separation control in a wide range of horizontal flight velocities in UAVs, air vehicles, trains, buses, marine vehicles and any axial flow fan system where there is significant lip separation distorting the inlet flow.

Most axial flow fans are designed for an inlet flow with zero or minimal inlet flow distortion. The DDF concept is proven to be an effective way of dealing with inlet flow distortions occurring near the tip section of any axial flow fan rotor system operating at high angle of attack.

Influence of Tip Clearance and Inlet Flow Distortion on Ducted Fan Performance in VTOL UAVs

This chapter describes an experimental study using total pressure measurements at the exit of the fan rotor to investigate effect of tip leakage flow in hover and forward flight conditions. Special attention is paid to obtain forward flight related experimental data near the tip region of the rotor where complex tip leakage flow and low momentum re-circulatory flow from the inlet lip separation area interact. The effect of duct flow on fan rotor exit performance was investigated in forward flight by the high resolution total pressure measurements. Measurements were obtained at various circumferential positions so that the inlet flow distortion effect on rotor performance was investigated, at a better spatial resolution.

A computational study that analyzed the flow fields around ducted fan rotors is also described in this chapter. Experimentally obtained high resolution total pressure results are used for validation of the computational algorithm.

The motivation of the study presented in this chapter is the need to investigate

aerodynamic performance of ducted fan rotors in hover and forward flight considering the effect of tip leakage flow. The aerodynamic performance drop of fan rotor due to distorted inlet flow and tip leakage flow is investigated. The following sections provide the detailed explanations of the experimental and computational integrated approach and important conclusions of this specific study.

4.1 Experimental Set-up

4.1.1 Penn State Mid-sized Wind Tunnel

The tests for this study were performed in Penn State mid-sized wind tunnel which is a closed circuit, single return, low speed facility. Figure 4.1 shows a schematic of the wind tunnel layout. A contraction section with an area ratio of 9.9:1, accelerates the flow to obtain a higher flow velocity in the test section. The maximum tunnel flow speed is 145 ft per second. The test section has a typical turbulence intensity of 0.6 %. The test section has a rectangular cross section with two feet wide, three feet tall and 20 feet in length dimensions. Figure 4.2 shows a typical VTOL UAV ducted fan installed in the wind tunnel test section.

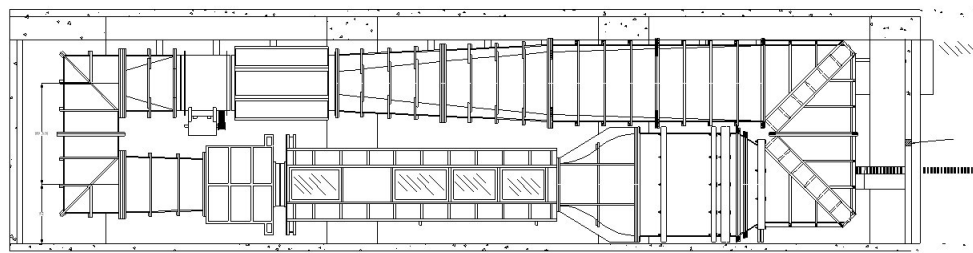


Figure 4.1. The Penn State mid-sized wind tunnel

4.1.2 Ducted Fan Model

The current study deals with ducted fan experiments in a wind tunnel environment simulating the hover and forward flight of a VTOL UAV system as shown in Figures 4.3 and 4.4. The brushless DC electric motor driving the five bladed

ducted fan rotor is speed controlled by an Castle Creation HV-110 electronic speed control (ESC) system. The high efficiency Neu 1521/1.5Y electric motor driving the fan can deliver 2.14 HP power (1.5 KW). The ducted fan provides a disk loading range from 5 to 35 lbf/ft² in a corresponding rotor speed range from 5000 rpm to 20,000 rpm.

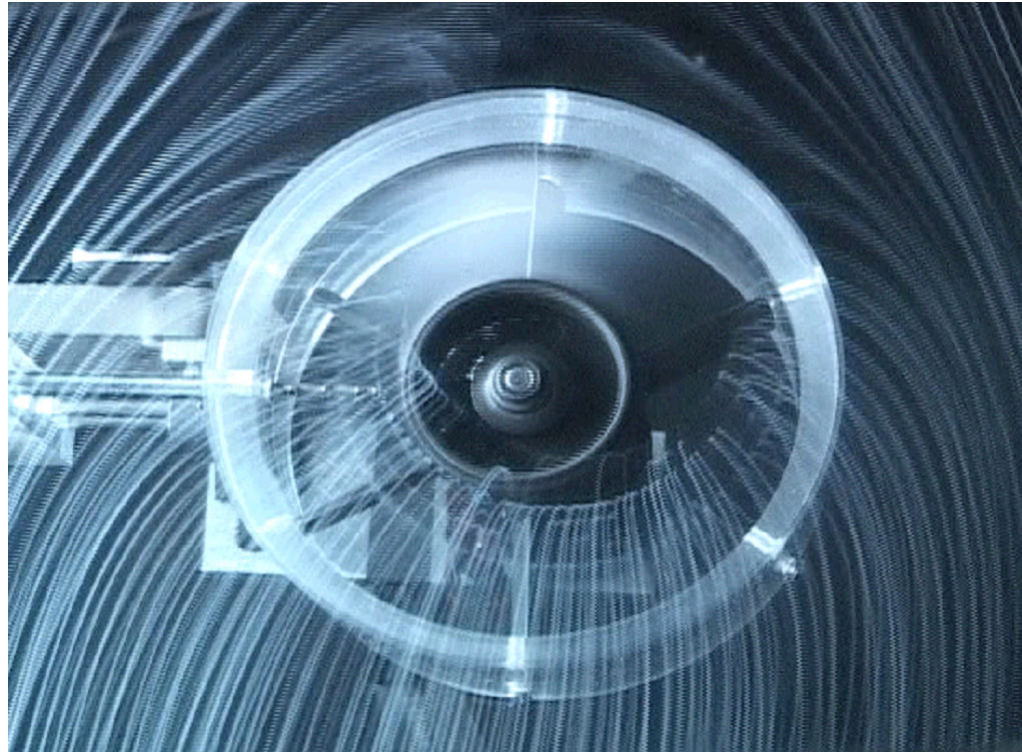


Figure 4.2. Wind tunnel model simulating VTOL UAV at forward flight

Figure 4.3 shows the five bladed ducted fan rotor that is used in the present experimental study. The main geometric parameters of the rotor system are presented in Table 4.1. This ducted fan unit manufactured from carbon composite material is designed for small scale uninhabited air vehicles. Six outlet guide vanes (OGV) remove some of the swirl at the exit of the rotor. The OGVs also cancel some of the torque acting on the vehicle. A tail cone is used to cover the motor surface and hide the electrical wiring for the wind tunnel model. An optical once-per-revolution device located near the hub of the rotor exit is used for the measurement of rotational speed of the fan rotor.

Tip clearance was calculated based on blade height which is the length of the blade from hub to tip. Calculation of tip clearance is shown in figure 4.3. Tip clearance value of the ducted fan system was adjusted by using different shroud inner diameter each manufactured for a specific tip gap size. The shrouds of the ducted fan used in experiments were made up of transparent plexiglass material. Table 4.1 shows tip clearances used for the experiments and corresponding inner diameters of shrouds. The rotor tip diameter in all experiments presented in chapter 4 was constant at 4.69”.

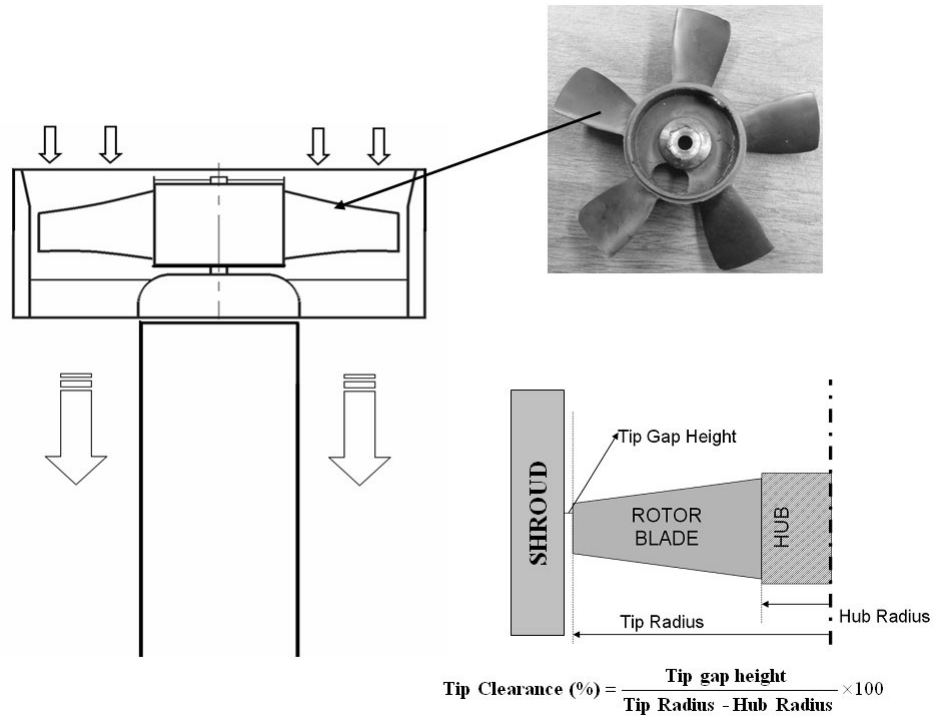


Figure 4.3. Ducted fan, five-bladed fan rotor and tip clearance definition

The ducted fan system was supported by a steel support shaft connected to the center of the tailcone as shown in Figure 4.4. The steel support shaft was held in place by two low friction linear bearings to minimize friction while effectively isolating only the thrust associated with ducted fan system.

	English	Metric
Rotor hub diameter	2.02 inches	52 mm
Rotor tip diameter	4.69 inches	120 mm
Rotor blade span	1.34 inches	34 mm
Max. blade thickness @ tip	0.06 inches	1.5 mm
Shroud inner diameter for %5.8 tip clearance	4.84 inches	122.9 mm
Shroud inner diameter for %3.6 tip clearance	4.78 inches	121.4 mm
Rotor blade section properties		
	Hub	Mid Span
Blade inlet angle β_1	60°	40°
Blade exit angle β_2	30°	45°
Blade chord	32 mm	30 mm
		28 mm

Table 4.1. Geometric specifications of five inch ducted fan

4.1.3 Instrumentation

The ducted fan test system was equipped with a Kiel total pressure rake, which was mounted on linear traverse system, and a uni-axial load cell, which was located under the steel support shaft. Figure 4.2 shows a sketch of the ducted fan test system. The test system was positioned on top of a precision rotary table for total pressure measurements at different circumferential positions.

4.1.3.1 Thrust Measurements

Thrust of the ducted fan was measured by an Omega LCCA-25 uni-axial load cell that has a range of 25 lbf (11.34 kgf) for hover condition. The load cell was connected to the steel support and mounted on a plate which is attached to the rotary table. This load cell was connected to an Omega model DP25B-S strain gage signal conditioner including a panel meter. The meter provided a 10 V excitation voltage, and conditioned the returning signal. The output of the load cell was previously calibrated by applying known static loads. Tabulated accuracy of the load cell is 0.037 % of the full scale load.

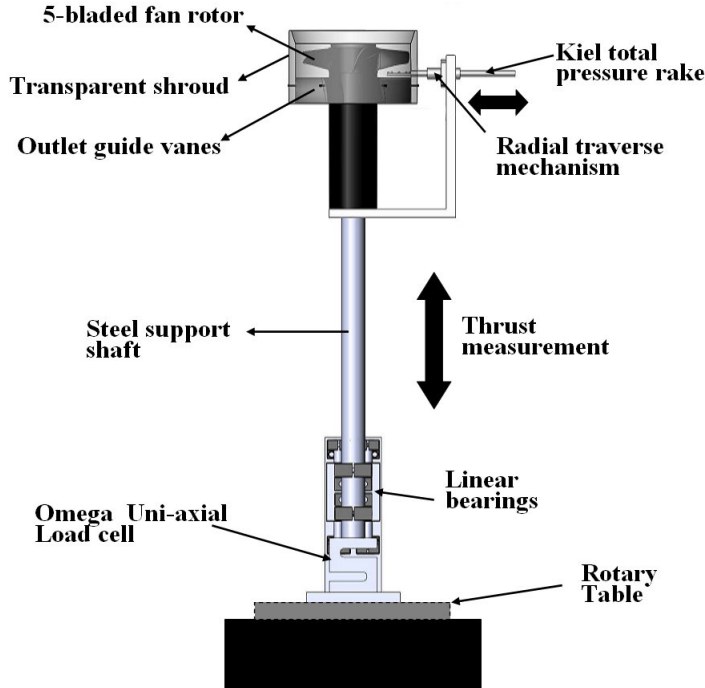


Figure 4.4. 5" diameter ducted fan test system

4.1.3.2 Total Pressure Measurements

Fan rotor exit total pressure measurements were performed by using a “*United Sensors Type A*” Kiel total pressure rake system as shown in Figure 4.5. The Kiel total pressure rake having five 2 mm diameter total heads was traversed in radial direction using a precision linear traverse mechanism. Total pressure rake was typically located 10 mm downstream of the fan rotor exit plane at 50% of blade span (mid-span). The Kiel probe was aligned with absolute rotor exit velocity at mid span position. Figure 4.6 shows the velocity triangle of the rotor blade section and position of the Kiel probe.

United Sensors type A Kiel probe is relatively insensitive to incoming angle of the flow (yaw angle). The range of insensitivity to misalignment for this probe is $\pm 52^\circ$ to see a more than 1 % deviation in inlet dynamic head [85].

Five Kiel total pressure heads in the rake system were connected to a multi-port Scanivalve system with $\frac{1}{8}$ " tubing that was 5ft long. The Scanivalve was used to take all the pressure measurements. The Scanivalve was connected to a Validyne

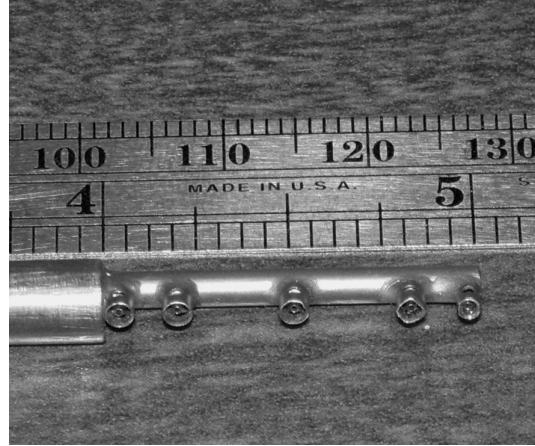


Figure 4.5. United Sensors Kiel total pressure rake

CD-15 pressure transducer that was referenced to atmospheric pressure.

The calibration of the pressure transducer required applying a known pressure to the transducer and recording the associated voltage. The relationship between the pressure and voltage was linear. The Validyne pressure transducer was connected to a Fluke 45 Dual Multimeter. The measured settling time of the system used in this project was 40 seconds, so the Kiel probe pneumatic output reached an equilibrium and mass averaged total pressure reading recorded.

4.2 Experimental Results

In the current study, the aerodynamic performance of the ducted fan used for VTOL UAVs was quantified by measuring radial distribution of fan rotor exit total pressure for both hover and forward flight. The effect of tip leakage flow on fan rotor performance was also investigated. Thrust measurements were performed in hover condition for various rotational speeds. Total pressure results were expressed in non-dimensional form as a total pressure coefficient throughout this chapter.

$$C_{p_{Total}} = \frac{P_t - P_a}{\frac{1}{2} \rho V_{ref}^2} \text{ where } \rho = \frac{P_a}{\mathfrak{R} T_a} \quad (4.1)$$

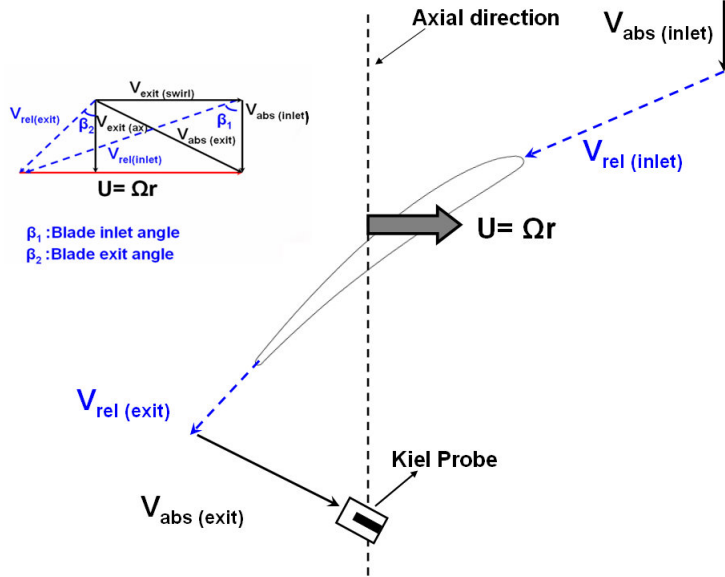


Figure 4.6. Rotor exit velocity triangle and orientation of Kiel probe

The reference velocity used in equation 4.1 was calculated from the fan rotor tip speed.

$$V_{ref} = \Omega \times R_{tip} \quad (4.2)$$

All the radial coordinates are given in non-dimensional form ($\frac{r}{R_{Tip}}$) throughout this chapter.

4.2.1 Hover Condition Results

Thrust measurements were obtained at hover condition for various rotor speeds. Thrust measurements are normalized in the form of disk loading, which is thrust force per unit rotor disk area. The disk loading parameter is a significant indicator of how a rotor disk is fluid mechanically loaded as a result of a complex energy addition process to air in a fan rotor passage. The flow quality in a fan rotor passage is directly controlled by the adverse pressure gradients and highly recirculatory/turbulent flow conditions, in a rotating frame of reference.

Three different configurations are compared in figure 4.7 including a fan “ro-

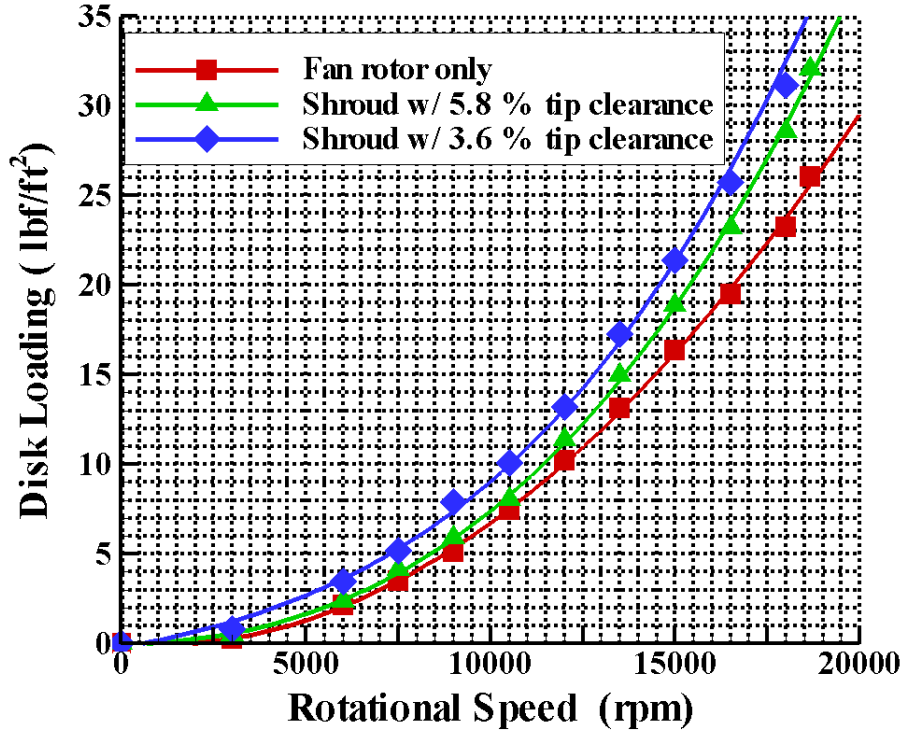


Figure 4.7. Disk loading versus rotational speed at hover condition for the current VTOL UAV wind tunnel model

tor without shroud" and two shrouds having specific tip clearances (5.8 and 3.6 %). Figure 4.7 shows that adding a shroud to the fan system increases the thrust leading to improved rotor disk loading. At higher rotational speeds, adding a shroud improved the rotor disk loading as much as 24%. Two different shrouds with different tip clearance were also compared in figure 4.7. Decreasing the tip gap height increases the thrust and disk loading. Figure 4.8 shows radial distribution of total pressure coefficient for two tip clearances at 12000 rpm in hover condition. Increasing the tip gap height increases leakage flow at the tip and reduces performance of the fan rotor. The existence of a significant tip leakage vortex in the rotating passage generate complex 3D flow patterns, aerodynamic losses and unsteady flow patterns. Decreasing the tip clearance resulted in approximately 20% increase in the measured total pressure at the rotor exit at mid span location.

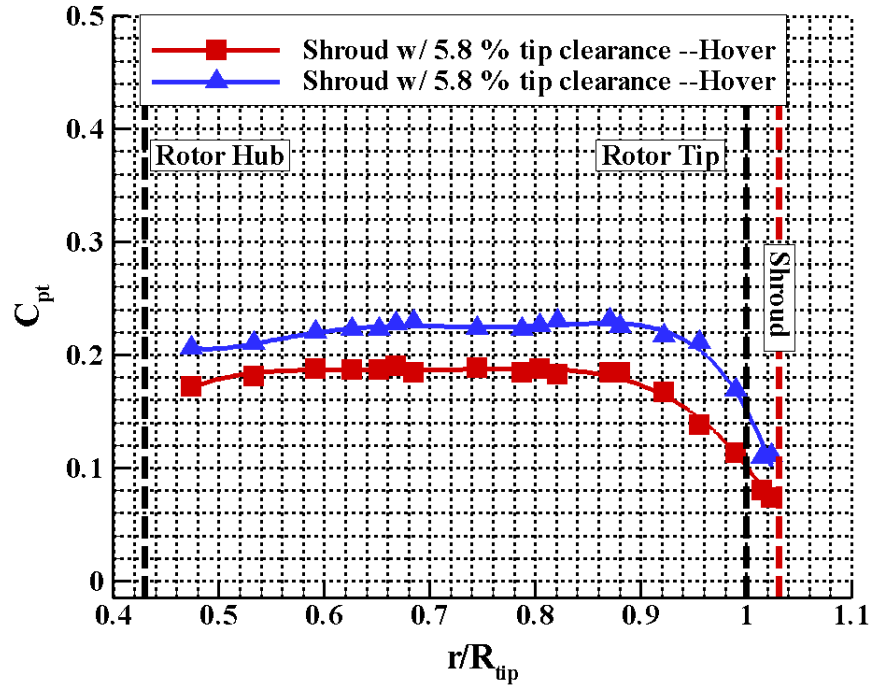


Figure 4.8. Radial distribution of total pressure coefficient at 12000 rpm hover condition

Total pressure increment generated by the fan rotor is reduced near the tip region for both clearances. That reduction in total pressure was due to tip leakage flow originating between the rotor tip and shroud. For 5.8 % tip clearance, total pressure started to drop at $r/R_{tip} \geq 0.88$ visibly as shown in Figure 4.8. However, for the reduced tip clearance of 3.6 %, it started to drop where $r/R_{tip} \geq 0.92$. The smaller tip clearance provides a higher overall total pressure near the tip section of the blade. The ability of the rotor to add energy to the flow near the tip section is generally hindered by the adverse effects of the tip leakage flow.

4.2.2 Forward Flight Results

Forward flight experiments were performed in Penn State low speed wind tunnel. As mentioned in the previous sections, ducted fan system was mounted on a

rotary table for circumferential movements. The test system was positioned inside the wind tunnel test section such that the interaction of ducted fan and boundary layer of the wind tunnel walls were effectively minimized. The test system was positioned so that the ducted fan was three rotor diameters (D_R) away from the top wall, $4.5 D_R$ away from the bottom wall and $2.8 D_R$ away from the side walls. For the measurements of upstream velocity of ducted fan, a hot-wire anemometer is positioned $4.5 D_R$ upstream of the duct. A sketch of experimental setup for wind tunnel measurements in forward flight is shown in figure 4.9.

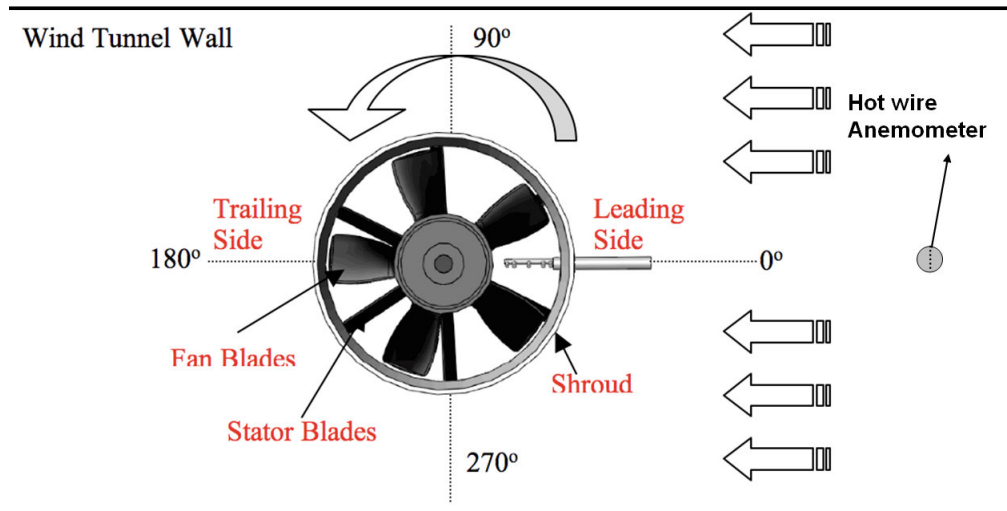


Figure 4.9. Wind tunnel experimental setup for forward flight condition

The “*windward side*” of the ducted fan is also named as the “*leading side*” and “*leeward side*” of it is named as the “*trailing side*” throughout this chapter. For forward flight conditions, four different circumferential stations were considered. The first circumferential position was 0° along tunnel axis as shown in figure 4.9. Total pressure rake was aligned with the leading side of the ducted fan. Other circumferential locations were obtained by turning the test system to 90° , 180° and 270° in counter-clockwise direction. In each circumferential direction, the radial distribution of total pressure was measured for 12000 rpm rotational speed and 10 m/s forward flight velocity.

4.2.3 Forward Flight Flow Visualization

Effects of forward flight on the flow field around the duct can be better understood by the help of a smoke flow visualization technique [86]. This technique utilized a thin 0.12 mm diameter, 30cm long stainless steel wire. The wire was carefully coated with a glycerol layer before each experiment. The wire was electrically heated to the glycerol evaporation temperature by joule heating, producing visible smoke for up to three seconds in the lowest speed cases. A few strips of white LEDs and strips of UV LEDs were used for visualization. The camera used for the visualization study was a three chip high resolution digital camera Sony DCR VX 2000. For the best visualization, the camera viewing angle was kept perpendicular to both the wire and the direction of incidence of the light on the field of view.

Figure 4.10 shows a smoke flow visualization image obtained at 5m/s wind tunnel test section speed and 6000 rpm rotor speed. Introducing forward flight is clearly disturbing the inlet flow characteristics on the windward side of the ducted fan system. Non uniformities can be seen in the side view images. Flow near the leading side is approaching to the duct lip with a significant momentum in the radial direction (fan) that is the same as the wind tunnel flow direction. Existence of the duct lip is a major obstacle in turning the almost horizontal inlet flow into the axial direction of the fan. A severe inlet flow distortion near the lip section of the fan unit is observed. The wind tunnel flow approaching the fan shroud as a blunt object stagnates over the external part of the shroud. This flow tries to reach the lip section of the shroud and turns around it to be part of the axial fan rotor energy addition process. Due to high adverse pressure gradient at the leading side duct lip, a separation flow occur near the leading edge of the lip section (before the rotor entrance plane) occurs. This flow separation, which is also known as inlet lip separation, partially blocks inlet of the fan rotor at the leading side. The air breathing ability of the fan rotor is adversely affected from the lip flow separation occurring under forward flight conditions.

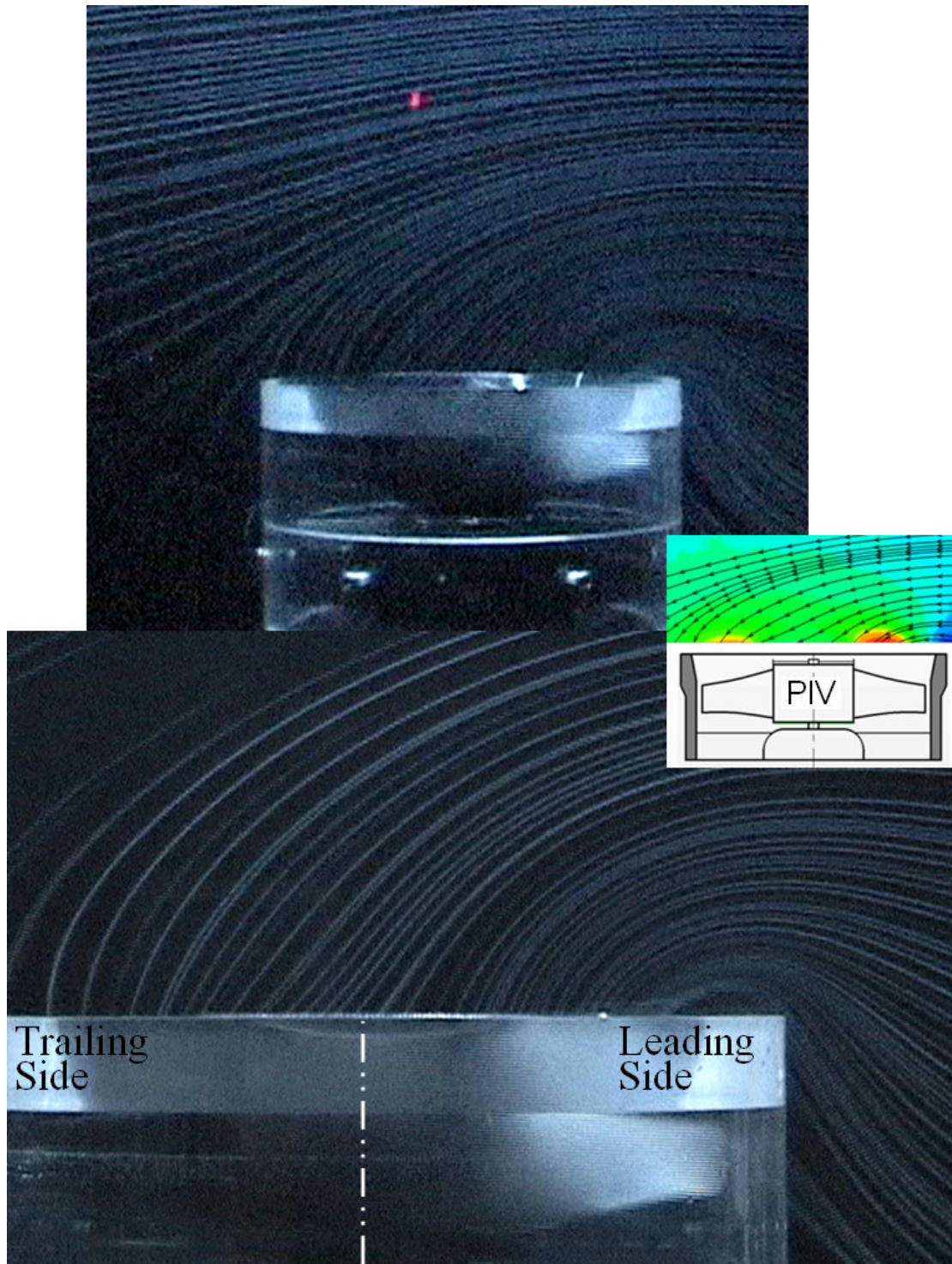


Figure 4.10. Smoke visualization at 6000 rpm and 5 m/s

4.2.4 Forward Flight Total Pressure Results

Figure 4.11 shows total pressure distribution measured at the exit of the fan rotor for different circumferential stations at hover and forward flight condition. Measurements were obtained at 12000 rpm rotational speed and 10 m/s forward flight velocity with a shroud that has a 5.8 % tip clearance.

The highest level of measured loss due to forward flight occurred at the leading side. By the effect of inlet lip separation and distortions in the inlet flow, a considerable defect in measured total pressure was noticed for $r/R_{Tip} \geq 0.7$. Especially for $r/R_{Tip} \geq 0.9$, total pressure losses increased tremendously compared to that of the hover condition. The adverse effects of tip leakage flow on the fan rotor performance was worsened by forward flight conditions. Distortions at the inlet flow of the fan rotor and inlet lip separation reduced the energy addition capability of the tip section of the rotor blade and resulted in a performance loss spread over approximately 80 % of blade span. Losses were especially increased around the tip region, near the leading side. Since tip clearance was not changed between hover and forward flight conditions, losses generated near the casing due to transition to forward flight are directly related to inlet lip separation and losses because of distorted inlet flow. It was also noted that for $r/R_{Tip} \leq 0.55$, there was a significant amount of total pressure loss due to forward flight.

Forward flight conditions caused separation from the rotor hub in this highly three dimensional and complex inlet flow environment. The existence of inlet lip separation arranged the streamlines at the inlet section in such a way that a more pronounced impingement of the inlet flow on the hub surface was observed. The hub separation occurring only near the 0° location is a direct result of the lip separation.

At 90° and 270° circumferential locations, the forward flight velocity affected the radial total pressure distribution and resulted in an increase in the losses near the tip region. There was more total pressure defect at 90° circumferential location. Since the measurements were performed at the downstream of the fan rotor, the effect of rotational direction of the fan rotor was noticed at 90° circumferential

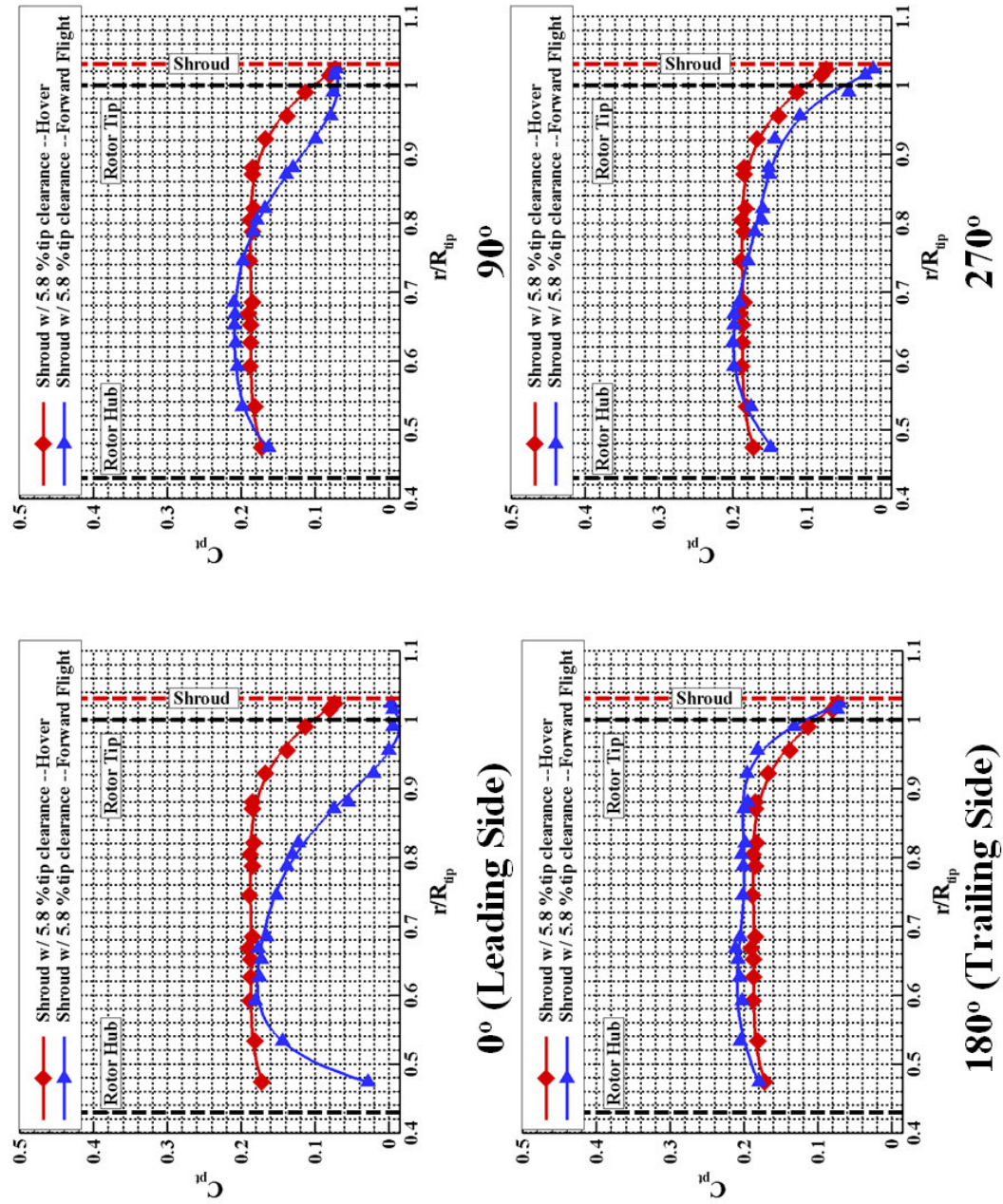


Figure 4.11. Comparison of hover and forward flight at 12000 rpm and 10 m/s forward flight speed

location. Because of counter-clockwise direction of the fan rotor, the re-circulatory low momentum fluid originating from the leading side (0° location) is effectively transported to 90° location. The defect in total pressure was more enhanced because of counter-clockwise direction of the fan rotor. In forward flight, the relative inlet velocity vector at the inlet plane changes its magnitude at each circumferential position. This is one of the reasons for the axisymmetric non-uniformity of the rotor exit total pressure field.

Unlike the leading side, the trailing side of the ducted fan is positively affected from forward flight velocity. The measured rotor exit total pressure in forward flight mode at all spanwise locations is slightly higher than that of hover. The significant inlet lip separation related momentum defect does not exist in the trailing side. The total pressure in front of the rotor at the trailing side is slightly higher than that of hover condition altering the blade loading near the tip section. It is obvious from Figure 4.11 that the tip related losses are slightly reduced in forward flight. Because of higher momentum fluid impinging on the inner casing near the trailing side , the adverse effect of tip leakage flow was slightly reduced. The rotor tip was performing better compared to hover condition. The flow impingement on the inner casing near the trailing side is a potential drag source in the forward flight zone.

4.2.5 Effect of Tip Clearance in Forward Flight

Effect of tip clearance at forward flight condition at 12000 rpm and 10 m/s forward flight speed is shown in figure 4.12. Like the hover condition, decreasing the tip gap height increases total pressure distribution in forward flight. When tip gap height was reduced, the tip leakage flow rate was also reduced resulting in smaller tip vortex. For other circumferential stations, behavior of total pressure distribution with a change in tip clearance resembles to the ones that were obtained for hover condition.

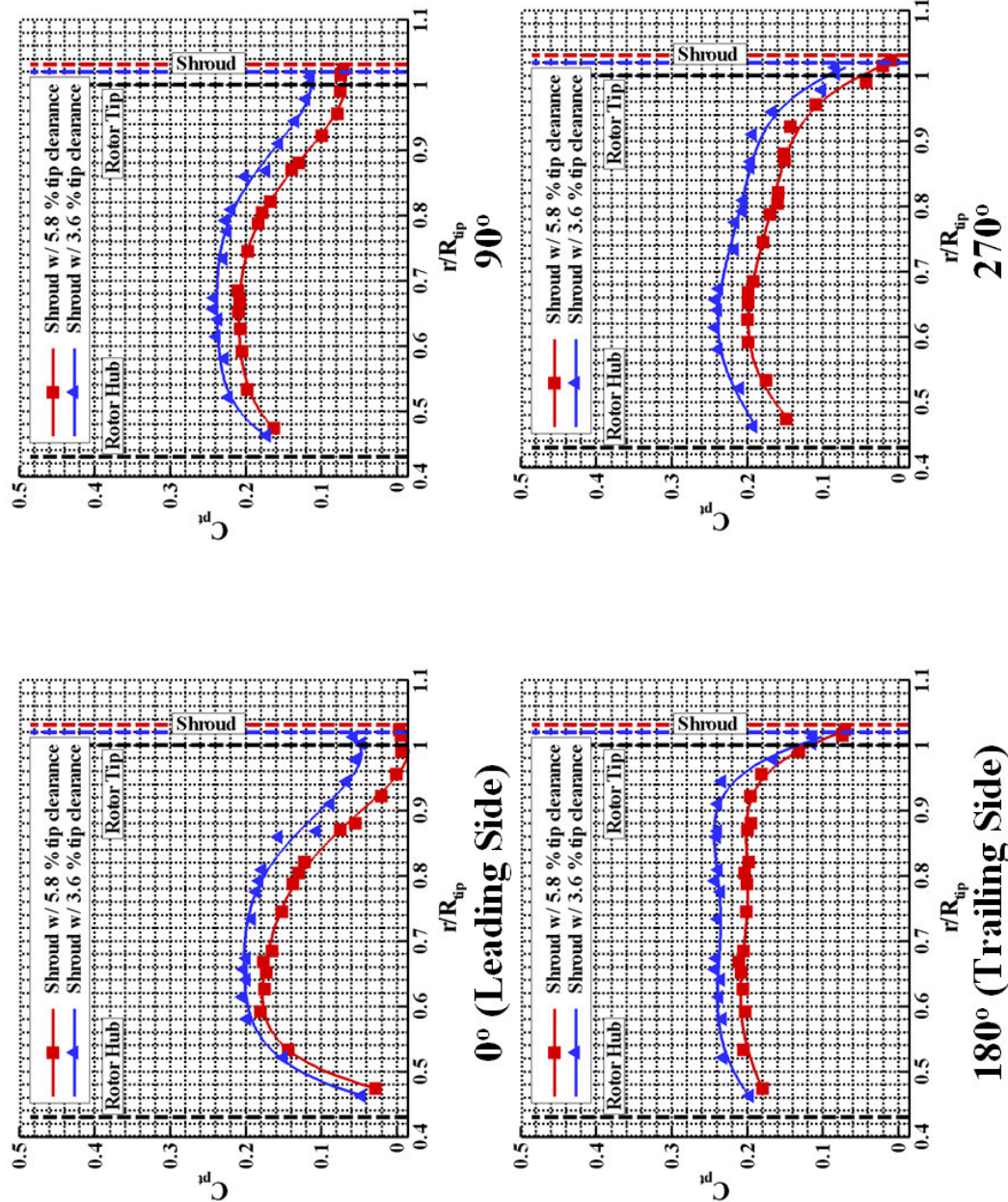


Figure 4.12. Comparison of tip clearance effect at forward flight at 12000 rpm and 10 m/s forward flight speed

4.2.6 Forward Flight Penalty

Transition to forward flight resulted in an increase in losses at the inlet lip region. It also elevated the tip region generated aerodynamic losses of the fan rotor. For a better understanding and comparison of forward flight and hover condition related flow physics, a new parameter called “*forward flight penalty (FFP)*” was defined. FFP is an indicator of total pressure loss generated for a configuration at forward flight in comparison to its own hover condition.

$$FFP = \frac{C_{pt\{H\}} - C_{pt\{FF\}}}{C_{pt\{H\}}} \quad (4.3)$$

Figure 4.13 shows FFP calculated from the measurements performed at 10 m/s forward flight velocity at 12000 rpm rotor speed for both tip clearances. Since the most significant loss generation due to forward flight occurred at the leading side, FFP was calculated at that location. FFP values closer to zero indicates minimum loss generated regions due to forward flight. This is only locally possible at the mid-span of the rotor where forward flight related flow problems are minimal. FFP=1 may result in when the rotor exit total pressure is at atmospheric level corresponding to a local stagnation zone which may occur in low momentum separated flow areas.

Both tip configurations resulted in a total pressure loss in forward flight. As discussed earlier, inlet flow distortion was the main reason for the loss generation in forward flight. When rotor exit conditions become closer to “*hover*” condition. Although the shroud with smaller tip clearance produced a measurable some total pressure loss, the shroud with larger tip clearance increased the total pressure loss tremendously. Especially near the tip region, increasing the tip gap height almost doubled the total pressure loss. The larger tip clearance resulted in a larger tip leakage vortex. Because the tip vortex size was increased, the effect of inlet lip separation was enhanced and fan rotor performance dropped dramatically. The effect of tip leakage and inlet lip separation was not only influencing the tip region. It was also observed that both shrouds generated a significant amount of loss near the hub region. However, loss generated near the hub was not dependent on tip clearance magnitude in forward flight. It was usually due to the 3D design of the

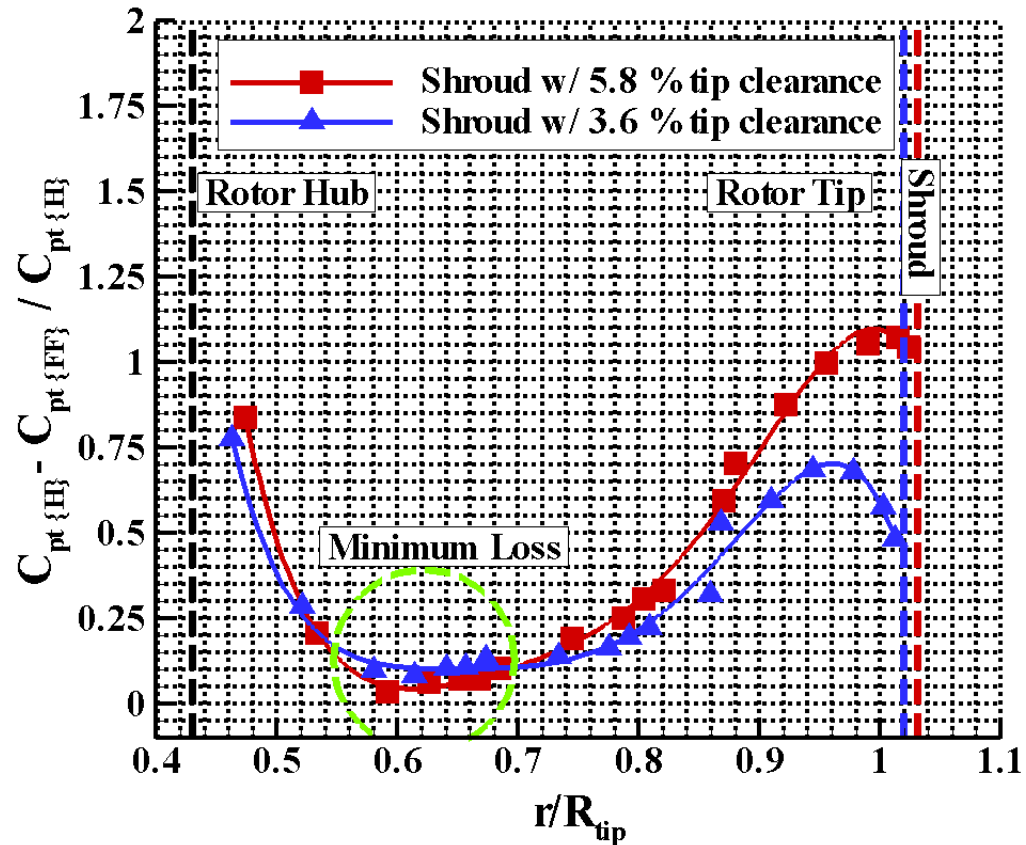


Figure 4.13. Forward flight penalty calculated at 12000 rpm and 10 m/s forward flight speed 0°

rotor blade and the hub endwall surface design including the hub corner region flow at the inlet.

4.2.7 Effect of Forward Flight Speed

The total pressure measurements at the leading side were also conducted for different forward flight speeds at 12000 rpm. Figures 4.14 and 4.15 show measurement results for 5.8 % and 3.6 % tip clearances respectively. The total pressure loss was increased by forward flight velocity. For lower speeds, the regions near the rotor tip was affected. As the flight speed was increased, inlet flow distortion

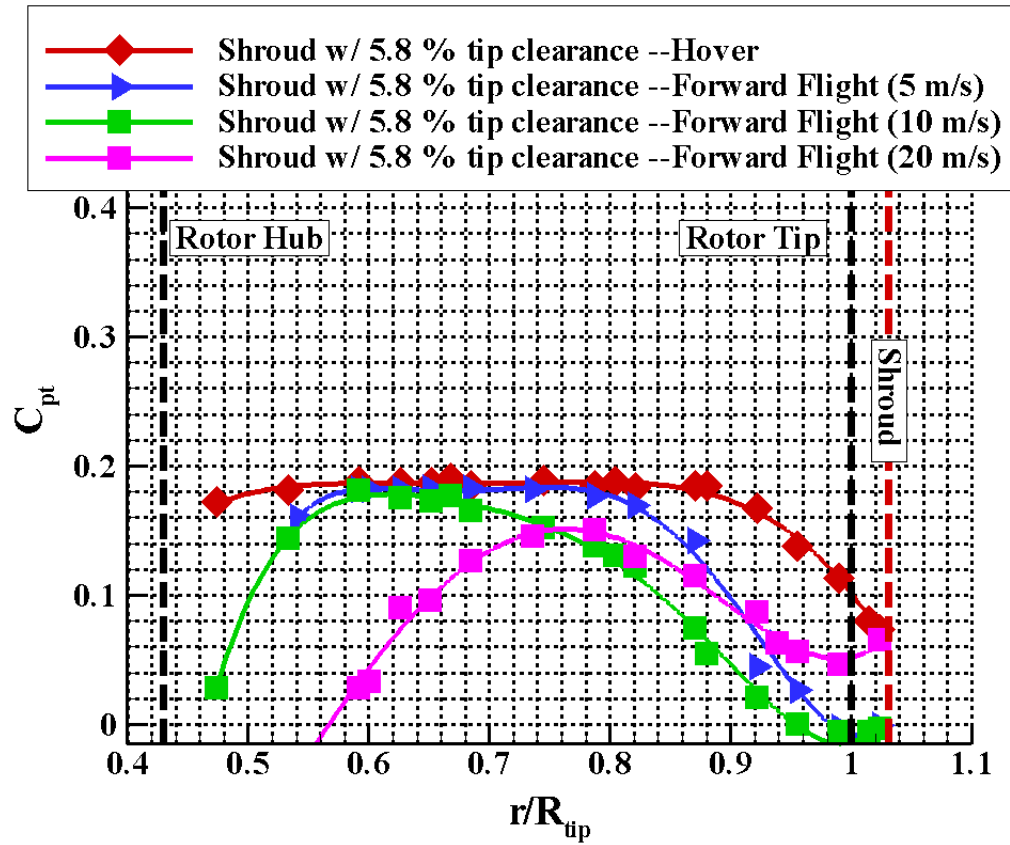


Figure 4.14. Effect of forward flight speed for 5.8% tip clearance

related effects were pronounced as shown in figure 4.14. For 20 m/s it was obvious that the rotor had difficulty to breath.

Figure 4.15 shows the total pressure losses at 3.6% tip clearance for hover and all other forward flight conditions. The qualitative shape of the loss curves in spanwise direction are very similar to that of 5.8% clearance. There is a visible elevation of overall total pressure loss for higher clearance 5.8 % as shown in Figure 4.15. Although the mid span of the blade has acceptable total pressure values, the hub and tip region total pressures were somewhat lower than that of hover results. The hub region total pressure deficit is more pronounced for the case of higher tip clearance.

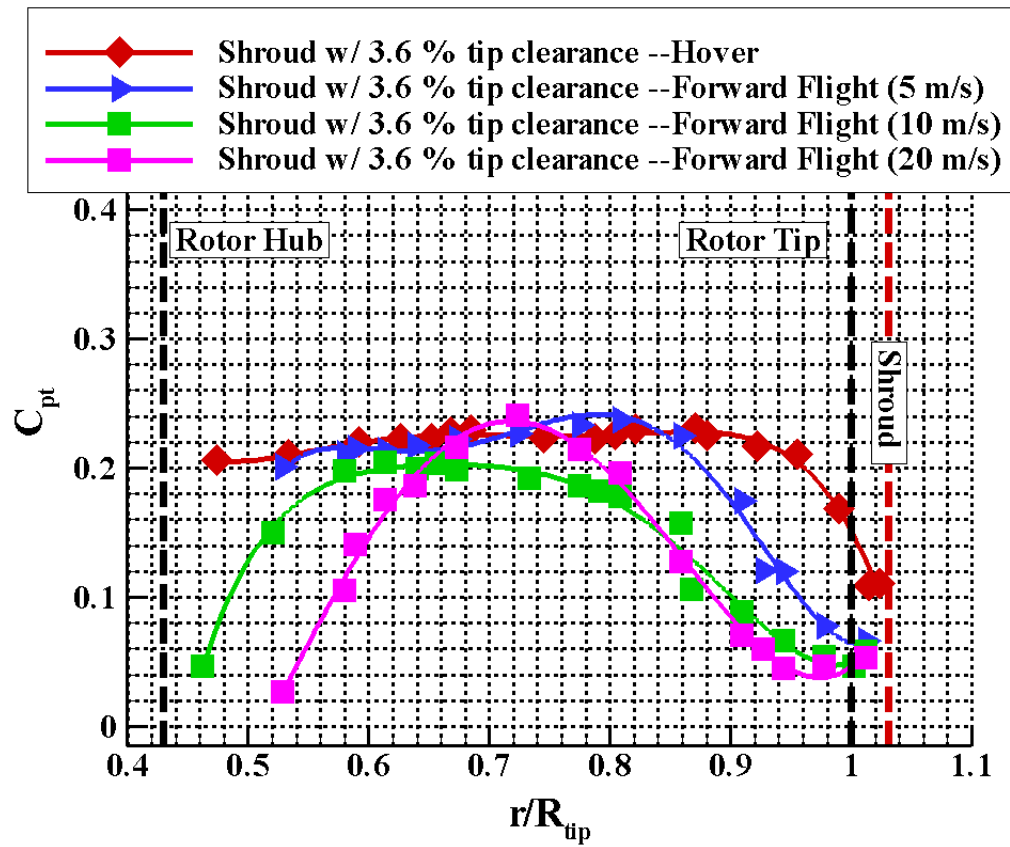


Figure 4.15. Effect of forward flight speed for 3.6% tip clearance

4.3 Computational Analysis of Ducted Fan in Hover Condition

Three dimensional computational methods can be used for analyzing viscous and turbulent flow field around and inside the ducted fan for hover and forward flight conditions. High resolution total pressure results experimentally obtained in this study constitute a good set of data for validation of computational algorithms. This section describes the details of the current approach used in the high performance computation of the 5" diameter ducted fan discussed in this chapter.

4.3.1 Computational Model Description

A simulation of the incompressible mean flow field around the ducted fan was performed using general purpose code Ansys-CFX [87, 88]. The specific computational system solves the Reynolds-Averaged Navier-Stokes equations using an element based finite volume method in the ducted fan rotor and around the ducted fan driven VTOL UAV. The mass, momentum and energy are simultaneously solved over an unstructured finite volume based mesh system.

4.3.1.1 Discretization of Governing Equations

Governing equations that provide a complete mathematical description of the fluid flow are conservation of mass, momentum and a passive scalar expressed in scalar coordinates in equations 4.4, 4.5, 4.6

$$\frac{\partial \rho}{\partial t} + \frac{\partial}{\partial x_j} (\rho U_j) = 0.0 \quad (4.4)$$

$$\frac{\partial}{\partial t} (\rho U_j) + \frac{\partial}{\partial x_j} (\rho U_j U_i) = -\frac{\partial P}{\partial x_i} + \frac{\partial}{\partial x_j} \left(\mu_{eff} \left(\frac{\partial U_i}{\partial x_j} + \frac{\partial U_j}{\partial x_i} \right) + S_{U_i} \right) \quad (4.5)$$

$$\frac{\partial}{\partial t} (\rho \phi) + \frac{\partial}{\partial x_j} (\rho U_j \phi) = \frac{\partial}{\partial x_j} \left(\Gamma_{eff} \left(\frac{\partial \phi}{\partial x_j} \right) \right) + S_\phi \quad (4.6)$$

These equations are integrated over control volume and Gauss' Divergence Theorem is applied to convert volume integrals involving divergence and gradient operators to surface integral. (Equations 4.7, 4.8 and 4.9) Equation 4.6 is usually used in the simulation of energy equation for temperature distribution over the domain.

$$\frac{d}{dt} \int_V \rho dV + \int_S \rho U_j dn_j = 0.0 \quad (4.7)$$

$$\frac{d}{dt} \int_V \rho U_i dV + \int_S \rho U_j U_i d n_j = \int_S P d n_j + \int_S \mu_{eff} \left(\frac{\partial U_i}{\partial x_j} + \frac{\partial U_j}{\partial x_i} \right) d n_j + \int_V S_{U_i} dV \quad (4.8)$$

$$\frac{d}{dt} \int_V \rho \phi dV + \int_S \rho U_j \phi d n_j = \int_S \Gamma_{eff} \left(\frac{\partial \phi}{\partial x_j} \right) d n_j + \int_V S_\phi dV \quad (4.9)$$

V and S in the equations 4.7, 4.8 and 4.9 respectively denote volume and surface regions of integration, and $d n_j$ are the Cartesian components of the outward normal surface vector. The volume and surface integrals in this section are discretized by using an unstructured mesh. A 2D single element shown in Figure 4.16 is considered to illustrate discretization procedure. Volume integrals are discretized within each element sector and accumulated to the control volume to which the sector belongs. Surface integrals are discretized at the integration points (ipn) located at the center of each surface segment within an element and then distributed to the adjacent control volumes. Because the surface integrals are equal and opposite for control volumes adjacent to the integration points, the surface integrals are guaranteed to be locally conservative. ANSYS CFX uses second order accurate approximations [87, 88].

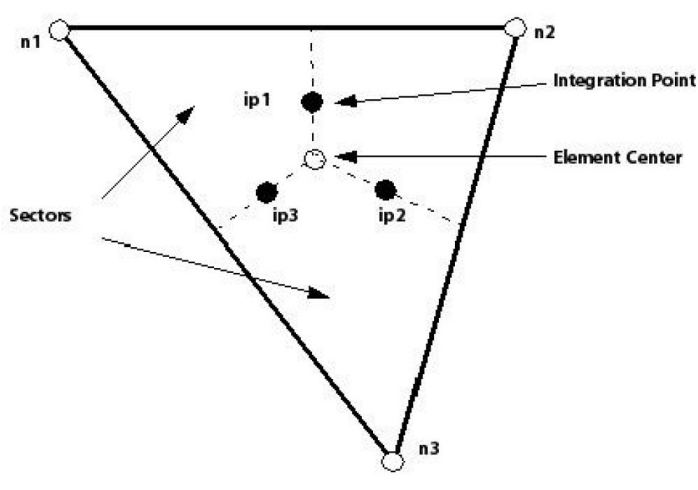


Figure 4.16. Two dimensional mesh element [87, 88]

Solution fields and other properties are stored at the mesh nodes. However,

to evaluate many of the terms, the solution field or solution gradients must be approximated at integration points. ANSYS-CFX uses finite-element shape functions to perform these approximations. Finite-element shape functions describe the variation of a variable ϕ varies within an element (equation 4.10). The shape functions used in ANSYS-CFX are linear in terms of parametric coordinates. various geometric

$$\phi = \sum_{i=1}^{N_{node}} N_i \phi_i \text{ where } N_i \text{ is shape function for node } i \text{ and variable } \phi_i \quad (4.10)$$

In this study, tetrahedral elements are used as shown in Figure 4.17. The tri-linear shape functions for nodes of a tetrahedral element are given in equation 4.11.

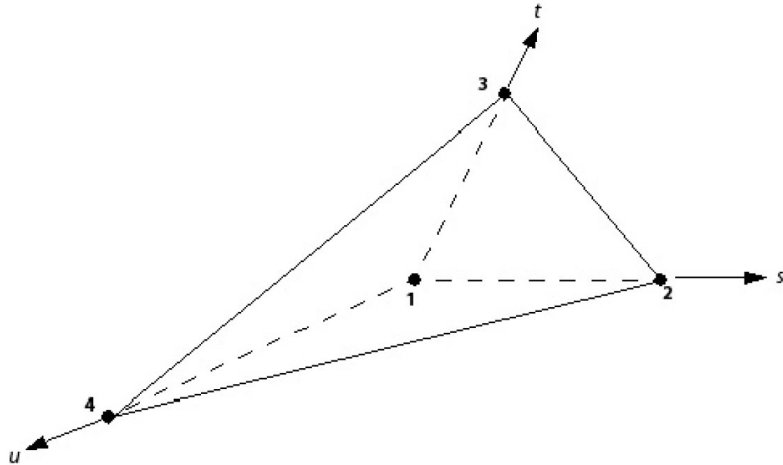


Figure 4.17. Tetrahedral element used in computations [87, 88]

$$\begin{aligned} N_1(s, t, u) &= 1 - s - t - u \\ N_2(s, t, u) &= s \\ N_3(s, t, u) &= t \\ N_4(s, t, u) &= u \end{aligned} \quad (4.11)$$

The advection term requires the integration point values of ϕ to be approximated in terms of the nodal values of ϕ . The advection schemes implemented in ANSYS CFX as $\phi_{ip} = \phi_{up} + \beta \nabla \phi \cdot \Delta \vec{r}$ where ϕ_{up} is the value at the upwind node and \vec{r} is the vector from the upwind node to the integration point (ip). Particular

choices for β and $\nabla\phi$ yield different schemes. For calculations performed for this study, the *Specified blend factor* method is used. In this method, β is specified as 0.75 and $\nabla\phi$ is set to the average of the adjacent nodal gradients.

Following the standard finite-element approach, shape functions are used to evaluate spatial derivatives for all the diffusion terms. Summation is over all the shape functions for the element. The Cartesian derivatives of the shape functions can be expressed in terms of their local derivatives by the Jacobian transformation matrix:

$$\begin{bmatrix} \frac{\partial N}{\partial x} \\ \frac{\partial N}{\partial y} \\ \frac{\partial N}{\partial z} \end{bmatrix} = \begin{bmatrix} \frac{\partial x}{\partial s} & \frac{\partial y}{\partial s} & \frac{\partial z}{\partial s} \\ \frac{\partial x}{\partial t} & \frac{\partial y}{\partial t} & \frac{\partial z}{\partial t} \\ \frac{\partial x}{\partial u} & \frac{\partial y}{\partial u} & \frac{\partial z}{\partial u} \end{bmatrix}^{-1} \begin{bmatrix} \frac{\partial N}{\partial s} \\ \frac{\partial N}{\partial t} \\ \frac{\partial N}{\partial u} \end{bmatrix} \quad (4.12)$$

As with the diffusion terms, the shape function used to interpolate Pressure can be evaluated at the actual location of each integration point. Linear-linear interpolation is used in our computations for this study. Pressure-Velocity, which is explained in details in [87, 88] coupling, is used in our computations. ANSYS CFX uses a Multigrid (MG) accelerated Incomplete Lower Upper (ILU) factorization technique for solving the discrete system of linearized equations.

4.3.1.2 Turbulence Model

The starting point of the present turbulence model is the $k-\omega$ model developed by Wilcox [89]. It solves two transport equations, one for the turbulent kinetic energy and one for the turbulent frequency, ω . The stress tensor is computed from the eddy viscosity concept.

k-equation:

$$\frac{\partial \rho k}{\partial t} + \nabla \cdot (\rho U k) = \nabla \left[\left(\mu + \frac{\mu_t}{\sigma_k} \right) \nabla k \right] + P_k + P_{kb} - \beta' \rho k \omega \quad (4.13)$$

ω -equation:

$$\frac{\partial \rho \omega}{\partial t} + \nabla \cdot (\rho U \omega) = \nabla \left[\left(\mu + \frac{\mu_t}{\sigma_\omega} \right) \nabla \omega \right] + P_k + P_{\omega b} - \beta \rho \omega^2 \quad (4.14)$$

In addition to the independent variables, the density, ρ , and the velocity vector, U , are treated as known quantities from the Navier-Stokes method. P_k is the production rate of turbulence, which is calculated as:

$$P_k = \mu_t \nabla U \cdot (\nabla U + \nabla U^T) - \frac{2}{3} \nabla \cdot U (3\mu_t \nabla \cdot U + \rho k) \quad (4.15)$$

The model constants are given by :

$$\begin{aligned} \beta' &= 0.09 \\ \alpha &= 5/9 \\ \beta &= 0.075 \\ \sigma_k &= 2 \\ \sigma_\omega &= 2 \end{aligned} \quad (4.16)$$

The $k-\omega$ based shear stress transport model is used in our computations. This model accounts for the transport of the turbulent shear stress and gives accurate predictions of the flow separation under adverse pressure gradient. The proper transport behavior can be obtained by a limiter to the formulation of the eddy-viscosity:

$$\mu_t = \frac{\rho a_1 k}{\max(a_1 \omega, S F_2)} \quad (4.17)$$

where F_2 is a blending function, which restricts the limiter to the wall boundary layer, as the underlying assumptions are not correct for free shear flows. S is an invariant measure of the strain rate.

$$F_2 = \tanh \left(\max \left[\frac{2\sqrt{k}}{\beta' \omega y}, \frac{500\nu}{y^2 \omega} \right]^2 \right) \quad (4.18)$$

where y is the distance to the nearest wall, ν is the kinematic viscosity and the magnitude of strain rate, S , is given as :

$$S = \frac{1}{2} \left(\frac{\partial U_i}{\partial x_j} + \frac{\partial U_j}{\partial x_i} \right) \quad (4.19)$$

4.3.1.3 Rotational Forces

For simulating flow in a rotating frame of reference, rotating at a constant angular velocity Ω , additional sources of momentum are required to account for the effects of the Coriolis force and the centrifugal force [87, 88]. Source term in equation 4.5 and 4.6 are modified as:

$$S_{M,rot} = S_{Cor} + S_{cfg} \quad (4.20)$$

where:

$$S_{Cor} = -2\rho\Omega \times U \quad (4.21)$$

$$S_{cfg} = -\rho\Omega \times (\Omega \times r) \quad (4.22)$$

and where r is the location vector and U is the relative frame velocity (that is, the rotating frame velocity for a rotating frame of reference) [87, 88].

4.3.2 Boundary Conditions for Hover

For the simulation of the ducted fan in hover condition, the computational domain is divided into two stationary (inlet and outlet regions) and one rotational frames (rotating fan blades). Figure 4.18 shows stationary and rotational frames. Inlet lip region includes an inlet lip surface that is considered as solid walls with no-slip condition. Atmospheric static pressure is prescribed on the top surface. On the side surface, opening boundary condition is assumed. An opening boundary condition allows the fluid to cross the boundary surface in either direction. For

example, all of the fluid might flow into the domain at the opening, or all of the fluid might flow out of the domain, or a mixture of the two might occur. An opening boundary condition might be used where it is known that the fluid flows in both directions across the boundary. [87, 88]

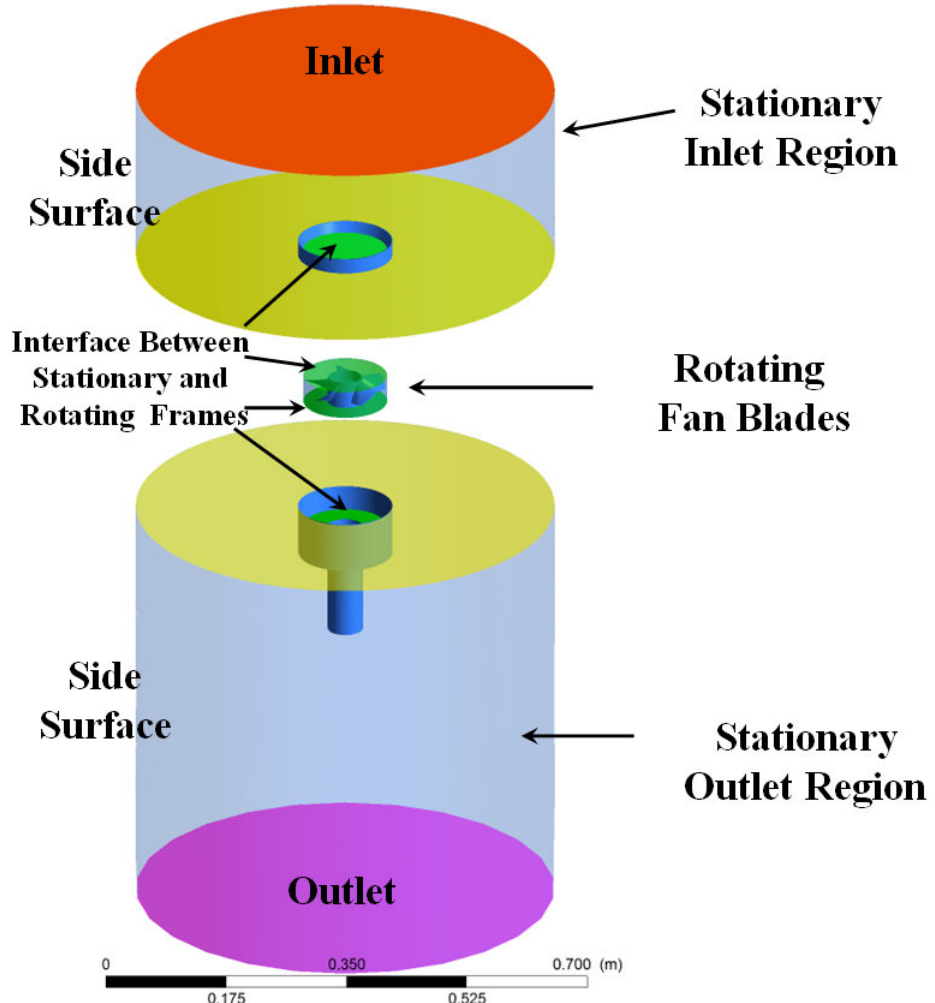


Figure 4.18. Computational domain and boundary conditions for hover condition

Outlet region includes outlet guide vanes, tailcone surface, duct inner surface and duct outer surface that is considered as solid walls with no-slip condition. Atmospheric static pressure is prescribed on the bottom surface. On the side surface, opening boundary condition is assumed.

Rotating region includes fan blades, rotor hub region and shroud surface. Rotating fluid motion is simulated by adding source terms for Coriolis forces and centrifugal forces that is mentioned in section 4.3.1.3. Counter rotating wall velocities are assigned at the shroud surface.

4.3.2.1 Interfaces Between Rotating and Stationary Frames

When one side is in a stationary frame and the other side is rotating frame of reference, interface should be used for connection. “*Stage*” type interface model is used in calculations for modeling frame change. The stage model performs a circumferential averaging of the fluxes on the interface. This model allows steady state predictions to be obtained for turbomachinery components. The stage averaging at the frame change interface introduce one-time mixing loss. This loss is equivalent to assuming that the physical mixing supplied by the relative motion between components. Between stationary frames an interface that provides general connection between two stationary domains. General grid interface (GGI) is used for mesh connections between interfaces. [87, 88]

4.3.3 Hover Condition Results and Flow Field around the Fan Rotor

The computational results are obtained at 12000 rpm for hover condition. Calculations are performed using a parallel processing. For the parallel processing, stationary and rotating frames are partitioned via vertex based partitioning with metis multilevel k-way algorithm [87, 88]. Computations are performed using 24 processors. Total processing time is approximately 48.5 hours. Steady state solutions are obtained after approximately 6061 iterations. Figure 4.19 shows the convergence history plot of mass flow rate at the downstream of the fan rotor.

Unstructured tetrahedral cells are used for the current computations. Regions

near the solid surfaces are meshed with prisms for generating viscous boundary layer grid. Non-dimensional wall distance (y^+) less than 2 is achieved near the casing and hub region. Region between solid casing and rotating blade tips are filled with prism layers.

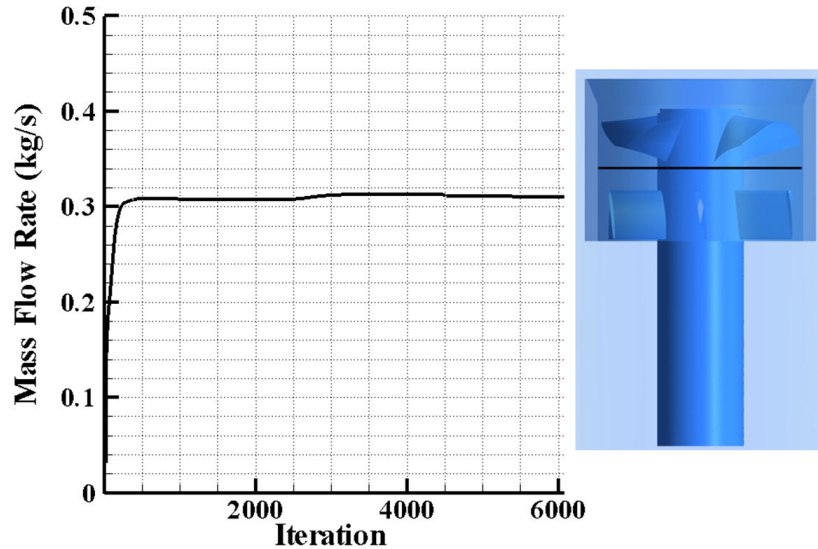


Figure 4.19. Convergence history plot of mass flow rate at the downstream of fan rotor

4.3.3.1 Validation of Numerical Results

Figure 4.20 shows comparison of experimental and computational results obtained for the 5" diameter ducted fan. In this steady state rotor computation, circumferentially averaged total pressure values computed at the exit of the fan rotor is compared to the experimental results. The computational and experimental results show very good agreement in the spanwise distribution except in a limited area near the hub where $r/R_{tip} \leq 0.6$. The computational results somewhat deviate from experimental results near the hub region. That is because of the highly complex low Reynolds number, separated turbulent flow field near the hub region. A combination of high rotational speed and low Reynolds number characteristic of the flow makes this computation highly challenging. A highly 3D and separated hub endwall flow system exists in this area.

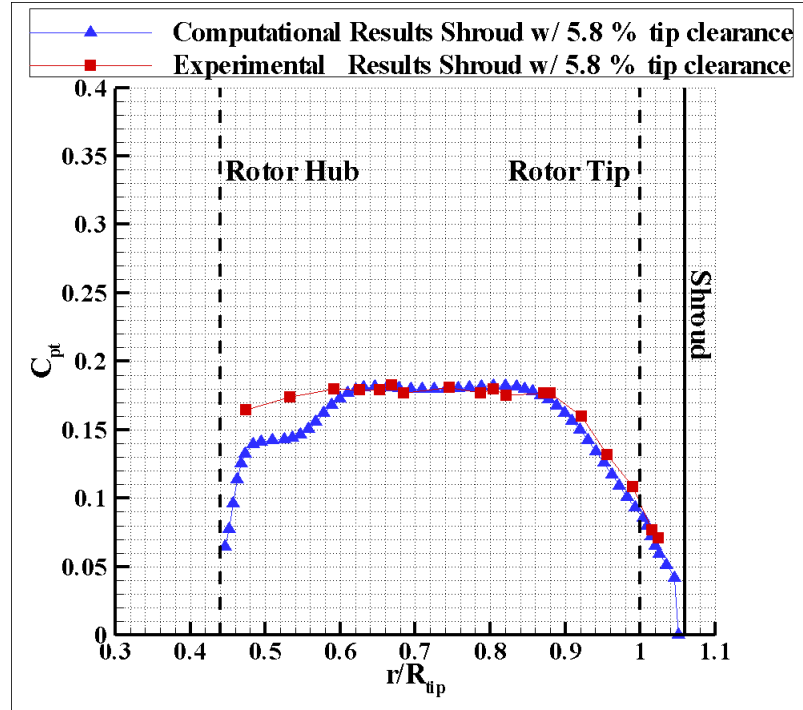


Figure 4.20. Comparison of experimental results to computational results at hover condition at 12000 rpm.

4.3.3.2 Grid Refinement Study

A grid independence study is performed to show that the computational results are not dependent on the computational mesh characteristics and that the resolution of the mesh is adequate to capture the significant flow characteristics. The grid independence is evaluated by comparing the computational solutions from 3 different mesh sizes, comprising coarse mesh with 3,350,000 tetrahedral cells, medium mesh with 4,500,000 cells and 5,000,000 cells. The static pressure distribution around the midspan blade profile is plotted as shown in Figure 4.21 for these different grid densities. The profile suggests that the computational results are grid independent when the 4,500,000 cells are exceeded. Therefore, the medium mesh is used for all predictions in this chapter.

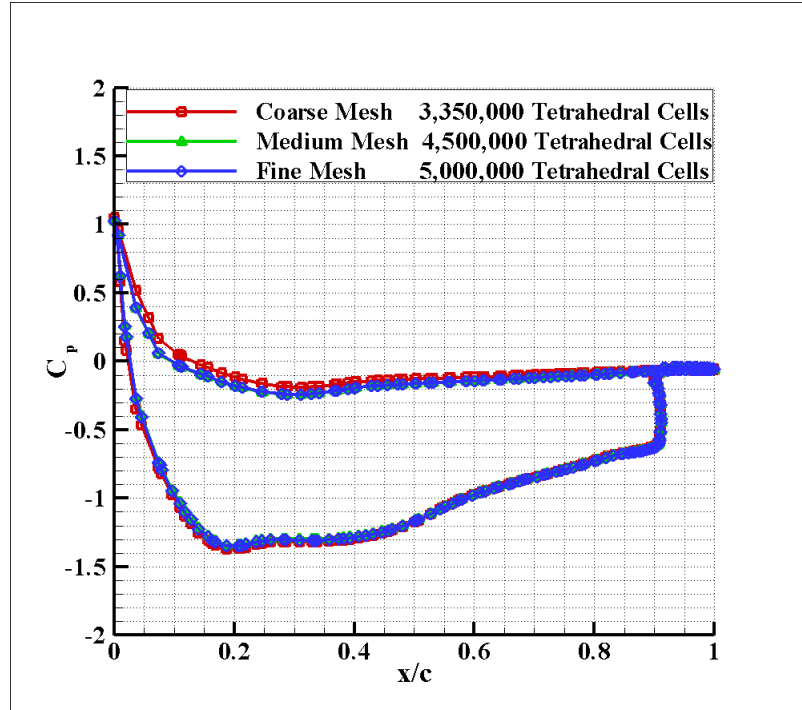


Figure 4.21. Grid independency study

4.3.3.3 Fan Rotor Exit Total Pressure

Figure 4.22 shows total pressure distribution drawn downstream of the fan rotor at 12000 rpm in relative frame. Contour plot is drawn on the plane that is tangent to the blade trailing edge at the rotor hub. Gains and losses in the flow field due to rotating fan rotor can be seen from the Figure. Red regions show high total pressure regions where rotor blade added energy to the flow whereas light and dark blue regions show low momentum fluid regions where energy of the flow is dissipated by aerodynamic losses. Loss generated from fan rotor blade surfaces are marked as “*rotor wake losses*” in the contour plot. Tip leakage losses are generated near the shroud. Leakage flow from the suction side to the pressure side generates significant amount of loss in the rotor exit flow field. It is obvious from the Figure that tip leakage losses are not only dominant near the tip but they also diffuse into the passage. Losses generated due to flow separation from the corner of the rotor hub and horseshoe vortex originating from the leading edge of the rotor blades can be seen in the light blue region near the rotor hub close to pressure side of the blade. A view of this separation vortex can be seen in Figure 4.23.

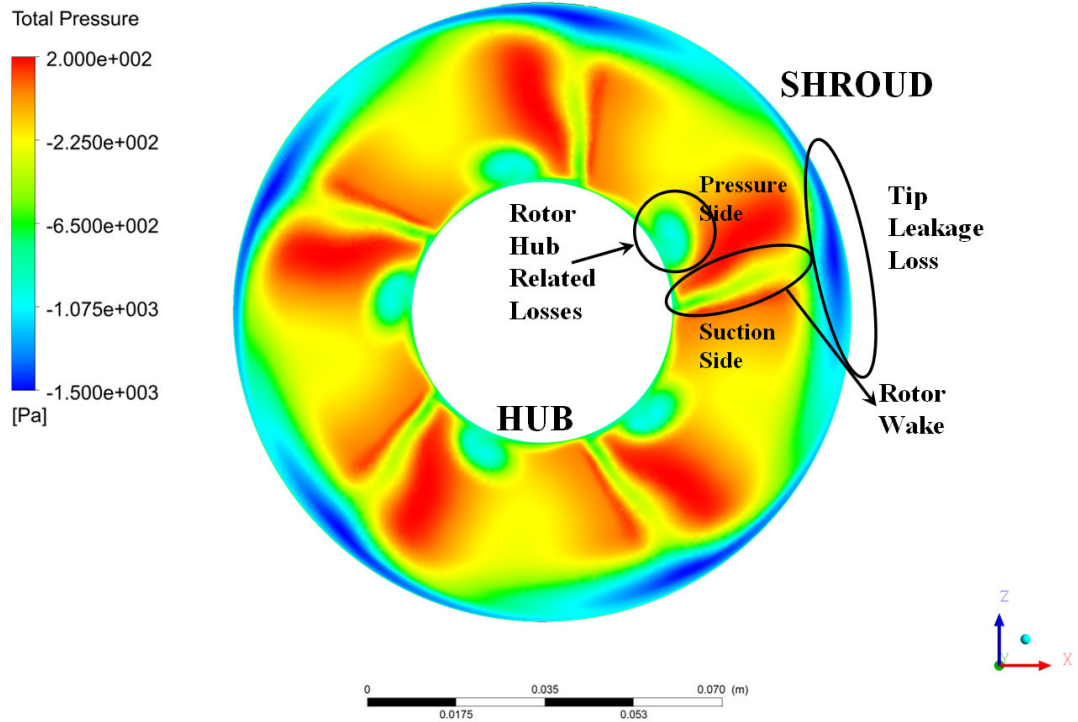


Figure 4.22. Fan rotor exit total pressure contour

Figure 4.23 shows streamlines drawn around the fan rotor at 12000 rpm in relative frame of reference. Streamlines are colored by velocity magnitude in the rotational frame, with the magnitude of relative velocity vector. Complex and detailed flow features around the fan rotor blades and rotating hub can be seen from the Figure. Low momentum fluid near the rotor hub is separated from the corner of the hub and rolled up into vortical structure. This vortical structure may combine with the horseshoe vortex originating from the leading edge of the rotor blades. The cross flows on the endwall surface may influence the final form of the hub separation region.

4.3.3.4 Effect of Rotor Hub Shape

Separation from the corner of the rotating hub is a significant source of loss for our five inch diameter fan rotor. It is noted that this separation effect is highly

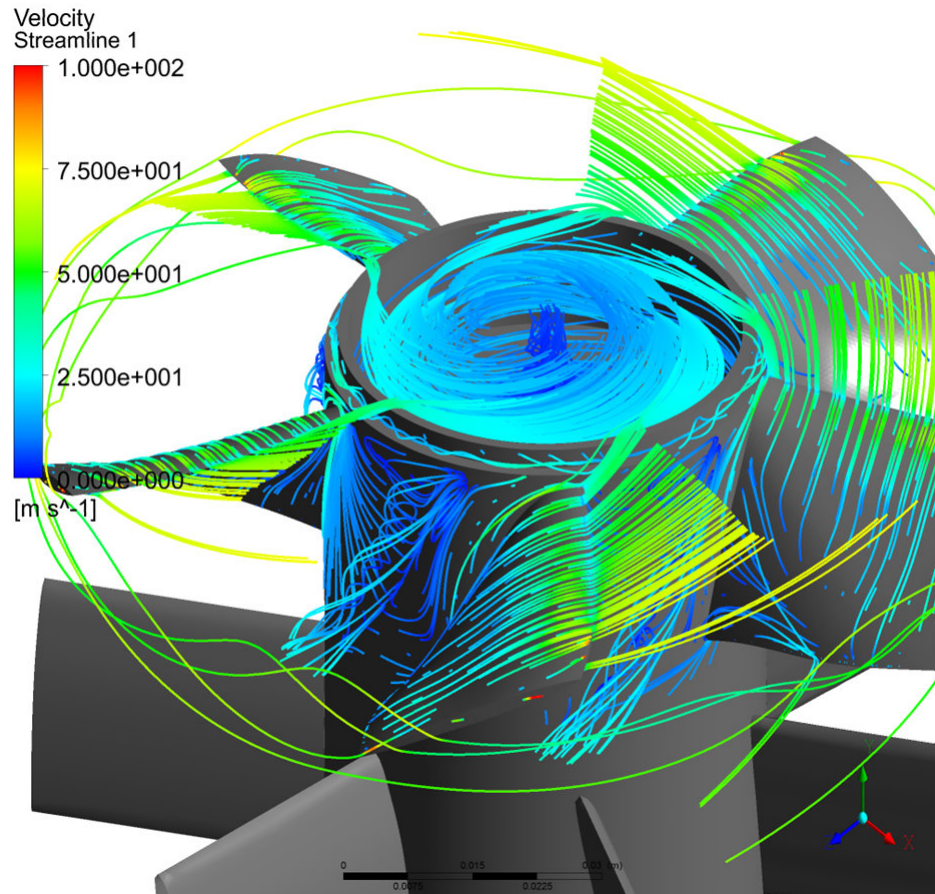


Figure 4.23. Computationally obtained streamlines near the ducted fan at 12000 rpm, in the relative frame of reference

dependent on the rotor hub geometry. During our initial calculations, a rotor hub without a cavity near the center was modeled as shown in Figure 4.24a. Figure 4.24 shows streamlines drawn around these rotor hub configurations. It can be concluded from Figure 4.24a that flow impinging on the rotor hub without a cavity has strong radial components. Because of this radial flow near the sharp corner of the rotor blade, it is hard to turn the flow near the hub region of the rotor blade. Because of increasing adverse pressure gradient on the junction of rotor blade leading edge and rotor hub, a vortical structure originates from the junction point and increases the strength of hub separation and losses from the hub. However a cavity on the center of the rotor hub as shown in 4.24b and step on the corner makes smooth transition for the flow from the rotor hub to the

rotor blade. It also reduce losses related to hub separation. Figure 4.22 shows the results with a cavity near the center of rotation.

4.4 Summary

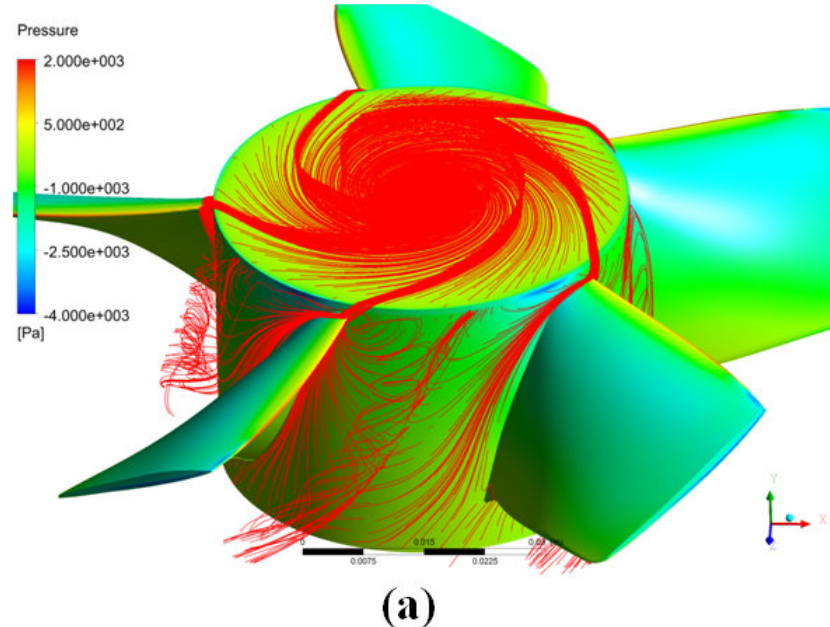
In this chapter, an experimental and computational investigation around a ducted fan for VTOL UAV applications was carried out. Total pressure measurements at the exit of the fan rotor to investigate the effect of tip leakage flow in hover and forward flight conditions were obtained in a low speed low turbulence wind tunnel.

Ducted fans offer higher disk loading compared to open rotors. Using a ducted fan improved hover disk loading up to 24 % compared to the open rotor.

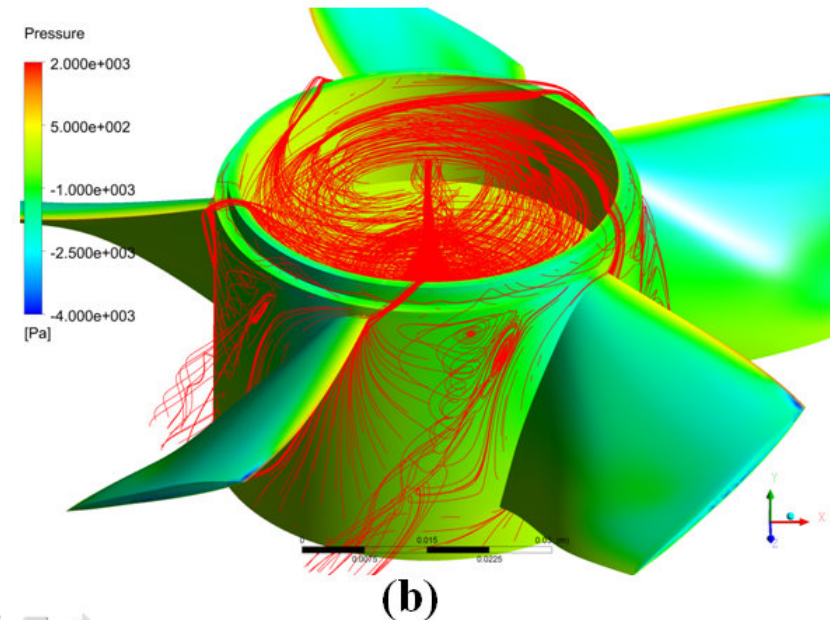
Tip clearance is one of the most important parameters affecting the ducted fan rotor performance. Decreasing tip clearance from 5.8 % to 3.6 % increased fan rotor exit total pressure by 17 % at mid span for hover condition. Hover tests also indicated that smaller tip gap improved overall performance of fan rotor along the span wise direction.

Exit total pressure of the fan rotor was measured at 4 circumferential stations during forward flight. The most significant total pressure losses occurred at the leading side (0°) for forward flight condition. Distortions at the inlet of the fan rotor and inlet lip separation stalled the tip of the rotor blade and resulted in a performance loss along 80 % of blade span.

Unlike leading side, the trailing side of the ducted fan is positively affected from forward flight velocity. More favorable inlet flow conditions near the trailing side of the rotor leads to a more effective rotor energy addition process. Decreasing tip gap height enhanced total pressure distribution in forward flight mode. The total pressure loss near the tip of the blade is decreased by reducing the tip gap height.



(a)



(b)

Figure 4.24. Streamlines drawn around fan rotor hub for two different configurations
(a) rotor hub without a cavity on center and step on corner (b) rotor hub with a cavity on center and step on corner

Especially near the tip region increasing tip gap height by approximately 40 %, doubled the total pressure loss at the leading side of the ducted fan at forward flight. The effect of tip leakage and inlet lip separation was spread overall blade span.

Forward flight conditions caused separation from the rotor hub in this highly three dimensional and complex inlet flow environment. The existence of inlet lip separation arranged the streamlines at the inlet section in such a way that a more pronounced impingement of the inlet flow on the hub surface was observed.

The total pressure loss was increased by forward flight velocity. For lower speeds, the regions near the rotor tip was affected. As the flight speed was increased, inlet flow distortion related effects became more pronounced. For 20 m/s flight speed, it was obvious that the rotor had tremendous difficulty to breath and unsteady effects were dominant.

The results from a 3D computational results using Reynolds Averaged Navier Stokes equations showed very good agreement with the measured total pressure distributions at the rotor exit, for hover conditions

Chapter **5**

Novel Tip Platform Extension Designs for Ducted Fan Tip Leakage Control

This chapter describes an experimental study of tip leakage minimization that used stereoscopic particle image velocimetry measurements (SPIV) at the exit of a seven bladed axial fan rotor. The fan rotor used for the experiment has a disk loading value of $3.65 \text{ lb}/\text{ft}^2$ and considered as “*low disk loading fan*” for rotocraft applications. All of the experiments were performed at a constant rotational speed of the fan (859 rpm). The large scale character of the experimental fan setup provided a high aerodynamic resolution for the current tip leakage minimization effort.

The study presented in this chapter is motivated by the need to develop tip platform design capability for minimization of tip leakage flow. The following sections provide the detailed explanations of the experimental approach and important conclusions of this effort.

5.1 Experimental Set-up

5.1.1 Test rig

The test rig consisting of an axial flow fan, a mock-up unit housing the fan and an electric drive system as shown in Figure 5.1 was designed to investigate the rotor exit flow phenomena using a stereoscopic PIV system. The set-up has also provisions for seeding the fan flow field with a smoke generator using a fluidized bed. The smoke generator is located near the inlet section of the mock-up unit where a perforated plate controlling the fan loading is mounted. The electric motor driving the fan rotor is speed controlled by an AC inverter unit. The current phase-locked SPIV measurements are triggered by using an optical once-per-revolution device located near the hub of the rotor inlet. An infrared beam is reflected from a highly reflective strip surface attached to the rotor hub. The relative position of the rotor can be adjusted accurately in relative to the position of the laser light sheet that forms the rectangular SPIV measurement area.

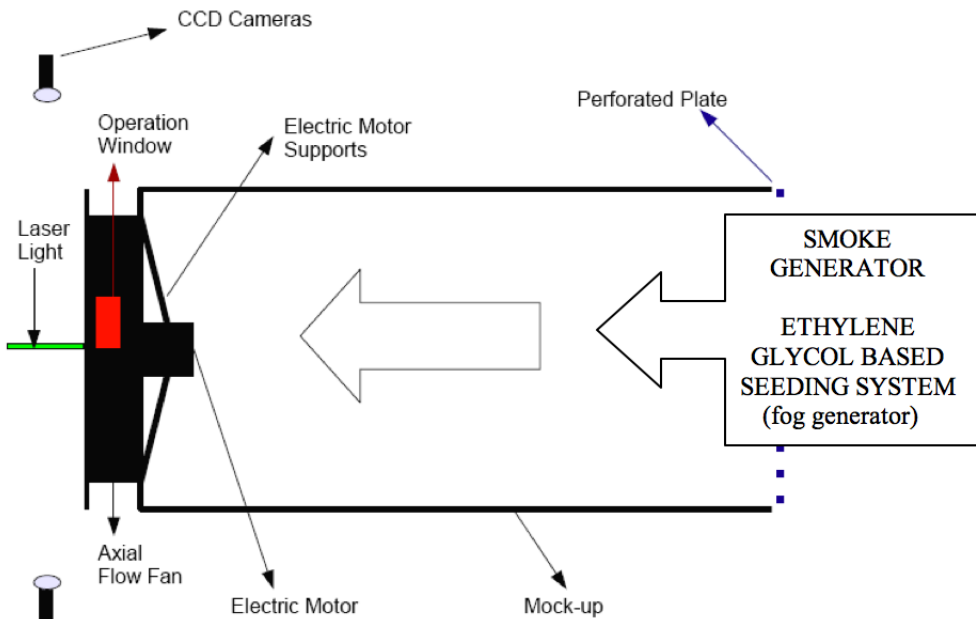


Figure 5.1. Test rig and stereoscopic SPIV setup

5.1.2 Ducted Fan Description and Performance

Figure 5.2 shows seven bladed axial flow fan unit including the orientation of the SPIV system components. The geometric specifications are presented in figure 5.3. A perforated plate at the inlet section of the mock-up unit is used for achieving realistic fan loading conditions. The tips of the blades are modified through a removable “*operation window*” as shown in Figure 5.1. Only one blade tip out of seven blades is modified since the current SPIV system is capable of measuring in the immediate vicinity of a selected blade tip due to the phase-locked and instantaneous nature of the SPIV measurements. A precision machined 0.030 inch (0.762 mm) constant thickness thermoplastic layer was used for the selected tip platform design.

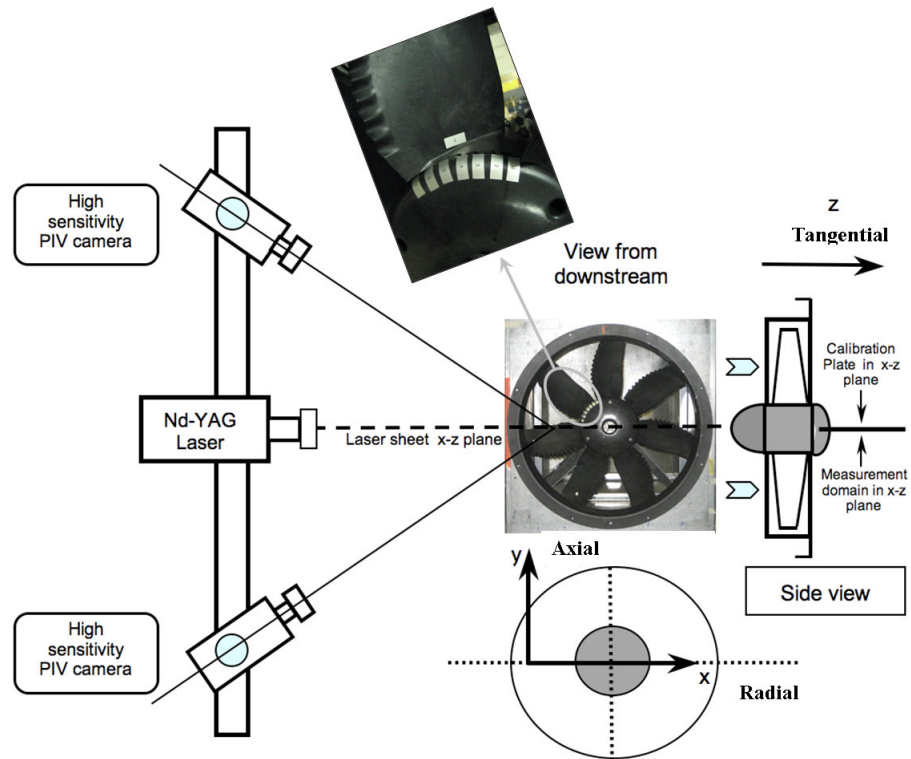


Figure 5.2. Axial flow fan as seen from the exit plane and the SPIV system orientation

The tip platform design was attached to the precision machined tip area in a non-intrusive way through the operation window as shown in figure 5.1. The modifications made on the selected tip did not cause a measurable rotor balance

problem since the rotor was manufactured out of relatively light weight thermoplastic material. The current rotor blades have serrated trailing edges for effective mixing of the blade boundary layers in the wake of each blade. The serrated trailing edges also provide an effective mixing of individual tip vortices with the wakes of the seven blades in the rotating frame of reference. It should be noted that the comparison of the flow with serrated trailing edges with smooth trailing edge flow is not the subject of the current chapter. The current chapter mainly deals with the minimization of tip leakage flow in the rotor.

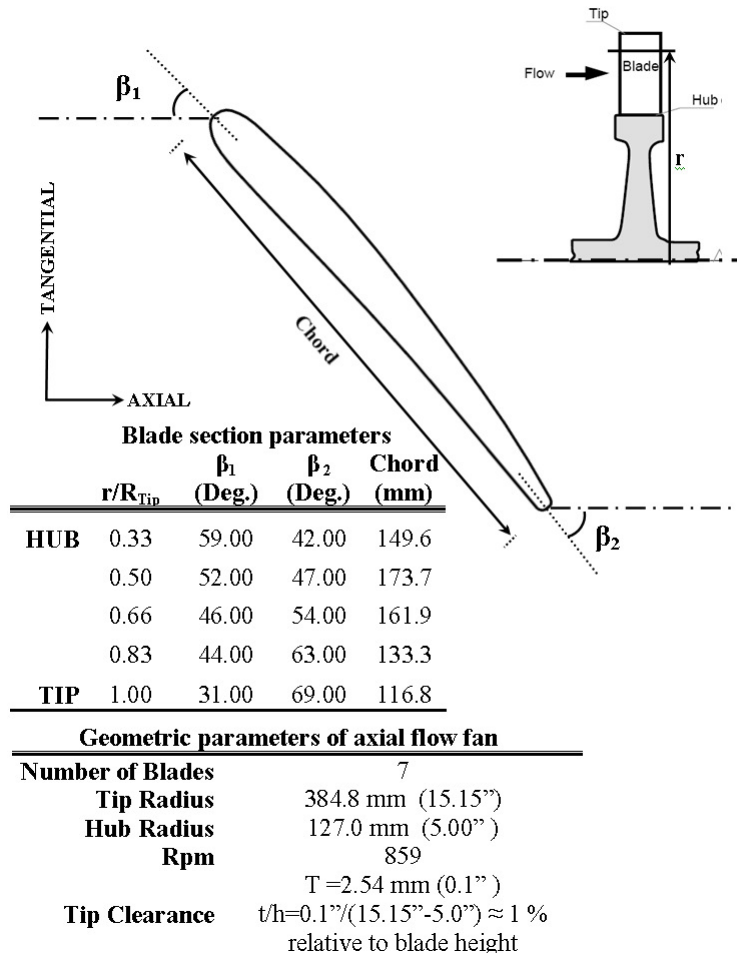


Figure 5.3. Geometric and blade section parameters of axial flow fan

Fan Performance: The performance of the fan unit is measured under three different loading conditions. The first performance point (80 m^3 , 140 Pa) shown

in Figure 5.4 is obtained by using a perforated steel plate having an open area ratio of 19.6%. A second perforated plate using a slightly larger open area ratio of 42.5% provides the middle point ($280 \text{ m}^3/\text{min}$, 88 Pa) in the performance curve as shown in figure 5.4. The third point with the highest volumetric flow rate at $340 \text{ m}^3/\text{min}$ is obtained when there is no perforated plate installed at the inlet section of the mock-up unit. The pressure change across the fan is measured by using pitot static holes mounted on all four sides of the mock-up unit. Wall-static pressures from all four sides are averaged. For the mass flow rate measurements, a hot-wire based volumetric flow measurement device is used at rotor downstream.

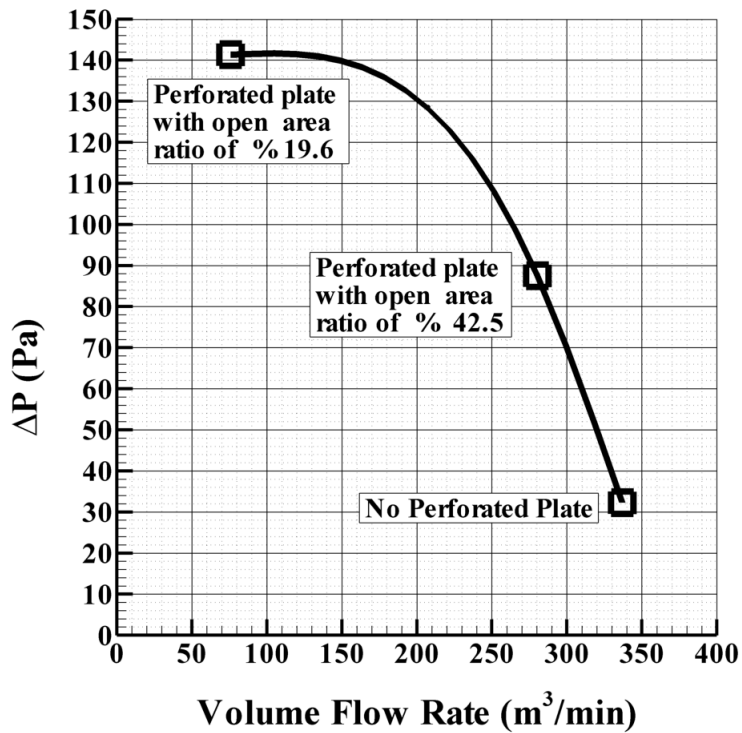


Figure 5.4. Axial flow fan performance

5.1.3 Stereoscopic PIV system

In stereoscopic PIV, there is an additional camera viewing the field from a different angle. The two-dimensional image obtained by each camera is slightly

different from each other, and they are afterwards combined to produce the three-dimensional velocity information. Stereoscopic vision principles are instrumental in this process of combining the two planar images obtained from the two cameras viewing the same flow-field simultaneously. The data reduction in a stereoscopic PIV system requires the processing of four independent images from the two cameras. For 3D analysis, in this study the 2D calibration images need additionally to be converted into 3D data by a Direct Linear Transform (DLT) model, in order to calculate the third component of the velocity. Correlation techniques are used to obtain raw vector maps out of image pairs taken during the experiments, and a number of calculation methods are used to evaluate these vector maps. In summary, the three dimensional space defined by the planar measurement area and the finite thickness of the laser sheet is analytically described in relation to the highly distorted images captured by the two CCD chips in each of the two cameras. The distortions observed on the planar CCD images are generated by the angled position of two cameras. For example, a perfect cube in the measurement space is seen as a distorted cube in each one of two images generated by two cameras.

Two of the 80C60 HiSense PIV/PLIF cameras with 1024 x 1280 pixels are used with 80N57 personality module fitted to processor, and a Nikon micro-Nikkor 60/2.8 objective, for each camera. The calibration plate, the cameras, Nd-Yag pulsed laser unit and axial fan rotor blades are shown in figure 5.2. Initial adjustment procedure requires that the laser light sheet generated by the Nd-Yag laser is aligned with the calibration plate carrying a standard high precision square grid machined on a custom made plate.

5.2 Experimental Methodology

5.2.1 Measurement Domain

The axial (y), radial (x) and tangential (z) components of velocity profiles were simultaneously measured near the tip region of the fan under the influence of a few novel tip platform extensions designed throughout this investigation. Figure

5.5 shows the measurement domain which is a rectangle in the x-y plane located at just downstream of the rotor. The x-y plane is horizontal and contains the axis of rotation. Most of the SPIV distributions covered a spanwise region from $r/R_{Tip}=0.6$ to $r/R_{Tip} = 1.3$. This measurement area corresponds to a region covering the last three quarters of the blade height including the tip region flow. The span-wise velocity distributions shown in Figures 5.8, 5.9, 5.10 and 5.11 are obtained at an axial position 46 mm away from the rotor exit plane. The radial direction is also marked with r/R_{Tip} in order to mark the exact position of the blade root and tip in the span-wise distributions of velocity. “ r/R_{Tip} ” is approximately 0.33 at blade root location (hub).

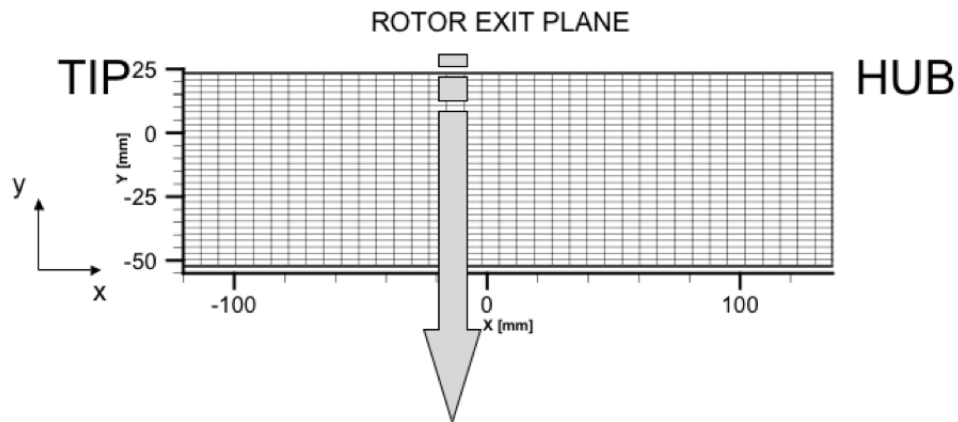


Figure 5.5. SPIV measurement plane (horizontal) downstream of the rotor exit and the coordinate system

5.2.2 Specific Rotor Positions for Phase-locked Measurements

The results from the custom designed tip platform extensions are compared to the results obtained from a baseline tip at two different tip clearance levels. All three components of the velocity vector were measured for 7 circumferential positions of the rotor (with respect to the SPIV measurement plane). These locations were chosen by dividing the rotor blade pitch into 7 equi-angular regions. Although the measurements were performed at seven positions, only the most pertinent data

from three selected positions are presented. The selected positions include blade tip leading edge, mid-chord and trailing edge (locations 3,4,5).

5.2.3 Statistical Stability of SPIV Measurements

An adequate number (N) of SPIV speckle images should be recorded and processed for satisfying statistical requirements for accurate mean velocity measurements. The ensemble average of measured velocity components approaches to a true mean as N goes to infinity. During an ensemble averaging of finite number of instantaneous velocity measurements, it should be noted that their average may have a deviation from the true mean value. This deviation is closely related to the sample size (N) which is a measure of the statistical stability of this ensemble averaging process. Table 5.1 shows deviations calculated from measured data for radial, axial and tangential velocity components obtained by averaging 50,100,150 and 250 PIV speckle images. Standard errors are calculated by using the central limit theorem [90]. The central limit theorem states that uncertainty can be approximately equal to the standard deviation of measured values (σ) divided by \sqrt{N} (i.e $\epsilon = \frac{\sigma}{\sqrt{N}}$).

	Radial Velocity	Axial Velocity	Tangential Velocity
N=50	$1.19 \times 10^{-1} U_a$	$1.11 \times 10^{-1} U_a$	$1.98 \times 10^{-1} U_a$
N=100	$7.47 \times 10^{-2} U_a$	$6.44 \times 10^{-2} U_a$	$1.28 \times 10^{-1} U_a$
N=150	$6.01 \times 10^{-2} U_a$	$4.85 \times 10^{-2} U_a$	$8.89 \times 10^{-2} U_a$
N=200	$4.77 \times 10^{-2} U_a$	$3.97 \times 10^{-2} U_a$	$7.93 \times 10^{-2} U_a$
N=250	$3.99 \times 10^{-2} U_a$	$3.39 \times 10^{-2} U_a$	$6.68 \times 10^{-2} U_a$

Table 5.1. Uncertainties of ensemble averaged velocities components

The uncertainties are estimated at locations of the highest standard deviations of individual components for each sampling image size. They are normalized by using averaged axial velocity (U_a) calculated from the mass flow rate of the fan for the condition that experiments are conducted ($340 \text{ m}^3/\text{min}$, 32 Pa). Note that the most uncertainties are smaller than 9% for the ensemble image size more than 150 images.

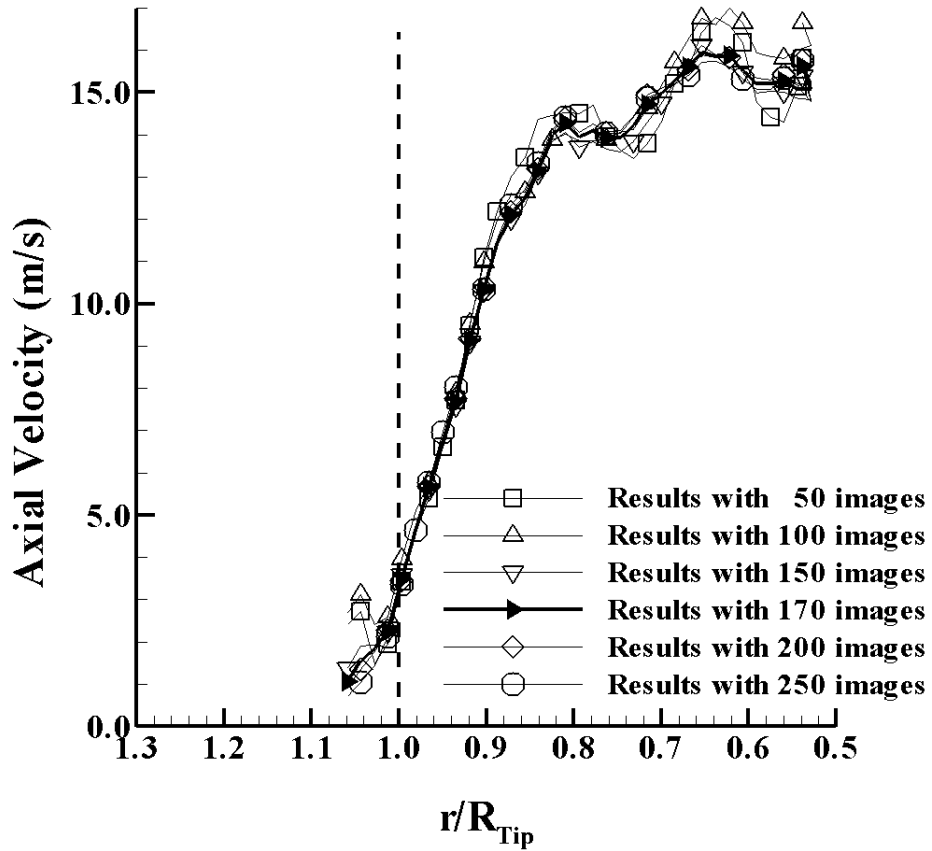


Figure 5.6. Influence of sample size in SPIV ensemble averaging

Based on the examination of data convergence with the number of speckle images, sampling image size (N) is selected to be 170. Figure 5.6 presents the influence of ensemble averaging sample size on the span-wise distribution of the most significant velocity component “*axial component*”. The baseline blade tip is used in this experiment with a nominal tip clearance of 1% of the blade height. The span-wise region where $0.9 \leq r/R_{Tip} \leq 1.02$ is not significantly influenced from the choice of the ensemble averaging sample size. The sample sizes of 150, 170, 200 and 250 produce very similar span-wise distributions in this region near the tip. All SPIV experiments presented in figures 5.8 - 5.13 are conducted using an ensemble averaging sample size of 170.

Tip Clearance Values: An effective control of tip leakage flow was achieved

using different tip platform extensions. The term “control of tip leakage flow” in this study could be defined as the “minimization of tip leakage flow mass flow rate”. Baseline profile was evaluated at two different tip clearance values of 0.1 inch and 0.135 inch corresponding to 1% and 1.35% of blade height. All of the “tip platform extensions” used in this study were evaluated at tip clearance values of 0.1 inch corresponding to 1 % of the blade height.

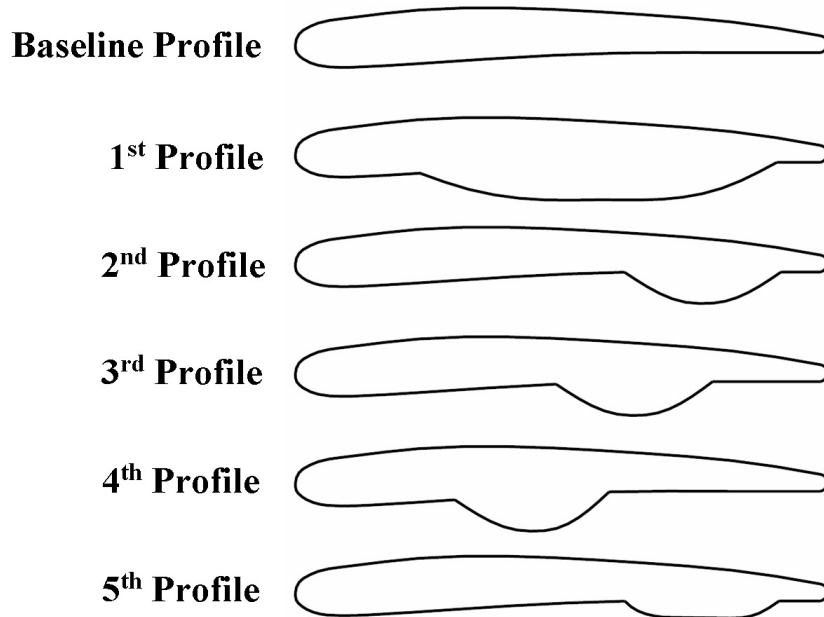


Figure 5.7. Novel tip platform extensions for tip leakage mitigation

5.3 The General Impact of Tip Platform Extensions

The main goal of this study is to minimize the tip leakage flow by interfering with the flow near the pressure side corner of the blade tip region. A new static pressure distribution near the blade tip section is established by the novel tip platform extension designs shown in figure 5.7.

The impact of the suggested tip platform extensions is visible in the “magnitude

enhancements” of the axial velocity component downstream of the tip region. It is also highly visible that the strong tangential velocity components induced by the baseline tip are almost eliminated by effective tip platform design. This observation is very clear especially near the tip diameter of the rotor exit flow

5.3.1 Geometrical Definition of the Five Tip Platform Extensions

The design idea behind the present tip platform extensions is based on estimating the blade chordwise position where the tip leakage potential is the highest for a given tip profile. It is obvious that the leakage potential is represented by the static pressure differential imposed by the shape design of the blade profile. Initial CFD based flow prediction is may be effective in finding the chordwise region where the leakage mass flow rate is maximum.

The tip platform extensions were designed by adding constant-thickness “**pressure side bumps**” of different designs to the base profile as shown in figure 5.7. The thickness of the platform extended on the pressure side of the blade is about 0.030 inch (0.762 mm) for all designs used in this investigation. Initially, a wide bump between the trailing edge and the leading edge was suggested as Profile 5.1 in figure 5.7. The maximum width of the bump was chosen as the same as the thickness of the airfoil at the bump centerline location. Three more tip platform extensions were derived from Profile 1 by dividing the bump width of Profile 1 into three almost equal chord-wise sections. The three new tip platform extensions are termed Profile 2 (near the trailing edge), Profile 3 (middle of the wide bump) and Profile 4 (almost mid-chord). The bump maximum widths were kept the same. Profile 5 is a derivative of the trailing edge bump named as Profile 2. Profile 5 uses a relatively small platform area when compared to all other tip platform extensions. The external contour of Profile 5 is almost parallel to the baseline profile except the end points where blending is suggested.

Only one rotor blade at a time out of seven blades was retrofitted with a sug-

gested design. Each experiment had six baseline blades and a seventh blade with the suggested tip platform extension. The effective clearance was kept same for all seven blades.

5.4 Experimental Results and Discussion

Figures 5.8, 5.9, 5.10 and 5.11 show the results of the exit flow measurements of the axial flow fan at the highest volumetric flow rate condition defined as ($340 \text{ m}^3/\text{min}$, 32 Pa) . Figure 5.12 complements these results from a data set obtained at the minimum mass flow rate condition where the pressure loading is maximum ($80 \text{ m}^3/\text{min}$, 140 Pa). All the velocity profiles are plotted at 1.811 inch (46 mm) downstream of the fan.

In addition to the magnitude of the velocity vector (total velocity); the radial, tangential and axial components of the velocity vector at the exit of the rotor is provided in function of the span-wise distance.

Baseline Tips: Near the tip, where $r/R_{Tip} \geq 0.9$, the two base profiles show very similar trends in Figure 5.8. The total velocity is significantly reduced in the core of the passage where $r/R_{Tip} \leq 0.9$ when tip clearance is high at $0.135''$ level. The $t=0.100''$ and $t=0.135''$ clearance base profiles show significant momentum deficit occurring in the core of the tip vortices from the two baseline tips (without any tip platforms). The tip vortices from the baseline cases greatly influence the core flow and reduce the mean kinetic energy when they are mixed with the wake fluid. The wake fluid and the tip leakage vortex is also modified and mixed by the serrated trailing edge geometry as shown in figure 5.2. This observation indicates that a significant momentum deficit in the core of the passage vortex exists because of the tip vortex and this momentum deficit becomes higher when the clearance increases. The direct impact of the baseline tip vortex is visible in the measured total velocity in the core of the passage, even under strong mixing conditions induced by the wake fluid originating from the serrated trailing edges.

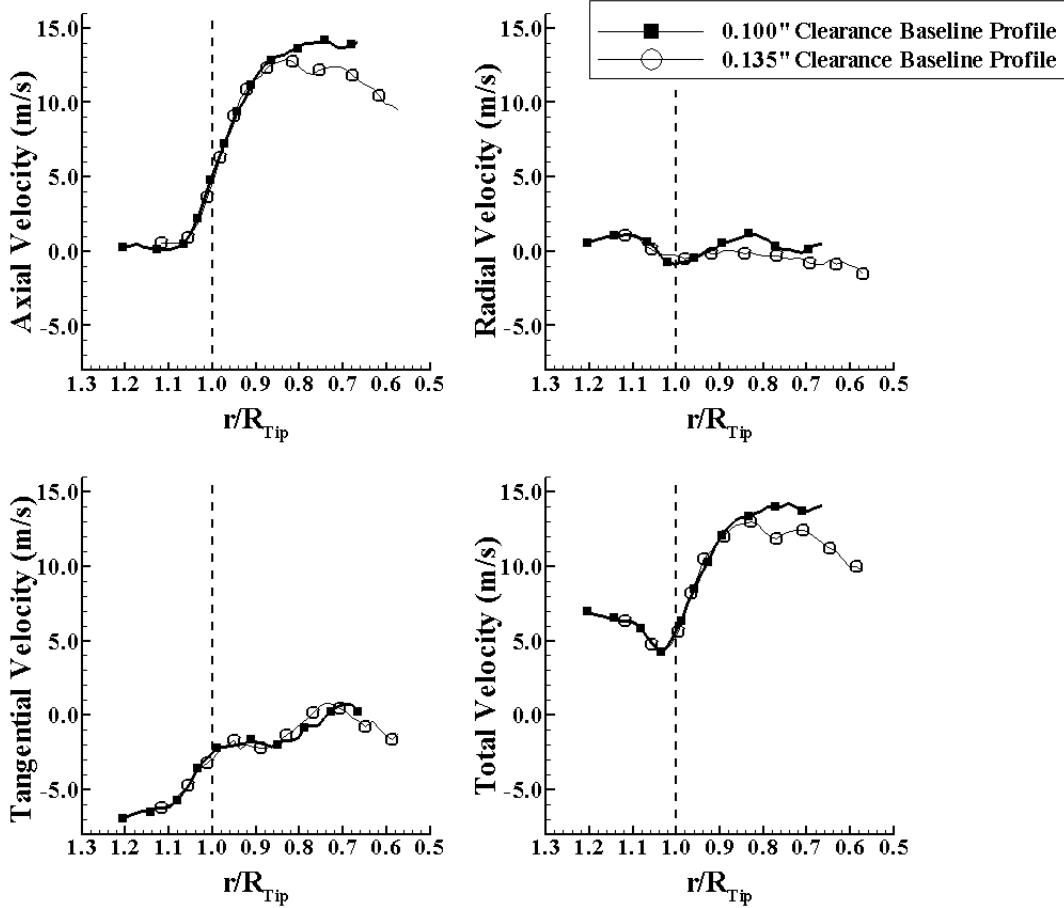


Figure 5.8. Velocity profiles measured at location 3 for two different tip clearances

The Radial Component: The radial components for all cases as shown in figures 5.8 - 5.12 are all very small magnitudes around ± 1 m/s. There is no significant influence of the magnitude of baseline clearance or the type of the tip treatment on the magnitude of the radial component at all spanwise locations.

Influence of Tip Platform Extensions on the Tangential Component: When the axial velocity component in figure 5.9 is compared to the total velocity, a striking observation in the tip region is apparent. The total velocity for the baseline tips are much higher than the axial component where $r/R_{Tip} \geq 1.05$. However, the total velocity distribution for baseline tips is about the same as the axial velocity component for five treated tips shown in figure 5.8. Since the radial components are extremely small for all tip shapes, one can infer that the significant

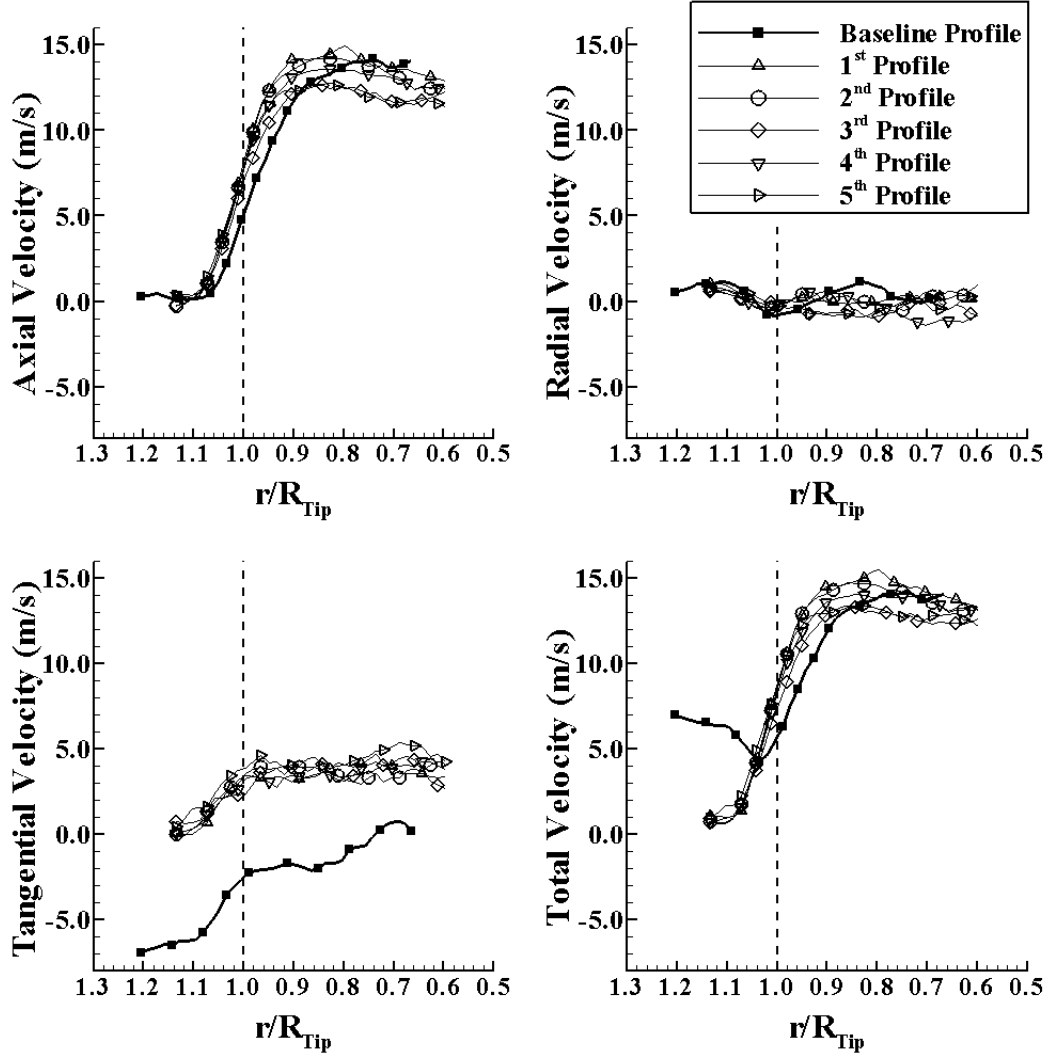


Figure 5.9. Velocity profiles measured at location 3 ($340\text{ m}^3/\text{min}$, 32 Pa)

difference between the baseline tips and the treated tips is due to a strong change in the tangential component of the velocity vector. The distribution of the tangential component shows a significant difference in the whole measurement region where $r/R_{Tip} \geq 0.6$.

One can conclude that there is a strong swirl component near the tip region when there is no tip treatment. The five treated tips defined in figure 5.7 provide significant reduction in the amount of swirl in rotor exit flow. The reduction in the amount of swirl near the tip region is about 4-5 m/s with the tip platform

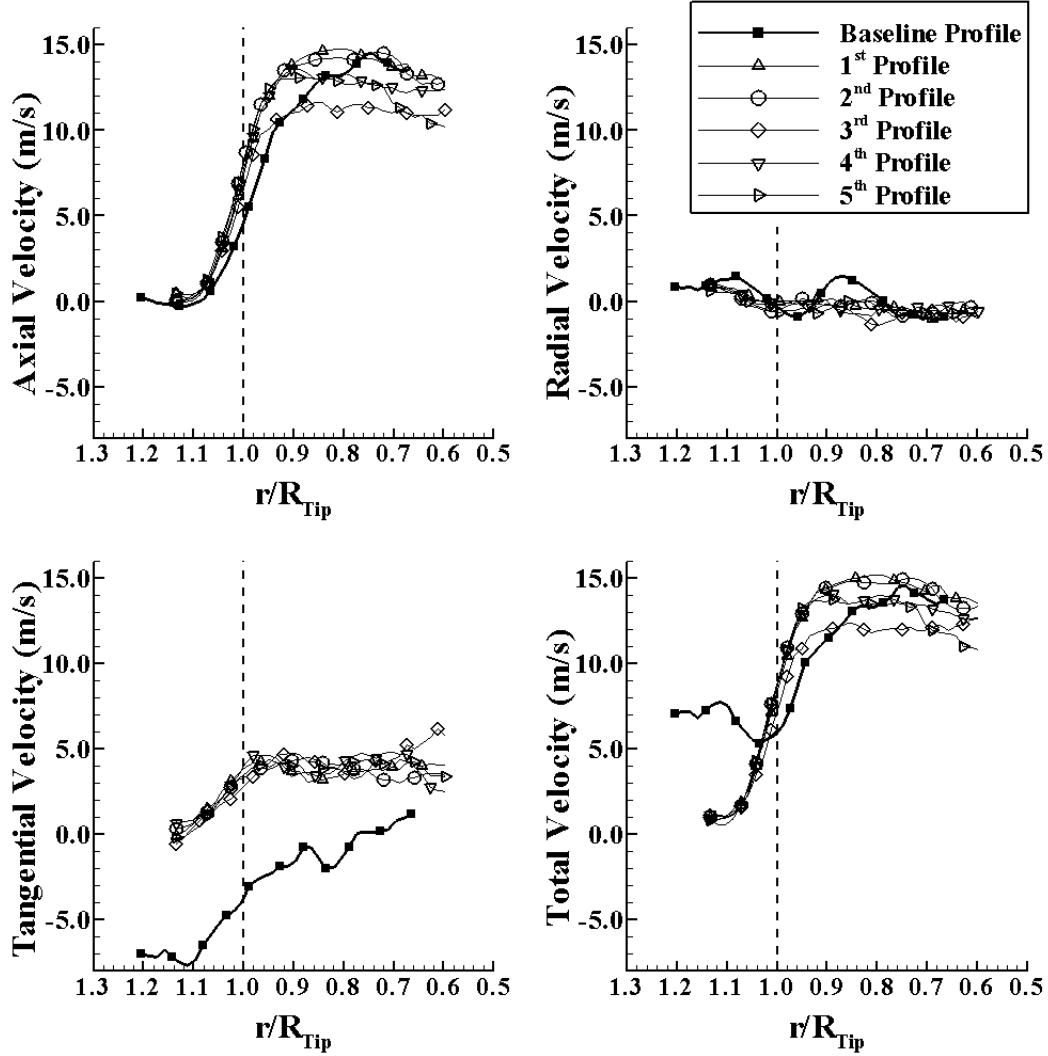


Figure 5.10. Velocity profiles measured at location 4 ($340 \text{ m}^3/\text{min}$, 32 Pa)

extensions shown in figure 5.7. The magnitude of the swirl component that is inherent to baseline tips is about one third of the total velocity existing in the core of passage.

Tip Platform Extensions with Highest Axial Velocity at Rotor Exit:

Figure 5.9 shows that the five new tip platform extension devices can be highly instrumental in reducing the amount of swirl coming out of the rotor. This feature is certainly a benefit in terms of the energy efficiency of the axial flow fan when the fan is operated on its high volumetric flow rate (low pressure rise) point. The tip

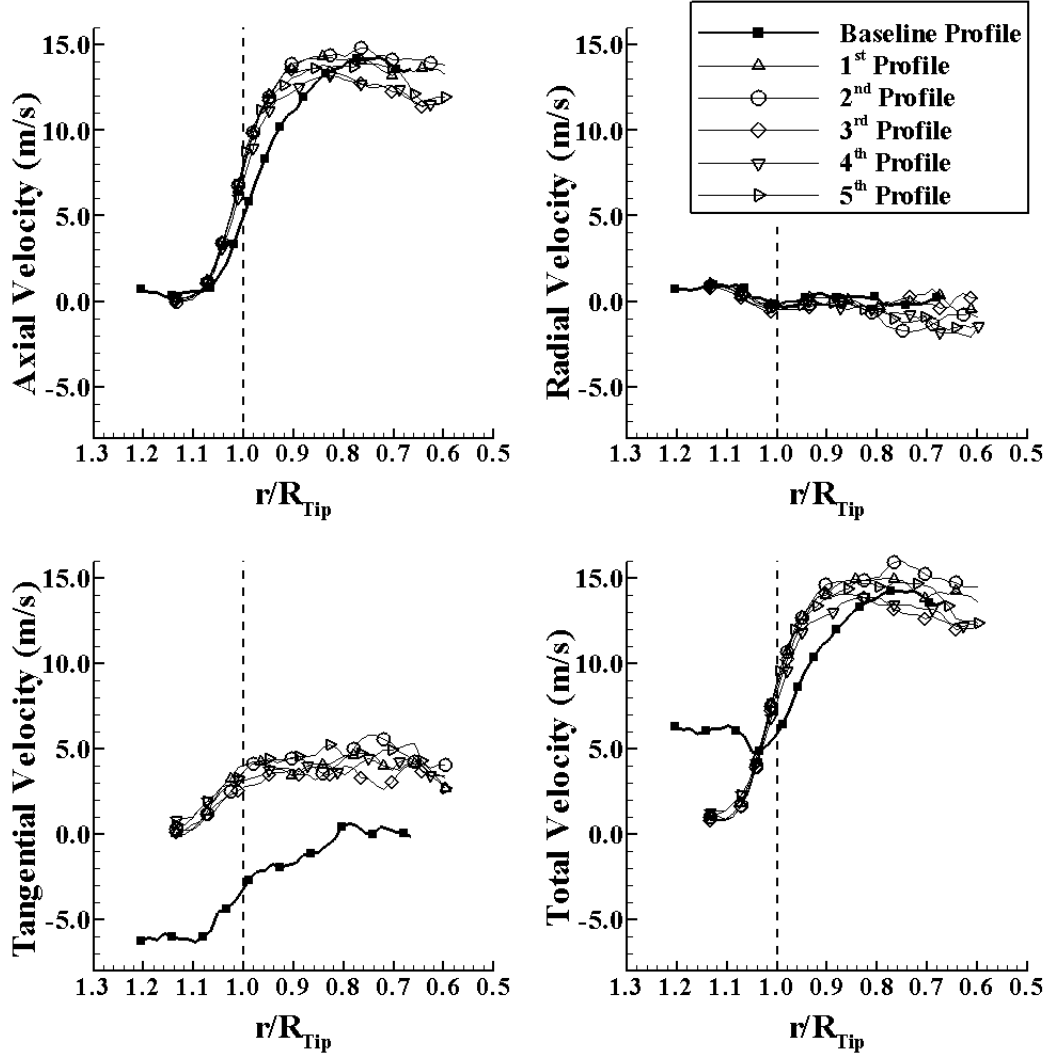


Figure 5.11. Velocity profiles measured at location 5 ($340 \text{ m}^3/\text{min}$, 32 Pa)

platform extensions help to reduce the tip leakage mass flow rate and its momentum deficit via local viscous flow modifications near the tip region. The Profile 1 and Profile 2 provide the two profiles with the highest total velocity in the core of the passage exit flow.

The Optimal Tip Platform Design: The experimental results suggest that “maximum width” of the bump is an important parameter in designing the tip de-sensitization geometry. The Profile 2 and 5 cover almost the same chordwise locations. The only difference between the two is the “maximum width” of the

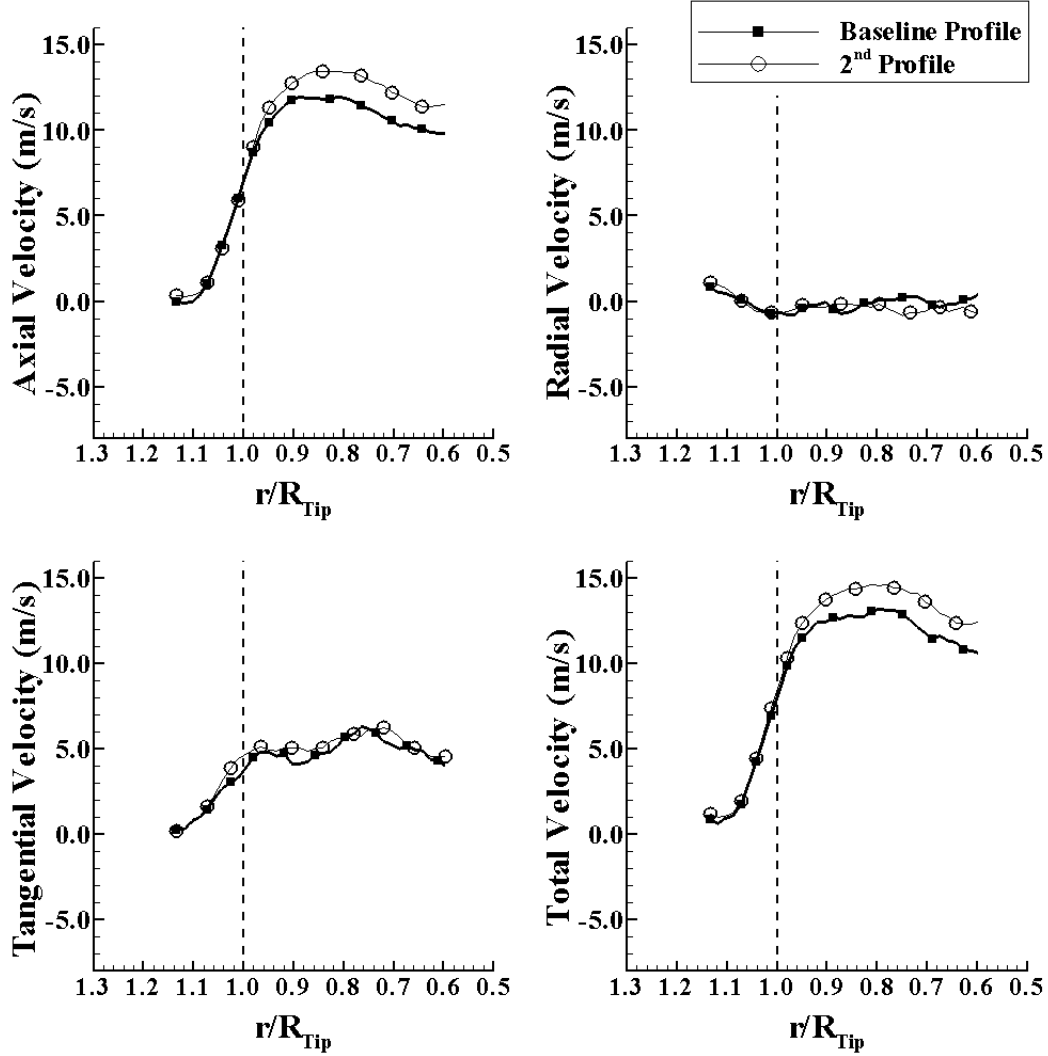


Figure 5.12. Velocity profiles measured at location 3 (high ΔP with 19.6% perforated plate, $80m^3/\text{min}$, 140 Pa)

bump. Figures 5.8, 5.9 and 5.10 clearly shows that the recovery of the axial velocity component and elimination of the tangential component is more effective with Profile 2 than with Profile 5. Figures 5.9, 5.10 and 5.11 show that the features observed in figure 5.9 for location 3 repeat for other angular positions of the rotor (location 4 and 5). Although there are slight flow field differences at different rotor positions, the general nature of the discussion does not change.

Fan Exit Flow at the Highest Pressure Rise: An interesting tip treatment

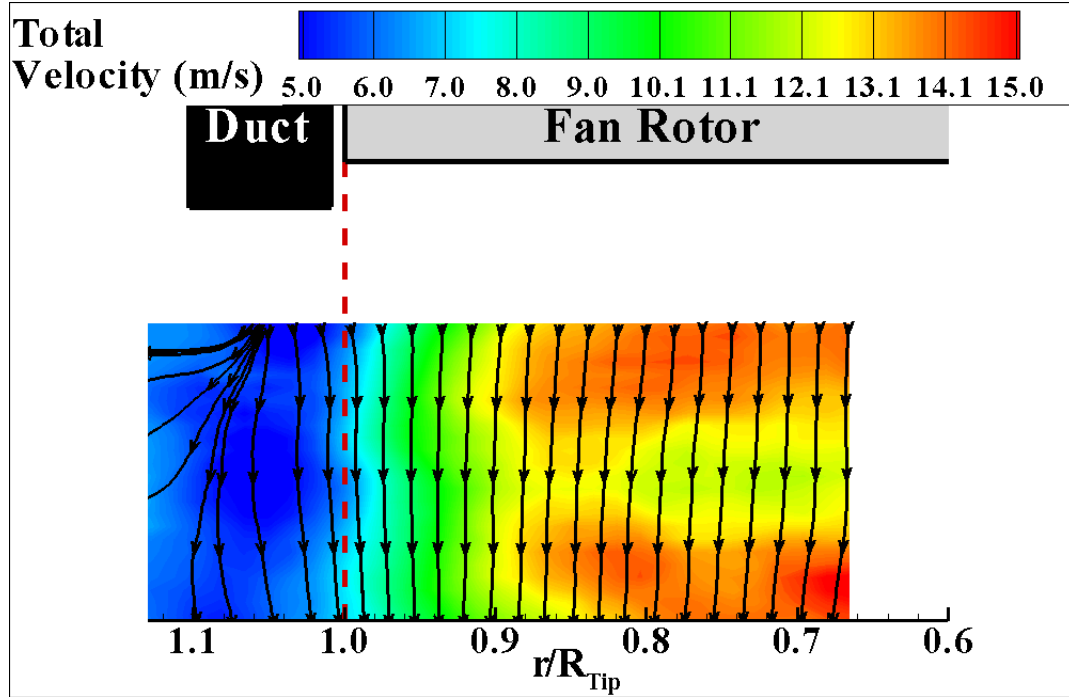


Figure 5.13. Total velocity contour and streamlines at location 3 for baseline profile (340 m^3/min , 32 Pa)

experiment could be performed by operating the fan at its highest pressure point by reducing the volumetric flow rate using a perforated steel plate at the mock-up inlet section as shown in figure 5.1. The experiments with the specific perforated plate with an open area ratio of 19.6% indicated that measurable gains in axial velocity component at the core of the exit flow still exist with Profile 2. Figure 5.12 shows that tangential and radial velocity components from Profile 2 are very similar to the baseline profile at the same effective clearance value of 0.100" (1%). However the elimination of the tangential component observed in high volumetric flow rate experiments does not occur under high pressure rise conditions (140 Pa) as shown in Figure 5.12. There is a consistent 2 m/s increase in axial (or total) velocity throughout the blade span when $r/R_{Tip} \geq 0.6$. Under high loading conditions the swirl component is minimal even with a baseline tip. The tip platform extensions for this case also perform their function by minimizing the tip leakage flow mass flow rate. The minimization of the tip leakage mass flow rate eventually provides the gain in axial (or total) velocity component. On the average, the gain in total velocity magnitude at the rotor exit is about 17% throughout the blade span. This

type of gain in mean kinetic energy of fan exit flow is expected to contribute to the energy efficiency of the fan.

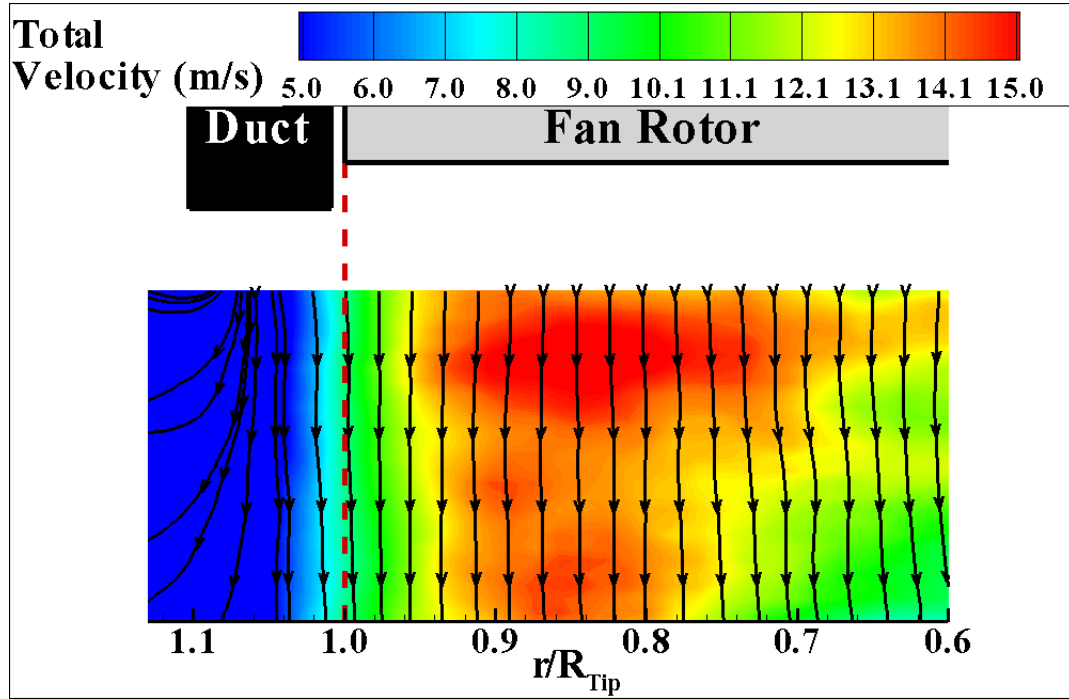


Figure 5.14. Total velocity contour and streamlines at location 3 for 2nd profile (340 m³/min, 32 Pa)

Rotor Exit Total Velocity Distributions: Figure 5.13 and 5.14 show total velocity contours drawn on axial and radial plane at the fan rotor exit for Baseline tip and Profile 2 respectively. Both contours are obtained from measurements performed at 0.1" tip clearance. Rotor tip ($r/R_{Tip} = 1.0$) is marked with the dashed red line. An enhancement of total velocity near the tip region is observed, when tip region total velocities are compared. It is also obvious that using Profile 2 enhances the area coverage of high momentum jet at the exit. That means rotor blade with tip platform Profile 2 is increasing kinetic energy of the fluid flow more efficiently. It also reduces momentum deficit near the tip due to tip leakage flow.

Influence of Tip Platform Extensions on the Flow Coefficient: Positive effect of the five new tip platform extensions on flow coefficient of the fan rotor is shown in Figure 5.15. Flow coefficient is plotted at 46 mm downstream of the fan.

For $r/R_{Tip} \geq 0.9$ (near the tip region), all the tip platform extensions increased flow coefficient. This increase is related to the increase in axial velocity near the tip region due to tip treatments. Measurable reduction in the tangential velocity component resulted in a measurable increase in the flow coefficient. Profile 1 and 2 are the two profiles with the highest flow coefficient in the core of the passage exit flow. Profile 3, 4 and 5 slightly increase the flow coefficient near the tip region, but they provide with lower flow coefficient in the core flow region. The lower flow coefficient in the core may be attributed to the specific location of the platform extensions. On the average, the gain in flow coefficient from profiles 1 & 2 at the rotor exit is about 18.6% throughout the blade span.

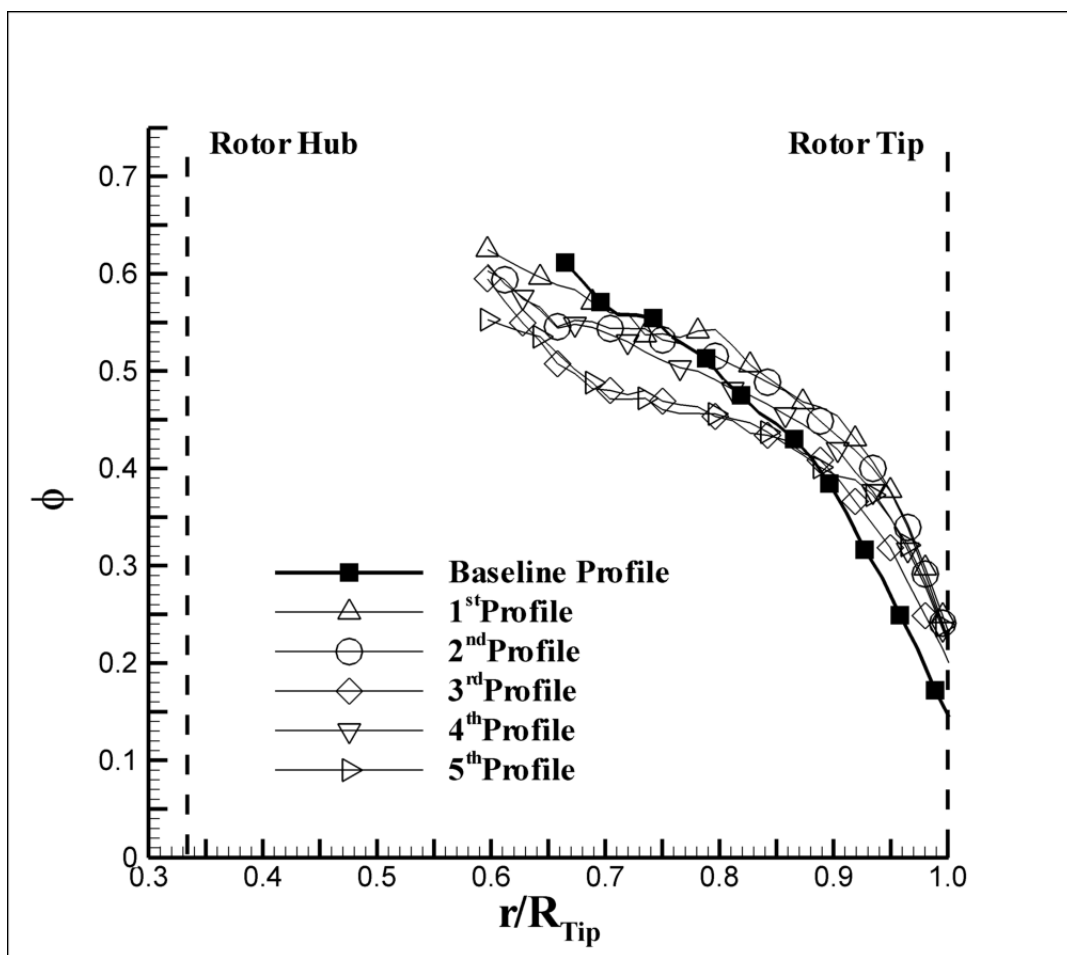


Figure 5.15. Flow coefficient calculated at location 3 ($340\text{ m}^3/\text{min}$, 32 Pa)

5.5 Summary

Novel tip platform extensions for energy efficiency gains and aeroacoustic improvements were designed for an axial flow fan where wake mixing is already enhanced with a serrated trailing edge design.

Five different tip platform extensions were introduced especially on the pressure side of the fan blades.

It is possible to reduce the tip leakage mass flow rate using the novel tip platform extensions. Profile 2 showed the best tip treatment performance out of the five new tip platform extensions designed in this investigation.

Tip treatment experiments performed at high volumetric flow rate/low pressure rise clearly showed the minimization of the tip vortex mass flow rate by significantly reducing the tangential components near the tip.

The tip platform extensions on the pressure side have proven to be effective swirl reducing devices at the exit of the fan. The magnitude of this reduction is about one third of the rotor exit total velocity in the core of the passage exit.

The reduction of tip leakage mass flow rate produced enhanced total velocity values between the mid-span and the tip at the passage exit.

Tip platform experiments performed at the highest pressure point by reducing the volumetric flow rate using a perforated steel plate at the mock-up inlet section also showed significant tip leakage control for the fan. However the elimination of the tangential component observed in high volumetric flow rate experiments does not occur under high pressure rise conditions.

Under high loading conditions the swirl component is minimal even with a baseline tip. With the tip platform extension “Profile 2”, there is a consistent 2 m/s increase in axial (or total) velocity throughout the blade span when $r/R_{Tip} \geq 0.6$.

Tip platform extensions perform their function by minimizing the tip leakage flow mass flow rate near the blade tip even under the high loading conditions. This effect eventually provides the gain in axial component.

The gain in total velocity magnitude at the rotor exit is about 17% throughout the blade span on the average. This type of gain in mean kinetic energy of fan exit flow is expected to contribute to the energy efficiency of the fan.

Development of a Realistic Ducted Fan Research Facility and Novel Tip Leakage Control Devices

This chapter describes a computational and an experimental study for improving aerodynamic performance of ducted fans by reducing fan rotor tip region related aerodynamic losses. Tip losses are reduced by designing novel tip treatment geometries. The novel geometries that are installed on the tip platform surfaces are the result of an aerodynamic design system driven by the solutions of three dimensional Reynolds-Averaged Navier-Stokes equations. Computational model used in this chapter uses a full rotor simulation in contrast to REBRM discussed in chapter 2. The current chapter makes uses of a comprehensive experimental effort for the validation of tip treatments developed computationally.

The second part of the present thesis is motivated by the need to develop an appropriate tip leakage control devices for realistic ducted fans used in vertical lift systems. A 22" diameter custom ducted fan test system is designed and manufactured. This chapter presents a set of comprehensive ducted fan aerodynamic measurements validating and supporting the computationally developed novel tip

treatments named full squealer tips and inclined squealer tips in hover condition.

6.1 22" Diameter Ducted Fan Test System

6.1.1 Facility Description

The 22" diameter ducted fan test system with a realistic disk loading character found in most present day VTOL UAV systems (up to $17.3 \text{ lb}/\text{ft}^2$). A schematic of the facility is shown in Figure 6.1. The main components in the flow path of this facility are listed below in order,

- Inlet lip section (replaceable)
- Eight-bladed axial fan
- 20 Hp DC brushless electric motor
- Diffuser section
- Six component force and torque measurement system

Figure 6.2 shows the main components of instrumentation integrated into this research facility. Test system is equipped with a radially traversing Kiel total pressure probe downstream of the axial flow fan rotor, a stationary total pressure probe at the inlet of the duct, an optical once per rev sensor, a pitot probe for velocity measurements at the duct inlet and an ATI six component force and torque measurement transducer. The system also has a number of thermocouples, a rotor once-per-rev device and many electrical monitoring systems for electrical safety.

6.1.2 Ducted Fan Model

The ducted fan used in experiments is composed of a shroud, axial flow fan, inlet lip and exit diffuser. The shroud is manufactured from PVC thermoplastic material and has an inner radius of 11.15 inches. It is connected to the main

support using four 0.5" diameter stainless steel threaded circular rods. Threaded rods connect shroud to the central support system. The center support holds the ducted fan so that the fan rotor is about three rotor diameters away from the ground which guarantees measurements are free of ground effect. The computational analysis performed in this chapter also shows that the ground effect is not affecting the current measurements as shown in Figure 6.20.

The 22" diameter ducted fan was designed to provide realistic disk loading typical to VTOL UAVs. Figure 6.4 shows power loading vs disk loading chart including two ducted fan systems used in this thesis. The 22" diameter ducted fan shown in Figure 6.1 provides $17.3 \text{ lb}/\text{ft}^2$ disk loading under nominal operating conditions (3500 rpm).

6.1.2.1 Inlet Lip and Diffuser

The geometry of the duct inlet lip shape can be described by two distinct characteristics: wall thickness (t_w) and leading edge radius of curvature (ρ_{LE}) as illustrated in figure 6.3a. Wall thickness is the maximum thickness of the airfoil shape used to make up the wall of the duct, and the leading edge radius of curvature describes the roundness of the duct lip. Figure 6.3a also shows the wall thickness and the leading edge radius of curvature used in this facility. The inlet lip shape was designed to have a relatively small leading edge radius. The reduced leading edge radius usually allows the adverse pressure gradient to change gradually inside lip. Changing pressure gradient gradually helps reducing inlet lip separations inside the duct lip especially under forward flight conditions. The Lip section is manufactured from ABS thermoplastic material. The diffuser section was designed to augment the thrust generated by the ducted fan. Figure 6.3b shows cross section view of the diffuser. Diffusion angle at the exit is six degrees. The axial length of the diffuser is about 117.85mm (4.64").

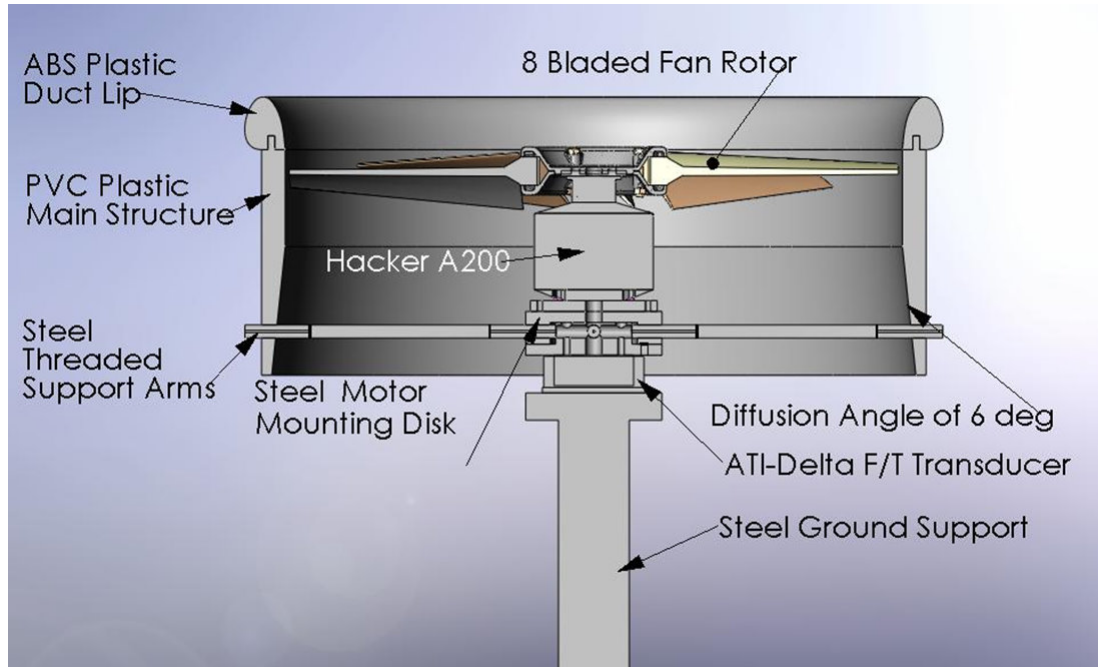


Figure 6.1. Schematic of the 22" diam. ducted fan test system

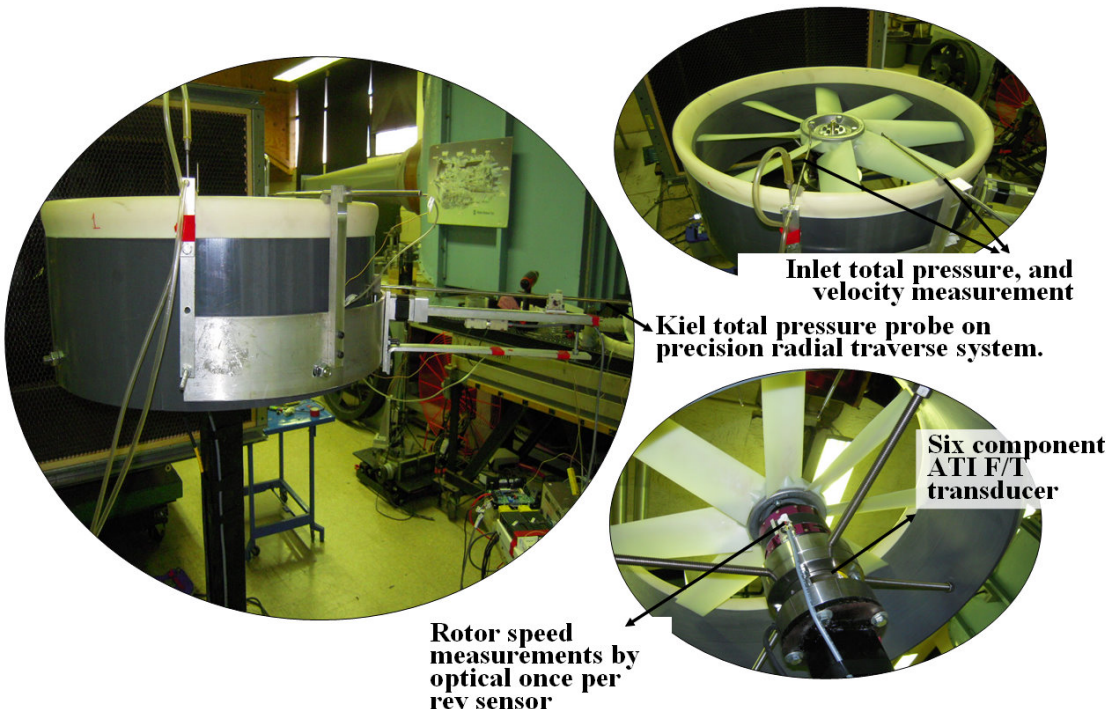


Figure 6.2. Instrumentation of the 22" diam. ducted fan system

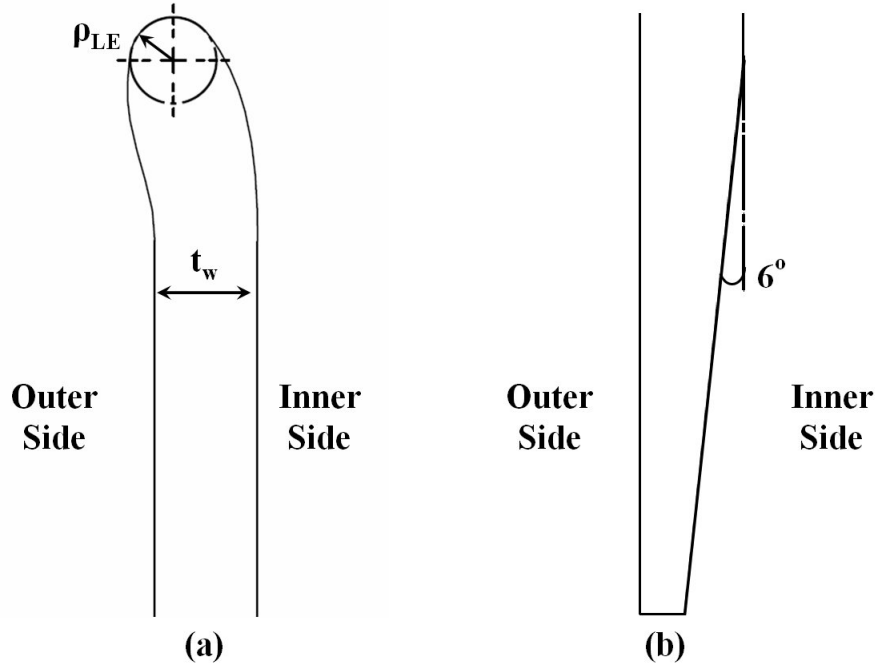


Figure 6.3. Cross section view of inlet lip(a) and diffuser(b)

6.1.2.2 Fan Rotor

The eight-bladed fan rotor was designed and manufactured by Multi-Wing International. The fan blades were designed for high flow coefficient. The rotor blades were manufactured from a high quality thermoplastic (Glass Reinforced Polyamide) with glass beads embedded during the forming process. Figure 6.5 shows blade profiles at various radial stations. Table 6.1 presents fan rotor and blade section geometrical properties.

A 20 Hp A200-6 brushless electric motor (Hacker) used to directly drive axial flow fan in the 22" diameter ducted fan research facility. The electric motor has 20 poles and is designed to provide high torque with its out runner configuration. Higher torque capability of this motor enables driving fan rotor without a gear box. The electric motor develops 110 rpm for every one volt of driving potential. The electric motor was controlled by an electronic speed controller (MasterSPIN-220-OPTO ESC). Electrical power for the motor was supplied by 4 deep cycle batteries connected in series. Due to high torque characteristic of the electric motor, the

electric current and temperature of the motor was monitored for operational safety. For current monitoring a current shunt meter is serially connected to the system. The motor temperature was monitored by using a K-type thermocouple at the stationary part of the motor. The motor allows a maximum operating temperature of 65.5 °C. The maximum current allowable into ESC is about 220 Amps at 48V.

Figure 6.5 shows the tip section of the blade. Overall geometric and blade section characteristics of fan rotor are also shown in Table 6.1. Fan rotor blades are manufactured from Glass Reinforced Polyamide (PAG). This thermoplastic material provides high tensile and impact strength. Rotor blades are attached to a custom designed aluminum hub. This specific hub system allows a quick replacement of the rotor assembly in this research facility.

Rotor hub radius	2.5 in (63.5 mm) ($r/R_{tip} = 0.227$)			
Rotor tip radius	11.0 in (279.4 mm) ($r/R_{tip} = 1.000$) for 1.71% tip clearance			
Rotor pitch angle	55°			
Number of blades	8			
Max thickness at rotor tip	0.216 in (5.15 mm)			
Blade section properties				
radius (in)	r/R_{tip}	β_1	β_2	chord (in)
3.00	0.27	71.87	40.77	3.32
4.00	0.36	72.81	43.50	3.21
5.00	0.45	76.56	46.30	3.10
6.00	0.55	78.37	49.94	2.99
7.00	0.64	79.52	52.13	2.88
8.00	0.73	80.31	53.64	2.78
9.00	0.82	82.87	56.51	2.68
10.00	0.91	84.00	58.39	2.59
11.00	1.00	85.21	60.92	2.51

Table 6.1. Fan rotor geometric and blade section properties

The current study concentrates on the rotor tip section aerodynamic performance with various clearances and tip shapes. Therefore the tip clearance of the rotor blade is precisely controlled. Tip clearance is the distance measured from the tip of the rotor blade to the shroud. The non-dimensional tip clearance is obtained by dividing tip clearance to the blade height which is the distance between the rotor hub and tip. The tip clearance values in this study are adjusted by using fan rotors of varying rotor diameters by keeping the shroud inner diameter constant at d=11.15" (283.21 mm). The tip clearances tested in this study are tabulated in

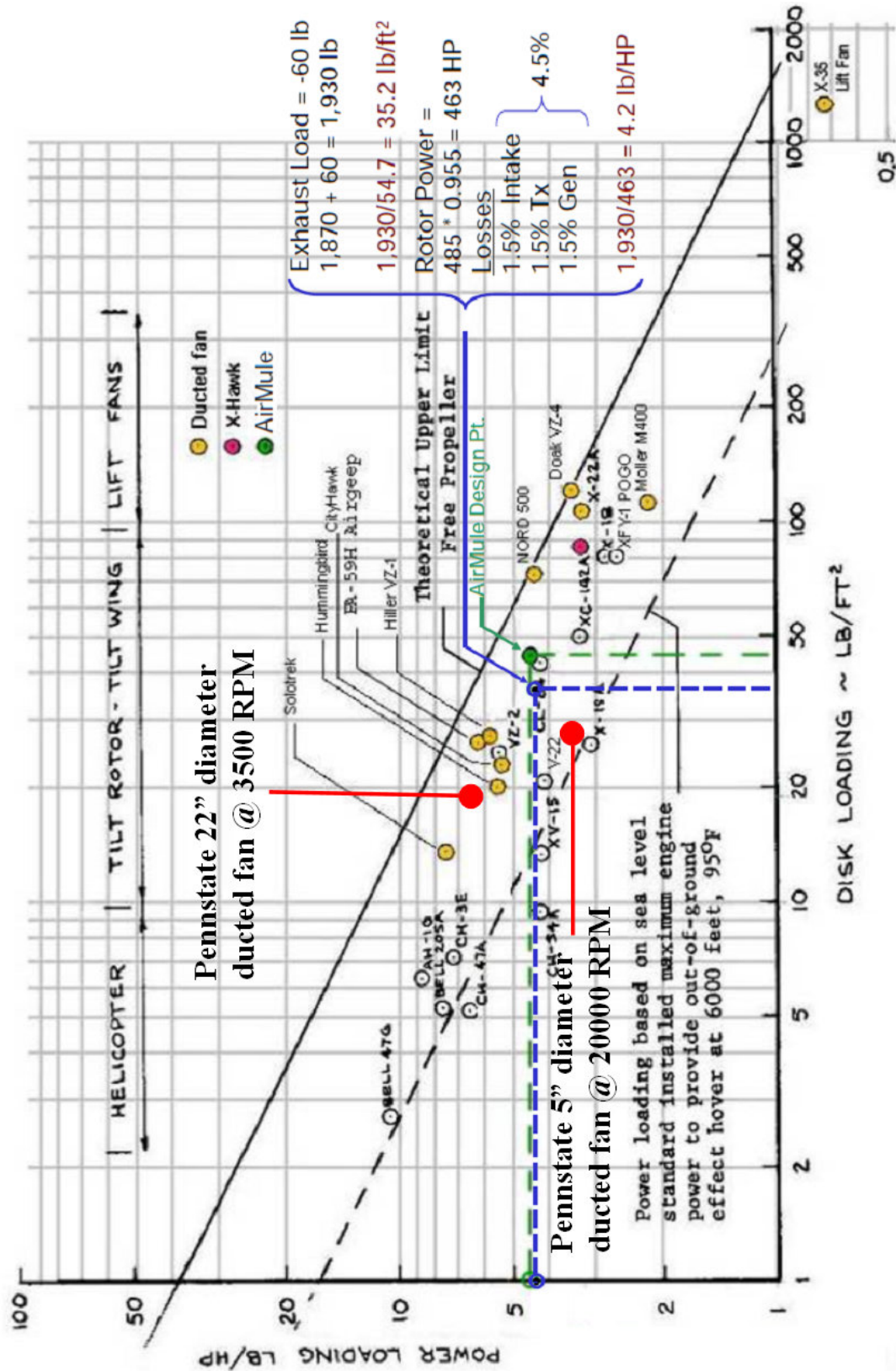


Figure 6.4. Rotor power loading vs disk loading chart [91]

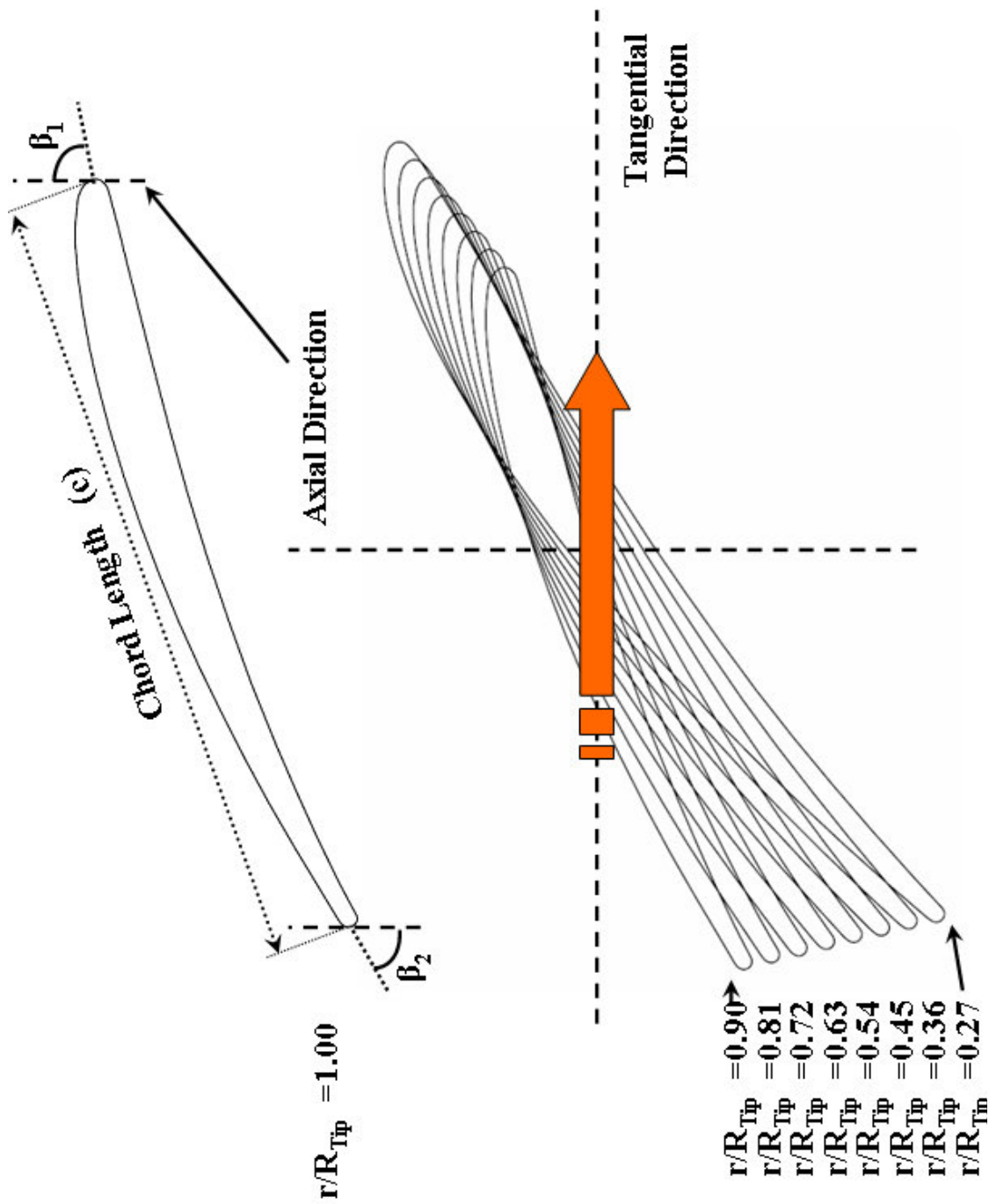


Figure 6.5. Cross section view of inlet lip(a) and diffuser(b)

table 6.2. Figure 6.6 shows the tip clearance measurements performed at various circumferential locations of the ducted fan. The clearances and corresponding rotor diameters are tabulated in table 6.2. Figure 6.6 presents the circumferential variation of the tip clearance due to slight changes in shroud inner diameter. The clearance values were always measured at the mid-chord location of one selected blade. 0° circumferential position is the location where fan rotor exit total pressure results were obtained. This location also marks the leading edge of the ducted fan. This location is also highlighted with a red box in Figure 6.6. Distribution of tip clearance around the total pressure measurement point is well controlled (from -60° to 120°) as shown in Figure 6.6.

Rotor radius (in)	Blade height (in)	Tip gap height (in)	Tip clearance (%)
11.00	8.50	0.15	1.71
10.89	8.39	0.251	3.04
10.57	8.07	0.57	7.13

Table 6.2. Penn State 22" fan rotor tip clearance measurements.

6.1.3 Instrumentation of the 22" Ducted Fan

6.1.3.1 Rotor Exit Total Pressure Measurements

Fan rotor exit total pressure measurements were performed by using a Kiel total pressure probe. The Kiel total pressure probe having a 5 mm diameter total head was traversed in radial direction using a precision linear traverse mechanism. The total pressure probe was always located 45.72 mm downstream of the fan rotor exit plane at 50% of blade span (mid-span). The Kiel probe was aligned with absolute rotor exit velocity at mid span position.

Kiel probe is relatively insensitive to incoming angle of the flow (yaw angle). The range of insensitivity to misalignment for this probe is $\pm 52^\circ$ to see a more than 1 % deviation from the inlet dynamic head [85]. The accurate orientation of the Kiel probe in a problem where yaw angle varies dramatically near the tip section of the blade is extremely challenging. A computational fluid dynamics approach

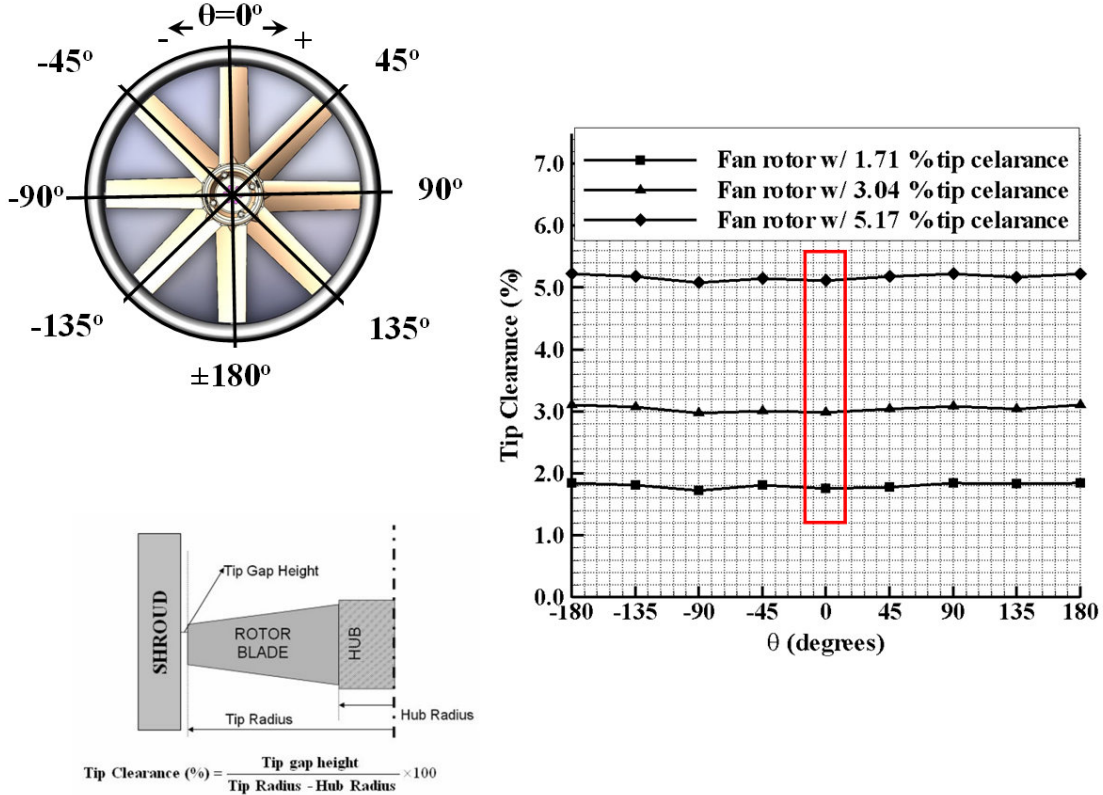


Figure 6.6. Circumferential distribution of tip clearance in the ducted fan

was used to properly align the probe with respect to axial direction. Preliminary computations of rotor exit flow field was performed using ANSYS CFX RANS solver. Details of this computational analysis can be found in section 4.3. Figure 6.7 shows computed distribution of absolute flow yaw angle at the fan rotor exit where Kiel probe was located. It can be concluded from the Figure 6.7 that the absolute yaw angle is not changing significantly near the mid-span for radial stations $0.38 \leq r/R_{tip} \leq 0.90$. The average yaw angle obtained on these stations is 18° which is shown by blue straight line in Figure 6.7. The kiel probe was aligned with this average at these locations. Although flow angles varied by the effect of the three dimensional features such as passage vortex and hub separation near the hub region, the Kiel probe was assumed to capture flow field because of its $\pm 52^\circ$ yaw angle tolerance. Because the tip region, where $r/R_{tip} \geq 0.90$, was affected by the tip leakage vortex, tangential velocity component changed due to this vortical field and yaw angle increased abruptly in this region. The Kiel probe was manually

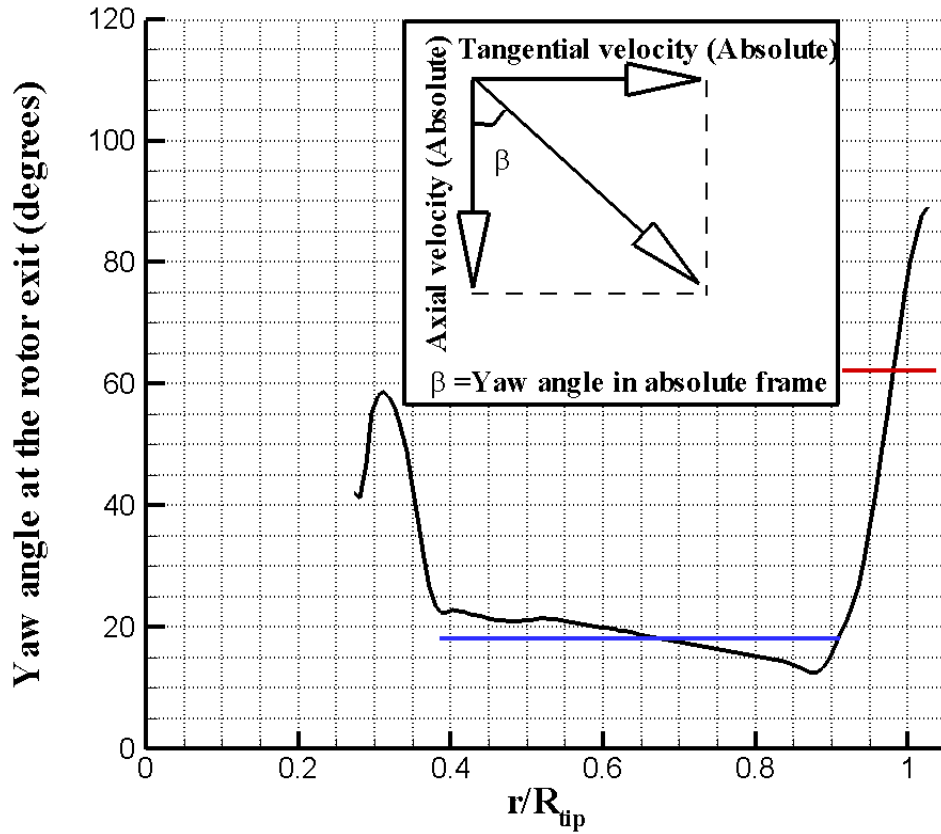


Figure 6.7. Yaw angle in absolute frame calculated from initial computations

aligned by the “*averaged*” computed absolute flow yaw angles on this region. The probe was aligned with 62° angle around the tip region.

The Kiel total pressure head was connected to a Validyne DP 15 pressure transducer that was referenced to atmospheric pressure with a $\frac{1}{8}$ ” tubing that was 2ft long. The output of the transducer directly connected to Validyne CD 15 carrier demodulator that gives a linearized analog output in the range of $\pm 10V$. The calibration of the pressure transducer required applying a known pressure to the transducer and recording the associated voltage. The relationship between the pressure and voltage was linear because an external Validyne linearization was employed. The Validyne carrier demodulator was connected to a 12bit data ac-

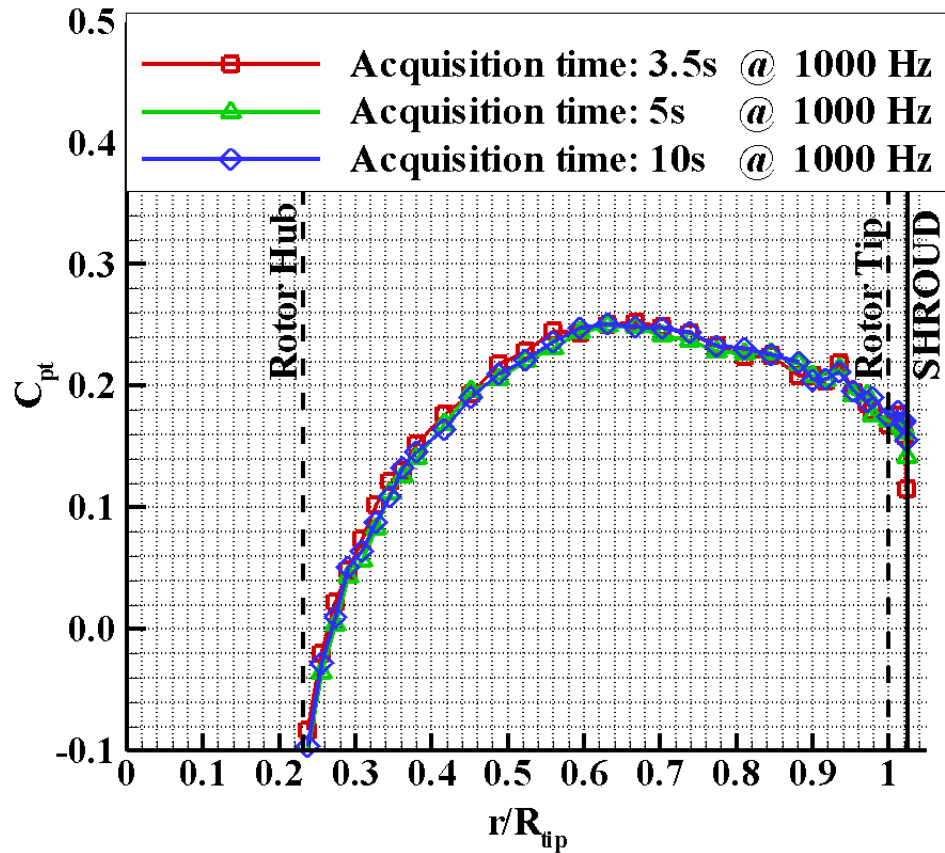


Figure 6.8. Influence of acquisition time in ensemble averaging

quisition board (MCC 1208FS). Analog signals were transferred to computer and analyzed by Labview data acquisition software, custom developed for the current research effort.

The data acquisition sampling time of the system used in this project was selected from preliminary total pressure measurements performed at various time settings. The acquisition times 3.5 seconds, 5 seconds and 10 seconds were tested using data acquisition rate of 1000 samples/sec. Figure 6.8 shows the preliminary total pressure measurement at these acquisition times. The results of 5 and 10 seconds acquisition times are very close. The 5 second acquisition time was selected as sampling time for experiments so the Kiel probe pneumatic output reached an

equilibrium and a statistically stable averaged total pressure reading was recorded.

The Kiel probe at the rotor exit was mounted on a radial traverser system that is controlled by a stepper electric motor using a Labview driven controller. Using this radial traverser, total pressure measurements were performed at 33 radial stations. Radial stations used in the measurements are also indicated in Figure 6.8.

The inlet conditions for ducted fan system was also monitored using a Kiel total pressure probe and a conventional pitot probe. Both probes were mounted on the duct lip at mid-span of fan rotor. The conventional Pitot probe with a static and total hole measured the magnitude of the inlet axial velocity at mid-span. Total pressure at duct inlet was measured using the same procedure outlined for the rotor exit total pressure probe without “nulling”. Data acquisition time for this probe was also set to 5 seconds. Pitot probe was used to obtain duct inlet velocity. Both probes were aligned with the axial flow direction, since the flow at the inlet of the ducted fan where flow was free of tangential and radial components.

6.1.3.2 Six Component Force and Moment Measurement

Ducted fan aerodynamic research performed in this study requires high accuracy force and moment measurements. The 22” diameter fan is equipped with ATI-Delta six component force and torque transducer which is shown in Figure 6.2. The ATI Multi-Axis Force/Torque Sensor system measures all six components of the force and moment. Three components of force and three components of moments are measured. It consists of a transducer, a shielded high-flex cable, and 16-bit data acquisition system and a F/T controller. A software system provided by ATI was used to convert the transducer readings into force and torque output in engineering units using the calibration data provided. The thrust and moment transducer is factory calibrated with known forces and moments. Calibration and accuracy report of the transducer is provided in the Appendix C. The accuracy of the transducer was $\pm 0.033\text{N}$ for forces in x direction, $\pm 0.033\text{N}$ for forces in y direction, $\pm 0.099\text{N}$ for forces in z direction, $\pm 0.003\text{N.m}$ for moments in x direction, $\pm 0.003\text{N.m}$ for moments in y direction and $\pm 0.003\text{N.m}$ for moments in z direction.

in z direction. The coordinate system for the force and torque measurements are shown in Figure 6.9.

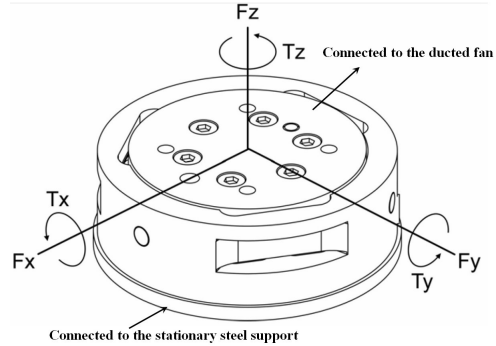


Figure 6.9. Applied force and torque vector on transducer [92]

6.1.3.3 Fan Rotor Rotational Speed Measurement

Rotational speed of the fan rotor was measured by using an optical sensor located near the electric motor as shown in Figure 6.2. This optical sensor uses a Hamamatsu p5587 photoreflector IC. The photoreflector IC consists of a high power LED and photodiode. A piece of aluminum tape was attached to the electric motor as a highly reflective surface. Once this reflective surface was sensed by the photodiode, a digital TTL signal was obtained once per revolution. Frequency of this digital TTL signal was measured by a Fluke 45 dual multimeter. Accuracy of the rotational speed measurement was ± 10 rpm.

6.2 Baseline Aerodynamic Measurements

This section describes baseline aerodynamic measurements that were performed in the 22" dia. ducted fan at hover condition. Hover condition aeromechanic performance was monitored by thrust and torque measurements. Aerodynamic performance quantification was performed by fan rotor inlet/exit total pressure.

6.2.1 Force and Torque Measurements

In the hover condition, the most significant force and moment component that is measured for the ducted fan system is thrust and rotor torque which are F_z and T_z as shown in figure 6.2 . Other components may become significant, when the ducted fan is operated in non-symmetric inlet conditions such as forward flight operation. Although three component of forces and three component of moments were measured, only the thrust and torque of the ducted fan will be presented throughout this chapter since all of the measurements are performed in hover condition. The thrust and torque measurements were obtained at hover condition for a number of rotor speeds. Thrust measurements are normalized as thrust coefficient, defined as;

$$C_T = \frac{Thrust}{\rho \Omega^2 D^4} \quad \text{where} \quad \rho = \frac{P_a}{\Re T_a} \quad (6.1)$$

Torque measurements were essential in calculating required power using the relationship between torque and power ($Power = Torque \times \Omega$). The measured power was normalized as a power coefficient.

$$C_P = \frac{Power}{\rho \Omega^3 D^5} \quad \text{where} \quad \rho = \frac{P_a}{\Re T_a} \quad (6.2)$$

The figure of merit was calculated as a measure of hover efficiency for the ducted fan. The figure of merit was defined as;

$$\text{Figure of Merit (FM)} = \frac{C_T^{3/2}}{\sqrt{2} C_P} \quad (6.3)$$

Figure 6.10 shows calculated thrust coefficient for the 22" ducted fan with baseline fan rotors at various rotational speeds. The ducted fan thrust was measured for various tip clearances. The fan rotor only thrust was also measured. The fan rotor only thrust was measured by using 10.89" tip diameter fan rotor which is the identical rotor used for 3.04 % tip clearance study. The tip clearances were adjusted by changing the fan rotor diameter as mentioned previously.

The variable tip clearance study presented in this chapter used custom made

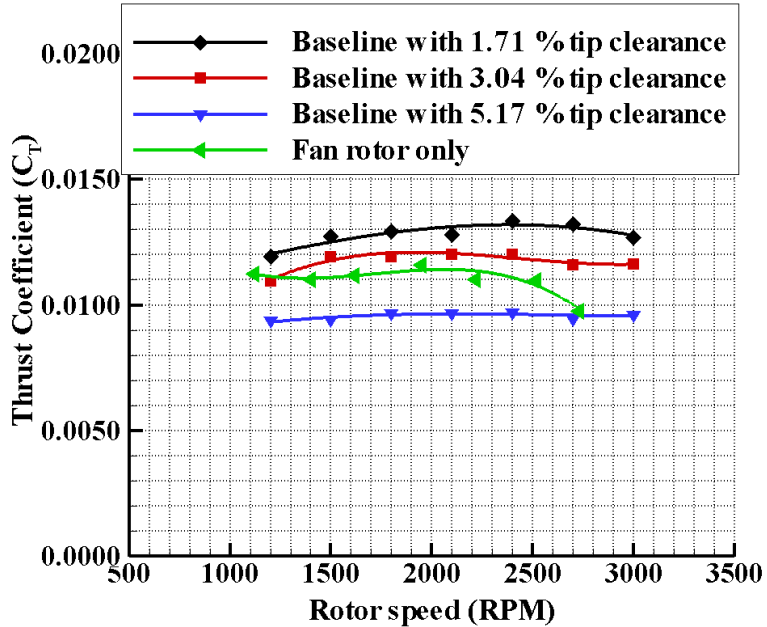


Figure 6.10. Thrust coefficient versus fan rotational speed during hover (baseline rotor)

rotors with accurately adjusted tip diameters in a shroud system having a constant inner diameter. Using a ducted fan around an open rotor improves the thrust of the system as compared to an open rotor for tip clearances of 3.04 % and 1.71 %. For the tip clearance of 5.17 %, the open rotor provides more thrust. This observation can be explained by the effect of increased viscous losses and tip leakage related losses. The losses generated when the shroud is added to the fan rotor is so high that the additional thrust due to duct lip and shroud is almost eliminated. It should also be noted that decreasing the tip gap height is effective at improving performance of the system and results in augmented thrust generation.

The thrust force generated per supplied power for various baseline configurations is shown in figure 6.11. The data is arranged in the form of thrust coefficient C_T versus power coefficient C_P . The smallest tip clearance configuration generates the highest thrust per unit of power supplied. Since increasing tip clearance is also increases losses in the system, power demand of the system also increases.

Figure 6.12 shows another key result of this study. The sensitivity of hover efficiency to increasing tip gap is shown. It should be noted that using a ducted fan configuration also improved hover efficiency by 38 % for the higher rotational speed. Decreasing tip clearance is effective in increasing the hover efficiency. Decreasing tip clearance from 3.04 % to 1.71 % increased hover efficiency of the system by 17.85 % at the higher rotor speed.

6.2.2 Total Pressure Measurements at Rotor Exit

The Aerodynamic performance of the ducted fan was quantified by rotor exit total pressure measurements at hover condition for 2400 rpm. The results are presented with non-dimensional total pressure coefficient which is defined as;

$$C_{pt} = \frac{P_{te} - P_{ti}}{\frac{1}{2}\rho U_m^2} \text{ where } \rho = \frac{P_a}{RT_a} \quad (6.4)$$

where U_m is the rotor speed calculated at the mid-span, $U_m = r_m \times \Omega$. Random uncertainty of total pressure coefficient was calculated as ± 0.002 . Details of the uncertainty estimate can be found in Appendix B.

Figure 6.13 shows the total pressure coefficient measured a downstream position from rotor hub to shroud. It should be noted that there is almost no change in total pressure coefficient by changing the tip clearance for $r/R_{tip} \leq 0.65$. Flow near the rotor hub is not affected by the tip leakage losses. When the tip clearance is 5.17 %, the losses related to the tip leakage vortex are increased at a significant rate, because of the increased tip vortex size.

The total pressure ratio (P_{te}/P_{ti}) of the fan rotor is calculated at 75 % of the blade span ($r/R_{tip}=0.82$) for three tip clearances. Results are plotted in figure 6.14 indicating how tip clearance is locally affecting the fan rotor. When results of changing tip clearance from 1.71 % to 3.04 % and from 3.04 to % 5.17 % are compared, it can be concluded that unsteady effects and viscous loss generation is increased visibly when clearance is increased to 5.17 %.

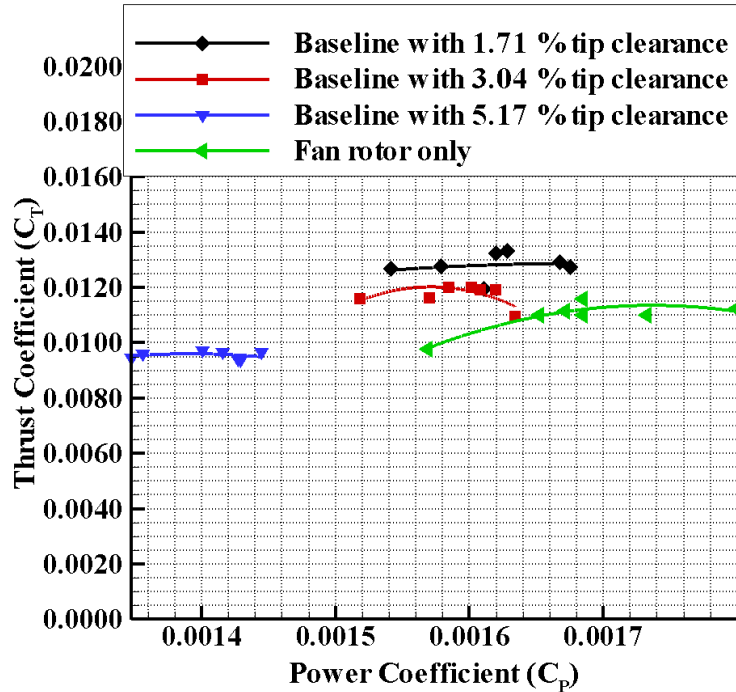


Figure 6.11. Thrust coefficient vs power coefficient for the baseline rotor

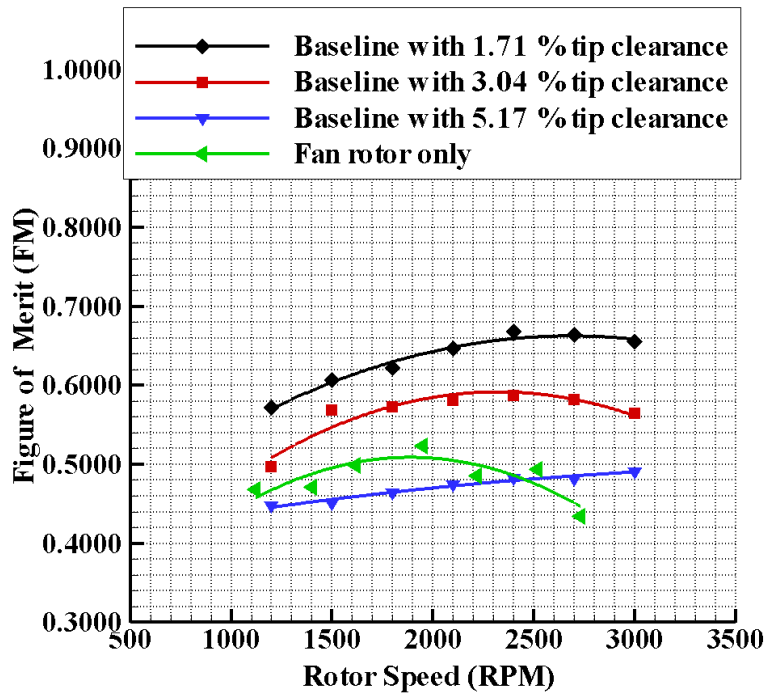


Figure 6.12. Figure of Merit (FM) vs fan rotational speed for the baseline rotor

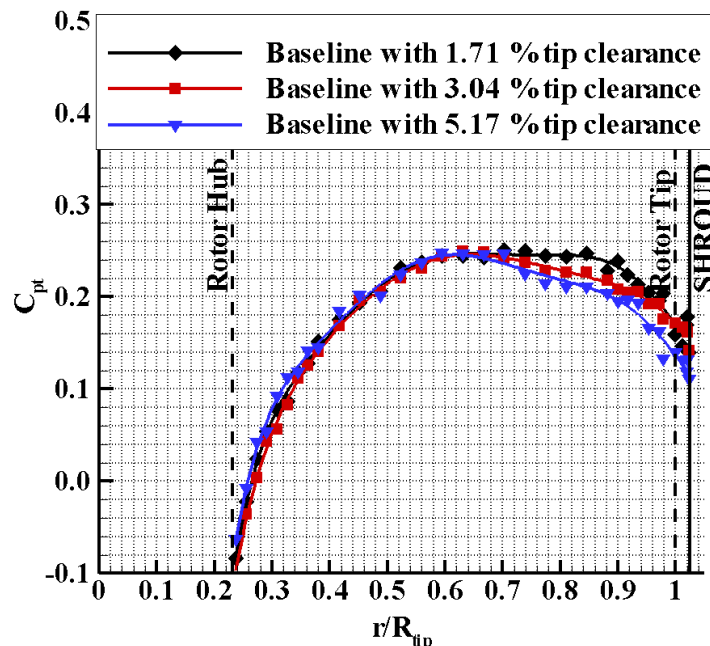


Figure 6.13. Total pressure measured at downstream of the rotor at 2400 rpm

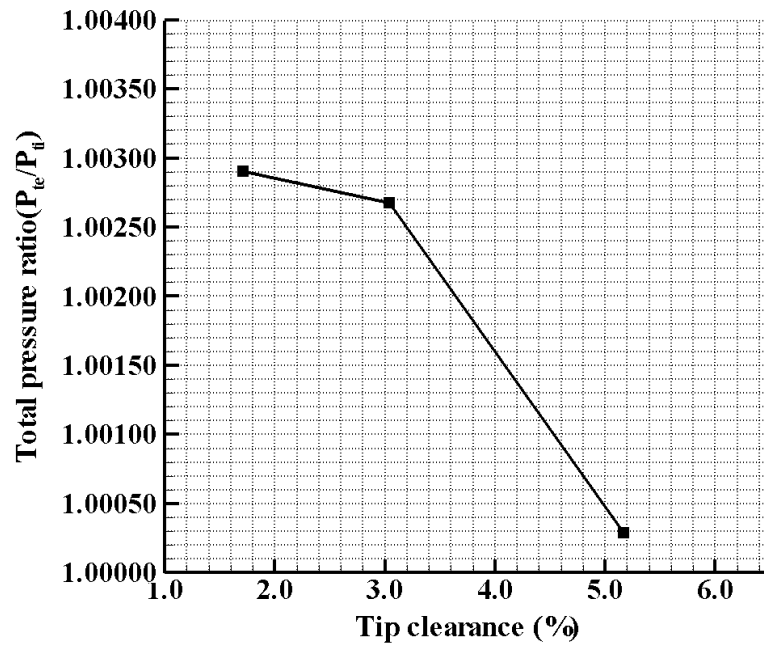


Figure 6.14. Total pressure ratio for three tip clearances at 2400 rpm

6.3 Design of Novel Tip Treatments for Effective Leakage Control

Tip clearance is an important operational parameter affecting the aerodynamic performance of a ducted fan both in hover and forward flight conditions. It is not possible to use tight tip clearance because of structural limits. Although a tip clearance level of 0.6 % of the blade height is possible in present day axial flow compressors and turbines, VTOL UAV systems are typically manufactured with relatively large clearance values ranging from 1.5% to 6%. Because of the vibrations originating from the engine driving fan blade, fan blade tips can easily rub against the stationary shroud during the tight clearance operations. Therefore, using large tip clearances are not uncommon especially in ducted fans used for vertical flying UAVs. The use of IC engines impose higher level of component displacements leading to larger tip clearances.

By changing rotor tip geometries, unfavorable aerodynamic effect of large tip

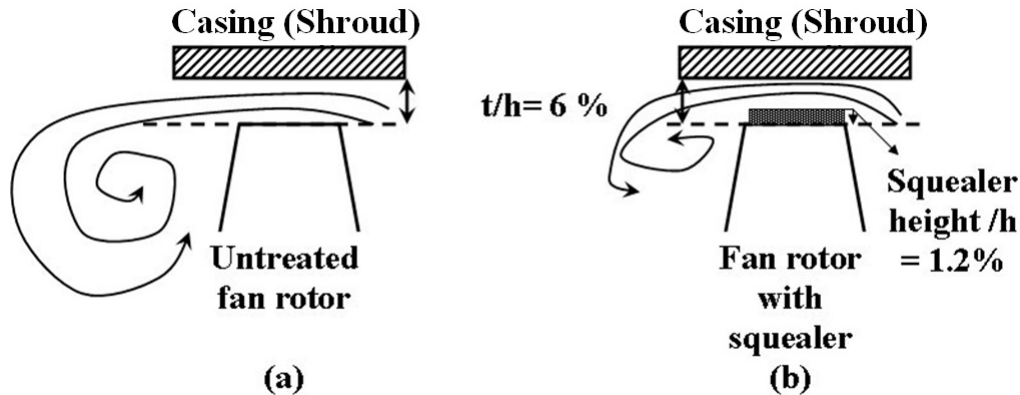


Figure 6.15. Baseline tip (a) and squealer tip (b) sketch

clearance can be somewhat avoided. This section describes the results of an effort for the design of novel rotor blade tips allowing a more reliable, safer and more fuel efficient ducted fan rotors. The main goal is to design novel squealer tip shapes and tip platform extensions in order to reduce tip leakage mass flow rate in clearances typical to present day VTOL UAV fans.

The squealer tips were originally developed and used in axial flow turbomachinery systems mainly to protect rotor tip sections during rub incidences. The

squealer tip geometries were much thinner than the main airfoil profile of the rotor blade. The squealer tips were truncated partially and fully during a rubbing incident between the rotor tip and shroud. In recent years, aerodynamic researchers realized that there are also significant aerodynamic benefits of using them in tip leakage mitigation. For example an untreated axial flow fan rotor having an original tip clearance gap of 6% can be treated with a squealer type tip treatment having a squealer height of 1.2 % of the blade height, as shown in Figure 6.15. Although a relatively small squealer tip part is added to the baseline design(6.15a) , the new design shown in Figure 6.15b will reduce the tip leakage mass flow rate. It is possible to design a novel squealer tip such that the final tip leakage mass flow rate can be reduced significantly to that of a blade having an untreated clearance of only 3 % blade height. The current chapter use a computational approach to design the novel squealer tip before a final set of qualifying experiments.

6.3.1 Computational Method

Three dimensional computational methods can be used for analyzing viscous and turbulent flow field around and inside the ducted fan for hover conditions and in forward flight regime. A computational method can be used to analyze complicated flow field near the fan rotor tip region flow and design various novel tip treatments for improving aerodynamic and aerothermodynamic performance of the ducted fan. Details of the computational method can be found in section 4.3. The computational effort presented in this part is for the design and improvement of novel tip treatments applied to VTOL UAV fans.

6.3.1.1 Computational Domains and Boundary Conditions

The computational analysis for the tip treatment development was performed on three separate computational domains, that are connected. The stationary inlet and outlet regions and rotating fan rotor region are shown in Figure 6.16. Inlet region includes an inlet lip surface that was considered as a solid wall with no-slip condition. Atmospheric static pressure was prescribed on the top surface. On

the side surface, an opening type boundary condition was assumed. An opening boundary condition allows the fluid to cross the boundary surface in either direction. For example, all of the fluid might flow into the domain at the opening, or all of the fluid might flow out of the domain, or a mixture of the two might occur. An opening boundary condition might be used where it is known that the fluid flows in both directions (any direction) across the boundary. [87, 88]

The outlet region includes the outer duct surface, circular rods, rotor hub surface and support structure underneath of the system that is considered as solid walls with no-slip condition. Bottom surface is also treated with no-slip boundary condition. On the side surface, an opening boundary condition is assumed.

The rotating region includes fan blades, rotor hub region and shroud surface where rotating fluid motion is simulated by adding source terms that is mentioned in section 4.3.1.3. Counter rotating wall velocities are assigned at the shroud surface.

Stationary and rotating regions were sub-sectional by periodic surfaces. By the help of periodicity, speed of numerical simulations were increased. The stationary surfaces were divided into 4 segments and rotating region was divided into 8 periodic segments. Only one of these segments for each region was used in numerical calculations. Difference in pitch angles of the frames are taken into account in interfaces that are connecting rotating and stationary surfaces. A stage type interface model was used.

6.3.1.2 Grid Refinement Study

A grid independence study is performed to show that the computational results are not dependent on the computational mesh and the resolution of the mesh is adequate to capture the significant flow characteristics. The grid independence is evaluated by comparing the computational solutions from 3 different mesh sizes, comprising coarse mesh with 3,000,000 tetrahedral cells, medium mesh with 4,750,000 cells and 6,00,000 cells. The static pressure distribution around the midspan blade profile at the radial station $r = 0.90$ for baseline fan rotor is plot-

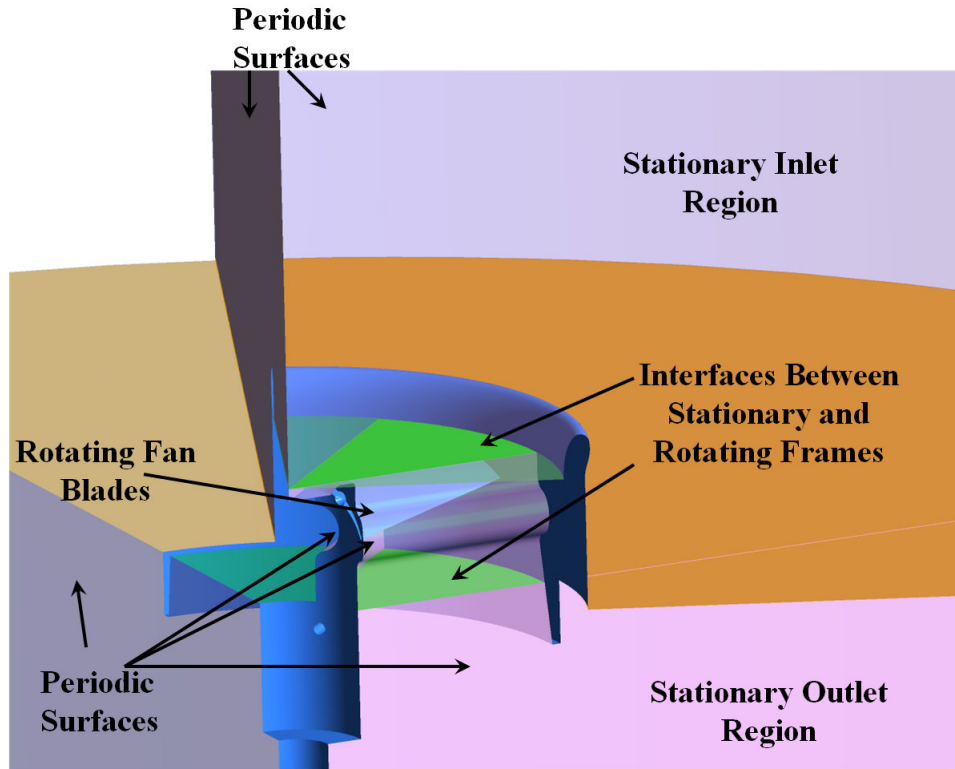


Figure 6.16. Computational domains and boundary conditions used in computations

ted as shown in figure 6.17 for three different grid densities. The profile suggests that the computational results are grid independent when the 4,700,000 cells are exceeded. Therefore, the medium mesh is used for all predictions in this chapter. Figure 6.18 illustrates a view from medium size computational mesh near the inlet lip region and rotor tip. The unstructured tetrahedral cells are used for computations. Regions near the solid surfaces are meshed with prisms for generating a better viscous boundary layer grid. Non-dimensional wall distance (y^+) less than 2 is achieved near the shroud and hub region. Region between solid shroud and rotating blade tips are filled with prism layers.

6.3.1.3 Validation of Numerical Results

Figure 6.19 shows a comparison of experimental and computational results. Circumferentially averaged total pressure coefficient at the downstream of the fan

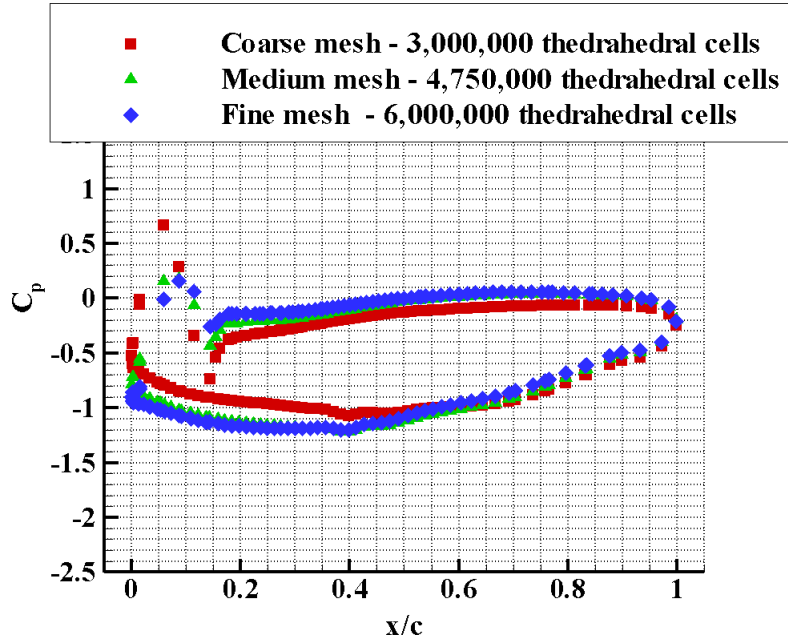


Figure 6.17. Grid independence study

rotor is compared to the experimental results. The computational and experimental results show very good agreement in the spanwise distribution except in a limited area near the hub where $r/R_{tip} \leq 0.65$. The computational results slightly deviate from experimental results near the hub region. That is because of the highly complex low Reynolds number and possibly re-circulatory turbulent flow field near the hub region. Low Reynolds number characteristic of the flow makes this computation highly challenging. Reynolds number based blade chord is approximately lower than 50,000 at the $r/R_{tip} \leq 0.6$. Low Reynolds number flows are relatively hard to compute using standard turbulent models as they are used in present day computational systems. The overall results show significant re-circulatory flow zones near the hub wall. The highly 3D and possibly unsteady flow zones are driven by the hub inlet (corner) region flows.

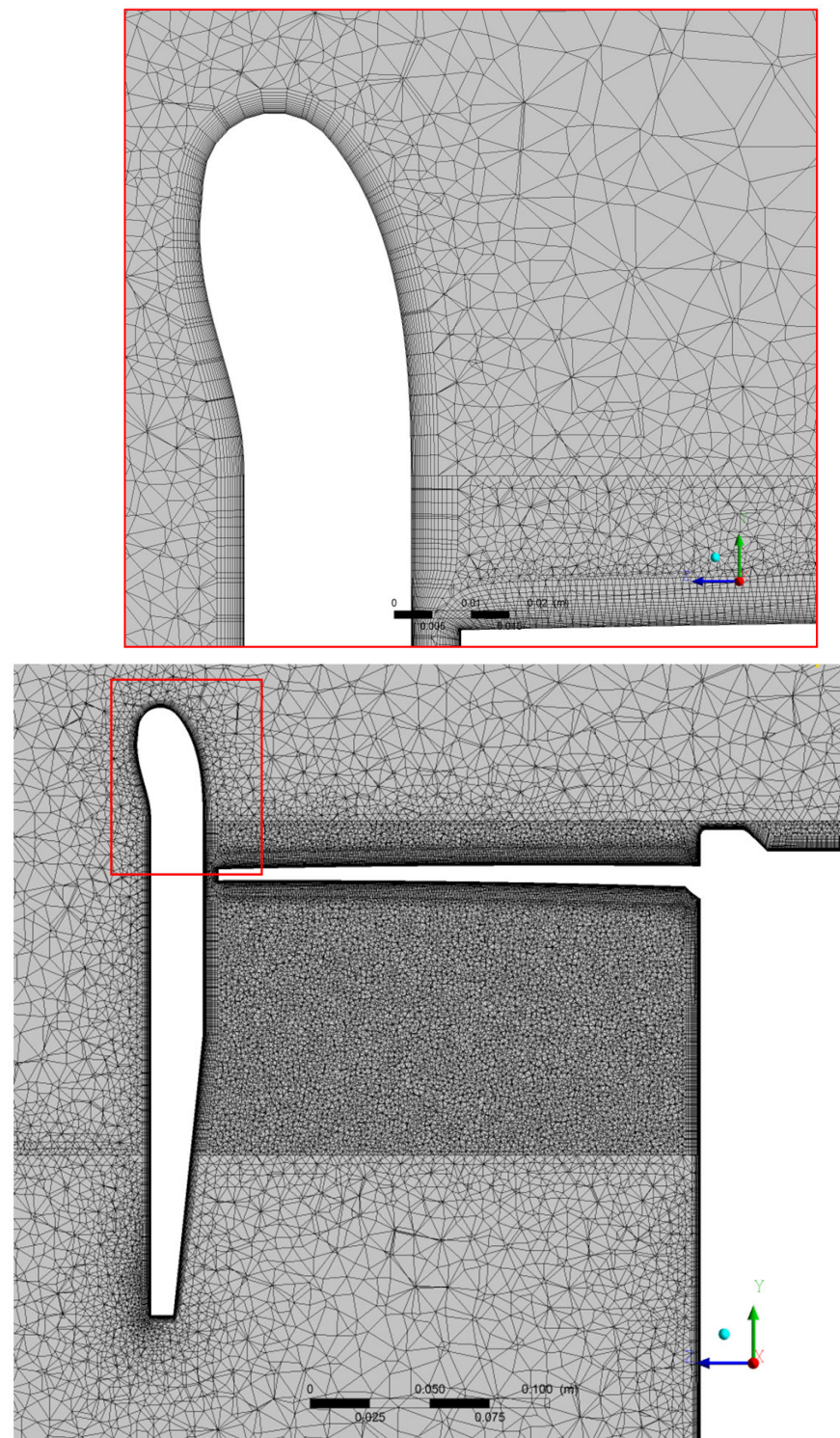


Figure 6.18. Medium size computational mesh used in computations

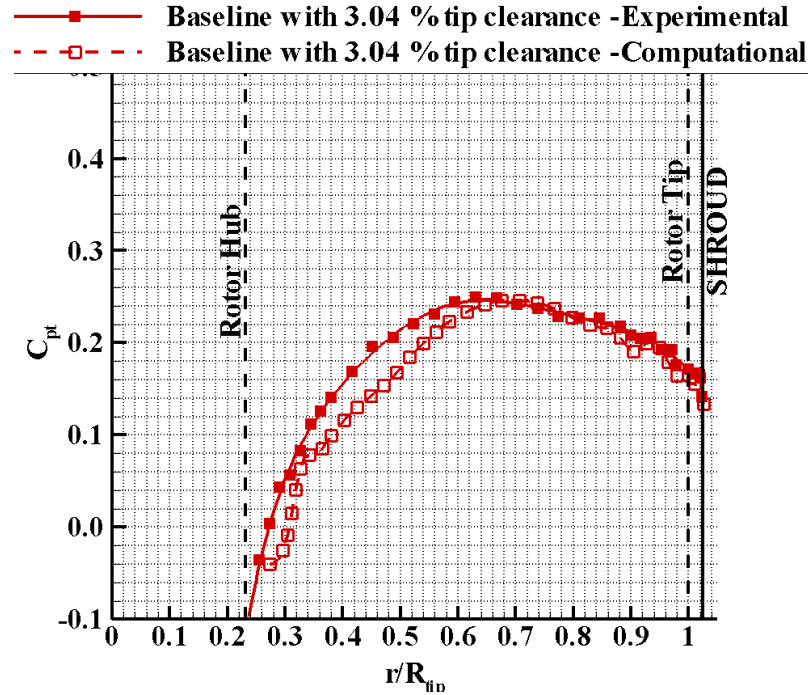


Figure 6.19. Total pressure coefficient comparison for experimental and computational analysis at 2400 rpm

6.3.1.4 Computational Result for Baseline

The numerical simulations were obtained at 2400 rpm rotor speed for hover condition. Calculations were performed using a parallel processing approach. For the parallel processing, the stationary and rotating frames were partitioned via vertex based partitioning with metis multilevel k-way algorithm. Computations were performed on a cluster having 24 processors. Total processing time is approximately 54.9 hours for 4466 iterations.

Figure 6.20 illustrates a numerical solution obtained for the ducted fan at 2400 rpm rotor speed for the baseline fan rotor with a 3.04 % tip clearance. Half of vertical cross section of the computational domain which is colored by absolute velocity magnitude is shown in the figure. It can be observed from the figure that streamlines are numerically visualized at the inlet and exit sections of the ducted fan. A high momentum exit jet impinges on the bottom wall and leaves domain from the side surfaces. The effect of flow reflecting from the ground surface is not

observed. A mild flow separation from the hub surface can be seen in the Figure 6.20. There are two low momentum recirculatory flow regions which are close to the rotor hub and bottom wall of the computational domain as shown in Figure 6.20.

Tip leakage and secondary flows in fan rotor exit flow: The flow field between the stationary shroud and rotor tip of a ducted fan is highly complex because of the interaction of the leakage flow, annulus wall boundary layer and rotor wake. Figure 6.21 shows the streamlines drawn around the rotor blade with 1.71 % tip clearance. The complex flow features near the tip region and hub are visualized at a high spatial resolution. Streamlines are colored by relative velocity magnitude and drawn in relative frame of reference. The flow impinging on the rotating hub surface separates from the corner of the rotating hub and generates a secondary vortical field near the endwall surface. This vortical structure combines with the highly complex three dimensional hub endwall flow and generates total pressure loss near the rotor hub region. The magnitude of the relative total pressure just at the downstream of the fan rotor is shown in figure 6.22. This figure is drawn just downstream of the fan rotor and the visualization plane is normal to the axis of rotation. Red regions in the figure shows the highest total pressure regions while dark blue region shows lowest total pressure regions. The dark blue region near the fan rotor hub clearly shows the loss generation near endwall surface due to the combination of hub corner separation and three dimensional hub endwall flow. The wake region of the rotor blade is shown with dashed lines in figure 6.22. The tip leakage flow and tip vortex is also visible near the rotor tip. The light blue region near the rotor tip shows the blockage effect that is induced by tip vortex originating from the rotor blade pressure side. There is also another light blue region near the pressure side of the rotor blade. That shows interaction of the tip vortex propagating from previous rotor blade with the pressure side as shown in Figure 6.22. This interaction can also be seen in Figure 6.21 by the streamlines drawn around the rotor tip. This interaction near the pressure side results in a measurable total pressure drop at the exit of the fan blade because of separation from the pressure side.

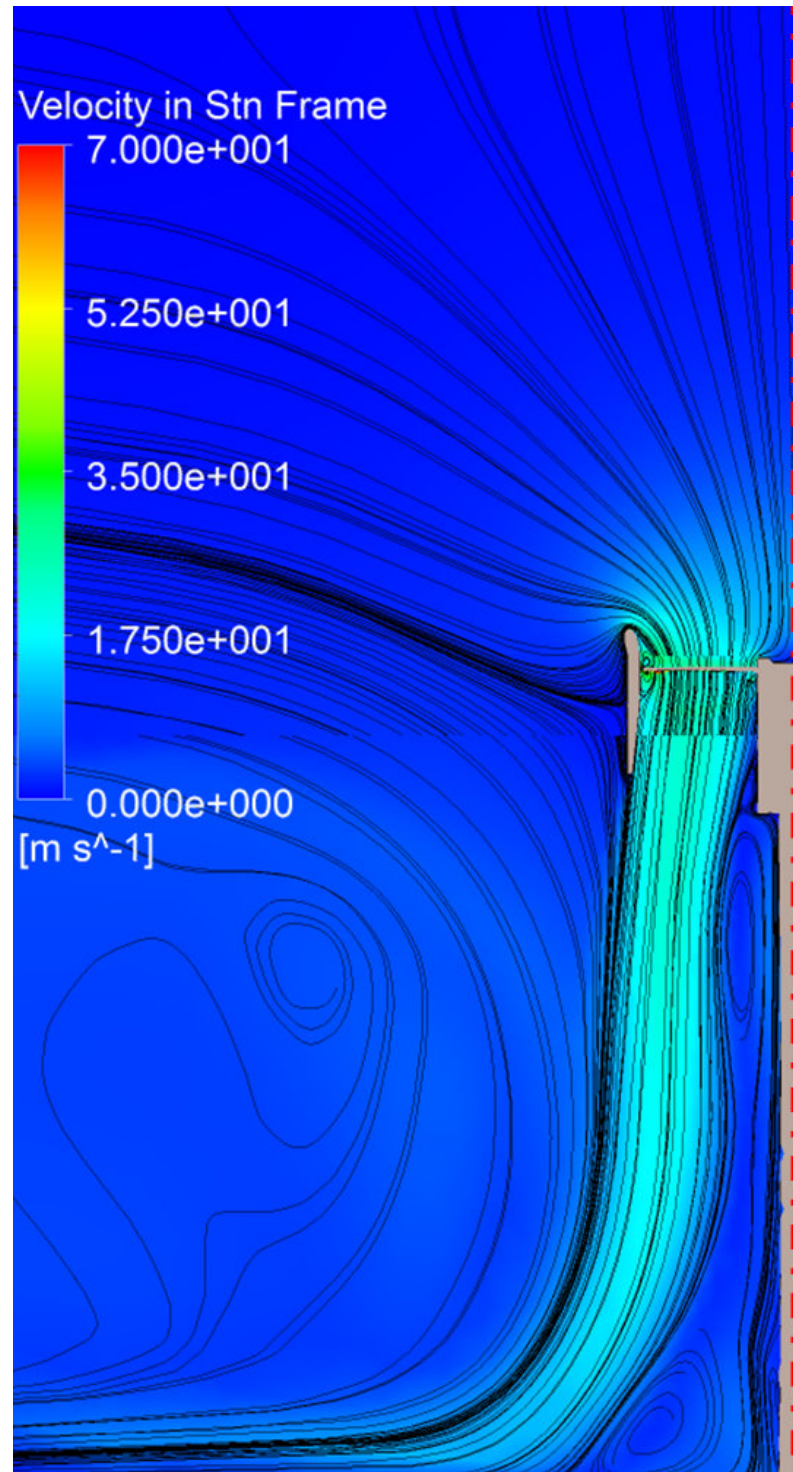


Figure 6.20. Absolute velocity magnitude and streamlines drawn on half of vertical cross section

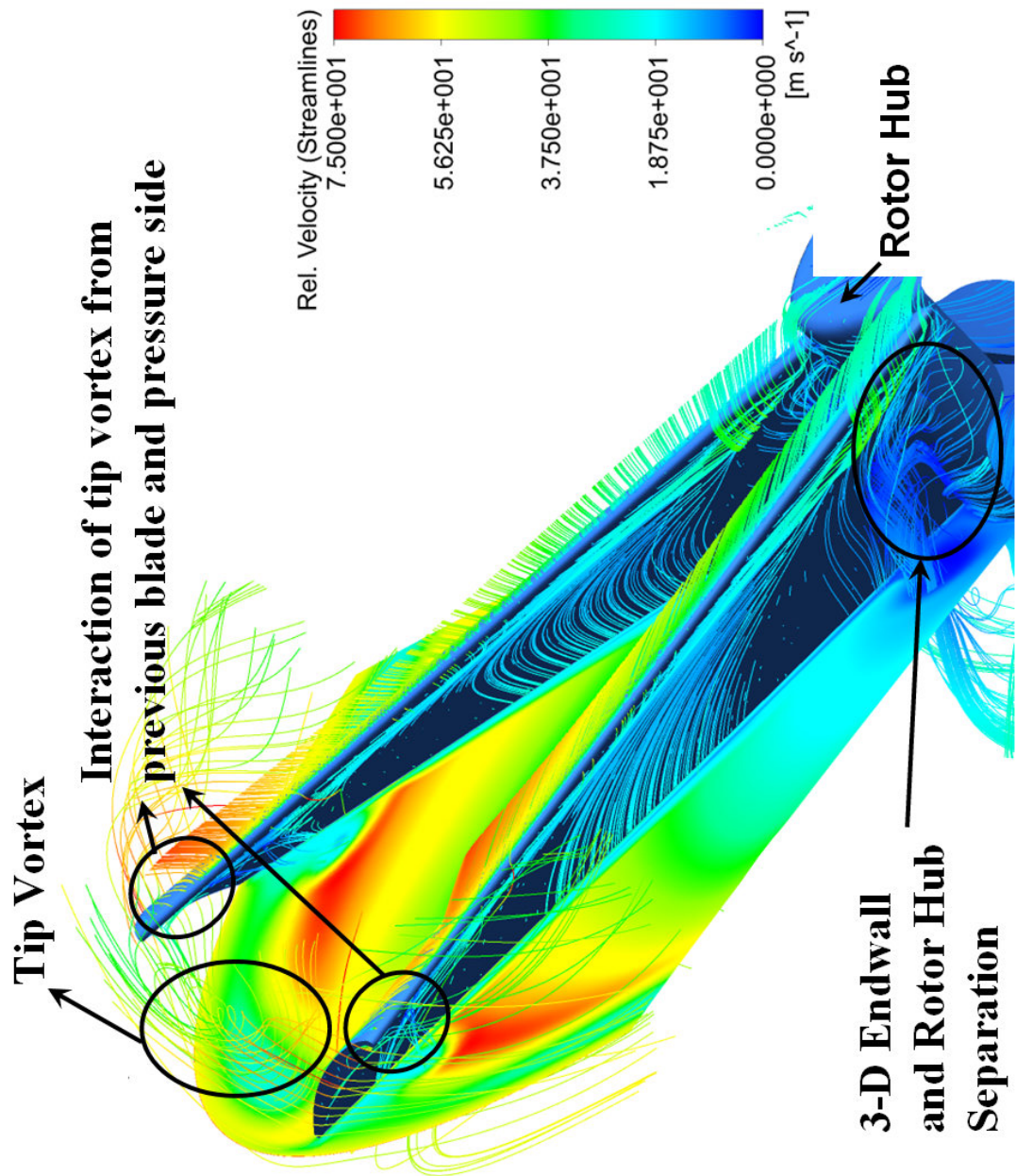


Figure 6.21. Streamlines around the baseline rotor blade with 1.71 % tip clearance and rotor hub at 2400 rpm

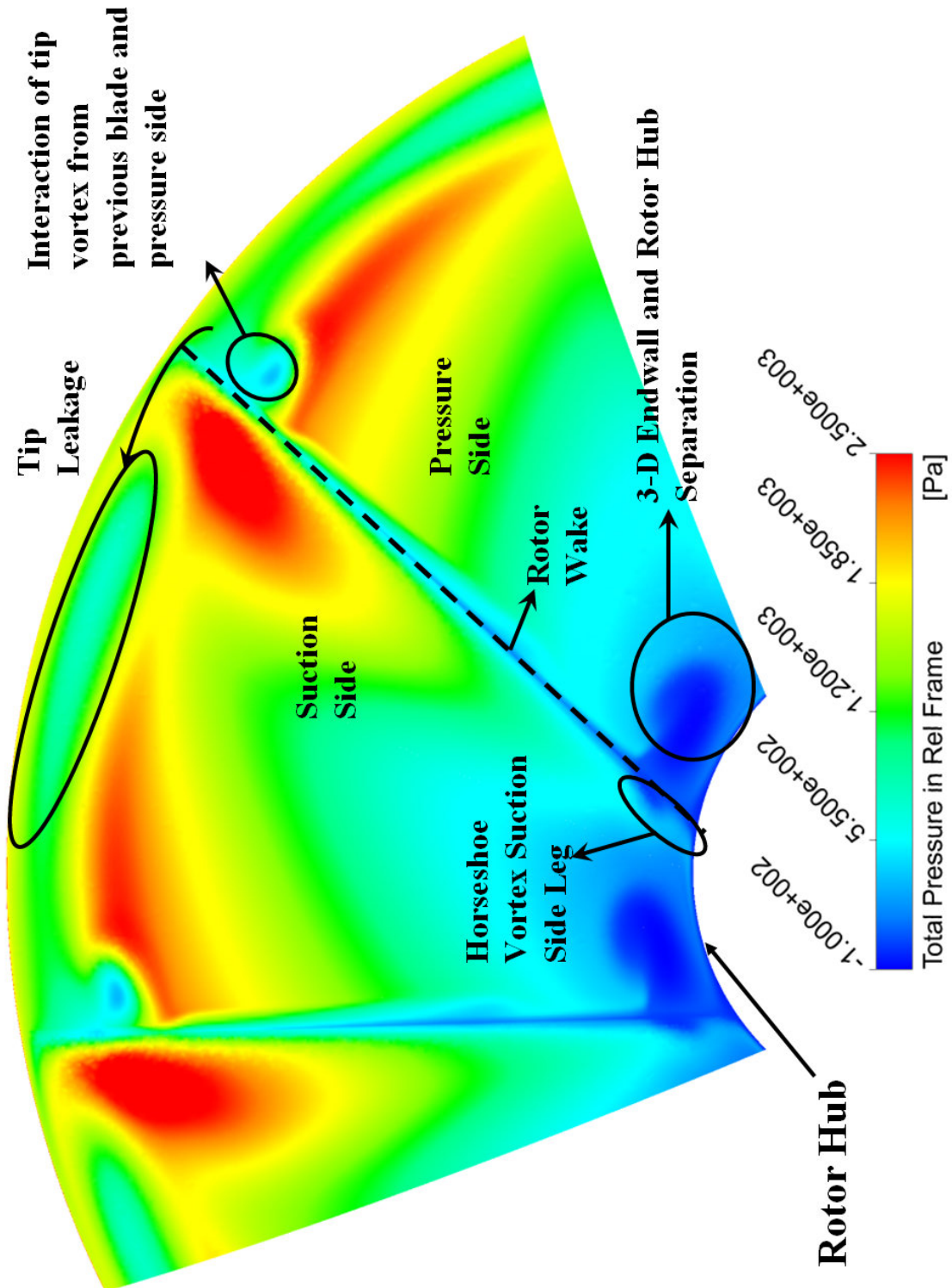


Figure 6.22. Relative total pressure distribution at the rotor exit plane for the baseline blade with 1.71 % tip clearance

Figure 6.23 clearly shows the effect of tip clearance and other important 3D passage flow features on the rotor exit relative total pressure distribution for a tip clearance value of 3.04%. Changing the clearance level didn't affect this distribution near the hub region. However, an increase in tip clearance resulted in more aerodynamic loss near the rotor tip. Overall blockage due to tip leakage is also increased. Besides, the interaction of tip vortex and rotor blade pressure side is much enhanced and more total pressure loss is obviously generated in the passage.

Blade tip constant circumferential planes: The visualization planes obtained at constant circumferential angles are generated at the rotor blade tip for a better understanding of rotor tip region flow. Figure 6.24 shows the location of these planes. They are all passing from the axis of rotation and drawn at fixed circumferential position. Figure 6.25 shows zoomed view of the planes that are drawn for the baseline rotor tip at 3.04 % tip clearance. Throughout this chapter this zoomed view of the planes will be used. Three of these planes (A,B and C) were drawn just upstream of the rotor tip and they are separated by 4° circumferential angle from each other and plane D. Plane D was drawn at the quarter chord of the tip profile. Planes D, E,F,G,H and I were equally distributed on the rotor tip profile by 2° circumferential angle. Plane I was drawn at the trailing edge.

Constant circumferential angle planes drawn in figure 6.25 are colored with stretched swirling strength. Swirling strength is the imaginary part of complex eigenvalues of velocity gradient tensor. It is positive if and only if there is existence of swirling local flow pattern and its value represents the strength of swirling motion around local centers. Stretched swirling strength is swirling strength times dot product of swirling vector and normal of swirling plane [87, 88]. An increase in this parameter indicates that swirling strength normal to swirling plane is increased.

The quantity color coded in these planes is the velocity stretched swirling strength drawn on the constant circumferential planes. The swirling strength shows the magnitude of the out of plane swirling motion. The red color indicates region that the highest swirling motion is occurring. Plane A, B and C shows swirling

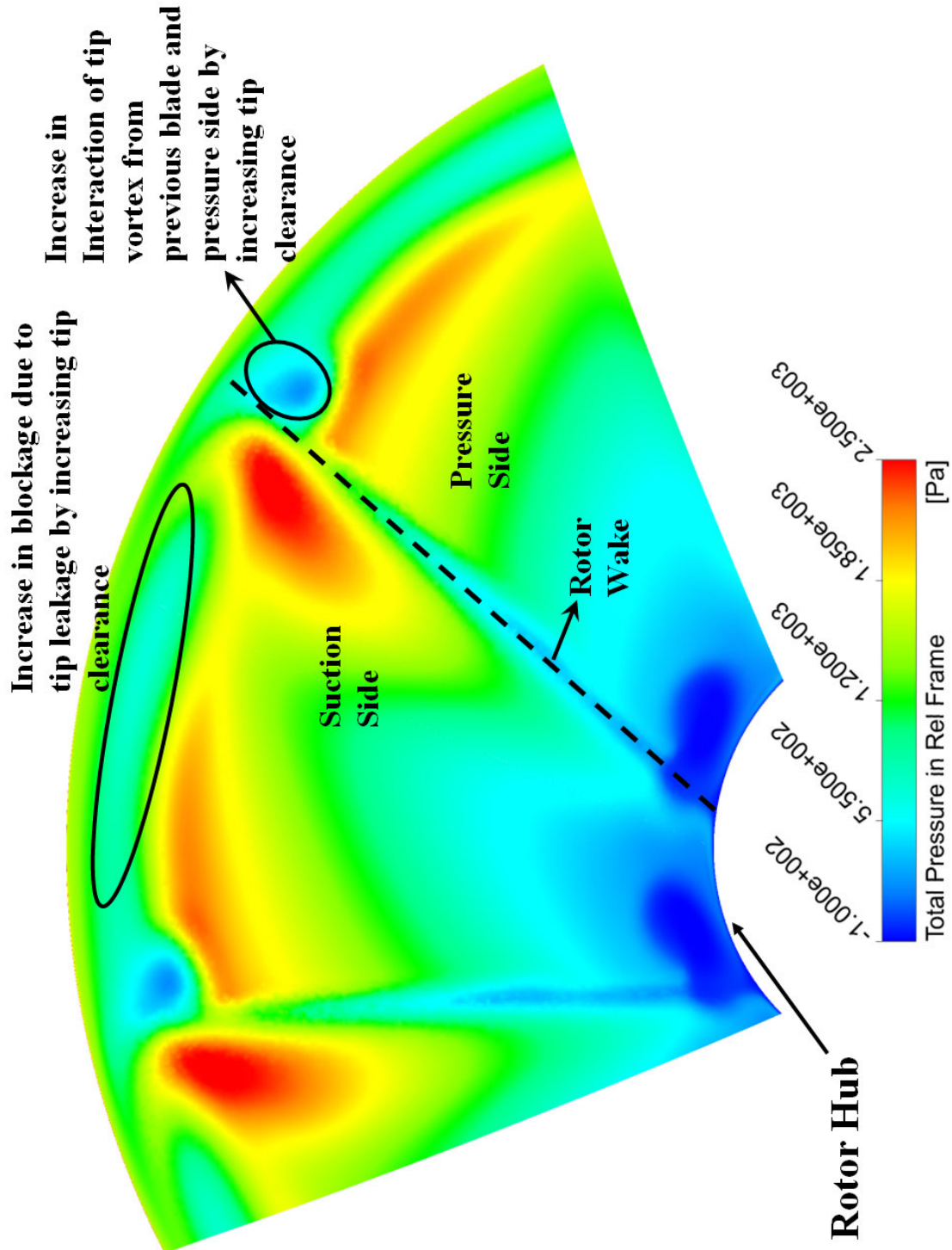


Figure 6.23. Relative total pressure distribution at the rotor exit plane for the baseline blade with 3.04 % tip clearance

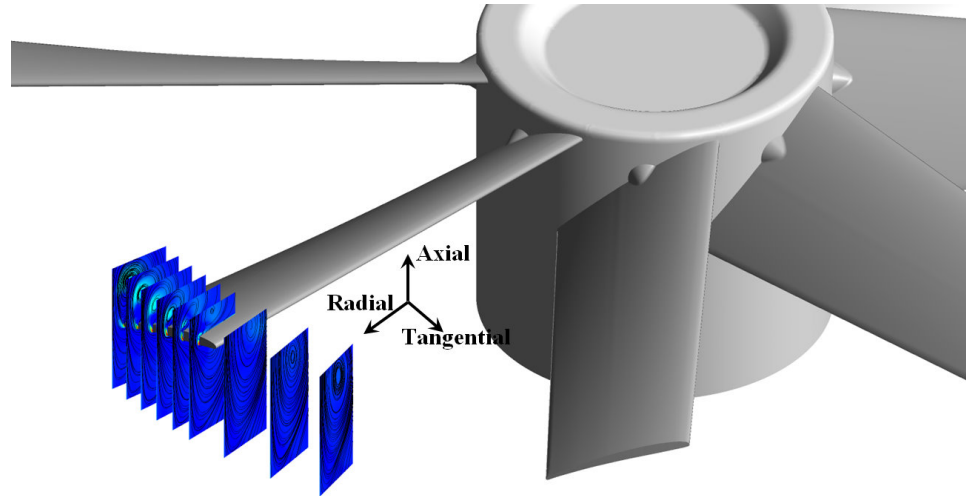


Figure 6.24. Location of blade tip constant circumferential planes

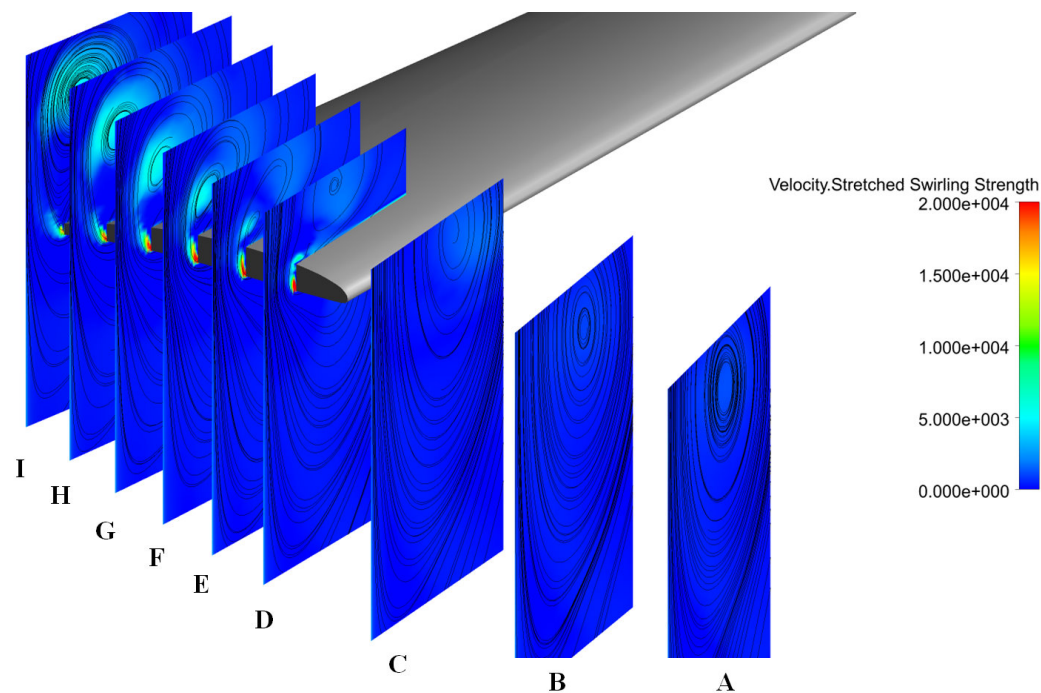


Figure 6.25. Blade tip constant circumferential planes drawn for baseline rotor tip with 3.04 % tip clearance

strength upstream of the rotor blade. A small amount of swirling motion can be observed in these planes which is related to the tip vortex originating from the previous blade. The positioning of each tip vortex influencing the neighboring blade is clearly shown in Figure 6.25. The vortical field originating from the previous blade tip vortex interacts with the blade tip. This vortical field is divided into two parts. Suction side and pressure side parts. The suction side part is integral with the tip vortex of the current blade. The pressure side part interacts with the pressure side of the rotor blade and generates additional loss at the exit plane which was shown in Figure 6.23. The strongest swirling motion starts at the quarter chord of the blade tip measured from the leading edge. Leakage flow tries to pass to suction side by generating a vortical structure which is visible at plane D. In planes E,F,G,H and I path of the released vortical structure from the pressure side corner can be viewed. Once the vortical structure forms, the strength of it is not as high as the one observed near the pressure side corner seen in plane D. The size of the structure dominated by light blue and green zones is increasing when one travels from leading edge to trailing edge.

6.3.2 Tip Treatments

Tip leakage flow results in a considerable amount of aerodynamic loss in rotor flow field as discussed in previous sections. One way of reducing tip losses is to use proper tip treatments. These treatments subject to investigation in this thesis include extension of rotor tip platform and squealer tips. Both treatments are widely used in axial flow fans and compressors. Chapter 5 outlines design methodology and tests for tip platform extensions for a lightly loaded axial flow fan rotor. The design idea behind the tip platform extensions designed in chapter 5 is based on estimating the blade chordwise position where the tip leakage potential is the highest for a given tip profile. In chapter 5 this estimation was performed in the light of Particle Image Velocimetry (PIV) measurements. In this section, a numerical procedure of designing efficient tip treatments for ducted fan rotor blades are developed by a computational approach. Figure 6.26 shows conceptually designed tip platform extensions and squealer tips, that are subject to investigation in this chapter.

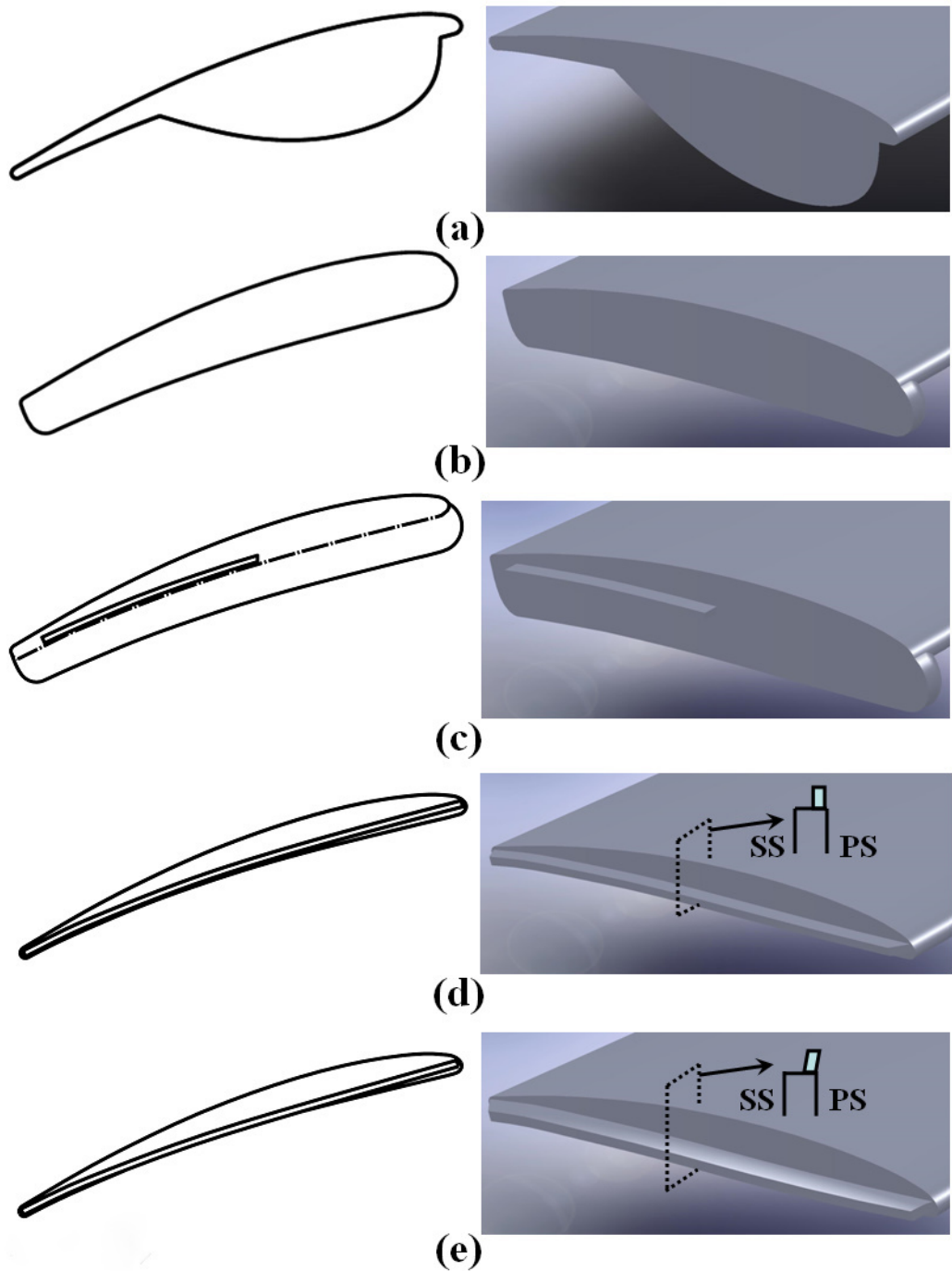


Figure 6.26. Tip treatments (a) Partial bump tip platform extension (t.p.e.), (b) Full bump t.p.e., (c) Full bump and partial squealer t.p.e., (d) Full squealer t.p.e., (e) Inclined full squealer t.p.e.

6.3.2.1 Partial Bump Tip Platform Extension

Effectiveness of partially blocking pressure side of the fan rotor tip in mitigating tip leakage was explained in chapter 5. It was shown that profiles 1 and 2 which are using partial bump type tip platform extension at the pressure side of the fan rotor tip were the best choices for reducing the effects of tip leakage and improving axial flow velocity at the rotor downstream for the lightly loaded fan rotor. Those two bump profiles were having the same thickness with the rotor tip profile at the bump center location.

The partial bump designed for highly loaded ducted fan shares same idea; *reducing the tip leakage flow from the pressure side*. It is visible from the figure 6.25 that the tip leakage starts very close to the leading edge of the tip profile. Therefore, a long bump that starts from the 5 % of chord location and ends at 66.6 % tip chord location was designed. The maximum thickness point was selected as the quarter chord (25 % of the tip chord) since the highest swirling strength was observed in that location. The maximum thickness of the bump was chosen as “*twice of the tip chord thickness*” at the quarter chord location. Figure 6.26a shows the shape of the bump designed. The maximum thickness of the bump is increased compared to the tip extensions discussed in chapter 5 because the loading of the fan blades are increased in 22” diameter ducted fan.

Figure 6.27 shows streamlines and stretched swirling strength contour for partial bump tip extension shown in 6.26a . Planes A,B and C are showing tip vortex coming from the previous blade moving radially inward compared to the baseline tip result. The strongest contribution to tip vortex is near plane G. However a gradual increase in the swirling strength is observed in planes D,E and F. Tip vortex can be seen in planes G, H and I with a light green and blue core . Strength of the vortex is slightly higher than the ones obtained for baseline tip.

6.3.2.2 Full Bump Tip Platform Extension

Since the leakage flow cannot be effectively blocked by using partial bump tip extension, a full coverage bump tip platform extension was designed to cover

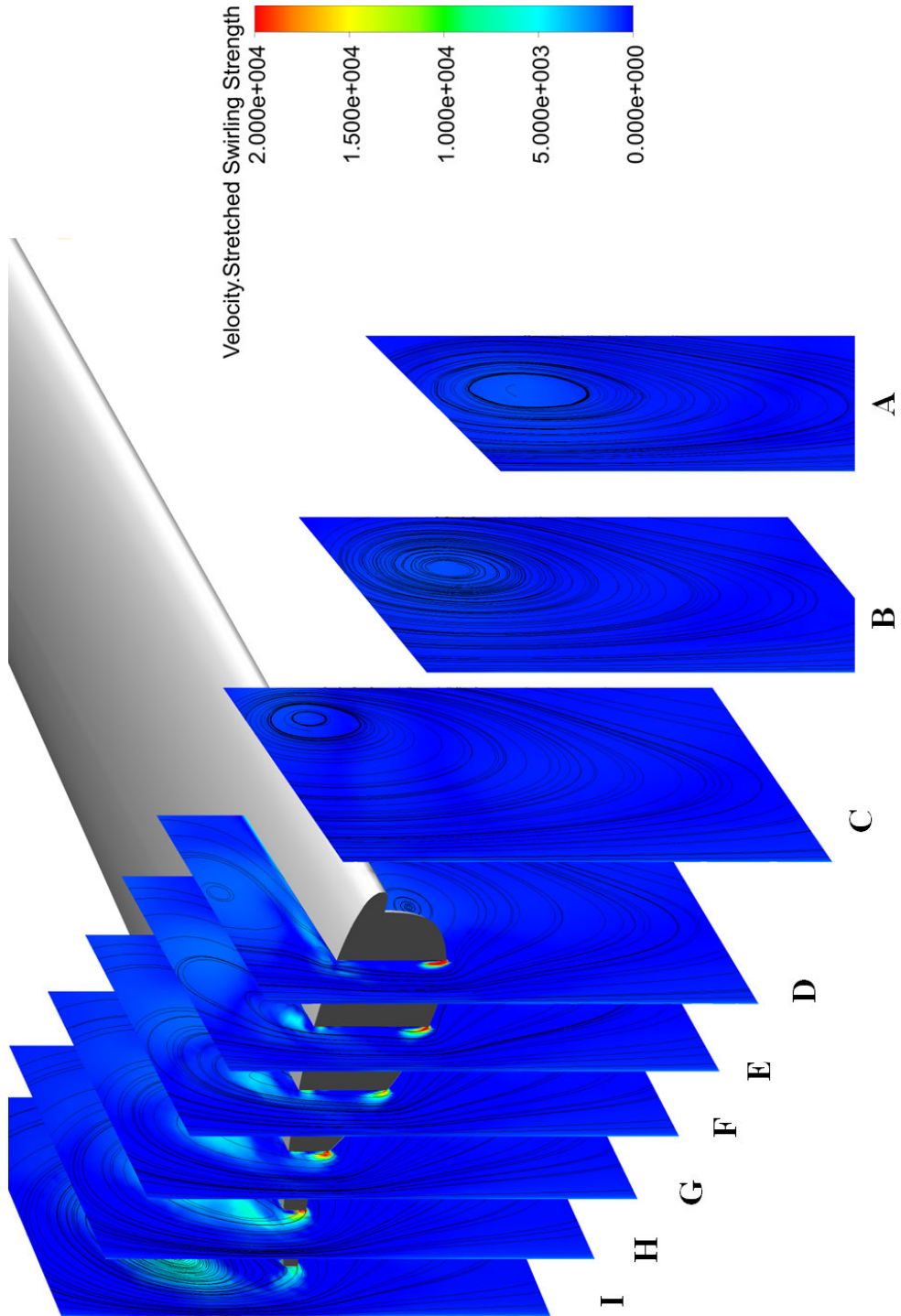


Figure 6.27. Blade tip constant circumferential angle planes drawn for “*partial bump*” tip extension with 3.04 % tip clearance

pressure side of the rotor tip completely. The bump starting from the leading edge and ends at trailing edge of the tip chord was designed. Bump is created by extending pressure side curvature by the airfoil thickness at the quarter chord point of the blade profile. Figure 6.26b shows the shape of the full bump designed.

Figure 6.28 shows the streamlines and stretched swirling strength contour for full bump tip extension. Planes A,B and C are showing tip vortex coming from the previous blade moved more axially compared to baseline tip and partial bump result. Full bump tip extension was not sufficient for effectively reducing leakage flow. Planes D,E,F,G,H and I shows that the strength of the vortical structure is almost same with the baseline rotor tip, without a beneficial tip mitigation influence.

6.3.2.3 Full Bump and Partial Squealer Tip Platform Extension

Since the leakage flow cannot be properly blocked by using only pressure side tip extensions, a combination of a full bump and partial squealer extension is designed for the region near the trailing edge. Figure 6.26c shows the shape of the combined full bump and partial squealer design. The squealer extension starts from 45 % chord measured from leading edge and ends at the trailing edge. The height of the squealer was 0.89 mm and thickness was 20 % of the tip gap height (1.27 mm for 3.04 % tip clearance). The squealer tip is located parallel to the pressure side of the rotor tip and approximately 0.5 mm away from the pressure side.

Figure 6.29 shows streamlines and stretched swirling strength contour for combination of the full bump and squealer tip extension. Planes A,B and C are showing tip vortex coming from the previous blade moving more axially compared to baseline tip and partial bump result. Full bump and squealer tip extension was not sufficient for blocking leakage flow. Planes F,G,H and I shows the effect of squealer on the flow field near the rotor tip. By the effect of the squealer the swirling strength is increased and tip vortex is moved radially outward which is a favorable effect. Moving the tip vortex radially out will reduce the interactions between the tip vortex and rotor blade and reduce the losses. However, the combination of full

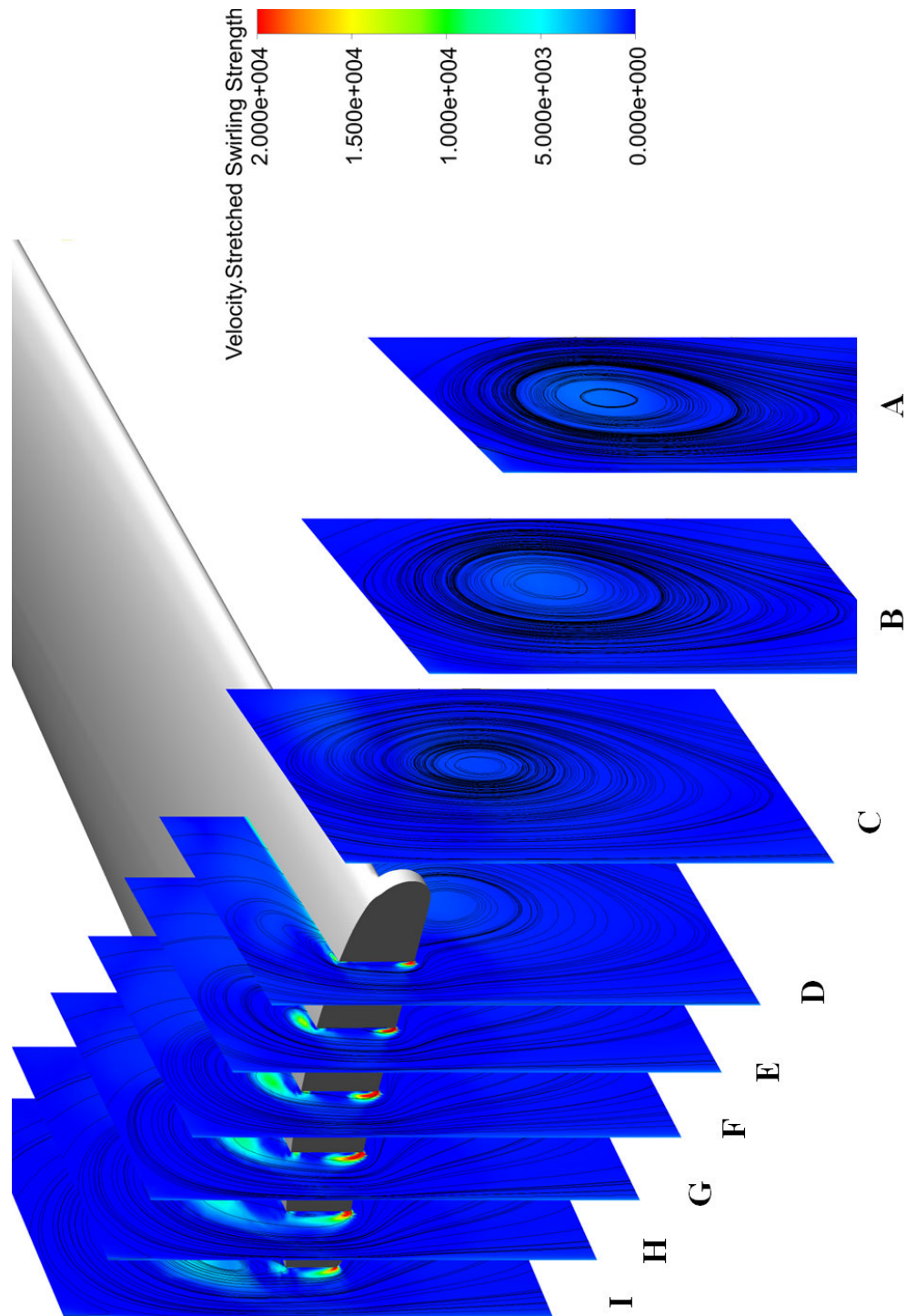


Figure 6.28. Blade tip constant circumferential angle planes drawn for “full bump” tip extension with 3.04 % tip clearance

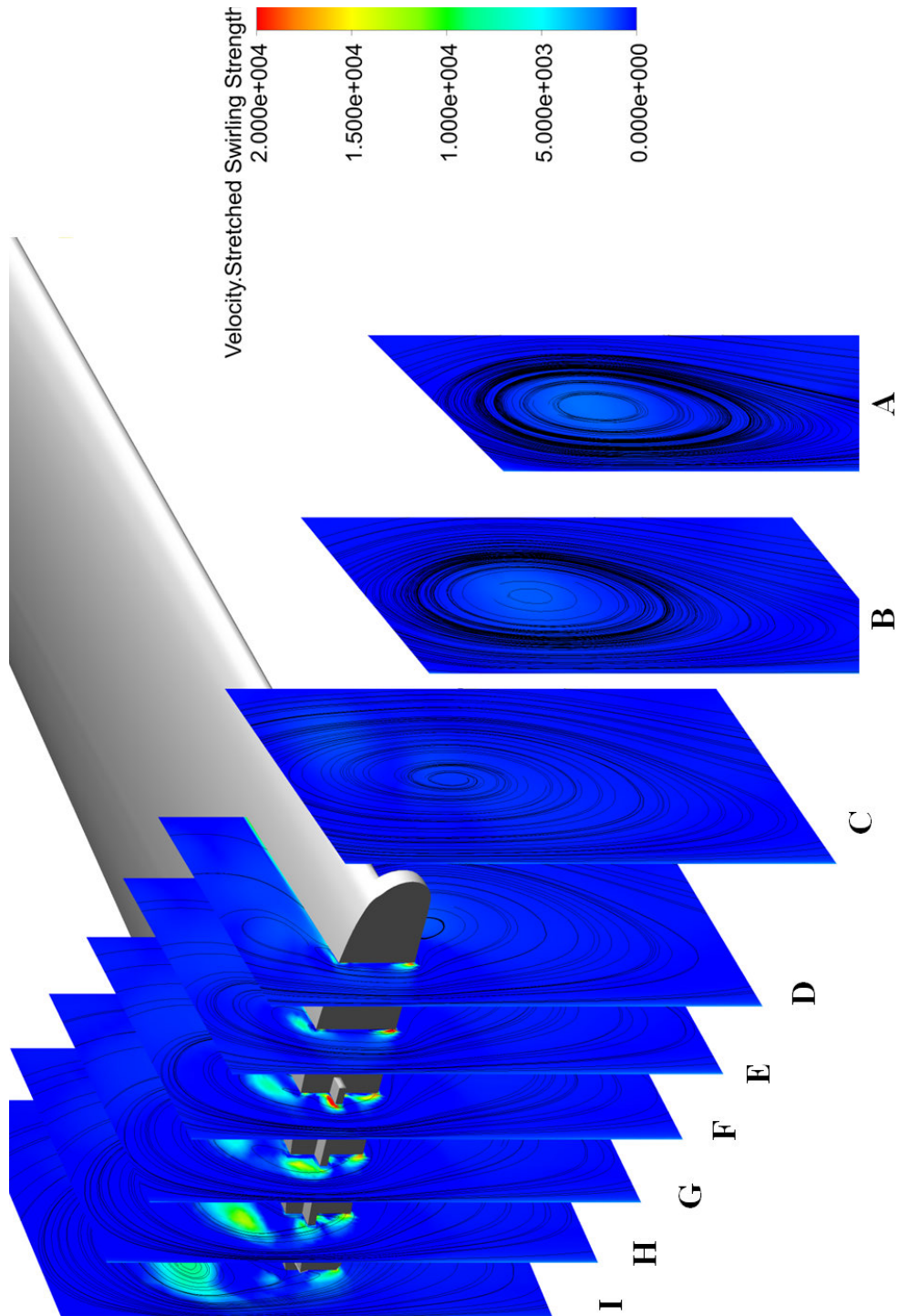


Figure 6.29. Blade tip constant circumferential angle planes drawn for “full bump and partial squealer” tip extension with 3.04 % tip clearance

bump and partial squealer is increasing swirling strength and losses.

6.3.2.4 Full Squealer Tip Platform Extension

Using a combination of bump and squealer is increasing turbulence and swirl at the rotor tip as shown in the previous section. A full squealer tip extension is designed to explore its potential as a possible aerodynamic tip mitigation device. Figure 6.26d shows the shape of the full squealer tip designed for this. Squealer extension starts from the leading edge of the rotor tip and ends at the trailing edge. The height of the squealer was 0.89 mm and thickness was 20 % of the tip gap height (1.27 mm for 3.04 % tip clearance). The squealer tip is located parallel to the pressure side of the rotor tip and 0.5 mm away from pressure side. At the leading edge of the tip profile, it is aligned with the stagnation point of the tip profile.

Figure 6.30 shows streamlines and stretched swirling strength contour for full squealer tip extension. Squealer tip extension decreased the strength of swirling at planes D, E, F, G, H and I. The leakage flow starting from the pressure side rolled up a small vortical structure between the squealer and suction side. After plane F, the vortical structure appears on the suction side of the rotor tip. Tip vortex starts to influence the passage flow beginning plane F. Using a squealer tip also moves tip vortex closer to the shroud and relieves the rotor passage from the adverse effect of tip vortex dominated flow. By that way interaction of tip vortex and rotor tip is reduced and rotor tip is loaded better than the baseline rotor tip, because of improvements in the passage aerodynamics near the tip.

6.3.2.5 Inclined Full Squealer Tip Platform Extension

Using the full squealer tip design moves tip vortex towards toyhe shroud. The most important effect of squealer tip was delaying tip vortex at the rotor tip. The leakage flow is filled into the space between squelar and suction side of the rotor blade and released on the suction side at the mid chord location. Delaying tip vortex release to a chordwise location close to the trailing edge helps to direct tip vortex radially out. Further improvement can be obtained by increasing space

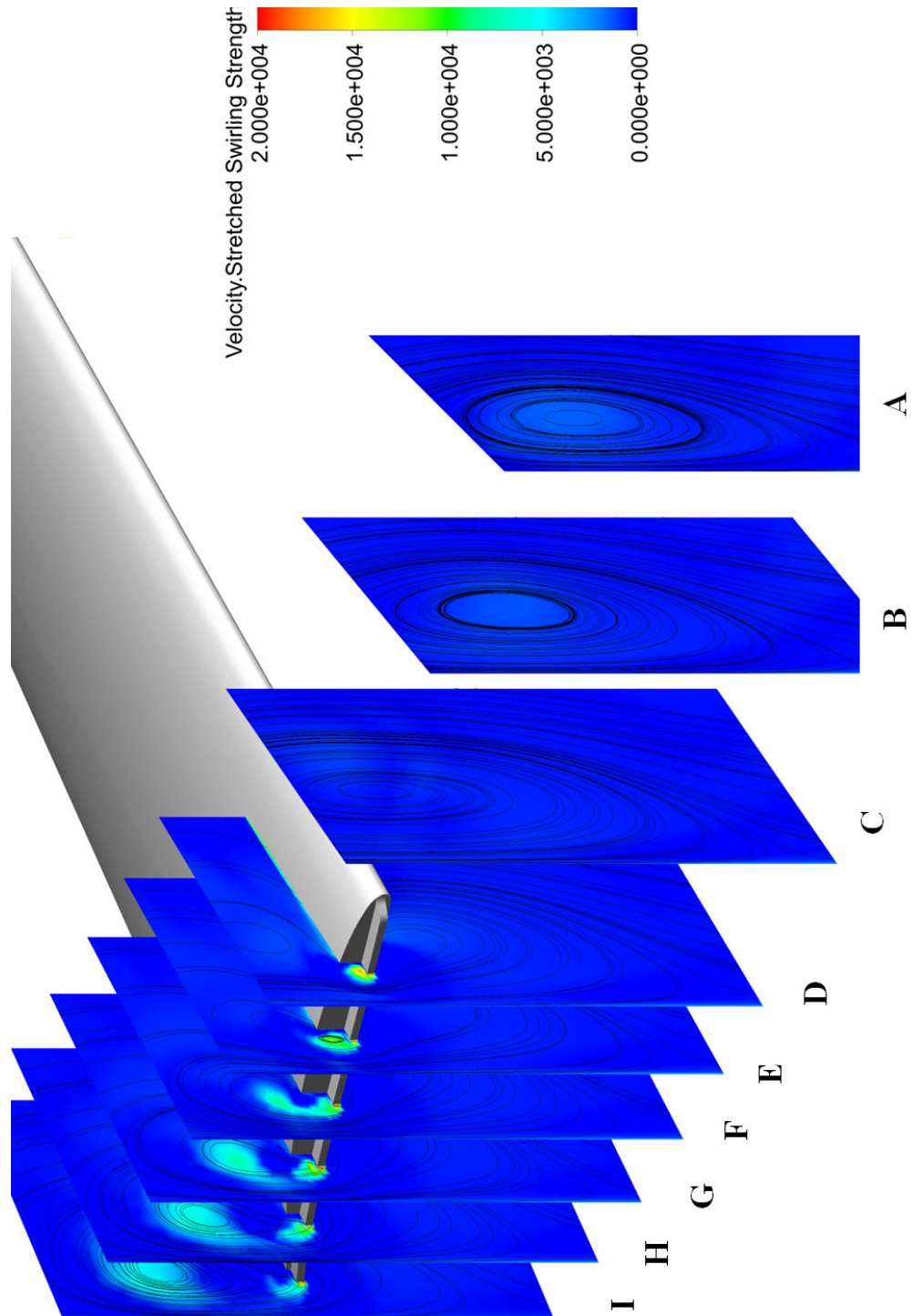


Figure 6.30. Blade tip constant circumferential angle planes drawn for “full squealer” tip extension with 3.04 % tip clearance

between the squealer and suction side of the rotor tip by bending squealer extension towards to pressure side. A full inclined squealer tip extension is designed by bending the existing squealer extension about 25° towards to pressure side. This inlined squealer design is shown in Figure 6.26e.

Figure 6.31 shows streamlines and stretched swirling strength contour for inclined squealer tip extension. The leakage flow originating from the pressure side rolled up a small vortical structure between inclined squealer and suction side. After plane G, vortical structure appears near the suction side of the rotor tip. Tip leakage vortex originates starting from plane G and is directed towards shroud region.

6.3.2.6 Overall Benefits of Tip Treatments

Overall benefits gained from the tip treatments are analyzed by total pressure improvements in the stationary frame of reference. Table 6.3 shows computed thrust and ratio of “*leakage mass flow rate*” to the “*fan rotor mass flow rate*” for baseline rotor tips for two tip clearances and treated tips. The leakage mass flow rate is calculated on a plane that was defined between the rotor tip and shroud surface. Figure 6.32 shows leakage surface used for leakage mass flow rate quantification in this study.

Two tip clearances, tight (1.71 %) and coarse(3.04 %) are compared in table 6.3. When the tip clearance decreased, the leakage mass flow rate also decreased and thrust was augmented. Decrease in leakage mass flow rate usually implies for an increase of overall mass flow rate passing from the duct. All of the tip treatments shown in the table 6.3 are tested at the same tip clearance of 3.04 %. Aeromechanic and aerodynamic performance improvements provided by tip treatments are also tabulated at table 6.3.

Figure 6.33 compares all of the tip treatments by comparing total pressure distributions in the stationary frame of reference. Total pressure distributions are drawn at the same plane in which the baseline measurements are performed. This plane is located at about 45.72 mm downstream from the midspan of the fan rotor.

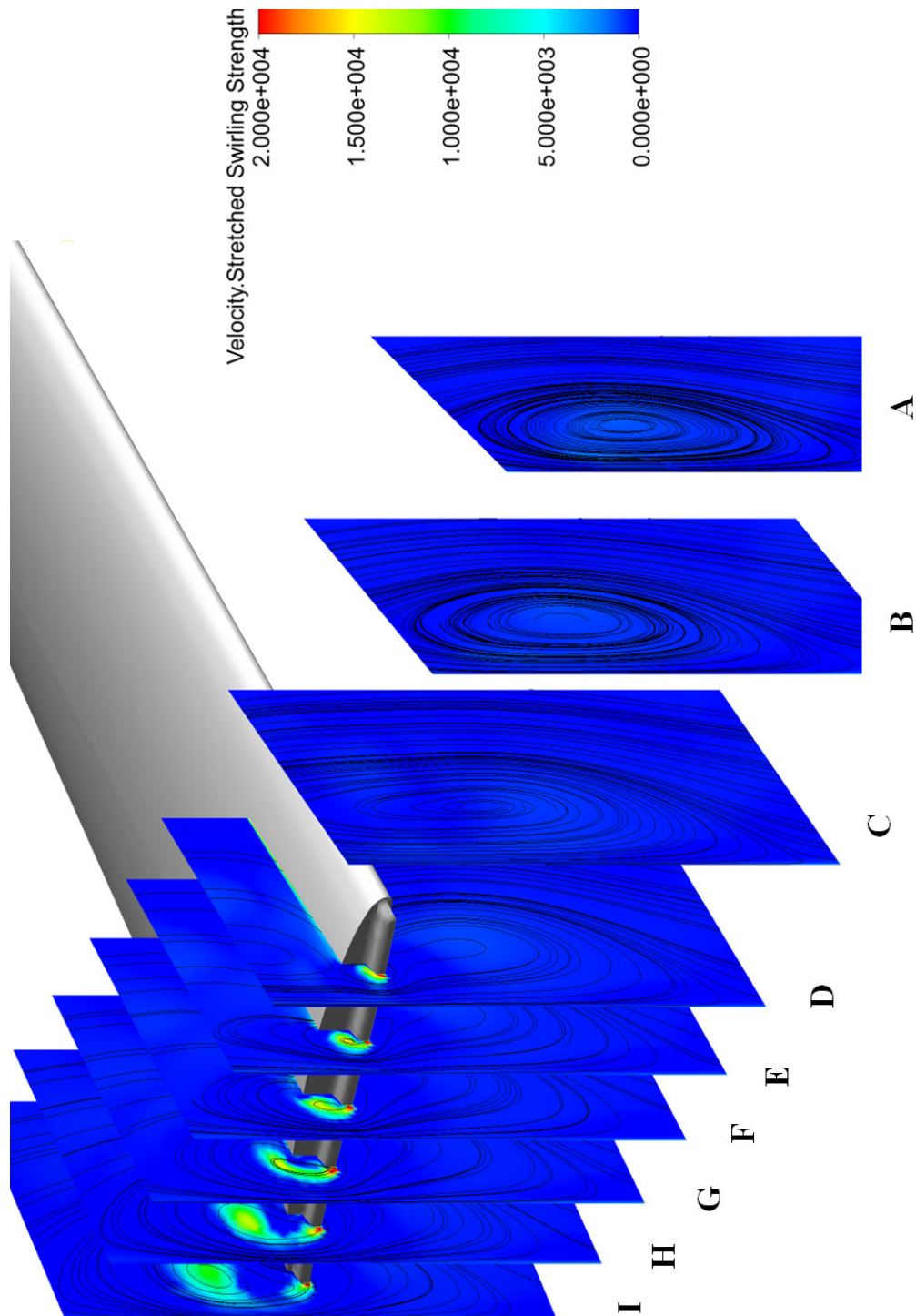


Figure 6.31. Blade tip constant circumferential angle planes drawn for “*inclined squealer*” tip extension with 3.04 % tip clearance

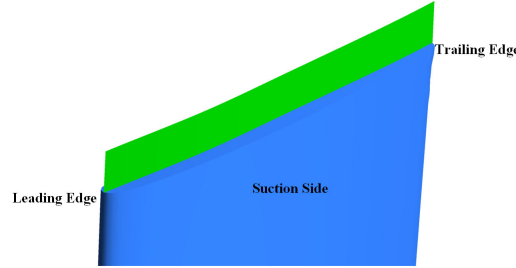


Figure 6.32. Leakage surface used to compute leakage mass flow rate.

Ducted fan performance with baseline fan rotor tip				
	$\frac{\dot{m}_{leakage}}{\dot{m}_{fan}}$ (%)	Total Thrust (N) (Comp.)	Total Thrust (N) (Exp.)	ϵ (%)
Baseline rotor tip with 1.71 % t. c.	1.81	94.24	92.68	1.68
Baseline rotor tip with 3.04 % t. c.	3.41	85.16	83.55	1.93
Ducted fan performance using treated fan rotor tips with 3.04 % tip clearance				
	$\frac{\dot{m}_{leakage}}{\dot{m}_{fan}}$ (%)	D. Thrust(N)	R. Thrust(N)	Total Thrust(N)
Baseline rotor tip	3.41	27.20	57.96	85.16
Partial bump t.p.e.	3.58	26.68	54.06	80.74
Full bump t.p.e.	3.28	26.70	58.20	84.90
Full bump and par. squealer t.p.e.	2.86	27.66	58.68	86.34
Full squealer t.p.e.	2.41	30.50	59.81	90.31
Full inclined squealer t.p.e.	2.35	30.76	63.55	94.31
				Thrust imp. (%)
				—
				-5.19
				-0.31
				1.37
				6.04
				10.73

Table 6.3. Tip treatments and their computed performance in hover condition at 2400 rpm

Because of the increased viscous losses induced at the rotor tip and radially tip leakage flow directed radially inward, performance of partial and full tip platform extensions was lower than baseline profile . Thrust obtained from the ducted fan was reduced for both treatments. Full tip platform extension combined with a partial squealer effectively reduce the tip leakage flow compared to partial and full tip platform extensions. However the gains that this treatment provided in thrust is not as high as the squealer tip treatments. Full squealer and inclined full squealer tip platform extensions are the best performing ones. They are improving the aerodynamic performance by moving the tip vortex towards the shroud. Inclined squealer tip is increasing the thrust provided by the ducted fan by 10.73 % at hover condition 2400 rpm. It also decreases tip leakage mass flow rate in a considerable rate.

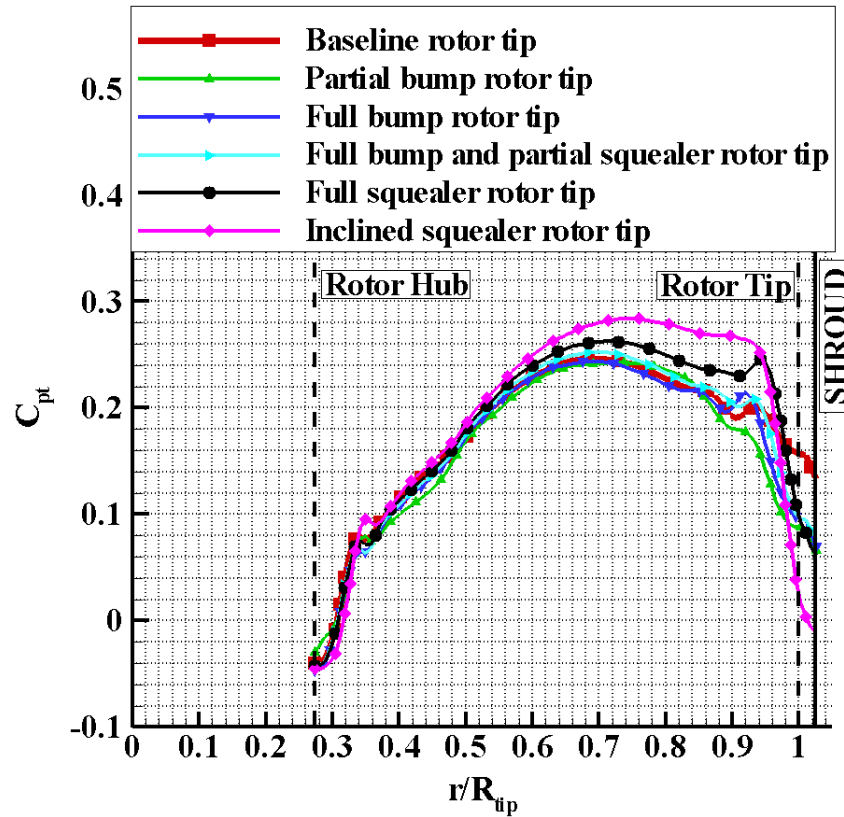


Figure 6.33. Comparison of stagnation total pressure distribution for all the blade treatments and baseline rotor tip.

6.4 Novel Tip Treatment Concept Development via Ducted Fan Experiments

6.4.1 Manufacturing Tip Platform Extensions Using a Stereolithography Based Rapid Prototyping Technique

In the previous sections, the computational analysis was performed for selecting the best tip profile geometries for improving aeromechanic and aerothermodynamic performance of the system. Squealer and inclined squealer tip extensions were both improving thrust of the system while reducing leakage mass flow rate. They were also improving fan rotor exit total pressure distribution compared to baseline rotor tips. These profiles were selected to be manufactured and experimentally tested

in hover condition. The baseline tip clearance level for computational analysis was 3.04 %. For experimental program, squealer and inclined squealer tip treatments were designed for 3.04 %. inclined squealer tip treatment was also tested for 5.17% tip clearance.

Selected tip shapes were designed as an extension to the tip of a baseline fan rotor tip. These extensions were 3.56 mm in thickness. Figure 6.34 shows drawings of the extensions designed for the baseline fan rotor tips. The extensions are glued to the top surface of the fan rotor blade using Cyanoacrylate that was having high viscosity and high impact strength. Figure 6.35 shows a rotor blade tip that has inclined squealer tip extension on it. Each tip concept tested had its own eight bladed rotor assembly.

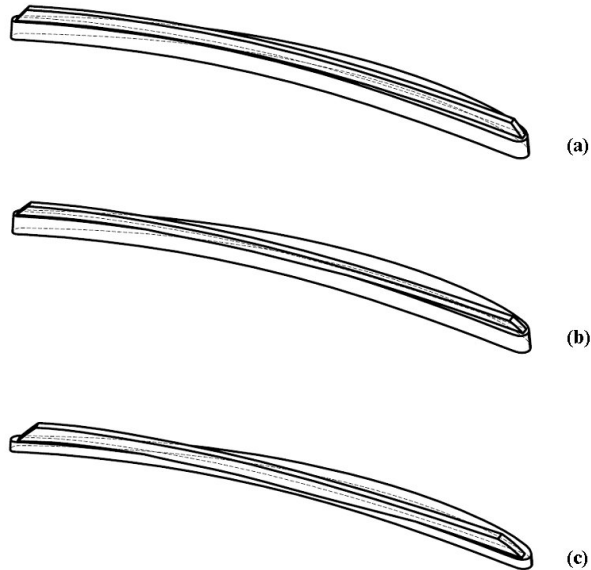


Figure 6.34. Squealer and inclined squealer tip extensions designed for SLA manufacturing (a)Squealer t.p.e.(3.04 % t.c.), (b)Inclined squealer t.p.e.(3.04 % t.c.), (c)Inclined squealer t.p.e.(5.17 % t.c.)

6.4.2 Force and Torque measurements

Force and torque measurements for fan rotors with treated tips were performed in the 22" diameter axial flow fan research facility described in this thesis. Figure



Figure 6.35. Inclined squealer t.p.e. applied to the rotor blade

6.36 shows measured thrust coefficient at various rotational speeds. Details of the calculation of thrust coefficient was discussed in section 6.2. The squealer and inclined tip squealer tip shapes were both augmenting thrust of the system compared to baseline rotor tip shapes. A maximum increase of 9.1 % was gained by using squealer tip shape at 2700 rpm. The maximum increase in thrust gained by using inclined squealer tip was around 9.6 % 2700 rpm. Compared to computational results, experimental performance of squealer tips was better than computational performance in terms of measured thrust values. Using tip treatments improved performance of the baseline rotor tips with 3.04 % tip clearance such that the fan rotor with treated tips at the same tip clearance performed almost as better as the baseline fan rotor performance with tighter tip clearance (1.71 %), without any tip treatment. These comparisons are based on measured thrust in 22" diameter ducted fan research facility.

Figure 6.37 illustrates the aeromechanic performance of inclined squealer at 5.17 % tip clearance compared to baseline rotor at the same clearance. When treatments were used with larger clearance, the improvements obtained was better. Total improvement in thrust was 15.9 % at 2700 rpm. Performance of the baseline rotor tips at 5.17 % tip clearance was enhanced so that they are almost performing like the 3.04 % tip clearance baseline rotor, without any tip treatment.

Figures 6.38 and 6.39 illustrates the figures of merit plotted against the rotational speed of the fan rotor. Squealer and inclined squealer rotor tips increasing hover efficiency compared to baseline rotor tips. Treated tip shapes at 5.17 % tip clearance are performing better than 3.04 % tip clearance (no tip treatments).

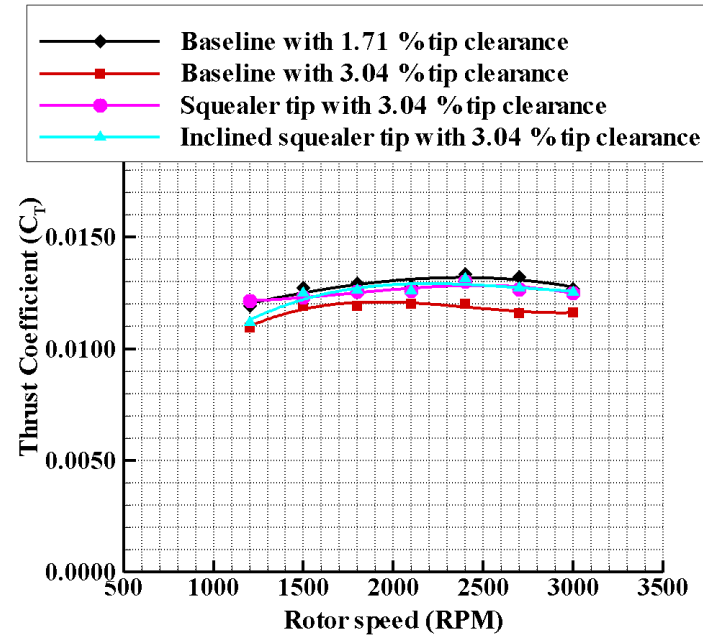


Figure 6.36. Thrust coefficient versus rotational speed for the rotor with squealer and inclined squealer tips at 3.04 % tip clearance

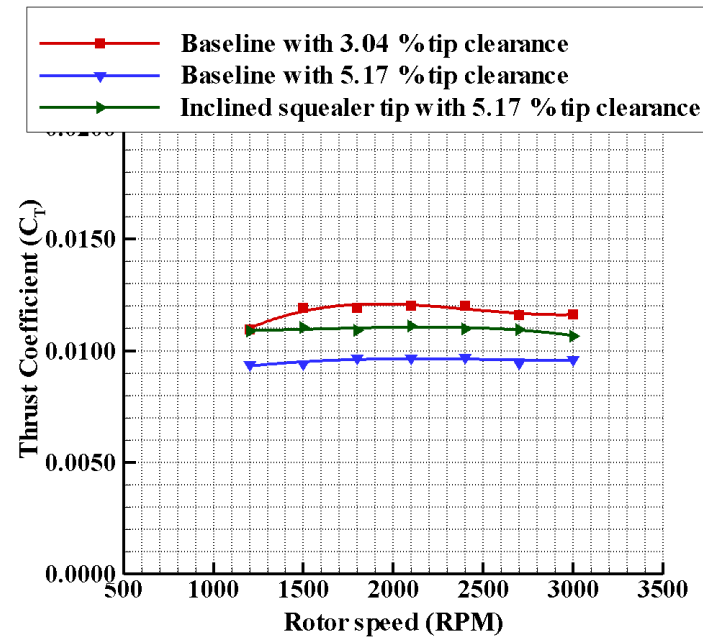


Figure 6.37. Thrust coefficient versus rotational speed for rotor with squealer and inclined squealer tips at 5.17 % tip clearance

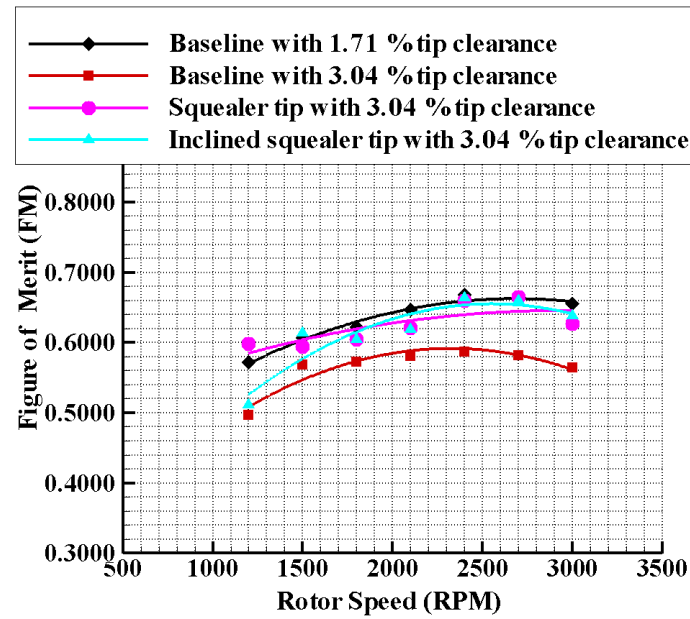


Figure 6.38. Figure of merit versus rotational speed for rotor with squealer and inclined squealer tips at 3.04 % tip clearance

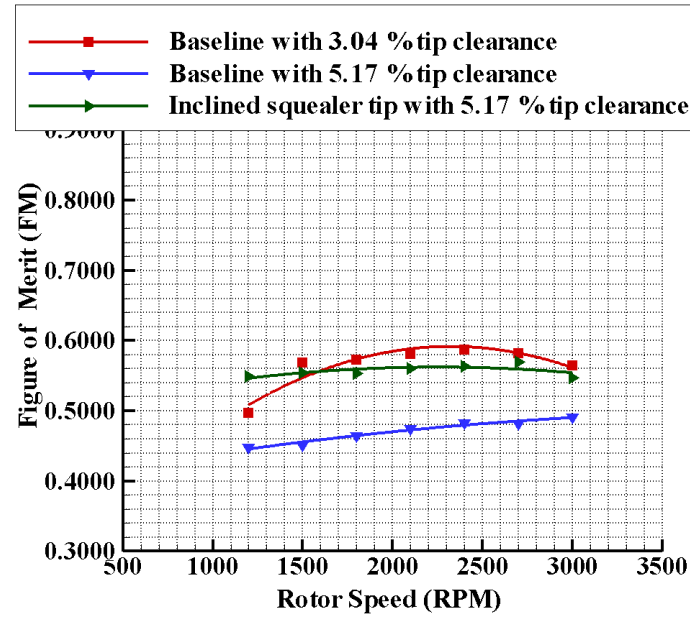


Figure 6.39. Figure of merit vs rotational speed for rotor with squealer and inclined squealer tips at 5.17 % tip clearance

6.4.3 Total Pressure Measurements

Aerothermodynamic performance of the ducted fan with squealer rotor tips was assessed by fan rotor exit total pressure measurements at hover condition. Figure

6.40 shows total pressure coefficient measured at fan rotor downstream from rotor hub to the shroud. It should be noted that there is almost no change in total pressure coefficient by using treated tips when $r/R_{tip} \leq 0.35$. Total pressure at the fan rotor exit plane is increased by using squealer and inclined squealer tip designs at 3.04 %tip clearance. Since the tip vortex that is originating from the rotor tip pressure side is re-positioned by squealer and inclined squealer tips as mentioned in previous sections, total pressure distribution at the rotor tip where $r/R_{tip} \geq 0.3$ is enhanced. A significant portion of the blade span above $r/R_{tip} \geq 0.3$ starts producing a measurably higher total pressure as shown in Figure 6.40. The total pressure augmentation from the tip treatments are particularly effective near the blade tip where $r/R_{tip} \geq 0.85$. For the larger tip clearance 5.17 %, using inclined squealer tip also improved the total pressure distribution near the rotor tip region and performed better than the smaller tip clearance baseline tip performance at 3.04 %.

6.5 Summary

Experimental investigations and computational analysis were performed for the development of novel tip geometries that are applicable to ducted fans used in VTOL UAV systems.

A 22" diameter ducted fan test system was designed and manufactured for experimental investigations of tip leakage flow in ducted fans. Fan rotor exit total pressure surveys and duct inlet total pressure and velocity measurements were carried out for aerodynamic performance quantifications. A six component force and torque transducer was used for aeromechanic performance quantification.

A high resolution simulation of the flow field around the rotating fan rotor blades was performed by solving Reynolds Averaged Navier Stokes equations using a general purpose solver ANSYS-CFX. The computational analysis was extensively used in designing the tip treatments.

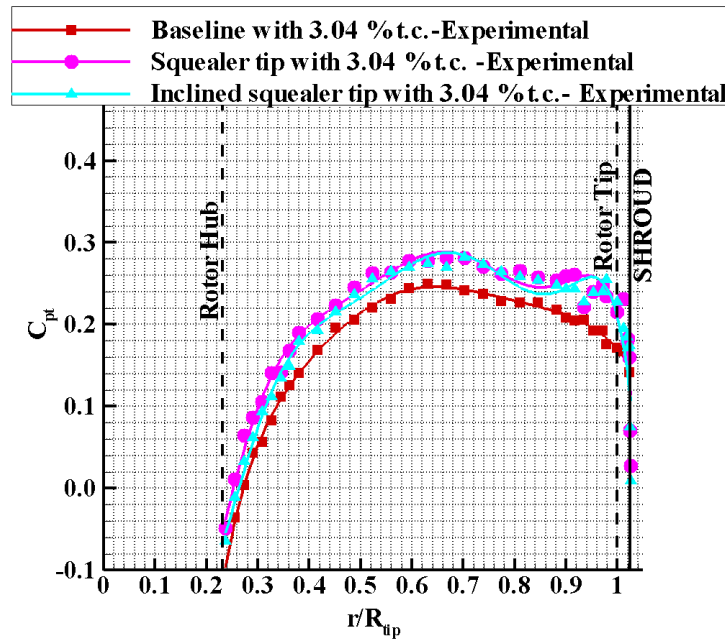


Figure 6.40. Total pressure measured at downstream of the rotor at 2400 rpm for squealer tips wit 3.04 % tip clearance

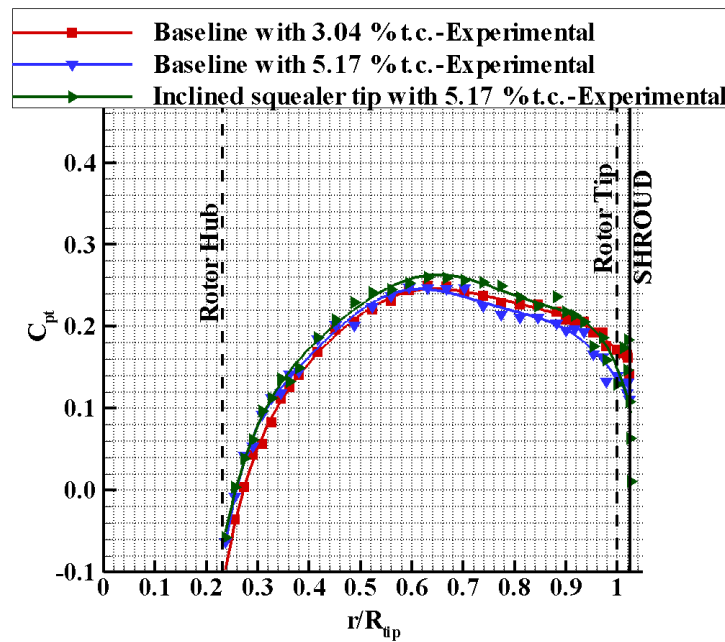


Figure 6.41. Total pressure measured at downstream of the rotor at 2400 rpm for squealer tips wit 5.17 % tip clearance

When 3.04 % clearance results are compared to the rotor only result, up to 38% increase in ducted fan hover efficiency can be obtained at higher rotor speeds. That increase is mainly the result of using duct around an open rotor.

A steady-state RANS simulation of fan rotor blades and duct geometry showed very good agreement with the measured total pressure distribution especially near the tip region of the rotor in the 22" diameter ducted fan research facility.

Experimental investigations of baseline rotor showed that decreasing tip clearance increased the thrust obtained from the ducted fan in hover condition. Decreasing the tip clearance from 3.04 % to 1.71 % also increased hover efficiency of the system by 17.85 % at higher rotor speeds.

When the tip clearance increased from 3.04 % to 5.17 %, Up to 18.1 % drop in hover efficiency was observed .

Five different tip treatments were designed. Partial and full bump tip platform extensions, a combined full bump and partial squealer extension, full squealer and inclined full squealer were designed using computational analysis.

The loss mechanism of tip leakage flow can be divided into two parts: losses due to the “*blockage*” effect of leakage flow itself and losses due to the interaction of leakage jet/vortex and rotor blade tip pressure side. This complex interaction usually stalled tip of the blade. Increasing the tip clearance from 3.04% to 5.17 % increased both losses.

The losses generated were highly related to the tip vortex traveling direction. If the tip vortex traveled radially inward, then the losses related to the blockage effect influenced a larger portion of the blade span and the rotor tip stall was more pronounced.

A full squealer rotor tip was effective in changing the direction of the tip vortex. The tip vortex was pushed radially out to the shroud area. The computational

results showed that the squealer tip successfully blocked the tip vortex between leading edge and mid-chord of the rotor tip profile.

An inclined full squealer tip was also conceived to move tip vortex originating location close to the trailing edge by leaving more space to the tip vortex to fill between squealer and suction side of the rotor tip. This configuration has successfully moved vortex away, near the trailing edge.

Overall aeromechanic performance gains obtained by using tip platform extensions were assessed from computations. Pressure side tip platform extensions were reduced thrust levels obtained from the ducted fan.

The best performing profiles were full and inclined full squealer extensions. Full squealer tip extension increased thrust of the ducted fan by 6.04 % and reduced the leakage mass flow rated by 29.3 % compared to the baseline rotor tips. Inclined squealer tips increased the thrust by 10.73 % while reducing the leakage mass flow rate by 31.0 % .

Experimental investigation was also performed by manufacturing squealer and inclined squealer tip extensions for 3.04 % tip clearance and inclined squealer tip extensions for 5.17 % tip clearance. Solid models of tip extensionpieces originally developed computational purposes were directly used to manufacture experimental models in a rapid prototyping process.

Aeromechanic and aerothermodynamic measurements showed that using full inclined squealer tips with 5.17 % tip clearance is equivalent to working with a 3.04 tip clearance baseline rotor. The squealer and inclined squealer tips at 3.04 % tip clearance also improved performance of the fan rotor. This operation was equivalent to working with a baseline rotor at 1.71 % tip clearance. This feature of the tip treatments allows using treated rotor blades at larger clearances while performing as well as the operating at much smaller clearances.

Chapter **7**

Conclusions and Future Work

Ducted fan based vertical lift systems are excellent candidates to be the next generation vertical lift aircraft, with many potential applications in general aviation and military missions for manned and unmanned systems. Ducted fans provide improved performance and safety, and lower noise levels compared to an open rotor. These three characteristics make them one of the most popular choices in vertical lift systems. Although a great quantity of work has been performed on ducted propellers and fans, there has been limited number of studies on the effect of duct on the performance of rotor blade in hover and forward flight where inlet flow of the ducted fan is highly distorted. Distorted inlet flow has resulted in lip separation occurring on the inner side of the lip section severely limits the lift generation and controllability of vertical lift systems. Inlet flow distortions passing through a typical ducted fan rotor became increasingly detrimental with elevated forward flight velocity. Fan rotor tip leakage flow has been another source of aerodynamic performance loss for ducted fan systems in hover and forward flight. Tip leakage has been pressure driven flow from pressure side to the suction side of the fan rotor blade, significantly affecting the overall performance of VTOL UAV systems.

This thesis had three major objectives: first, to investigate and improve the aerodynamic performance of the ducted fan in forward flight, and second, to investigate and reduce the effect of aerodynamic performance loss occurring due to finite tip clearance, and third, to constitute a reliable set of experimental data for validation of analytical and computational tools, used in the further development

of ducted fans applicable to VTOL UAVs.

7.1 Summary and Conclusions

A combination of experimental and computational investigations were used to achieve the goals of this study. Experimental techniques including quantitative and qualitative investigations were presented. Qualitative investigation of flow around the ducted fan was studied using smoke flow visualization. Quantitative measurements consisted of 2D and 3D velocity measurements using planar and stereoscopic Particle Image Velocimetry (PIV and SPIV), high resolution total pressure measurements downstream of the rotor exit using Kiel total pressure probes and high speed six component force and torque measurements in hover condition. The computational techniques included radial equilibrium based rotor model in hover and forward flight and three dimensional Reynolds-Averaged Navier Stokes based CFD model of fan rotor in hover. This research has utilized experimental and computational techniques to investigate major problems of ducted fan vertical lift systems in two categories: forward flight related issues and tip leakage flow related issues.

7.1.1 Forward Flight Related Investigations

The first phase of this research consisted of aerodynamic performance investigation of 5" diameter ducted fan in hover and forward flight at 90° angle of attack (edgewise flight) as outlined in chapter 2. The velocity field around the ducted fan was measured using a planar PIV system. Axial and radial velocity components at the inlet/exit region of the ducted fan were measured in hover and forward flight at 6m/s. The effect of changing rotational speed was also investigated. Beside the experimental study, a computational study based on solving incompressible Reynolds-Averaged Navier-Stokes (RANS) equations was carried out. The specific radial equilibrium based rotor model (REBRM) was developed and implemented into the RANS computations.

More detailed experimental and computational investigation around the 5" diameter ducted fan which was designed for vertical lift systems was carried out in chapter 4. Total pressure measurements at the exit of the fan rotor to investigate the effect forward flight on the fan rotor performance were obtained in a low speed wind tunnel. Total pressure measurements were carried out at 4 equiangular circumferential locations around the ducted fan at 10 m/s forward flight velocity, at 90° angle of attack. Total pressure measurements for different forward flight speeds were also performed. Smoke flow visualization of ducted fan inflow in forward flight was also performed for qualitative investigation. The effect of tip leakage flow and its behavior in forward flight was also mentioned in this chapter.

Development of a novel ducted fan inlet flow conditioning concept that will significantly improve the performance and controllability of ducted fan based vertical lift systems was described in chapter 3 by making use of the ducted fan aerodynamic investigations discussed in chapter 2 and part of the chapter 4. The new Double Ducted Fan (DDF) concept developed in this study deals with most of the significant technical problems in ducted fans operating at almost 90° angle of attack, in the forward flight mode. The current concept uses a secondary stationary duct system to control "*inlet lip separation*" related momentum deficit at the inlet of the fan rotor occurring at elevated forward flight velocities. The DDF is self-adjusting in a wide forward flight velocity regime. DDF's corrective aerodynamic influence becomes more pronounced with increasing flight velocity due to its inherent design properties. The design of the DDF was performed by using the numerical solutions obtained from REBRM-RANS simulations which were developed in chapter 2. The most optimal approach was summarized after evaluating nine different double ducted fan geometries for a wide range of forward flight velocities.

7.1.1.1 Conclusions

The following conclusions are drawn from the forward flight related results,

1. The results of PIV measurements have proven that the performance of the

ducted fan was adversely affected from the forward flight velocity. By the effect of the forward flight velocity, a separation region that restricts the effective breathing area of the fan rotor, was always observed at the leading side of the ducted fan. That separation bubble has proven to affect the exit flow of the fan rotor.

2. By the introduction of inlet distortion at the leading side (windward side), the flow characteristics of the fan were highly altered compared to the fan design conditions.
3. Exit total pressure of the fan rotor was measured at 4 circumferential stations during forward flight. The most significant total pressure losses occurred at the leading side (0°) for forward flight condition. Distortions at the inlet of the fan rotor and inlet lip separation, which were also observed in PIV velocity results, stalled the tip of the rotor blade and resulted in a performance loss along 80 % of blade span.
4. Reduced thrust generation from the upstream side of the duct was observed due to the rotor breathing low-momentum re-circulatory turbulent flow.
5. Forward flight conditions caused separation from the rotor hub in this highly three dimensional and complex inlet flow environment. The existence of inlet lip separation arranged the streamlines at the inlet section in such a way that a more pronounced impingement of the inlet flow on the hub surface was observed.
6. The total pressure loss was increased by elevated forward flight velocity. For lower speeds, the regions near the rotor tip was affected. As the flight speed was increased, inlet flow distortion related effects were more pronounced. For 20 m/s it was obvious that the rotor had tremendous difficulty to breath and unsteady effects were dominant.
7. Unlike the leading side, the trailing side of the ducted fan is positively affected from forward flight velocity. More favorable inlet flow conditions near the trailing side of the rotor leads to a more effective rotor energy addition process. A severe imbalance of the duct inner static pressure field resulting

from the low momentum fluid entering into the rotor on the leading side and high momentum fluid unnecessarily energized on the trailing side of the rotor.

8. The experimental results show that an increase in the rotational speed of the fan enhances the axial velocity component at the inlet and exit sections in hover condition, as expected. That increase in the rotational speed of the fan rotor has proven to improve the performance of the ducted fan in forward flight due to improved axial momentum change in the ducted fan. An increase in the rotational speed of the 5" diameter fan from 9000 rpm to 15000 reduced the effect of the leading side separation bubble.
9. The REBRM RANS simulations was able to predict the inlet flow axial flow velocity distribution well at 9000 rpm hover and forward flight conditions.
10. A new concept that will significantly reduce the inlet lip separation related performance penalties in the forward flight zone was developed and named as "*DOUBLE DUCTED FAN*" (DDF). The concept development uses a time efficient 3D computational viscous REBRM RANS flow solution approach developed specifically for ducted fan flows.
11. Case-B was the best DDF configuration designed. It has improved mass flow rate passing from the duct by 40 % and improved thrust force obtained from the ducted fan by 56.2 % relative to baseline duct in forward flight condition.

7.1.2 Tip Leakage Related Investigations

The second phase of this research aimed to investigate and reduce the effect of aerodynamic performance loss occurring due to increasing tip clearance. A pressure side driven flow occurs at fan rotor blade tips from pressure side to suction side which is also known as "*tip leakage*" and generates aerodynamic loss for ducted fans. In this research,a preliminary investigation of tip leakage was performed on 5" diameter ducted fan for hover and forward flight conditions which has been discussed in part of chapter 4. Part of this chapter constitutes a baseline study for understanding the effects of tip leakage loss in hover and forward flight. Rotor

exit total pressure measurements were performed in 4 equiangular circumferential locations for two different tip clearances. Beside the experimental technique, development of a steady-state RANS simulation of fan rotor blades and duct geometry was also discussed in this chapter.

An experimental method for designing tip platform extensions for a 36" diameter axial flow fan was discussed in chapter 5. This study used stereoscopic particle image velocimetry for measuring 3D velocity measurements at the fan rotor exit. Velocity components were measured for two different tip clearances for quantification of performance loss due to tip leakage. Five different tip platform extensions were introduced especially on the pressure side of the fan blades. A comparison of their performances was presented in chapter 5. This study has clearly demonstrated the effectiveness of pressure side tip extensions for axial flow fans. It should be noted that axial fan used in this study is considered to be a relatively low disk loading fan.

A more detailed experimental and computational investigation of tip leakage flow was performed on a 22" diameter ducted fan which was designed specifically for vertical lift systems carried out in chapter 6. The results of this study using a realistic ducted fan research facility was presented in chapter 6. The ducted fan test system that includes a 22" ducted fan was custom designed and manufactured. Experimental instrumentation of the system included a radial traversing kiel total pressure probe at the exit of the fan rotor, a kiel total pressure and pitot probe at the inlet of the ducted fan and a six component force and torque transducer underneath of the ducted fan. Baseline fan rotor exit flow performance and ducted fan aeromechanic performance were measured and constituted a good set data for computational studies. Steady state RANS simulation of the fan rotor flows which was developed in chapter 4 were validated by using experimental measurements. Using the knowledge gained on the rotor tip pressure side extensions for axial flow fans, design of tip treatments was performed in chapter 6 for 22" diameter ducted fan system. Partial and full pressure side bump, full pressure side bump and partial squealer , full pressure side squealer and inclined pressure side squealer were designed and analyzed using RANS simulations. The best performing treatments

were the full and inclined pressure side sealers. These treatments were manufactured using a stereolithography based rapid prototyping technique. Tip treated fan rotor exit performance and ducted fan aeromechanic performance were tested.

7.1.2.1 Conclusions

The following conclusions are drawn from the forward flight related study,

1. Tip clearance is one of the most important parameters affecting ducted fan rotor performance. Decreasing tip clearance from 5.8 % to 3.6 % increased fan rotor exit total pressure by 17 % at mid span for hover condition for 5" diameter ducted fan test system. Hover tests also indicated that smaller tip gap increased overall performance of the fan rotor along the span wise direction.
2. Increasing tip gap height resulted in a decrease in total pressure distribution in forward flight. Especially near the tip region increasing tip gap height by approximately 40 %, doubled the total pressure loss at the leading side of the ducted fan at forward flight, for the 5" diameter ducted fan.
3. It is possible to reduce the tip leakage mass flow rate using the tip platform extensions. Profile 2 showed the best tip treatment performance out of the five new tip platform extensions designed for 36" diameter axial flow fan.
4. Tip treatment experiments performed at high volumetric flow rate/low pressure rise axial flow fan clearly showed the minimization of the tip vortex mass flow rate by significantly reducing the tangential components near the tip. The magnitude of this reduction is about one third of the rotor exit total velocity in the core of the passage exit.

5. Tip platform extensions perform their function by minimizing the tip leakage flow mass flow rate near the blade tip even under the high loading conditions. This effect eventually provides a significant gain in axial velocity component.
6. On the average, the gain in total velocity magnitude at the rotor exit is about 17% throughout the blade span for 36" diameter axial flow fan.
7. Decreasing the tip clearance from 3.04 % to 1.71 % also increased hover efficiency of the system by 17.85 % at higher rotor speeds for 22" ducted fan system in hover condition.
8. The loss mechanism of tip leakage flow can be divided into two parts: losses due to the "*blockage*" effect of leakage flow itself and losses due to the interaction of leakage jet/vortex and rotor blade tip pressure side. This complex interaction usually stalled tip of the blade. Increasing the tip clearance from 3.04% to 5.17 % increased both losses.
9. The losses generated were highly related to the tip vortex traveling direction. If the tip vortex traveled radially inward than the losses related to blockage effect influenced a larger portion of the blade span and the rotor tip stall was more effective.
10. Full squealer rotor tips was effective in changing the direction of the tip vortex. The tip vortex was pushed radially out to the casing area. The computational results showed that squealer tip successfully blocked the tip vortex between the leading edge and mid-chord of the rotor tip profile.

The best performing profiles were full and inclined full squealer extensions. Full squealer tip extension increased thrust of the ducted fan by 6.04 % and reduced the leakage mass flow rated by 29.3 % compared to the baseline rotor tips. Inclined squealer tips increased the thrust by 10.73 % while reducing the leakage mass flow rate by 31.0 % .

11. Aeromechanic and aerodynamic measurements showed that using full inclined squealer tips with 5.17 % tip clearance is equivalent to working with a 3.04 % tip clearance baseline rotor. The squealer and inclined squealer tips at 3.04 % tip clearance also improved performance of the fan rotor. This operation was equivalent to working with a baseline rotor at 1.71 % tip clearance. This feature of the tip treatments allows using treated rotor blades at larger clearances while performing as well as the operating at much smaller clearances.
12. A steady-state RANS simulation of the flow around rotor blades and duct geometry showed very good agreement with the measured total pressure distribution especially near the tip region. The slight discrepancy near the hub wall attributed to the re-circulatory hub endwall flows occurring at relatively low Re numbers

7.2 Recommendations for Future Work

This experimental and computational study has addressed two major problems of ducted fans designed for vertical lift systems:

- Aerodynamic performance losses in forward flight applications
- Tip leakage losses related with the interaction of duct and fan rotor

Experimental and computational investigation of the flow field around the ducted fan was performed in this study. Radial equilibrium based rotor model (REBRM) was developed and implemented into 3D RANS solutions and used in hover and forward flight calculations. There are however certain limitations that cannot be addressed in this computational method. The tip leakage flow loss models can be implemented to REBRM model for better accuracy. A hub endwall viscous loss model can also be considered in future studies.

Double ducted fan (DDF) was one of the major contributions of this thesis. It was designed to condition the inlet flow of the ducted fan in forward flight against severe lip separation. There may be many improvements of DDF concept. DDF

can be designed and implemented partially only at the leading side of the ducted fan. Combining DDF with control surfaces may also be possible to improve the performance and controllability of DDF. The applicability of DDF with an inflatable duct system can be a topic for further study.

The tip leakage losses were also investigated in this thesis. Pressure side tip platform extensions and squealer tips were developed and tested for improving the performance of the fan rotor with larger tip clearance in hover. Pressure side squealer tips found to be effective in reducing tip leakage related losses. Beside pressure side squealers, suction side squealer tips may be designed and investigated. Optimization based parametric design algorithm may be developed and coupled with 3D RANS solutions for designing more advanced squealer tips. Casting treatments also offer tip leakage loss reduction, improvements on aeromechanic fan rotor performance and lower noise levels. Their application to ducted fans may be performed.

Finally, the fan rotor performance may also be enhanced by 3D rotor blade aerodynamic design which is specifically optimized for distorted inlet flow. Computational and experimental results discussed in this thesis indicated that hub separation is another source of loss in ducted fans. Aerodynamic performance of the rotor hub region may also be improved by optimized fan rotor design.

Further study of the tip treatments manufactured out of flexible rubber type material may prove to be useful in operating VTOL UAV ducted fans at a relatively large clearance with reduced tip leakage mass flow rate. The future flexible tip designs may be beneficial during “*rubbing*” incidents while they are clearly reducing the tip leakage mass flow rate in the ducted fans.

Implementation Radial Equilibrium Theory Based Rotor Model in ANSYS FLUENT Using User Defined Functions

A.1 Introduction

A user-defined function, or UDF, is a coded function that is developed by the user for dynamic loading into ANSYS-FLUENT solver environment to enhance the standard features of the code. UDFs are written in the C programming language using any text editor and the source code is saved with a .c extension. [84] The theoretical approach leading to the development of the Radial Equilibrium Based Rotor model was defined in section 2.4

A.2 UDF for Fan Boundary Condition "*fan.c*"

Implementation of radial equilibrium based rotor model into FLUENT is done by using UDF given below:

```

#include <stdio.h>
#include <string.h>
#include <math.h>
=====
c This program is invoked at intervals by Rampant to read a
c profile-format file that contains radially averaged data at
c a fan face, compute new pressure-jump and swirl-velocity
c components, and write a new profile file that will subsequently
c be read by Rampant to update the fan conditions.
c
c Usage: fatest < input_profile > output_profile
=====

#define npmax 900

const char zone[10] = "fan-5"; /* fan-->zone name of fan;5-->zone id of fan -->USER INPUT */
static int i,inp; /* input: number of profile points*/
static int iptype; /* input: profile type (0=radial, 1=point)*/
static float ir[npmax]; /* input: radial positions*/
static float ip[npmax]; /* input: pressure*/
static float idp[npmax]; /* input: pressure-jump*/
static float irho[npmax]; /* input: density*/
static float iva[npmax]; /* input: axial velocity*/
static float ivr[npmax]; /* input: radial velocity*/
static float ivt[npmax]; /* input: tangential velocity*/
static char zonename[50];
static int status,len;
static char outfile[50],infile[50];
/* MODIFIED BY ALI AKTURK @ 12/2008 */
float omega;
float param1;
float param2;
float param3;
float tot1;
float tot2;
int rfanprof();
void wfanprof();
int main()
{
status = rfanprof();
if (status!= 0)
{
printf("error reading input profile file /n");
}
else
{
for(i = 1;i<= inp;i++)
{
/* MODIFIED BY ALI AKTURK @ 06/2009 */
}
}
}

```

```

param1=0.0;
param2=0.0;
param3=0.0;
omega = 942.477; /* Omega in 1/s */ /* 9000 RPM*/
param1 = -436.43*ir[i]*ir[i] + 54.082*ir[i] - 0.7195;
param2 = omega*ir[i] - iva[i]*tan(param1);
param3 = param2/cos(param1);

idp[i] = irho[i]*param2*(omega*ir[i]-0.5*param2); /* variation of pressure-jump */
ivt[i] = -1.0*param2; /* variation of tangential velocity */
ivr[i] = 0.0; /* variation of radial velocity */
}
wfanprof();
}
return 0;
idp[inpl]=0;
}
static char readbracket(FILE *fd)
{
char temp;
do
{
temp = getc(fd);
}while ((temp != '(') && temp != ')');
return temp;
}

int rfanprof()
{
FILE *fd;
int n,n_field;
int n_data;
char field[50];
sprintf(outfile,"%s-out.prof",zone);

/*printf("Reading file.... %s \n\n",outfile);*/
fd = fopen(outfile,"r");
readbracket(fd);
readbracket(fd);
fscanf(fd,"%s",zonename);
fscanf(fd,"%s",field);
fscanf(fd,"%d",&inp);
readbracket(fd);
/* printf("No Of Points =%d \n\n",inp);*/
if (strcmp(zonename,zone) != 0)
{
/* printf("zone name is not same \n");*/
return 1;
}
if (inp > npmax)

```

```

{
    fprintf(stderr, "\nread-fan-profile: Too many data points: %d > %d.\n",
    inp, npmax);
    return 1;
}
if (strcmp(field,"radial") == 0)
    iptype = 0;
else if (strcmp(field,"point") == 0)
{
    iptype = 1;
    printf ("Cannot read point type of specification \n");
}
else
{
    fprintf(stderr, "\nread-fan-profile: Wrong profile type: %s instead of radial or point.\n",
    field);
    return 1;
}
readbracket(fd);
do
{
    char temp[50];
    fscanf(fd,"%s",temp);
    strcpy(field,temp);
    if (strcmp(field,"r")==0)
    {
        for(i=1;i<=inp;i++)
        fscanf(fd,"%f",&ir[i]);
        readbracket(fd);
    }
    else if(strcmp(field,"pressure")==0)
    {
        for(i=1;i<=inp;i++)
        fscanf(fd,"%f",&ip[i]);
        readbracket(fd);
    }
    else if(strcmp(field,"pressure-jump")==0)
    {
        for(i=1;i<=inp;i++)
        fscanf(fd,"%f",&idp[i]);
        readbracket(fd);
    }
    else if(strcmp(field,"density")==0)
    {
        for(i=1;i<=inp;i++)
        fscanf(fd,"%f",&irho[i]);
        readbracket(fd);
    }
    else if(strcmp(field,"axial-velocity")==0)
    {

```

```

for(i=1;i<=inp;i++)
fscanf(fd,"%f",&iva[i]);
readbracket(fd);
}
else if(strcmp(field,"radial-velocity")==0)
{
for(i=1;i<=inp;i++)
fscanf(fd,"%f",&ivr[i]);
readbracket(fd);
}
else if(strcmp(field,"tangential-velocity")==0)
{
for(i=1;i<=inp;i++)
fscanf(fd,"%f",&ivt[i]);
readbracket(fd);
}
else
{
/* printf("Unrecognised variable name while reading the file \n"); */
return 1;
}
}
while(readbracket(fd) != ')');
return 0;
}
void wfanprof()
{
/* writes a FLUENT profile file for input by the user fan model */
FILE * out;
char * typename;
sprintf(infile,"%s-in.prof",zone);
out = fopen(infile,"w");
/*printf("Writing File.....%s \n\n",infile);*/
if (iptype==0)
typename = "radial";
else
typename = "point";
fprintf(out, "(");
fprintf(out, "(%s %s %d)\n",zone,typename,inp);
fprintf(out, "(r \n");
for (i=1;i<=inp;i++)
fprintf(out,"%f \t",ir[i]);
fprintf(out,")\n");
fprintf(out,(pressure \n");
for (i=1;i<=inp;i++)
fprintf(out,"%f \t",ip[i]);
fprintf(out,")\n");
fprintf(out,(pressure-jump \n");
for (i=1;i<=inp;i++)
fprintf(out,"%f \t",idp[i]);
}

```

```
fprintf(out,")\n");
fprintf(out,"(density \n");
for (i=1;i<=inp;i++)
fprintf(out,"%f \t",irho[i]);
fprintf(out,")\n");
fprintf(out,"(axial-velocity \n");
for (i=1;i<=inp;i++)
fprintf(out,"%f \t",iva[i]);
fprintf(out,")\n");
fprintf(out,"(radial-velocity \n");
for (i=1;i<=inp;i++)
fprintf(out,"%f \t",ivr[i]);
fprintf(out,")\n");
fprintf(out,"(tangential-velocity \n");
for (i=1;i<=inp;i++)
fprintf(out,"%f \t",ivt[i]);
fprintf(out,")\n");
fprintf(out,")\n");
}
```

Uncertainty Analysis

B.1 Introduction

A sample of random uncertainty calculation is shown in this section. The propagation of uncertainty is calculated by Central Limit Theorem. Details of the theorem can be found in [93, 94]. The expansion for the total pressure coefficient is given in equation B.1.

$$C_{pt} = \frac{P_{te} - P_{ti}}{\frac{1}{2}\rho U_m^2} \quad (\text{B.1})$$

Total random uncertainty is calculated by calculating and combining all the standard deviations for all measured parameters used in the equation B.1. Statistically stable solution requires two steps: [94]

$$\sigma_{Result} = \sqrt{\sum_{\text{For all Measurements}} \sigma^2} \quad (\text{B.2})$$

$$\text{Random Uncertainty} = \frac{t_{95}\sigma_{Result}}{\sqrt{N}} \text{ where } N \text{ is the sample size} \quad (\text{B.3})$$

Student's t_{95} is tabled as a function of degrees of freedom. For a large sample size, assuming $t_{95}=2$ is an acceptable approximation. This suggestion was accepted by all major committees [94].

	P_{ti}	P_{te}	U_m
σ	0.0027	0.01448	0.06846

Table B.1. Standard Deviations (σ) calculated for P_{ti}, P_{te} and U_m

Table B.1 shows standard deviations calculated for all parameters used in the equation B.1. Sample size for the experiments was chosen as 5000. Tabulated standard deviations are inserted into equation B.2 to calculate random uncertainty of total pressure coefficient (C_{pt}). Random uncertainty for C_{pt} is calculated as ± 0.002 .

Six Component Force and Torque Transducer Calibration and Accuracy Reports

The calibration accuracy report provided by ATI [92] is attached. The report is divided into three sections. The "Full-Scale Loads" section lists the transducers rated range for each axis. The second section, "Applied Load", lists the loads applied during calibration and testing. These sections are shown in figure C.1. The final section, "Full-Scale Error", shows the sensor systems measurement error as a percentage of full scale for each axis in each loading case and shown in figure C.2.

Full-Scale Loads						
	Fx	Fy	Fz	Tx	Ty	Tz
	330	330	990	30	30	30

Applied Loads						
	Fx	Fy	Fz	Tx	Ty	Tz
1	0.000	200.170	0.000	-22.864	0.000	0.000
2	-200.170	0.000	0.000	0.000	-22.864	0.000
3	0.000	-200.170	0.000	22.864	0.000	0.000
4	200.170	0.000	0.000	0.000	22.864	0.000
5	0.000	289.134	0.000	-10.997	0.000	0.000
6	-289.134	0.000	0.000	0.000	-10.997	0.000
7	0.000	-289.134	0.000	10.997	0.000	0.000
8	289.134	0.000	0.000	0.000	10.997	0.000
9	0.000	173.481	0.000	-2.203	0.000	-19.829
10	0.000	173.481	0.000	-2.203	0.000	19.829
11	-173.481	0.000	0.000	0.000	-2.203	-19.832
12	-173.481	0.000	0.000	0.000	-2.203	19.840
13	0.000	-173.481	0.000	2.203	0.000	-19.829
14	0.000	-173.481	0.000	2.203	0.000	19.829
15	173.481	0.000	0.000	0.000	2.203	-19.840
16	173.481	0.000	0.000	0.000	2.203	19.832
17	0.000	0.000	266.893	-20.337	0.000	0.000
18	0.000	0.000	266.893	0.000	-20.337	0.000
19	0.000	0.000	266.893	20.337	0.000	0.000
20	0.000	0.000	266.893	0.000	20.337	0.000
21	0.000	0.000	889.644	0.000	0.000	0.000
22	0.000	0.000	-889.644	0.000	0.000	0.000
23	0.000	0.000	-266.893	20.337	0.000	0.000
24	0.000	0.000	-266.893	0.000	20.337	0.000
25	0.000	0.000	-266.893	-20.337	0.000	0.000
26	0.000	0.000	-266.893	0.000	-20.337	0.000

Figure C.1. Full scale loads and applied loads during calibration [92]

	Full-Scale Error					
	Fx	Fy	Fz	Tx	Ty	Tz
1	0.00%	0.00%	0.06%	0.04%	0.11%	0.12%
2	0.07%	-0.04%	0.10%	0.00%	0.00%	0.03%
3	-0.03%	0.00%	0.08%	0.03%	0.10%	0.01%
4	0.11%	-0.03%	0.06%	-0.11%	-0.01%	0.03%
5	-0.06%	0.06%	0.08%	-0.05%	0.01%	0.05%
6	0.04%	0.00%	0.07%	-0.02%	-0.05%	0.11%
7	-0.07%	0.03%	0.08%	0.07%	0.02%	0.14%
8	0.06%	-0.03%	0.09%	-0.01%	0.03%	0.13%
9	-0.02%	-0.01%	0.04%	-0.02%	0.13%	0.02%
10	-0.02%	0.03%	0.04%	0.08%	-0.11%	0.02%
11	0.02%	-0.01%	0.03%	-0.12%	0.09%	0.01%
12	0.02%	-0.03%	0.02%	0.08%	0.03%	0.01%
13	-0.01%	0.04%	0.03%	-0.04%	-0.12%	0.00%
14	0.02%	0.04%	0.03%	-0.08%	0.15%	0.01%
15	-0.01%	0.00%	0.03%	0.17%	-0.01%	0.01%
16	-0.04%	-0.02%	0.03%	-0.10%	0.01%	0.00%
17	-0.04%	-0.01%	-0.02%	0.06%	-0.04%	-0.02%
18	0.09%	-0.02%	-0.03%	-0.03%	0.17%	-0.01%
19	-0.04%	-0.02%	0.00%	-0.03%	0.03%	0.04%
20	-0.04%	-0.05%	0.01%	0.01%	0.11%	0.07%
21	0.06%	-0.15%	0.02%	-0.05%	-0.39%	-0.04%
22	0.05%	-0.14%	-0.04%	-0.02%	-0.24%	-0.03%
23	0.00%	-0.03%	0.02%	0.03%	0.04%	0.01%
24	0.06%	-0.03%	0.04%	-0.01%	-0.17%	-0.02%
25	-0.03%	-0.04%	0.06%	-0.04%	0.10%	0.00%
26	-0.03%	-0.05%	0.04%	-0.08%	-0.20%	0.05%

Figure C.2. Full scale errors [92]

Bibliography

- [1] Winchester, J., 2005, *The World's Worst Aircraft: From Pioneering Failures to Multimillion Dollar Disasters*, Amber Books Ltd., London.
- [2] Metz, C. D., 1988, “Use of fiber optic data links in marine corps unmanned vehicles,” *Unmanned Systems/AUVS-88*, **6**(4), pp. 13–53.
- [3] Cycon, J. P., 1992, “Sikorsky aircraft uav program,” *Vertiflite*, **38**(3), pp. 26–30.
- [4] Micropilot, “Clients using micropilot product:mass helispy,” <http://www.micropilot.com/clients.htm>.
- [5] Lipera, L., Colbourne, J., Rotkowitz, M., and Patangui, P., 2001, “The micro craft istar micro air vehicle: Control system design and testing,” , pp. 44–56.
- [6] Michelson, R., 1999, “Traffic surveillance drone,” <http://avdil.gtri.gatech.edu/RCM/> DroneProject.html.
- [7] 2006, “Bae continues ducted fan development,” *Vertiflite*.
- [8] 2004, “Goldeneye ducted-fan vtol uav,” Defense Update International Online Defense Magazine, (2).
- [9] McHale, J., 2007, “Honeywell micro air vehicles protect troops against ieds,” Military and Aerospace Electronics.
- [10] Avanzini, G. and Matteis, G., 2002, “Design of a shipboard recovery system for a shrouded-fan uav,” International Council of the Aeronautical Sciences.
- [11] Dorman, H. A. and Dorman, B. A., 1960, “Aircraft having a plurality of annular wings,” U.S. Patent No: 2951661.
- [12] Bright, C. E., 1961, “Ducted fan aircraft,” U.S. Patent No: 2968453.

- [13] Yoeli, R., 2002, "Ducted fan vehicles particularly useful as vtol aircraft," U.S. Patent No: 6464166.
- [14] Piasecki, F. N., 1965, "Flying platform," U.S. Patent No: 3184183.
- [15] Fletcher, C. I., 1961, "Ducted fan aircraft," U.S. Patent No: 2988301.
- [16] Boyd, E. S., Mallory, M., and Skinner, L. R., 1970, "Vertical takeoff and landing aircraft," U.S. Patent No: 3519224.
- [17] Wen, L., 1977, "Vertical takeoff and landing aircraft," U.S. Patent No: 4049218.
- [18] Moller, P. S., 1989, "Robotic or remotely controlled flying platform," U.S. Patent No: 4795111.
- [19] Cycon, J. P., Rosen, K. M., and Whyte, A. C., 1992, "Unmanned flight vehicle including counter rotating rotors positioned within toroidal shroud and operable to provide all required vehicle flight control," U.S. Patent No: 5152478.
- [20] Moffit, R. C. and Owen, S. J., 1992, "Shroud geometry for unmanned aerial vehicles," U.S. Patent No: 5150857.
- [21] Flemming, R. J., Rosen, K. M., and Sheehy, T. W., 1995, "Ancillary aerodynamic structures for an unmanned aerial vehicle having ducted, coaxial counter-rotating rotors," U.S. Patent No: 5419513.
- [22] Swinson, J., Walker, S., and James, T. J., 1999, "Horizontal and vertical take off and landing unmanned aerial vehicle," U.S. Patent No: 5890441.
- [23] Cycon, J. P., Scott, M. W., and DeWitt, C. W., 2001, "Method of reducing a nose-up pitching moment on a ducted unmanned aerial vehicle," U.S. Patent No: 6170778.
- [24] Cycon, J. P., Scott, M. W., and DeWitt, C. W., 2001, "Unmanned aerial vehicle with counter-rotating ducted rotors and shrouded pusher-prop," U.S. Patent No: 6270038.
- [25] Moller, P. S., 2002, "Stabilizing control apparatus for robotic or remotely controlled flying platform," U.S. Patent No: 6450445.
- [26] Wagner, J., Pruszynski, A., and Milde, K. F., 2005, "Vtol personal aircraft," U.S. Patent No: 6886776.
- [27] Yoeli, R., 2005, "Vehicles particularly useful as vtol vehicles," U.S. Patent No: 6883748.

- [28] Yoeli, R., 2007, "Ducted fan vtol vehicles," U.S. Patent No: 2007/0034739.
- [29] Yoeli, R., 2007, "Ducted fan vehicles particularly useful as vtol aircraft," U.S. Patent No: 7275712.
- [30] Abrego, A. I. and Bulaga, R. W., 2002, "Performance study of a ducted fan system," AHS Aerodynamics, Aeroacoustic , Test and Evaluation Technical Specialist Meeting.
- [31] Martin, P. and Tung, C., 2004, "Performance and flowfield measurements on a 10-inch ducted rotor vtol uav," 60th Annual Forum of the American Helicopter Society.
- [32] Fleming, J., Jones, T., Lusardi, J., Gelhausen, P., and Enns, D., 2004, "Improved control of ducted fan vtol uavs in crosswind turbulence," AHS 4th Decennial Specialist's Conference on Aeromechanics.
- [33] Graf, W., Fleming, J., and Wing, N., 2008, "Improving ducted fan uav aerodynamics in forward flight," 46th AIAA Aerospace Sciences Meeting and Exhibit.
- [34] Graf, W. E., 2005, *Effects of Duct Lip Shaping and Various Control Devices on the Hover and Forward Flight Performance of Ducted Fan UAVs*, Master's thesis, Virginia Polytechnic Institute and State University, Blacksburg, Virginia.
- [35] Lazareff, M., 2008, "Improving ducted fan uav aerodynamics in forward flight," 46th AIAA Aerospace Sciences Meeting and Exhibit.
- [36] Van Weelden, S. D., Smith, D. E., and Mullins, B. R., Jr., 1996, "Preliminary design of a ducted fan propulsion system for general aviation aircraft," AIAA 34th Aerospace Sciences Meeting and Exhibit.
- [37] Kriebel, A. R. and Mendehall, M. R., 1966, "Predicted and measured performance of two full-scale ducted propellers," CAL/USAAVLABS Symposium on Aerodynamic Problems Associated with V/STOL Aircraft, Vol II: Propulsion and Interference Aerodynamics.
- [38] Mort, K. W. and Gamse, B., 1967, "A wind tunnel investigation of a 7-foot-diameter ducted propeller," Tech. Rep. NASA TND-4142.
- [39] Mort, K. W. and Yaggy, P. F., 1962, "Aerodynamic characteristics of a 4-foot-diameter ducted fan mounted on the tip of a semispan wing," Tech. Rep. NASA TND-1301.

- [40] Yaggy, P. F. and Mort, K. W., 1961, "A wind-tunnel investigation of a 4-foot-diameter ducted fan mounted on the tip of a semispan wing," Tech. Rep. NASA TND-776.
- [41] Weir, R. J., 1988, "Aerodynamic design consideration for a free flying ducted propeller," AIAA Atmospheric Flight Mechanics Conference.
- [42] Pereira, J. L., 2008, *Hover and Wind-tunnel Testing of Shrouded Rotors for Improved Micro Air Vehicle Design*, Ph.D. thesis, University of Maryland, Maryland.
- [43] Martin, P. B. and Boxwell, D. A., 2005, "Design, analysis and experiments on a 10-inch ducted rotor vtol uav," AHS International Specialists Meeting on Unmanned Rotorcraft: Design, Control and Testing.
- [44] Lind, R., Nathman, J. K., and Gilchrist, I., 2006, "Ducted rotor performance calculations and comparisons with experimental data," 44th AIAA Aerospace Sciences Meeting and Exhibit.
- [45] He, C. and Xin, H., 2006, "An unsteady ducted fan model for rotorcraft flight simulation," 62th AHS Forum.
- [46] Chang, I. C. and Rajagopalan, R. G., 2003, "Cfd analysis for ducted fans with validation," 21th AIAA Applied Aerodynamics Conference.
- [47] Ahn, J. and Lee, K. T., 2004, "Performance prediction and design of a ducted fan system," 40th AIAA/ASME/SAE/ASEE Joint Propulsion Conference and Exhibit.
- [48] Ko, A., Ohanian, O. J., and Gelhausen, P., 2007, "Ducted fan uav modeling and simulation in preliminary design," AIAA Modeling and Simulation Technologies Conference and Exhibit.
- [49] Zhao, H. W. and Bil, C., 2008, "Aerodynamic design and analysis of a vtol ducted-fan uav," 26th AIAA Applied Aerodynamics Conference.
- [50] Peacock, R. E., 1982, "A review of turbomachinery tip gap effects part 1: Cascades," Int. J. Heat & Fluid Flow.
- [51] Peacock, R. E., 1982, "A review of turbomachinery tip gap effects part 2: Rotating machinery," Int. J. Heat & Fluid Flow.
- [52] Mikolajczak, A. A., 1975, "The practical importance of unsteady flow. unsteady phenomena in turbomachinery," AGARD CP 177.
- [53] Williams, D. D. and Yost, J., 1973, "Some aspects of inlet engine flow compatibility," J. Royal, Aero. Soc. LXXVII.

- [54] Peacock, R. E. and Overli, J., 1975, "Dynamic internal flows in compressors with pressure maldistributed inlet conditions. unsteady phenomena in turbomachinery," AGARD CP 177.
- [55] Lee, G. H., Baek, J. H., and Myung, H. J., 2003, "Structure of tip leakage in a forward-swept axial-flow fan," *Flow, Turbulence and Combustion*, **70**, pp. 241–265.
- [56] Jang, C. M., Furukawa, M., and Inoue, M., 2001, "Analysis of vortical flow field in a propeller fan by ldv measurements and les - parts i, ii," *Journal of Fluids Engineering*, **123**, pp. 748–761.
- [57] Storer, J. A. and Cumpsty, N. A., 1991, "Tip leakage flow in axial compressors," *Journal of Turbomachinery*, **113**.
- [58] Lakshminaraya, B., Zaccaria, M., and Marathe, B., 1995, "The structure of tip clearance flow in axial flow compressors," *Journal of Turbomachinery*, **117**, pp. 336–347.
- [59] Inoue, M., Kuroumaru, M., and Furukawa, M., 1986, "Behavior of tip leakage flow behind an axial compressor rotor," *Journal of Gas Turbine and Power*, **108**, pp. 7–14.
- [60] Furukawa, M., Inoue, M., Kuroumaru, M., Saik, i. K., and Yamada, K., 1999, "The role of tip leakage vortex breakdown in compressor rotor aerodynamics," *Journal of Turbomachinery*, **121**, pp. 469–480.
- [61] Fujita, H. and Takata, H., 1984, "A study on configurations of casing treatment for axial flow compressors," *Bulletin of the JSME*, **27**, pp. 1675–1681.
- [62] Moore, R. D., Kovich, G., and Blade, R. J., 1971, "Effect of casing treatment on overall and blade-element performance of a compressor rotor," Tech. Rep. TN-D6538, NASA.
- [63] Reynolds, B., Lakshminaraya, B., and Ravindranath, A., 1979, "Characteristics of near wake of a fan rotor blade," *AIAA Journal*, **17**, pp. 959–967.
- [64] Ravindranath, A. and Lakshminaraya, B., 1980, "Mean velocity and decay characteristics of near and far-wake of a compressor rotor blade of moderate loading," *Journal of Engineering for Power*, **102**, pp. 535–547.
- [65] Myung, H. J. and Baek, J. H., 1999, "Mean velocity characteristics behind a forward-swept axial-flow fan," *JSME Int. J.*, **42**, pp. 476–488.
- [66] Adrian, R., 1991, "Particle imaging techniques for experimental fluid mechanics," *Ann. Rev. Fluid Mech.*, **23**, pp. 261–304.

- [67] Kahveci, H. S. and C., C., 2006, "Flow around helicopter blade tip sections using 2d particle image velocimeter-part i," 11th Int. Symp. on Transport Phenomena and Dynamics of Rotating Machinery (ISROMAC-11), (136).
- [68] Kahveci, H. S. and C., C., 2006, "Flow around helicopter blade tip sections using a (3d) stereoscopic particle image velocimeter-part ii," 11th Int. Symp. on Transport Phenomena and Dynamics of Rotating Machinery (ISROMAC-11), (137).
- [69] Kahveci, H. S., 2004, *Implementation of a Stereoscopic PIV in Rotating Machinery Including Helicopter Rotor Flows*, Master's thesis, The Pennsylvania State University, University Park, PA.
- [70] Yoon, J. H. and Lee, S. J., 2004, "Exit flow field and performance of axial flow fans," Experimental Thermal and Fluid Science, **28**, pp. 791–802.
- [71] Yen, S. C. and Lin, F. K. T., 2006, "Exit flow field and performance of axial flow fans," Journal of Fluids Engineering, **128**, pp. 332–340.
- [72] Wernet, M. P., Van Zante, D., Strazisar, T. J., John, W. T., and Prahst, P. S., 2005, "Characterization of tip clearance flow in an axial compressor using 3-d digital piv," Experiments in Fluids, **39**, pp. 743–753.
- [73] Alessandro, C., Franco, R., and Sheard, A. G., 2010, "Shaping of tip end-plate to control leakage vortex swirl in axial flow fans," Journal of Turbomachinery, **132**(3).
- [74] Corsini, A., Perugini, B., Rispoli, F., Kinghorn, I., and Sheard, A. G., 2006, "Investigation on improved blade tip concept," ASME Paper, (GT2006-90592).
- [75] Corsini, A., Rispoli, F., and Sheard, A. G., 2006, "Development of improved blade tip end-plate concepts for low-noise operation in industrial fans," Proceedings of Conference on Modeling Fluid Flows CMMF06.
- [76] Corsini, A., Perugini, B., Rispoli, F., Kinghorn, I., and Sheard, A. G., 2007, "Experimental and numerical investigations on passive devices for tip-clearance induced noise reduction in axial flow fans," Proceedings of the 7th European Conference on Turbomachinery.
- [77] Corsini, A., Perugini, B., Rispoli, F., Sheard, A. G., and Kinghorn, I., 2007, "Aerodynamic workings of blade tip end-plates designed for low-noise operation in axial flow fans," ASME Paper, (GT2007-27465).
- [78] Wisler, D., 1985, "Tip clearance effects in axial turbomachines," Von Karman Institute for fluid dynamics Lecture Series, (5).

- [79] Akturk, A. and C., C., 2010, "Axial flow fan tip leakage flow control using tip platform extensions," *J. Fluids Eng.*, **132**(5).
- [80] Akturk, A. and C., C., 2010, "Influence of tip clearance and inlet flow distortion on ducted fan performance in vtol uavs," 6th AHS Forum, (AHS 2010-338).
- [81] Akturk, A. and C., C., 2009, "Piv measurements and computational study around 5-inch ducted fan v/stol uav," 47th AIAA Aerospace Sciences Meeting and Exhibit, (AIAA-2009-332).
- [82] Akturk, A. and C., C., 2009, "Double ducted fan (ddf) for performance improvements in vtol uavs," The Pennsylvania State University, Invention Disclosure No: 2009-3639.
- [83] DANTEC, 2000, "Flowmap particle image velocimetry instrumentation-installation & user's guide," .
- [84] ANSYS, 2009, "Anssys-fluent v12 user's guide," .
- [85] Corp, U. S., "United sensors corporation kiel probe: general information," <http://www.unitedsensorcorp.com/kiel.html>.
- [86] Yarusevych, S., Sullivan, P., and Kawall, J., 2009, "Smoke-wire flow visualization in separated flows at relatively high velocities," *AIAA Journal*, **4**(6).
- [87] ANSYS, 2009, "Anssys-cfx solver theory guide," .
- [88] ANSYS, 2009, "Anssys-cfx solver modeling guide," .
- [89] Wilcox, D. C., 1993, *Turbulence modeling for CFD*, La Caada: DCW Industries, Canada.
- [90] Ott, R. L. and Longnecker, M. T., 2000, *An Introduction to Statistical Methods and Data Analysis*, Duxbury Press, California.
- [91] Yoeli, R., 2010, "Fancraft: Extending the reach of aviation," AHS 66th forum Phoenix, Arizona.
- [92] Automation, A. I., 2010, *ATI Delta Six-Axis Force/Torque Sensor System Compilation of Manuals*.
- [93] Abemethy, R. B., Benedict, R. P., and B., D. R., 1985, "Asme measurement uncertainty," *ASME Journal of Fluids Engineering*.
- [94] Abemethy, R. B. and B., R., 1985, "The history and statistical development of the new asme-sae-aiaa-iso measurement uncertainty methodology," *AIAA/SAE/ASME/ASEE 21st Joint Propulsion Conference & Exhibit*.

Vita

Ali Aktürk

Ali Aktürk was born on June 23rd 1980 in Kırıkkale, Turkey to Ruhiye and Kemal Aktürk. He graduated from Middle East Technical University Aerospace Engineering department in June 2003 with Bachelor of Science degree in Aerospace Engineering. He then attended the same department where he obtained in July 2005 his Master of Science in Aerospace Engineering. During his studies, he spent two years (2003-2005) working for Turkish Aerospace Industries (TAI) in Ankara, Turkey. He then came to The Pennsylvania State University where he began the Ph. D. program in the Aerospace Engineering department in 2006. He is a member of the American Institute of Aeronautics and Astronautics, American Helicopter Society and American Society of Mechanical Engineers.